# Preparation of fly ash-$TiO_2$-metal hybrid composites for adsorption and photocatalytic applications

*A thesis submitted for the award of the degree of*

**Doctor of Philosophy**

*Submitted by*

RIDHIMA SHARMA

**Roll no: 902009030**

**Dr. Bonamali Pal**
**Professor**
**DCBC**

**Dr. Sanghamitra Barman**
**Professor**
**CHED**

THAPAR INSTITUTE
OF ENGINEERING & TECHNOLOGY
(Deemed to be University)

7/1/2026

7/1/2026

**DEPARTMENT OF CHEMISTRY & BIOCHEMISTRY**

**THAPAR INSTITUTE OF ENGINEERING AND TECHNOLOGY**

**PATIALA-147004, INDIA**

**June 2026**

12/01/26

# Certificate

This is to certify that the work incorporated in this thesis entitled "**Preparation of fly ash–$TiO_2$–metal hybrid composites for adsorption and photocatalytic applications,**" submitted by Ridhima Sharma to the Department of Chemistry and Biochemistry, Thapar Institute of Engineering and Technology, Patiala, in fulfillment of the requirements for the award of the Degree of Doctor of Philosophy, embodies the authentic research work carried out by the candidate under my supervision and guidance.

We also certify that the work represented in this thesis is original and has not been submitted to any other University or Institution in part or whole for the award of any degree or diploma.

**(Supervisor)**

**Dr. Bonamali Pal**
Professor
Department of Chemistry and Biochemistry
Thapar Institute of Engineering and Technology
Patiala-147004, India

**(Supervisor)**

**Dr. Sanghamitra Barman**
Professor
Department of Chemical Engineering
Thapar Institute of Engineering and Technology
Patiala-147004, India

**(Head)**

**Dr. Manmohan Chhiber**
Professor
Department of Chemistry and Biochemistry
Thapar Institute of Engineering and Technology
Patiala-147004, India

# Candidate's Declaration

I, hereby declare that the work presented in the thesis entitled "**Preparation of fly ash–$TiO_2$–metal hybrid composites for adsorption and photocatalytic applications,"** in fulfillment of the requirement for the award of the Degree of Doctor of Philosophy, submitted to the Department of Chemistry and Biochemistry, Thapar Institute of Engineering and Technology, Patiala is an authentic record of my work carried out under the supervision of Dr. Bonamali Pal (Professor, Department of Chemistry and Biochemistry, Thapar Institute of Engineering and Technology, Patiala, India) and Dr. Sanghamitra Barman (Professor, Department of Chemical Engineering, Thapar Institute of Engineering and Technology, Patiala, India). The matter embodied in this thesis has not been submitted in part or whole to any other university or institute for the award of any degree in India or abroad.

**Ridhima Sharma**

**Dr. Bonamali Pal**

Professor and Supervisor

Department of Chemistry and Biochemistry

Thapar Institute of Engineering and Technology

Patiala-147004

**Dr. Sanghamitra Barman**

Professor and Supervisor

Department of Chemical Engineering

Thapar Institute of Engineering and Technology

Patiala- 147004

# Acknowledgment

The completion of this thesis would not have been possible without the support and encouragement of several notable people. Hence, I would like to take this opportunity to express my gratitude to all those who have assisted me in numerous ways.

I am deeply grateful to my supervisors, **Dr. Bonamali Pal** (Professor) and **Dr. Sanghamitra Barman** (Professor), for their unwavering support and insightful critiques throughout my research journey. Their strong commitment to academic quality and careful attention to detail have meaningfully contributed to the preparation of this thesis.

I sincerely acknowledge **Dr. Padamakumar Nair,** Honourable Director**, Dr. R.S. Kaler,** Dean of Research and Development Centre (DRDC)**, and Dr. Bhupendrakumar Chudasama,** Associate Dean RDC, TIET, Patiala, for providing all the necessary facilities that have been immensely helpful in carrying out this research.

I sincerely thank **Dr. Manmohan Chhibber,** Professor and Head, Department of Chemistry and Biochemistry, Thapar Institute of Engineering and Technology, Patiala, for constantly encouraging all research scholars.

I gratefully acknowledge the doctoral committee members, **Dr. Soumen Basu, Dr. Banibrata Maity, and Dr. Rajeev Mehta**, who were involved in the validation survey for this research project. Their valuable suggestions and scientific discussions helped me present my research work better. I am obliged to all the authorities, technical and office staff in the DCBC, especially **Mr. Chander Thakur, Mr. Hemant,** and **Mr. Mayank Sharma,** for their cooperation and assistance during my research tenure.

I am eternally thankful to my friends and lab mates, **Dr. Mehak Bansal, Dr. Davinder Kaur, Dr. Priti Rohilla, Abinash Mohapatra, Dr. Sukhandeep Kaur, Shifali, Damanjot Kaur, Dr. Jemini, Shreya Sharma, Kirti Bisht, Ravneet Kaur, Samridhi Kochar, Chandini, Dr. Rajneesh Kumar Verma, Dr. Yogita Bohra, and Dr. Varinder Sardana** for their continual love, support, and friendship made this journey easier.

I am forever indebted to my parents, **Dr. Vineet Kumar Sharma** and **Mrs. Rashmi Sharma**. I have always looked up to them, and I hope to make them proud with this achievement. Throughout this journey, I would like to acknowledge the endless love and encouragement of my brother, **Shivam Sharma.**

I am deeply grateful to my life partner **Mr. Vivek Prashar** for his endless support, understanding, and encouragement throughout this research journey.

I would also like to express my deepest gratitude to my beloved grandparents **Smt. Chanderkanta Vyas** and **Smt. Kamla Dohroo**, for their unconditional love, blessings, and constant encouragement throughout my academic journey.

The help from different institutes and laboratories like SAI Lab TIET, Avantha Lab TIET, and SPRINT Mumbai is highly acknowledged. Besides these, I am grateful to the people who, knowingly or unknowingly, helped me during the successful completion of this work.

Ridhima Sharma

*Dedicated*

*To*

*My Parents*

# Table of contents


| | |
|---|---|
| **Abbreviations** | i-ii |
| **Symbols** | iii-iv |
| **Abstracts** | iv-vii |


# Chapter-1

## Introduction and literature review


| | |
|---|---|
| **1.1 Introduction** | **1-20** |
| Adsorption & photocatalytic degradation | 1 |
| 1.1.2 Utilization of fly ash as support | 2 |
| 1.1.3 Limitations of fly ash in pollutant removal | 3 |
| 1.1.4 Fly ash-$TiO_2$ (FT) composite for improved photocatalytic activity | 3 |
| 1.1.5 Cu photo-deposited fly ash -$TiO_2$ composite (FT-Cu) for visible light activation | 4 |
| 1.1.6 Zeolite (ZSM-5) modified fly ash-$TiO_2$- metal (ZFT-Cu) composite | 5 |
| 1.1.7 Literature survey | 7 |
| **1.2 Research gaps** | **11** |
| **1.3 Objectives** | **11** |
| **1.4 Characterization techniques** | **12-13** |
| 1.4.1 X-ray diffraction (XRD) analysis | 12 |
| 1.4.2 Morphological analysis | 12 |
| 1.4.3 Surface area and pore size analysis | 12 |
| 1.4.4 Optical absorption and band gap analysis | 12 |
| 1.4.5 X-ray photoelectron spectroscopy (XPS) analysis | 13 |
| 1.4.6 Raman analysis | 13 |
| | 13 |
| **1.5 Adsorption and photocatalytic studies** | **14-15** |
| 1.5.1 Adsorption studies | 14 |
| 1.5.2 Photocatalytic degradation analysis | 14 |

| | |
|---|---|
| **References** | **16-20** |


# Chapter-2

## Utilization of fly ash-$TiO_2$ composites for efficient adsorption and photocatalytic degradation of fuchsin blue dye


| | |
|---|---|
| **2.1 Introduction** | **21-23** |
| **2.2 Experimental section** | **24-26** |
| 2.1.1 Chemicals and reagents | 23 |
| 2.2.2 Synthesis of $TiO_2$ | 23 |
| 2.2.3 Synthesis of FA- $TiO_2$ (FT) composites | 24 |
| 2.2.4 Catalyst characterization | 24 |
| 2.2.5 The point of zero charge (PZC) of the composite | 25 |
| 2.2.6 Adsorption of FB dye | 25 |
| 2.2.7 Photocatalytic degradation of FB dye | 26 |
| **2.3 Results and discussion** | **26-37** |
| 2.3.1 X-Ray diffraction analysis | 26 |
| 2.3.2 Raman analysis | 29 |
| 2.3.3 BET analysis | 29 |
| 2.3.4 UV-vis diffuse reflectance spectroscopy | 30 |
| 2.3.5 Scanning electron microscopy | 31 |
| 2.3.6 EDS spectra | 32 |
| **2.4 Adsorption Studies** | **37-49** |
| 2.4.1 The effect of adsorbent dosage on the removal of FB dye | 33 |
| 2.4.2 The effect of adsorbate initial concentration on the removal of FB dye | 33 |
| 2.4.3 The effect of contact time on the removal of FB dye | 34 |
| 2.4.4 The effect of pH on the removal of FB dye | 35 |
| 2.4.5 Adsorption equilibrium studies | 36 |
| 2.4.6 Adsorption kinetic studies | 37 |
| **2.5 Photocatalytic degradation of FB dye** | **39** |
| **2.6 Degradation pathway analysis** | **41** |
| **2.7 Reusability studies** | **42** |
| **2.8 Plausible mechanism** | **43** |
| **2.9 Conclusion** | **44** |
| **References** | **44-47** |

# Chapter-3

## Influence of copper deposition on fly ash–$TiO_2$ composites for combined adsorption and visible-solar photocatalytic degradation of fuchsin blue


| | |
|---|---|
| **3.1 Introduction** | **48-51** |
| **3.2 Materials and methods** | **51-53** |
| 3.2.1 Materials and reagents | 51 |
| 3.2.2 Characterization methods of prepared samples | 51 |
| 3.2.3 Cu photo deposited fly ash-$TiO_2$ (FT-Cu) composite | 51 |
| 3.2.4 Measurement of point of zero charge(pzc) of composite | 52 |
| 3.2.5 Dark adsorption study of fuchsin blue dye | 53 |
| 3.2.6 Photocatalytic degradation study | 54 |
| **3.3 Results and discussion** | **55-62** |
| 3.3.1 XRD analysis | 55 |
| 3.3.2 FESEM, HRTEM and EDS analysis | 59 |
| 3.3.3 Surface area and pore size analysis | 60 |
| 3.3.4 Optical absorption and band gap analysis | 61 |
| 3.3.5 XPS analysis | 62 |
| **3.4 Adsorption study** | **63-68** |
| 3.4.1 Effect of adsorbent dosage on the removal of FB dye | 63 |
| 3.4.2 Impact of initial dye concentration on FB dye removal | 65 |
| 3.4.3 The effect of contact times on the removal of FB dye | 65 |
| 3.4.4 The pH effect on FB dye removal | 65 |
| 3.4.5 Adsorption isotherm studies | 66 |
| 3.4.6 Adsorption kinetics | 68 |
| 3.5.1 Photocatalytic degradation under visible light | 71 |
| 3.5.2 Photocatalytic degradation of FB under direct sunlight | 72 |
| 3.5.3 Active species detection | 73 |
| **3.6 Proposed photocatalytic degradation mechanism** | **74** |

| | |
|---|---|
| **3.7 Identification of intermediate photo products during the FB dye degradation pathway** | **75** |
| **3.8 Photostability and reusability of prepared photocatalysts** | **76** |
| **3.9 Conclusion** | **78** |
| **References** | **79-84** |


# Chapter-4

## Fabrication and evaluation of ZSM-5-fly ash–$TiO_2$–Cu hybrid catalysts for efficient photocatalytic and adsorptive removal of crystal violet dye


| | |
|---|---|
| **4.1 Introduction** | **85-88** |
| **4.2 Materials and methods** | **89-91** |
| 4.2.1 Materials and reagents | 89 |
| 4.2.2 Techniques used for characterizing the synthesized sample | 89 |
| 4.2.3 Synthesis of ZSM-5 loaded fly ash-$TiO_2$-Cu (ZFT-$Cu_1$) composite | 89 |
| 4.2.4 Adsorption in dark and photocatalytic studies | 91 |
| **4.3 Results and discussion** | **92-98** |
| 4.3.1 XRD analysis | 92 |
| 4.3.2 FESEM analysis | 92 |
| 4.3.3 EDS analysis | 95 |
| 4.3.4 FT-IR analysis | 96 |
| 4.3.5 BET surface area and pore size distribution | 97 |
| 4.3.6 DRS analysis of ZFT-Cu | 98 |
| **4.4 Adsorption study on crystal violet dye (CV)** | **99-109** |
| 4.4.1 Influence of adsorbent dosage on CV dye removal | 99 |
| 4.4.2 Role of initial dye concentration on the removal of CV dye | 100 |
| 4.4.3 Impact of contact duration on the removal of CV dye | 101 |
| 4.4.4 The effect of solution pH on CV dye removal | 101 |
| 4.4.5 Adsorption isotherm studies | 103 |
| 4.4.6 Adsorption kinetic studies | 107 |

| | |
|---|---|
| **4.5 Photocatalytic studies** | **108-111** |
| **4.5.1 Photocatalytic efficacy under visible light irradiation** | **109** |
| **4.5.2 Photocatalytic degradation under direct sunlight** | **111** |
| **4.6 Detection of active species** | **112** |
| **4.7 Proposed photocatalytic degradation mechanism** | **114** |
| **4.8 Reusability and photostability of the prepared photocatalysts** | **115** |
| **4.9 Conclusion** | **117** |
| **References** | **118-123** |
| **Conclusion and future aspects** | **124** |
| **List of publications** | **125** |
| **Conferences and workshops** | **126** |
| **Publication front pages** | **127-129** |

# Abbreviations

| | |
|---|---|
| µl | Micro-liter |
| a.u. | Arbitrary unit |
| FB | Fuchsin blue |
| Ar | Argon |
| B.E. | Binding energy |
| BET | Brunauer Emmett Teller |
| BJH | Barrett-Joyner-Halenda |
| CB | Conduction band |
| DI | Deionized |
| DRS | Diffuse reflectance spectroscopy |
| CV | Crystal Violet |
| EDA | ethylenediamine |
| EDS | Energy dispersive X-ray spectroscopy |
| Eg | Band gap |
| eV | Electron volt |
| VB | Valence band |
| FESEM | Field emission scanning electron microscopy |
| HRTEM | High-resolution transmission electron microscopy |
| IPA | Isopropyl alcohol |
| HR-MS | High resolution-Mass spectroscopy |
| Mg | Milli gram |

| | |
|---|---|
| Min | minute |
| mL | Milli-litre |
| mM | Milli molar |
| nM | Nanometre |
| NMs | Nanomaterials |
| NPs | Nanoparticles |
| Ppm | Parts per million |
| SAED | Selected area diffraction |
| SC | Semiconductor |
| SEM | Scanning electron microscopy |
| SPR | Surface plasmon resonance |
| TEM | Transmission electron microscopy |
| $TiO_2$ | Titanium di-oxide |
| TBT | Titanium butoxide |
| UV | Ultraviolet |
| VB | Valence band |
| Vis | Visible |
| wt% | Weight percentage |
| XPS | X-ray photoelectron spectroscopy |
| XRD | X-ray diffraction spectroscopy |

# Symbols

| | |
|---|---|
| $e^-$ | Electron |
| $h^+$ | Hole |
| $\cdot O_2^-$ | Superoxide radical |
| $\cdot OH$ | Hydroxyl radical |
| Å | Angstrom |
| A | Absorption coefficient |
| A | Absorbance |
| ° | Degree |
| Λ | Wavelength |
| $\Lambda_{max}$ | Wavelength of maximum absorption |
| Cu | Copper |
| % | Percentage |
| M | Micro |
| M | Meter |
| hr | Hour |
| Y | Light frequency |
| Θ | Theta |
| S | Second |

| | |
|---|---|
| V | Volt |
| G | Gram |
| Mg | Milligram |
| $E_f$ | Fermi energy |
| W | Watt |
| H | Planck constant |
| *K* | Pseudo first-order rate constant $min^{-1}$ |

# Abstracts

## Chapter-1

This chapter provides an overview of adsorption and semiconductor photocatalysis as effective strategies for wastewater treatment, with a focus on fly ash–$TiO_2$–metal–zeolite hybrid materials. It discusses the environmental impact of industrial effluents and the drawbacks of conventional remediation technologies. The chapter highlights the role of fly ash as an inexpensive, porous support, its functionalization with $TiO_2$ to enhance photocatalytic activity, and subsequent performance improvements achieved through metal doping and zeolite incorporation. A critical review of recent studies illustrates how these components work synergistically to broaden light absorption, enhance charge separation, and improve catalyst durability for degrading dyes. Methods for material synthesis, structural and optical characterization, and performance evaluation are summarized. The chapter concludes by identifying existing research gaps and emphasizing the need for advanced hybrid composites capable of achieving superior efficiency under visible and solar light irradiation.

## Chapter-2

This study emphasizes the need to achieve both high photocatalytic efficiency and strong adsorption capacity in a catalyst to ensure complete removal of fuchsine blue dye (FB) from wastewater. In this work, $TiO_2$ and fly ash–$TiO_2$ composites (0.5–5wt%) were prepared using a sol–gel method combined with wet impregnation, and their performance was evaluated for combined processes of adsorption and photocatalytic breakdown of fuchsin blue dye. The materials were characterized using XRD, UV–DRS, SEM, EDS, Raman spectroscopy, and $N_2$ adsorption analysis. Adsorption and degradation experiments were conducted to evaluate the effects of pH (2–10), adsorbent dosage (1–9 mg), contact time (30–180 min), and initial dye concentration (5–30 mg/L) on FB dye removal efficiency. Among the tested samples, the 5 wt% fly ash–$TiO_2$ composite exhibited the highest adsorption capacity of 20.32 mg/g and achieved 76% FB dye removal. These results indicate that adsorption occurs primarily through monolayer coverage on a homogeneous surface, in agreement with the Langmuir isotherm, and governed by pseudo-first-order kinetics. Under UV irradiation, the same 5wt% fly ash–$TiO_2$ composite reached a maximum photocatalytic degradation of 88% after 180 minutes, following pseudo-first-order kinetics. The catalyst demonstrated excellent reusability, maintaining its dye removal performance consistent over five consecutive cycles.

## Chapter-3

In this study, copper (Cu) photo-deposited fly ash-$TiO_2$ composites (FT-$Cu_{0.5-2}$) with Cu content ranging from 0.5 to 2wt% were synthesized to evaluate their adsorption and photocatalytic activity toward the photodegradation of fuchsin blue (FB) dye under visible light as well as natural sunlight. Structural characterization was performed using X-ray diffraction (XRD) and diffuse reflectance spectroscopy (DRS), while morphological and surface chemical analyses were carried out through high-resolution transmission electron microscopy (HR-TEM), X-ray photoelectron spectroscopy (XPS), and $N_2$ adsorption Brunauer-Emmett-Teller (BET) analysis. These confirmed the successful fabrication of fly ash-$TiO_2$ (FT) and Cu-modified composites (FT-$Cu_{0.5-2}$). Copper nanoparticles, with sizes in the range between 7 and 17 nm, were uniformly distributed on the FT composite surface. The impact of various adsorption parameters, including FB dye concentration, adsorbent dose, solution pH, and contact duration, was systematically investigated. Following 180 minutes of adsorption in the dark, the 1wt% Cu-loaded FT composite (FT-$Cu_1$) showed the highest dye removal efficiency of 77% and fitted well to the Langmuir adsorption model. A notable enhancement in photocatalytic activity was observed for FT-$Cu_1$, which achieved 92% FB degradation under sunlight and 94% under visible light, compared to the unmodified FT catalyst with only 68% and 71% removal, respectively. This enhancement in removal efficiency is attributed to the synergistic interaction between Cu, fly ash, and $TiO_2$ components. The presence of Cu improved the efficient separation of photogenerated charge carriers and expanded visible light absorption by introducing intermediate energy states within the $TiO_2$ bandgap. The degradation pathway of FB dye was elucidated via trapping experiments using hole scavengers and detection of intermediate species through High-Resolution Mass Spectrometry (HRMS). Additionally, the FT-Cu composite exhibited strong photostability and could be reused effectively, maintaining approximately 83% degradation efficiency after five consecutive cycles, demonstrating its potential for sustainable treatment of organic contaminants.

## Chapter-4

In this work, copper photo-deposited fly ash–$TiO_2$ (FT-$Cu_1$) composites were modified with ZSM-5 zeolite at loadings of 1%, 3%, and 5% by weight, designated as 1ZFT-$Cu_1$, 3ZFT-$Cu_1$, and 5ZFT-$Cu_1$, respectively. These composites were investigated for their capability to adsorb and photo-catalytically degrade crystal violet (CV) dye under visible and solar light exposure. Characterization techniques, including UV-Vis diffuse reflectance spectroscopy (DRS), field

emission scanning electron microscopy (FE-SEM), X-ray diffraction (XRD), and BET surface area analysis, revealed that the addition of ZSM-5 enhanced crystallinity, minimized particle aggregation, and increased visible light absorption by the composites. Among the samples, the 3wt% ZSM-5-loaded composite (3ZFT-$Cu_1$) exhibited the best photocatalytic performance, achieving dye removal efficiencies of 98% under visible light and 95% under solar irradiation, using a catalyst dosage of 5 mg, initial dye concentration of 5 mg/L, a contact time of 180 minutes, and solution pH 9. The adsorption process fitted well with the Freundlich isotherm model, indicating multilayer adsorption, while the degradation kinetics followed a pseudo-first-order rate. The superior activity is credited to the synergistic interaction of copper doping, the porous structure of ZSM-5, and the fly ash support, which collectively enhanced light absorption and dye uptake. The 3ZFT-$Cu_1$ composite also showed commendable stability, retaining 84% of its degradation efficiency after five cycles of reuse. Free radical trapping studies using hole scavengers elucidated the photocatalytic degradation pathway of CV dye, highlighting the composite's effectiveness under visible light for potential wastewater treatment applications

# Chapter-1

## Introduction and literature review

### 1.1 Introduction

Rapid technological advancements and transformations in human lifestyles have greatly accelerated the emergence of intricate environmental and social issues. To lessen these negative effects, it is now crucial to develop prompt and efficient remedial techniques. The increasing demand for water, caused by industrialisation, agricultural development, and population growth, has increased wastewater output, demanding good resource management. [1]. The pervasive increase in pollution has become a serious global issue that is negatively damaging the marine environment and people's health. [2]. Improper treatment of industrial effluents generated from diverse sectors, such as food and beverage processing, paper and pulp manufacturing, textiles, dyeing, and chemical industries, has resulted in the continuous discharge of large volumes of contaminated wastewater into natural water bodies, streams, and rivers. [3]. Dyes, owing to their complex chemical structures, pose a substantial threat to aquatic ecosystems, with adverse effects on human health, as well as plant and animal life [4]. Some synthetic dyes are known to negatively affect vital organs such as the kidneys, liver, heart, brain, nerve system, skin, and certain compounds within this group may also act as mutagens or carcinogens. Several physical, chemical, and biological approaches have been developed to mitigate water pollution [5,6]. Methods that are very effective in eliminating big particles and solids include coagulation [7], membrane filtration, biofiltration [8], and electrochemical oxidation [9]. However, their high operating costs and the requirement for proper secondary waste management prevent these methods from being widely used. Among the emerging alternative techniques, adsorption and photocatalytic degradation have gained significant prominence. [10]. These techniques have garnered significant interest due to their eco-friendly nature, high reproducibility, and effectiveness in eliminating persistent organic contaminants. [11].

### 1.1.1 Adsorption & Photocatalytic Degradation

Adsorption is extensively employed because of its straightforward operation, cost-effectiveness, and excellent removal efficiency. [12]. Various materials, including activated carbon [13], zeolites [14], fly ash [15], and lignocellulose-based substances [16], have demonstrated remarkable performance in water purification processes. However, adsorption faces key limitations, including the requirement for adsorbent regeneration, challenges in managing secondary waste, and a reduction in performance after multiple cycles of reuse. [17]. Unlike adsorption, photocatalytic degradation facilitates the breakdown of organic contaminants under sunlight exposure, effectively minimizing the generation of secondary waste. [18]. Widely investigated photocatalytic materials comprise ZnO. [19], $WO_3$ [20], g-$C_3N_4$ [21], and a range of $TiO_2$-based semiconductors that have been doped or structurally modified to enhance their performance. The synergistic integration of adsorption and photocatalysis offers an efficient strategy for removing organic pollutants. Initially, pollutants are adsorbed onto the material, preventing photocatalyst surface fouling. Upon light exposure, photocatalysis then mineralizes the adsorbed contaminants into harmless byproducts like $CO_2$ and $H_2O$, regenerating the catalyst surface and enhancing long-term efficiency and sustainability. [22].

### 1.1.2 Utilization of fly ash as support

Fly ash, a waste product from coal combustion, is increasingly recognized as a low-cost and widely available support material in pollution control technologies. The synergy of its porosity, high surface area, and reactive surface sites makes it an excellent host matrix for binding photocatalytic and adsorptive materials. [23]. Fly ash serves as an effective support material, promoting better dispersion, enhanced durability, and improved reusability of active agents such as $TiO_2$, ZnO, and metal nanoparticles. Its aluminosilicate structure provides good ion-exchange capacity and mechanical stability under different environmental conditions. Employing fly ash in this role not only boosts the effectiveness of contaminant removal processes but also contributes to sustainable material reuse and environmental conservation. [24].

### 1.1.3 Limitations of fly ash in pollutant removal

Although fly ash holds considerable potential for pollutant removal, its practical application is limited by several challenges. A major concern is the risk of releasing toxic metals and other harmful substances inherently present in raw fly ash, which can introduce secondary

contamination. Furthermore, inconsistencies in its physicochemical properties, such as composition, particle size, and surface morphology due to variations in fuel type and combustion conditions, may lead to unpredictable treatment performance. In its unmodified form, fly ash often exhibits limited adsorption efficiency for certain contaminants, necessitating chemical or physical activation to improve its functionality. These modifications, however, can increase both the operational complexity and overall treatment cost. Additional issues, such as difficulty in recovering the material after treatment, reduced effectiveness over repeated cycles, and the need for environmentally sound disposal methods, also pose significant barriers to its large-scale use in wastewater treatment [24, 25].

### 1.1.4 Fly ash-$TiO_2$ (FT) composite for improved photocatalytic activity

The combination of titanium dioxide ($TiO_2$) with fly ash has gained attention as an effective method to enhance photocatalytic efficiency and mitigate the individual shortcomings of both materials. $TiO_2$ is a well-established photocatalyst due to its high oxidative strength, chemical inertness, and capability to degrade various organic contaminants under light irradiation. [26]. Nevertheless, its practical deployment faces several constraints, including limited surface area, rapid recombination of photogenerated charge carriers, and challenges in post-treatment separation.

Utilizing fly ash as a supporting material for $TiO_2$ (shown in **Scheme 1.1**) addresses many of these limitations. The inherent porosity and extensive surface area of fly ash promote uniform dispersion of $TiO_2$ particles, which improves light utilization and interaction with pollutants. Immobilizing $TiO_2$ on the fly ash matrix also enhances catalyst durability, reduces nanoparticle aggregation, and facilitates recovery and reuse. [27]. Additionally, the naturally occurring metal oxides and silica in fly ash may further aid in photocatalytic efficiency by assisting in charge separation or acting as co-active sites. [28]. The resulting composite harnesses both the adsorption potential of fly ash and the photocatalytic power of $TiO_2$, presenting a cost-effective and environmentally friendly solution for treating wastewater contaminated with recalcitrant organic compounds.

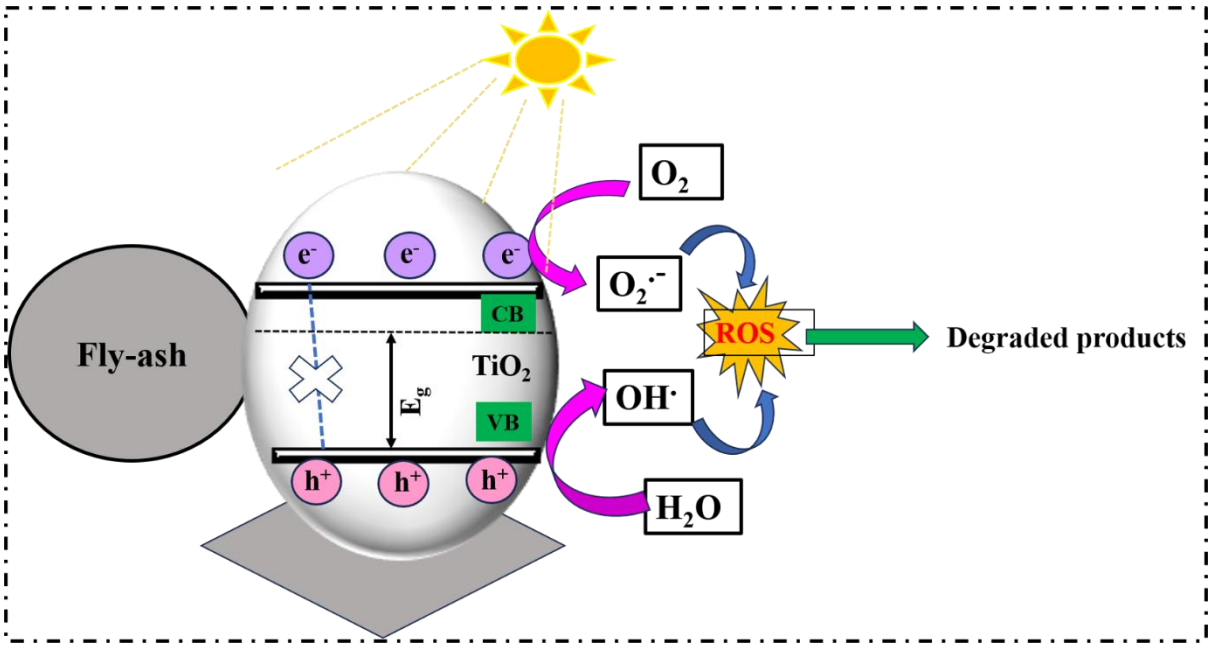


**Scheme 1.1** A schematic illustration of the photocatalytic mechanism over fly ash-$TiO_2$ (FT) Composite

### 1.1.5 Cu photo-deposited fly ash-$TiO_2$ composite (FT-Cu) for Visible-Light Activation

Metal doping of fly ash–$TiO_2$ composites (shown in **Scheme 1.2**) offers a compelling strategy to boost photocatalytic efficiency under visible light irradiation. Since pristine $TiO_2$ is primarily active under UV light owing to its wide band gap (~3.2 eV), introducing transition metals like Cu, Fe, Ag, or Ni can create intermediate electronic states that facilitate visible-light activation [29–31] Among these, copper stands out by forming $Cu^{+}/Cu^{2+}$ redox pairs, which enhance charge separation and act as effective electron traps, thereby minimizing recombination. Additionally, copper's strong affinity with $TiO_2$ and its economic viability make it more favourable than many other dopants. [32]. Supporting the composite with fly ash further enhances surface area, improves $TiO_2$ dispersion, and provides structural durability. Together, the adsorption properties of fly ash, the oxidative degradation ability of $TiO_2$, and the extended light responsiveness from metal doping create a synergistic system for efficient pollutant removal under ambient light conditions.

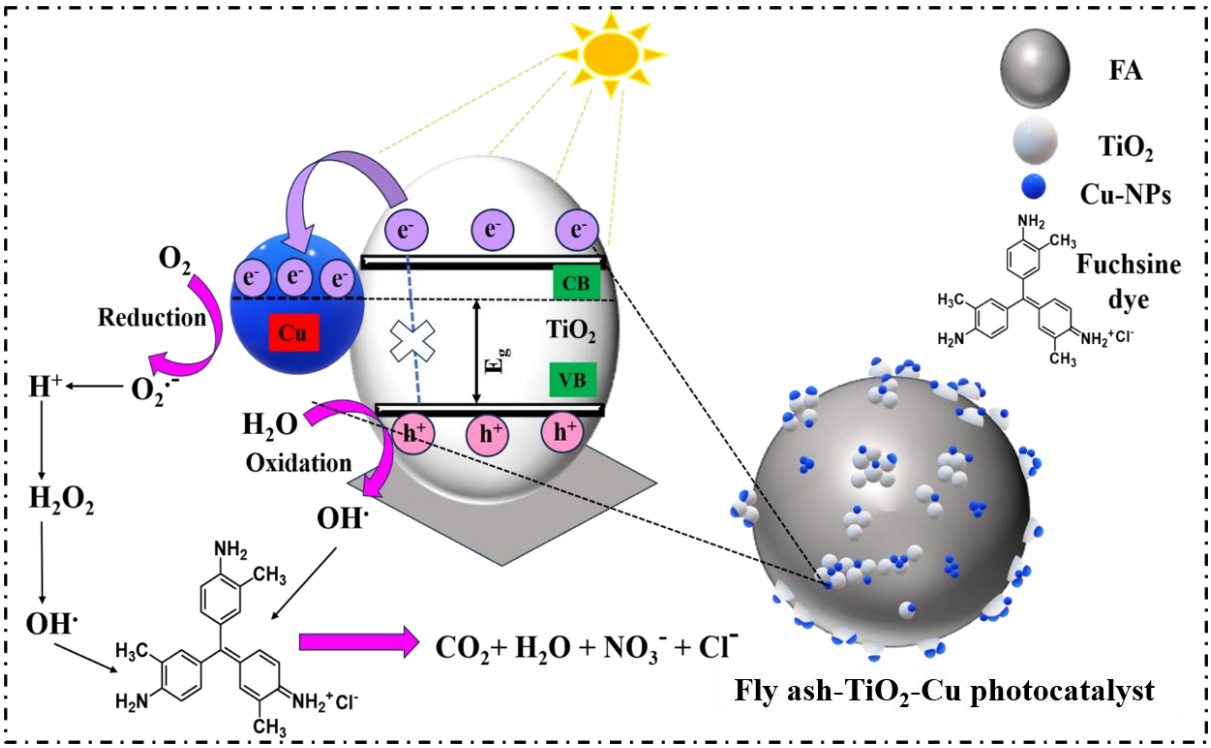


**Scheme 1.2** The proposed mechanism of fuchsin blue dye degradation by copper-doped fly ash-$TiO_2$ (FT-Cu) under visible-solar light**.**

### 1.1.6 Zeolite (ZSM-5) modified fly ash-$TiO_2$-metal (ZFT-Cu) composite

In the development of multifunctional materials for environmental remediation, the addition of zeolites to composite systems has garnered considerable attention. The integration of zeolites, particularly ZSM-5, into fly ash–$TiO_2$–metal composites significantly augments their photocatalytic and adsorptive efficiency. ZSM-5, known for its high surface area, well-organised microporous framework, and strong ion-exchange capacity, facilitates the accumulation of pollutants near the reactive sites, thereby increasing contact efficiency [33]. Its presence in the composite promotes enhanced dispersion of $TiO_2$ and metal dopants while maintaining structural porosity for improved light penetration. Additionally, the acidic nature and cation-exchange properties of ZSM-5 can influence the electronic characteristics of the composite, aiding in better charge carrier separation and redox reactions. This synergistic effect contributes to improved catalytic performance, structural stability, and long-term reusability under solar or visible-light-driven pollutant degradation conditions. [34].

The synthesis of multifunctional hybrid composites combining fly ash, $TiO_2$, metal dopants, and zeolites has emerged as an effective approach for addressing complex water pollution challenges. Each component plays a complementary role: fly ash acts as a porous [35], low-cost support that enhances the dispersion and anchoring of active photocatalytic materials; $TiO_2$

serves as the core semiconductor, capable of generating reactive species for pollutant degradation. However, pure $TiO_2$ exhibits photocatalytic activity predominantly under UV irradiation owing to its wide bandgap, and its efficiency is further limited by the rapid recombination of photogenerated charges [36, 37]. To address these limitations, metal doping, especially with elements like Cu, is employed to induce localized energy states inside the band structure, hence improving visible light absorption.

Incorporating ZSM-5 zeolites into the fly ash-$TiO_2$-Cu composite further improves the efficiency of the composite by offering a high surface area, uniform pore distribution, and strong adsorption capacity. These properties enable effective concentration of pollutants near catalytic sites and contribute to improved light penetration and mass transfer. [38]. (shown in **Scheme 1.3**).

Overall, this synergistic material design not only improves the degradation of recalcitrant organic pollutants in wastewater but also supports sustainable remediation strategies by utilizing industrial byproducts like fly ash. Such hybrid systems are promising materials for practical wastewater treatment, especially under visible or solar light conditions.

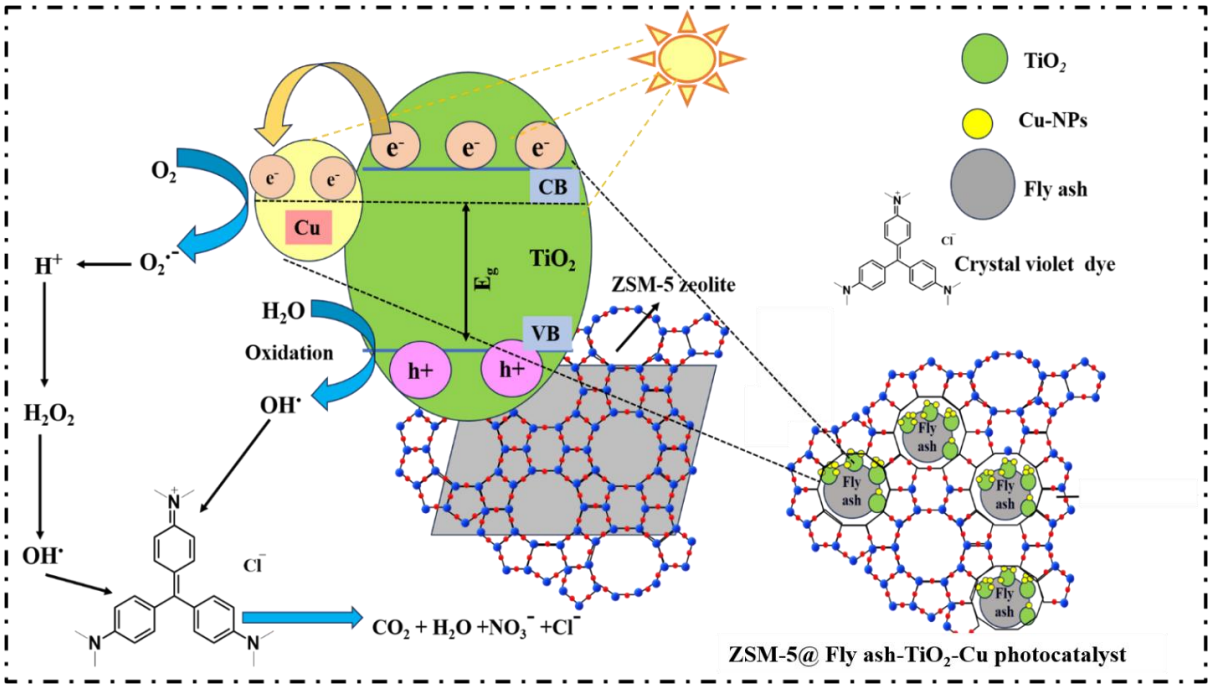


**Scheme 1.3** The photocatalytic degradation mechanism of crystal violet dye by ZFT-Cu composite.

### 1.1.7 Literature Survey

A wide range of studies has reported the application of fly ash–$TiO_2$ composites, metal-doped fly ash–$TiO_2$ systems, and zeolite-modified fly ash–$TiO_2$ composites for the adsorption and photocatalytic removal of various pollutants, including dyes, antibiotics, pesticides, and pharmaceuticals. Representative findings from these studies are summarized in **Table 1.1.**

Mpelane et al. [39] prepared a C–$TiO_2$–coal fly ash (CFA) nanocomposite using the sol–gel method, followed by immobilization onto a polyacrylonitrile (PAN) membrane through phase inversion. The incorporation of carbon and the high specific surface area of the composite (114 $m^2/g$) contributed to its outstanding photocatalytic efficiency. When tested under sunlight for 300 minutes, the material achieved degradation rates of 99.8% for methyl orange (MO) and 99.2% for gentian violet (GY), highlighting its potential for solar-driven wastewater treatment.

Tu et al. [40] developed a fly ash cenosphere (FAC)-supported $TiO_2$ composite using a wet mechanical grinding method, enabling even distribution of nano-$TiO_2$ across the FAC surface. This photocatalyst effectively removed 98% of methyl orange from aqueous solutions and performed on par with commercial P25 $TiO_2$, all while utilizing a reduced amount of $TiO_2$. The study highlights its potential as a more economical and efficient option for real-world wastewater treatment applications**.**

Sawunyama et al. [41] synthesized a cost-effective ceramic membrane by modifying coal fly ash with $TiO_2$ and ZnO through co-pressing and sintering techniques. The resulting composite showed notable photocatalytic activity under visible light, removing around 77% of tetracycline within 100 minutes. It also maintained about 73% of its efficiency after five consecutive cycles, highlighting its durability and potential for repeated use. The synergistic integration of ZnO and $TiO_2$ onto the fly ash matrix improved both light harvesting and charge separation, making it a viable and sustainable option for eliminating antibiotics from contaminated water sources.

Song et al. [42] synthesized a floating photocatalyst by incorporating iron (Fe) and nitrogen (N) co-doped $TiO_2$ onto fly ash cenospheres through a sol–gel process. The Fe–N–$TiO_2$/FAC composite exhibited notable photocatalytic activity under visible light, achieving 92.6% degradation of Rhodamine B in 6 hours. The co-doping effectively broadened the light absorption spectrum and enhanced charge separation efficiency.

Lin and Ali [43] synthesized a $Fe^3$-doped ZnO/$TiO_2$ photocatalyst using the calcination method for dye removal. The optimized composite achieved 90.68% removal of methyl orange under incandescent light and 97.14% under sunlight after 4 hours, demonstrating high photocatalytic efficiency.

Visa et al. [44] produced a Pt/$TiO_2$–fly ash zeolite composite using a mild hydrothermal

synthesis. The material was applied for industrial dye removal, achieving about 25% removal of Brilliant Blue and 43.9% of Brilliant Red under sunlight in 360 minutes, which increased to 80.7% and 93.4%, respectively, when $H_2O_2$ was added.

Aghajari et al. [45] developed a nanocomposite photocatalyst comprising Ag-doped Fe–ZSM-5 supported on $TiO_2$ through a combination of hydrothermal synthesis and sol–gel methods. This multifunctional material was tailored for the degradation of Reactive Red 195 (RR195) dye under natural sunlight exposure. The inclusion of silver and iron into the ZSM-5@$TiO_2$ framework enhanced the photocatalyst's surface characteristics and light absorption in the visible region. Under optimized conditions (pH 3 and 400 mg/L dosage), the system achieved around 98% degradation of RR195 within 2 hours, while maintaining effective performance over several reuse cycles.

Cahyanti et al. [46] synthesized an Fe-doped $TiO_2$/zeolite H-A composite via the impregnation method to enhance photocatalytic performance. The incorporation of Fe into the $TiO_2$/zeolite structure improved light absorption and charge separation efficiency. When applied for methylene blue degradation under UV irradiation, the photocatalyst achieved approximately 89.6% removal within 50 minutes, demonstrating its high efficiency for dye wastewater treatment.

Sambakanya et al. [47] synthesized a carbon-doped $TiO_2$–$SnO_2$ nanocomposite supported on coal fly ash (C-$TiO_2$-$SnO_2$/CFA) via a sol-gel method subsequently calcined at 550 °C. The photocatalyst was applied for dye degradation, achieving 97.75 % removal of methyl orange and 99.25 % removal of methylene blue within 3 h under visible light.

Raashid et al. [48] synthesized a dual-catalyst system comprising $TiO_2$ as a photocatalyst and Fe-coated 4 Å zeolite as an ozonation catalyst for the degradation of CONFIDOR pesticide (imidacloprid). Under UV irradiation (253.7 nm, 250 W/m²) and an ozone flow rate of 100 mg/h, the combined catalytic process achieved over 99 % removal of imidacloprid within 20 minutes, demonstrating a 1.4-fold higher degradation rate compared to $TiO_2$ alone.

Ramutshatsha-Makhwedzha et al. [49] prepared a magnetic $Fe_3O_4$@$TiO_2$@zeolite nanocomposite using a sol–gel method, combining the magnetic properties of $Fe_3O_4$ for easy separation, the adsorption ability of $TiO_2$, and the high surface area and ion-exchange capacity of zeolite. The material was applied for the removal of levofloxacin from water, achieving a removal efficiency of 92.43–96.95 % and maintaining good reusability up to five adsorption–desorption cycles.

Mergenbayeva et al. [50] prepared $TiO_2$/zeolite (TZ) and $TiO_2$/ZSM-5 (TZSM) composites via

mechanical mixing and impregnation for SMX degradation, achieving 100 % removal in 10 min under UV light with a rate constant of 0.501 $min^{-1}$ (2.08× higher than $TiO_2$) and ~67 % mineralization within 120 min.

Li et al. [51] synthesized a CTAB-modified Mo-doped $TiO_2$ coated on fly ash cenosphere (CTAB-Mo-$TiO_2$/FAC) via a sol–gel method. The photocatalyst showed an extended absorption range (200–800 nm) and abundant oxygen vacancies, enabling enhanced visible-light activity. At a dosage of 2 g/L, it achieved 99.75 % removal of methylene blue (MB) within 60 min, compared to 42 % for Mo-$TiO_2$/FAC and 24 % for $TiO_2$/FAC.

Kanakaraju et al. [52] prepared a copper-doped $TiO_2$/fly ash composite (Cu–$TiO_2$/FA) using adsorption–photocatalysis synergy, optimized via response surface methodology. Under visible light, at a 2 g/L dosage and 5 ppm methyl orange (MO), it achieved 99.91 % removal of MO in 100 min, demonstrating a "capture-and-destroy" mechanism.

Gong et al. [53] developed an Ag-nanoparticle embedded magnetic fly ash composite (AgNPs/MCFA) by impregnation–reduction–sintering. Under visible light, it removed 99.89 % methyl orange in 15 min, with a degradation rate constant k = 0.3133 $min^{-1}$, and retained >90 % efficiency after five reuse cycles.

**Table 1.1** Summary of recent studies on fly ash-supported photocatalysts for dye and pollutant degradation under various light sources.

| S. No. | Photocatalyst | Pollutant(s) | Source of Light | Degradation / Removal Efficiency | Ref. |
|---|---|---|---|---|---|
| 1 | $TiO_2$-doped mesoporous silica (TDMS) from CFA | Rhodamine B, Acid Orange II | Not specified | 99.9% (RhB), 99.9% (AOII) in 6 h; TOC removal 90.3% / 84.1% | [54] |
| 2 | $TiO_2$/ZSM-5 (Z-T, 450 °C) | Methyl orange (MO) | UV light | ~99% | [55] |
| 3 | Na-Y/$TiO_2$–Pd | Methylene blue (MB) | Visible light | > 98% | [56] |
| 4 | NaP-zeolite@$TiO_2$ sheets | Methylene blue (MB) | Solar light | 99.6% in 2 h; > 90% COD reduction | [57] |
| 5 | Fe-$TiO_2$/BEA zeolite | Tetracycline | Visible light (50 W blue LED) | 100% in 90 min (3 wt% Fe) | [58] |
| 6 | CdS/$TiO_2$/$CeO_2$ on zeolite | Methylene blue (MB) | Visible light | ~99.9% (synthetic); ~78.7% (sewage); ~86% retained after 4 cycles | [59] |

| S. No. | Photocatalyst | Pollutant(s) | Source of Light | Degradation / Removal Efficiency | Ref. |
|---|---|---|---|---|---|
| 7 | $TiO_2$/HZSM-5 | Methyl orange (MO) | UV light | 82.4% after 3 reuse cycles | [60] |
| 8 | X-zeolite/$TiO_2$ from CFA | Methylene blue (MB) | Visible light | 98.36% (0.36 g/L, 30 min adsorption + 100 min photocatalysis) | [61] |
| 9 | $TiO_2$–zeolite composites (from CFA) | Methyl orange (MO) | UV light | 82.4% | [62] |
| 10 | $TiO_2$-modified fly ash (MFA) | Cd(II), Pb(II) | Adsorption (no light) | 94.3% (Cd), 93.1% (Pb) | [63] |
| 11 | Fe-$TiO_2$/HY zeolite | Methylene blue (MB) | Visible light | > 98% (10 wt% Fe-$TiO_2$/HY); UV degradation with $TiO_2$/HY | [64] |
| 12 | $TiO_2$-N/zeolite-NaY | Methylene blue (MB) | UV light | Up to 99% in 3 h | [65] |
| 13 | Z@Ag/$TiO_2$ | $Cd^{2+}$ adsorption | Not specified | ~99% (198 mg/L $Cd^{2+}$); ~168 mg/L adsorption capacity | [66] |
| 14 | CuO/Ag-zeolite (CAZ) | Methylene blue (MB) | Not specified | ~99% (0.10 CAZ); 70.4 mg $g^{-1}$ adsorption; antibacterial vs. *S. aureus* | [67] |
| 15 | $TiO_2$/$Fe_2O_3$/zeolite | Cyanide | UV/$H_2O_2$ | 89% (zeolite); 97% (PAC); 1.3× faster rate | [68] |
| 16 | $TiO_2$ + Fe-zeolite (ozonation) | Acid Red 1 dye | UV/$O_3$ | 95% in 9 min (5 min with Fe-zeolite); $TiO_2$ alone 28% in 15 min | [69] |
| 17 | Cu-$TiO_2$/zeolite/PMMA tablets | Methylene blue (MB) | Simulated solar | 21% degradation (240 min); zeolite/PMMA adsorbed 69% MB | [70] |
| 18 | $TiO_2$/clinoptilolite | Crystal violet | Not specified | 89% in 100 min (pseudo-first-order kinetics) | [71] |
| 19 | $TiO_2$/zeolite | Malachite Green | UV light | 82–66% adsorption; 92–90% combined removal | [72] |
| 20 | $Ag_2O$@Y zeolite | Ranitidine | Simulated sunlight | 97.5% in 75 min (neutral pH) | [73] |

## 1.2 Research Gaps

Based on the literature survey, the following gaps have been identified:

1. Limited studies have explored the use of $TiO_2$–fly ash–metal–zeolite composites as adsorbent/photocatalyst is less commonly done.
2. Adsorbents/Photocatalysts like $TiO_2$-fly ash metals- nonmetals- have not been used much to remove these organic pollutants, such as antibiotics, EDCs, dyes, etc.
3. Very little literature is available on adsorptive removal of organic pollutants like EDCs and antibiotics using $TiO_2$-fly ash metal-zeolite composite.

## 1.3 Objectives

The main aim of this research is to develop and evaluate a range of adsorbents/photocatalysts for the removal of hazardous organic pollutants from aqueous solutions. The specific objectives are:

1. To synthesize and characterize fly ash–$TiO_2$ hetero-composites.
2. To investigate the effect of metal incorporation into fly ash–$TiO_2$ composites on their adsorption capacity and photocatalytic efficiency.
3. To assess the impact of zeolite incorporation into fly ash–$TiO_2$–metal composites on the photocatalytic degradation of organic contaminants.

## 1.4 Characterization of fly ash–$TiO_2$ hetero-composites.

Freshly prepared Copper-deposited fly ash–$TiO_2$ composites and ZSM-5 zeolite-loaded fly ash–$TiO_2$–copper composites were characterized by different techniques such as XRD, FESEM, BET, DRS, XPS, and Raman spectroscopy to evaluate their structural, morphological, optical, and surface properties, as outlined below.

### 1.4.1 X-ray diffraction (XRD) analysis

The crystal structure of the synthesized materials was examined using a Smart Lab SE X-ray diffractometer with Cu-Kα radiation (λ = 1.54 Å) as the source. The equipment was operated at 45 kV to provide sufficient X-ray intensity for clear diffraction peaks. Data collection was carried out within a 2θ range of 5° to 80°, allowing the detection of both low- and high-angle reflections. A slit width of 10 mm was used to maintain beam precision, while the step size was fixed at 0.01° to ensure high-resolution measurements. The scan rate was maintained at 5° per minute to obtain accurate and well-defined diffraction patterns for phase identification and structural analysis.

### 1.4.2 Morphological analysis

Field Emission Scanning Electron Microscopy (FESEM, JEOL JSM-7600F, Japan) operating at 30 kV was employed to examine the surface morphology and microstructural features of the prepared catalysts. The elemental composition and spatial distribution of elements were determined using Energy Dispersive Spectroscopy (EDS, Bruker). In addition, detailed lattice and particle structures were visualized through High-Resolution Transmission Electron Microscopy (HRTEM, JEOL JEM-2100, Japan).

### 1.4.3 Surface area and pore size analysis

The surface area and pore size characteristics of the prepared samples were determined using the Brunauer–Emmett–Teller (BET) method on an Autosorb iQ analyzer (Quantachrome Instruments, version 3.01, USA). Before measurement, the samples were subjected to vacuum degassing to eliminate any adsorbed gases or moisture, ensuring precise results. Nitrogen adsorption–desorption isotherms were obtained at 77 K (liquid nitrogen temperature), and the resulting data were used to determine the specific surface area, average pore diameter, and total pore volume.

### 1.4.4 Optical absorption and band gap analysis

The optical characteristics of the prepared samples were analyzed using a Diffuse Reflectance Spectrophotometer (JASCO V-750, Japan) to evaluate their light absorption behaviour and band gap characteristics. Barium sulfate ($BaSO_4$) was employed as a reference standard due to its nearly perfect diffuse reflectance, ensuring precise baseline correction. The measurements were carried out over a wavelength range of 400–800 nm, covering the visible light spectrum. This enabled detailed analysis of absorbance and reflectance profiles, which were subsequently used to estimate the optical band gap energies of the samples through Tauc plot analysis.

### 1.4.5 XPS analysis

The oxidation states and chemical environments of the constituent elements in the composite were determined using X-ray Photoelectron Spectroscopy (XPS) on a Thermo Fisher Scientific NEXSA system (UK). The analysis was performed under ultra-high vacuum conditions, employing a monochromatic Al Kα X-ray source.

### 1.4.6 Raman analysis

Raman spectroscopy was carried out using a LabRAM HR micro-Raman spectrometer (Horiba) outfitted with a 532 nm laser for excitation.

## 1.5 Adsorption and photocatalytic studies

The adsorption and photocatalytic activities of the prepared fly ash–$TiO_2$, copper-deposited fly ash–$TiO_2$, and ZSM-5 zeolite–loaded fly ash–$TiO_2$–copper composites were evaluated by assessing their effectiveness in removing organic pollutants. The pollutant removal mechanism involves two successive stages:

### 1.5.1 Adsorption Studies

The adsorption capacity of the synthesized photocatalysts toward various organic pollutants was evaluated in the absence of light. A measured quantity of the photocatalyst was introduced into separate test tubes containing aqueous solutions of the target pollutants. These mixtures were stirred in dark conditions to avoid any photoreactions. Samples were withdrawn at predetermined intervals and subjected to ultracentrifugation to isolate the catalyst particles. The concentration of residual pollutants in the supernatant was determined using a UV–visible spectrophotometer (JASCO V-750) by recording and comparing the absorption spectra before and after the adsorption process. To elucidate the adsorption mechanism, experimental data were modelled using the Freundlich and Langmuir isotherm models. Additionally, pseudo-first-order and pseudo-second-order kinetic models were applied to predict and analyze the adsorption kinetics. Detailed descriptions of the procedures, equations, and calculations are provided in the corresponding sections.

### 1.5.2 Photocatalytic Degradation Analysis

The photocatalytic degradation experiments for different pollutants were carried out in individual test tubes, each containing a known quantity of photocatalyst dispersed in 5–10 mL of the pollutant's aqueous solution. Before light exposure, the mixtures were stirred in the dark to establish adsorption–desorption equilibrium at the interface between the surface of the catalyst and pollutant molecules. Subsequently, the samples were irradiated with visible LED light (50 W, WIPRO Garnett B22, intensity ~100 W/m², $\lambda > 365$ nm) housed within a wooden chamber. At predetermined intervals, aliquots were withdrawn, and the photocatalyst particles were removed via ultracentrifugation. The concentration of the residual pollutants in the supernatant was measured using UV–visible spectroscopy. Photodegradation efficiency and kinetic parameters for each photocatalyst were calculated using the methods and equations described in the subsequent chapters. The reaction intermediates generated during the photocatalytic degradation were identified using high-resolution mass spectrometry (Waters

QTOF mass spectrometer equipped with an XEVO G2 XS UPLC system and coupled to APCI and ESI ionization sources, 10 min retention time).

**References**


[1] Brillas E, Garcia-Segura S, Benchmarking recent advances and innovative technology approaches of Fenton, photo-Fenton, electro-Fenton, and related processes: A review on the relevance of phenol as model molecule, Sep Purif. Technol. 237(2020)116337, https://doi.org/10.1016/j.seppur.2019.116337.

[2] Mishra RK, Mentha SS, Misra Y, Dwivedi N, Emerging pollutants of severe environmental concern in water and wastewater: A comprehensive review on current developments and future research, Water-Energy Nexus 6(2023)74–95. https://doi.org/10.1016/j.wen.2023.08.002.

[3] Parthasarathy P, Sajjad S, Saleem J, Alherbawi M, McKay G, A Review of the Removal of Dyestuffs from Effluents onto Biochar, Separations 9(2022)139, https://doi.org/10.3390/separations9060139.

[4] Dutta S, Adhikary S, Bhattacharya S, Roy D, Chatterjee S, Chakraborty A, et al, Contamination of textile dyes in aquatic environment: Adverse impacts on aquatic ecosystem and human health, and its management using bioremediation, J Environ Manage, 353 (2024),120103. https://doi.org/10.1016/j.jenvman.2024.120103.

[5] Shetty SS, D D, S H, Sonkusare S, Naik PB, Kumari N S, et al. Environmental pollutants and their effects on human health, Heliyon 9(2023)19496, https://doi.org/10.1016/j.heliyon.2023.e19496.

[6] Saravanan A, Senthil Kumar P, Jeevanantham S, Karishma S, Tajsabreen B, Yaashikaa PR, et al, Effective water/wastewater treatment methodologies for toxic pollutants removal Processes and applications towards sustainable development, Chemosphere 280(2021)130595, https://doi.org/10.1016/j.chemosphere.2021.130595.

[7] Precious Sibiya N, Rathilal S, Kweinor Tetteh E, Coagulation treatment of wastewater: Kinetics and natural coagulant evaluation, Molecules 26(2021)https://doi.org/10.3390/molecules26030698.

[8] Lin P, Liao Z, Wu G, Yang L, Fu J, Luo Y, Recent Advances in Biofiltration for PPCP Removal from Water, Water,16(2024) 1888, https://doi.org/10.3390/w16131888.

[9] Zhang C, Yu Z, Wang X. A review of electrochemical oxidation technology for advanced treatment of medical wastewater, Front Chem 10(2022)1–6, https://doi.org/10.3389/fchem.2022.1002038.

[10] Iyyappan J, Gaddala B, Gnanasekaran R, Gopinath M, Yuvaraj D, Kumar V, Critical review on wastewater treatment using photo catalytic advanced oxidation process: Role of photocatalytic materials, reactor design and kinetics, Case Studies in Chemical and Environmental Engineering 9(2024)100599. https://doi.org/10.1016/j.cscee.2023.100599.

[11] Wear SL, Acuña V, McDonald R, Font C. Sewage pollution, declining ecosystem health, and cross-sector collaboration. Biol Conserv, 255(2021)109010, https://doi.org/10.1016/j.biocon 255(2021)109010.

[12] Osman AI, El-Monaem EMA, Elgarahy AM, Aniagor CO, Hosny M, Farghali M, et al. Methods to prepare biosorbents and magnetic sorbents for water treatment: a review, Environmental Chemistry Letters, 21(2023) 2337–2398, https://doi.org/10.1007/s10311-023-01603-4.

[13] Pet I, Sanad MN, Farouz M, ElFaham MM, El-Hussein A, El-sadek MSA, et al, Review: Recent Developments in the Implementation of Activated Carbon as Heavy Metal Removal Management, Water Conservation Science and Engineering 9(2024)1–15, https://doi.org/10.1007/s41101-024-00287-3.

[14] Serna-Galvis EA, Arboleda-Echavarría J, Echavarría-Isaza A, Torres-Palma RA, Removal and elimination of pharmaceuticals in water using zeolites in diverse adsorption processes and catalytic advanced oxidation technologies—a critical review, Environmental Science and Pollution Research, 31(2024) 63427–63457, https://doi.org/10.1007/s11356-024-35204-7.

[15] Singh NB, Agarwal A, De A, Singh P. Coal fly ash: an emerging material for water remediation, International Journal of Coal Science & Technology, 9(2022) 44, https://doi.org/10.1007/s40789-022-00512-1.

[16] Vasić V, Kukić D, Šćiban M, Đurišić-Mladenović N, Velić N, Pajin B, et al. Lignocellulose-Based Biosorbents for the Removal of Contaminants of Emerging Concern (CECs) from Water: A Review, Water, 15(2023)1853. https://doi.org/10.3390/w15101853.

[17] Satyam S, Patra S. Innovations and challenges in adsorption-based wastewater remediation: A comprehensive review, Heliyon, 10(2024) e29573, https://doi.org/10.1016/j.heliyon.2024.e29573.

[18] Bissenova M, Idrissov N, Kuspanov Z, Umirzakov A, Daulbayev C, Hybrid adsorption–photocatalysis composites: a sustainable route for efficient water purification, Mater Renew Sustain Energy, 14(2025)1–26, https://doi.org/10.1007/s40243-025-00319-5.

[19] Sun Y, Zhang W, Li Q, Liu H, Wang X. Preparations and applications of zinc oxide based photocatalytic materials, Advanced Sensor and Energy Materials, 2(2023),100069. https://doi.org/10.1016/j.asems.2023.100069.

[20] Ni Z, Wang Q, Guo Y, Liu H, Zhang Q. Research Progress of Tungsten Oxide-Based Catalysts in Photocatalytic Reactions, Catalysts, 13(2023)579, https://doi.org/10.3390/catal13030579.

[21] Hou S, Gao X, Lv X, Zhao Y, Yin X, Liu Y, et al, Decade Milestone Advancement of Defect-Engineered g-$C_3N_4$ for Solar Catalytic Applications, Nano-Micro Letters,16(2024) 70, https://doi.org/10.1007/s40820-023-01297-x.

[22] Feng J, Ran X, Wang L, Xiao B, Lei L, Zhu J, et al, The Synergistic Effect of Adsorption-Photocatalysis for Removal of Organic Pollutants on Mesoporous $Cu_2V_2O_7/Cu_3V_2O_8$/g-$C_3N_4$ Heterojunction, Int. J. Mol Sci, 23(2022) 14264. https://doi.org/10.3390/ijms232214264.

[23] Aigbe UO, Ukhurebor KE, Onyancha RB, Osibote OA, Darmokoesoemo H, Kusuma HS, Fly ash-based adsorbent for adsorption of heavy metals and dyes from aqueous solution: a review, Journal of Materials Research and Technology, 14(2021)2751–74. https://doi.org/10.1016/j.jmrt.2021.07.140.

[24] Ge JC, Yoon SK, Choi NJ, Application of Fly Ash as an adsorbent for removal of air and water pollutants, Applied Sciences 8(2018) 1116. https://doi.org/10.3390/app8071116.

[25] Gupta P, Nagpal G, Gupta N, Fly ash-based geopolymers: an emerging sustainable solution for heavy metal remediation from aqueous medium, Beni Suef Univ J Basic Appl Sci, 10(2021)43, https://doi.org/10.1186/s43088-021-00179-8.

[26] Shi Z, Yao S, Sui C. Application of fly ash supported titanium dioxide for phenol photodegradation in aqueous solution, Catal Sci Technol, 1(2011)817–22, https://doi.org/10.1039/c1cy00019e.

[27] Fan H, Chen D, Ai X, Han S, Wei M, Yang L, et al. Mesoporous $TiO_2$ coated $ZnFe_2O_4$ nanocomposite loading on activated fly ash cenosphere for visible light photocatalysis. RSC Adv 8(2018)1398–406. https://doi.org/10.1039/c7ra11055c.

[28] Son BT, Long NV, Nhat Hang NT, Fly ash-, foundry sand-, clay-, and pumice-based metal oxide nanocomposites as green photocatalysts, RSC Adv, 11(2021)30805–26, https://doi.org/10.1039/d1ra05647f.

[29] Mragui A El, Logvina Y, Luís Pinto da Silva luis silva@fc up pt, Zegaoui O, da Silva JCGE, Synthesis of fe-and co-doped $TiO_2$ with improved photocatalytic activity under visible irradiation toward carbamazepine degradation, Materials,12(2019)4–6. https://doi.org/10.3390/MA12233874.

[30] Thakur I, Verma A, Ormeci B, Sangal V, Applications of waste-derived visibly active Fe-$TiO_2$ composite incorporating the hybrid process of photocatalysis and photo-Fenton for the inactivation of E. coli, Environmental Science and Pollution Research 29(2022)72247–59. https://doi.org/10.1007/s11356-022-19202-1.

[31] Chelli VR, Chakraborty S, Golder AK, Ag-doping on $TiO_2$ using plant-based glycosidic compounds for high photonic efficiency degradative oxidation under visible light, J Mol Liq, 271 (2018)380–8. https://doi.org/10.1016/j.molliq.2018.08.140.

[32] Sharma R, Pal B, Barman S. Synergistic effect of adsorption and photocatalytic activity of Cu deposited fly ash-$TiO_2$ composites for fuchsin blue removal under visible-solar light, Solar Energy287(2025) 113198. https://doi.org/10.1016/j.solener.2024.113198.

[33] Jansson I, Suárez S, García-García FJ, Sánchez B, ZSM-5/$TiO_2$ Hybrid Photocatalysts: Influence of the Preparation Method and Synergistic Effect, Top Catal 60(2017)1171–82. https://doi.org/10.1007/s11244-017-0805-1.

[34] Subagyo R, Tehubijuluw H, Utomo WP, Rizqi HD, Kusumawati Y, Bahruji H, et al, Converting red mud wastes into mesoporous ZSM-5 decorated with $TiO_2$ as an eco-friendly and efficient adsorbent-photocatalyst for dyes removal, Arabian Journal of Chemistry 15(2022),103754. https://doi.org/10.1016/j.arabjc.2022.103754.

[35] Kanti P, Sharma K V., Revanasiddappa M, Ramachandra CG, Akilu S, Thermophysical properties of fly ash–Cu hybrid nanofluid for heat transfer applications, Heat Transfer 49(2020)4491–510. https://doi.org/10.1002/htj.21837.

[36] Abdu M, Tibebu S, Babaee S, Worku A, Msagati TAM, Nure JF, Optimization of photocatalytic degradation of Eriochrome Black T from aqueous solution using $TiO_2$-biochar composite, Results in Engineering, 25(2025) 104036. https://doi.org/10.1016/j.rineng.2025.104036.

[37] Soman B, Challagulla S, Payra S, Dinda S, Roy S, Surface morphology and active sites of $TiO_2$ for photoassisted catalysis, Research on Chemical Intermediates, 44(2018) 2261–73. https://doi.org/10.1007/s11164-017-3227-6.

[38] Al-Wasidi AS, Saad FA, AlReshaidan S, Naglah AM, Facile Synthesis of ZSM-5/$TiO_2$/Ni Novel Nanocomposite for the Efficient Photocatalytic Degradation of Methylene Blue Dye, J Inorg. Organomet. Polym. Mater. 32(2022)3040–52. https://doi.org/10.1007/s10904-022-02336-7.

[39] Mpelane A, Katwire DM, Mungondori HH, Nyamukamba P, Taziwa RT, Application of novel C-$TiO_2$-CFA/PAN photocatalytic membranes in the removal of textile dyes in wastewater, Catalysts 10(2020)1–17. https://doi.org/10.3390/catal10080909.

[40] Tu Y, Zhong J, Ding H, Zhang H, Lv G, Zhang J, et al, Preparation of fly ash supporting nano-$TiO_2$ composite photocatalyst by a wet mechanical grinding method, Chem Phys Lett, 805(2022)139978, https://doi.org/10.1016/j.cplett.2022.139978.

[41] Sawunyama L, Oyewo OA, Makgato SS, Bopape MF, Onwudiwe DC, $TiO_2$–ZnO functionalized low-cost ceramic membranes from coal fly ash for the removal of tetracycline from water under visible light, Discover Nano 20(2025). https://doi.org/10.1186/s11671-024-04178-3.

[42] Song J, Wang X, Bu Y, Zhang J, Wang X, Huang J, et al, Preparation, characterization, and photocatalytic activity evaluation of Fe–N-codoped $TiO_2$/fly ash cenospheres floating photocatalyst, Environmental Science and Pollution Research,23( 2016)22793–802. https://doi.org/10.1007/s11356-016-7353-2.

[43] Lin L, Ali KA. Photocatalytic degradation of organic compounds in dye wastewater by $Fe^{3+}$ doped nano-ZnO/$TiO_2$ composite photocatalyst, Indian Journal of Chemical Technology,31(2024)506–20. https://doi.org/10.56042/ijct.v31i3.3324.

[44] Visa M, Cosnita M, Moldovan M, Marin CA, Mihaly M. Fly ash waste recycling by pt/$TiO_2$ incorporation for industrial dye removal, Int J Environ Res Public Health, 18(2021)3887. https://doi.org/10.3390/ijerph18083887.

[45] Aghajari N, Ghasemi Z, Younesi H, Bahramifar N, Synthesis, characterization and photocatalytic application of Ag-doped Fe-ZSM-5@$TiO_2$ nanocomposite for degradation of reactive red 195 (RR 195) in aqueous environment under sunlight irradiation, J Environ Health Sci Eng,17(2019)219–32. https://doi.org/10.1007/s40201-019-00342-5.

[46] Cahyanti R, Sumari S, Fajaroh F, Asrori MR, Prakasa YF, Fe-$TiO_2$/zeolite H-A photocatalyst for degradation of waste dye (methylene blue) under UV irradiation, AIMS Mater Sci,10(2023)40–54. https://doi.org/10.3934/matersci.2023003.

[47] Sambakanya S, Nyamukamba P, Katwire DM, Mungondori HH, Mukumba P, Okoh O, Synthesis and application of novel coal fly ash supported C-doped $TiO_2$–$SnO_2$ photocatalytic nanocomposite for the removal of dyes in water, Asian J Chem, 32(2020)3239–3248. https://doi.org/10.14233/ajchem.2020.22972.

[48] Raashid M, Kazmi M, Ikhlaq A, Iqbal T, Sulaiman M, Shakeel A, Degradation of aqueous CONFIDOR® pesticide by simultaneous $TiO_2$ photocatalysis and Fe-zeolite catalytic ozonation, Water, 13(2021)3327. https://doi.org/10.3390/w13233327.

[49] Ramutshatsha-Makhwedzha D, Mavhungu ML, Baloyi J, Mbaya R, Synthesis and characterization of $Fe_3O_4$@$TiO_2$@Zeolite nanocomposite adsorbent for the removal of levofloxacin antibiotic from environmental water matrices, J Iran Chem Soc, 22(2025)113–128. https://doi.org/10.1007/s13738-024-03135-2.

[50] Mergenbayeva S, Abitayev Z, Batyrbayeva M, Vakros J, Mantzavinos D, Atabaev TS, et al., $TiO_2$/zeolite composites for SMX degradation under UV irradiation, Catalysts, 14(2024)1–17. https://doi.org/10.3390/catal14020147.

[51] Li G, Mang C, Xing L, Cao P, Cai Y, Luo J, et al., Surfactant-assisted synthesis of Mo-doped $TiO_2$/FAC (fly ash cenosphere) for degradation of methylene blue dye under visible light irradiation, Colloids Surf A, 651(2022)129669. https://doi.org/10.1016/j.colsurfa.2022.129669.

[52] Kanakaraju D, Jasni MAA, Pace A, Ya MH, Enhanced dye-removal performance of Cu–$TiO_2$–fly ash composite by optimized adsorption and photocatalytic activity under visible light irradiation, Environ Sci Pollut Res, 28(2021)68834–68845. https://doi.org/10.1007/s11356-021-15440-x.

[53] Gong L, Li J, Jin R, Li M, Peng J, Zhu J, Dual-functional AgNPs/magnetic coal fly ash composite for wastewater disinfection and azo dye removal, Molecules, 30(2025)3155. https://doi.org/10.3390/molecules30153155.

[54] Wang B, Zhou Y, Li L, Xu H, Sun Y, Du Y, et al., In situ synthesis of $TiO_2$-doped mesoporous silica from coal fly ash for the photocatalytic degradation of dyes, Ind Eng Chem Res, 57(2018)15632–15637. https://doi.org/10.1021/acs.iecr.8b03190.

[55] Duan X, Yang J, Hu G, Yang C, Chen Y, Liu Q, et al., Optimization of $TiO_2$/ZSM-5 photocatalysts: Energy band engineering by solid-state diffusion method with calcination, J Environ Chem Eng, 9(2021)105563. https://doi.org/10.1016/j.jece.2021.105563.

[56] Bello MO, Shelake SP, Abdus-Salam N, Adekola FA, Vennapoosa CS, Sesha Sainath AV, et al., Na-Y zeolite supported $TiO_2$/Pd nanoparticles for enhanced photoredox catalytic properties and green hydrogen generation, Catal Commun, 186(2024)106817. https://doi.org/10.1016/j.catcom.2023.106817.

[57] Zendehdel M, Cruciani G, Barghi B, Micro-meso structure NaP zeolite@$TiO_2$ nanocomposite: eco-friendly photocatalyst for simultaneous removal of COD and degradation of methylene blue under solar irradiation, Photochem Photobiol Sci, 21(2022)1011–1029. https://doi.org/10.1007/s43630-022-00190-7.

[58] Jalloul G, Al-Mousawi A, Chocr F, Merhi A, Awala H, Boyadjian C, Fe-sensitized zeolite supported $TiO_2$ for the degradation of tetracycline using blue LED irradiation, Front Environ Sci, 10(2022)1–13. https://doi.org/10.3389/fenvs.2022.873257.

[59] Mahamud M, Taddesse AM, Bogale Y, Bezu Z, Zeolite supported CdS/$TiO_2$/$CeO_2$ composite: synthesis, characterization and photocatalytic activity for methylene blue dye degradation, Mater Res Bull, 161(2023)112176. https://doi.org/10.1016/j.materresbull.2023.112176.

[60] Zhang W, Wang K, Yu Y, He H, $TiO_2$/HZSM-5 nano-composite photocatalyst: HCl treatment of NaZSM-5 promotes photocatalytic degradation of methyl orange, Chem Eng J, 163(2010)62–67. https://doi.org/10.1016/j.cej.2010.07.042.

[61] Xue H, Lv G, Fly ash–based X zeolite–$TiO_2$ composite catalysts in photocatalytic performance, Water Air Soil Pollut, 236(2025)822. https://doi.org/10.1007/s11270-025-08411-2.

[62] Supelano García I, Palacio Gómez CA, Weber MH, Saavedra Gaona IM, Castañeda Martínez CP, Martínez Zambrano JJ, et al., Physicochemical properties of $Ti^{3+}$ self-doped $TiO_2$ loaded on recycled fly-ash based zeolites for degradation of methyl orange, Condens Matter, 7(2022). https://doi.org/10.3390/condmat7040069.

[63] Singh K, Singh AK, Kumar A, Agarwal A, Fly ash and $TiO_2$-modified fly ash as adsorbing materials for removal of Cd(II) and Pb(II) from aqueous solutions, J Hazard Mater Adv, 10(2023)100256. https://doi.org/10.1016/j.hazadv.2023.100256.

[64] Foura G, Chouchou N, Soualah A, Kouachi K, Guidotti M, Robert D, Fe-doped $TiO_2$ supported on HY zeolite for solar photocatalytic treatment of dye pollutants, Catalysts, 7(2017). https://doi.org/10.3390/catal7110344.

[65] Muhamad Iqbal R, Susanti I, Abdul Rachman R, Agusta Pradana T, Prasetya Toepak E, Synthesis, characterization, and photocatalytic activity of N-doped $TiO_2$/zeolite-NaY for methylene blue removal, J Pure Appl Chem Res, 10(2021)132–139. https://doi.org/10.21776/ub.jpacr.2021.010.02.572.

[66] Us Saqib N, Haleem MA, Aamir A, Shah I, Zaman F, Adnan R, et al., Green synthesis of Zeolite@Ag/$TiO_2$ heterostructure for the enhanced $Cd^{2+}$ adsorption from aqueous solution, Inorg Chem Commun, 171(2025)113498. https://doi.org/10.1016/j.inoche.2024.113498.

[67] Yahya NAA, Samir OM, Al-Ariki S, Ahmed AAM, Swillam MA, Synthesis of novel antibacterial nanocomposite CuO/Ag-modified zeolite for removal of MB dye, Sci Rep, 13(2023)1–16. https://doi.org/10.1038/s41598-023-40790-6.

[68] Eskandari P, Farhadian M, Solaimany Nazar AR, Jeon BH, Adsorption and photodegradation efficiency of $TiO_2/Fe_2O_3$/PAC and $TiO_2/Fe_2O_3$/zeolite nanophotocatalysts for the removal of cyanide, Ind Eng Chem Res, 58(2019)2099–2112. https://doi.org/10.1021/acs.iecr.8b05073.

[69] Raashid M, Kazmi M, Ikhlaq A, Sulaiman M, Akram A, Afaf A, et al., Removal of acid red dye 1 from textile wastewater by heterogeneous photocatalytic ozonation employing titanium dioxide and iron zeolite, Discov Chem Eng, 4(2024). https://doi.org/10.1007/s43938-024-00059-4.

[70] Armaković SJ, Perić M, Bilić A, Brkić B, Maja Š, Cu–$TiO_2$/zeolite/PMMA tablets for efficient dye removal, Catalysts, 14(2024)746. https://doi.org/10.3390/catalysts1411746.

[71] Ullah R, Liu C, Panezai H, Gul A, Sun J, Wu X, Controlled crystal phase and particle size of loaded-$TiO_2$ using clinoptilolite as support via hydrothermal method for degradation of crystal violet dye in aqueous solution, Arab J Chem, 13(2020)4092–4101. https://doi.org/10.1016/j.arabjc.2019.06.011.

[72] Imessaoudene A, Mechraoui O, Aberkane B, Benabbas A, Manseri A, Moussaoui Y, et al., Synthesis of a $TiO_2$/zeolite composite: Evaluation of adsorption–photodegradation synergy for the removal of Malachite Green, Nano Struct Nano Objects, 38(2024)101191. https://doi.org/10.1016/j.nanoso.2024.101191.

[73] Al-Jubouri SM, Sabbar HA, Khudhair EM, Ammar SH, Al Batty S, Yas Khudhair S, et al., Silver oxide–zeolite for removal of an emerging contaminant by simultaneous adsorption–photocatalytic degradation under simulated sunlight irradiation. J Photochem Photobiol A Chem, 442(2023)114763. https://doi.org/10.1016/j.jphotochem.2023.114763

# Chapter-2

## Utilization of fly ash–$TiO_2$ composites for efficient adsorption and photodegradation of fuchsin blue dye

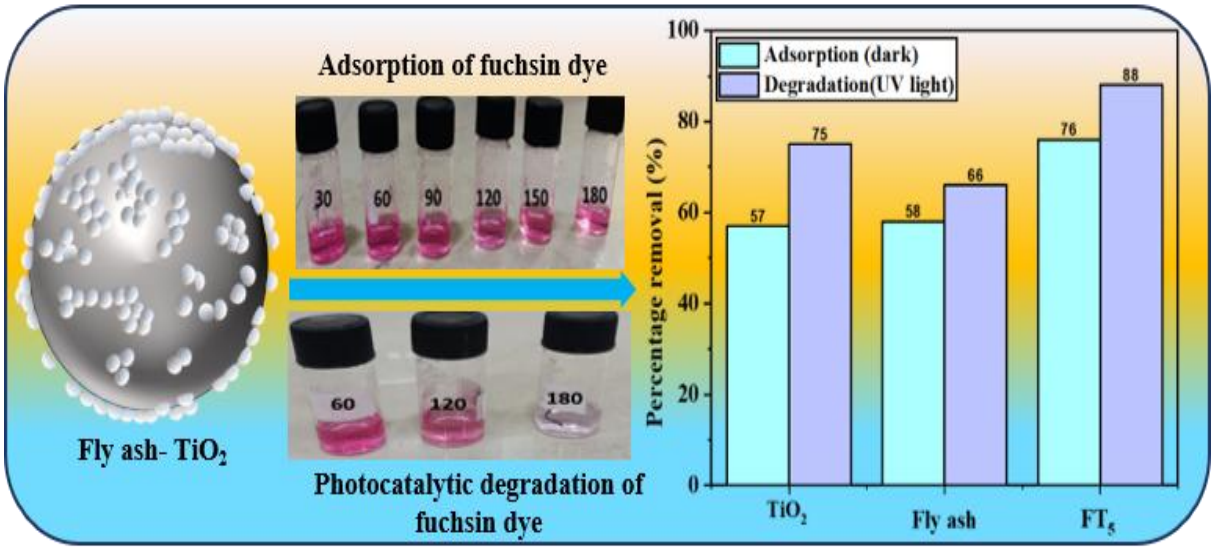


**Schematic summary**

### 2.1 Introduction

Coal power stations significantly meet the world's energy needs [1]. Fly ash is a solid waste produced in huge quantities from the combustion of raw coal in power plants [2]. The amount of coal fly ash produced annually is expected to be 750 million tonnes, and is only used in some industries to the extent of 25% [1]. Coal fly ash is one of many industrial solid wastes (by-products) that are attractive and low-cost adsorbents exhibiting high specific surface area, porosity, and particle size due to its ability to adsorb a variety of hazardous and non-biodegradable dyes from coloured effluents [3, 4]. Fly ash is improperly handled, stored, and disposed which causes significant contamination to the earth, air, water, and even living creatures. The environment is contaminated, and human health is at risk when untreated fly ash from power plant chimneys is released into the atmosphere [5, 6]. As a result, recycling fly ash has sparked a lot of interest in research scientists to find sustainable and environmentally friendly ways to deal with this waste product [7]. The composite material made up of fly ash and $TiO_2$ is reported to show improved photocatalytic properties [8–10]. The fly ash provides a large surface area for dye adsorption and accelerates photocatalytic processes when combined

with $TiO_2$ nanoparticles. By incorporating fly ash, the composite photocatalyst becomes more durable and stable, increasing its capacity for reuse. The $TiO_2$ nanoparticles in the composite photocatalyst are activated when exposed to UV light [11,12]. The absorbed light energy creates electron-hole pairs in the $TiO_2$, leading to the generation of reactive oxygen species, such as superoxide radicals and hydroxyl radicals (•OH). The reactive oxygen species interact with the dye molecules that have been adsorbed, oxidizing them to generate smaller, less harmful chemicals [13,14]. Recent research on the production and application of photocatalysts has focused mostly on titanium dioxide ($TiO_2$) due to its exceptional performance, chemical stability, and lack of toxicity [15].

Over the last decades, FA/$TiO_2$ composites have been studied as an affordable adsorbent for eliminating different water pollutants during wastewater treatment [3, 4]. Gilja et al. [13] synthesized $TiO_2$/ treated FA nanocomposites to increase the specific surface area for removing reactive Red 45 (RR45) azo dye via photocatalytic treatment with UV-A light. The study found that all FA1/TiB nanocomposite photocatalysts have high photosensitivity, with 96% of discolouration. Mpelane et al. [16] utilized the sol-gel technique to synthesize the C-$TiO_2$-CFA nanocomposite, which was then immobilized on a PAN membrane by the phase inversion method. Carbon doping and the nanocomposite's huge surface area (114 $m^2/g$) resulted in excellent photodegradation efficiency (99.8% and 99.2% for MO and GY, respectively) under sunlight irradiation, in 300 min. Tu et al. [14] employed a wet mechanical grinding approach to produce an FA-$TiO_2$ composite using nano $TiO_2$ and FACs to remove 98% methyl orange. Duta and Visa [17] effectively synthesized $TiO_2$/FA novel substrate in a hydrothermal process for concurrent heavy metal ($Cd^{2+}$ and $Cu^{2+}$) and surfactant (1-hexadecyl trimethylammonium bromide – HTAB and dodecyl benzenesulfonate – SDBS) elimination, optimised conditions led to excellent removal efficiency (over 90%) for heavy metals and surfactants. Kanakaraju [18] synthesized a Cu/$TiO_2$/FA composite using the wet impregnation method to achieve a 99% removal of methyl orange under visible light.

For instance, dyes are hazardous pollutants that must be removed [19]. Basic fuchsin (BF), or magenta or Fuchsin dye, is a synthetic dye from the triarylmethane class [20]. Although widely used in textile mills, the cationic dye is not biodegradable when disposed of with wastewater [21]. Releasing fuchsin dye into water will significantly harm the ecosystem and endanger human health [22]. Continuous exposure to this dye may result in headaches, vertigo, muscular cramps, disorders in the digestive system, gastrointestinal discomfort, nausea, and vomiting [23, 24]. The dye's aromatic rings are extremely stable, which leads to considerable

bioaccumulation. As a result, it is critical to eliminate it from the water using an easy, inexpensive, and efficient method [25]. Fuchsin removal from wastewater systems is a serious issue that needs to be researched and addressed because of its poor biodegradability, toxicity, carcinogenicity, and odour [26]. However, the adsorption and degradation of fuchsin dye by $TiO_2$-fly ash composite have not been reported anywhere.

The current studies describe the synthesis, characterization, comparative adsorption, and photocatalytic degradation of fuchsin dye by $TiO_2$, fly ash, and fly ash-$TiO_2$ composites. $TiO_2$ was synthesized using the sol-gel method, and FA-$TiO_2$ composites were prepared using the wet-impregnation method with $TiO_2$ concentrations ranging from 0.5 to 5wt%.

## 2.2 Experimental section

### 2.2.1 Chemicals and reagents

Titanium Butoxide $Ti(OC_4H_9)_4$, Di decyl dimethyl ammonium chloride ($C_{22}H_{48}ClN$) were purchased from Sigma-Aldrich (India), Acetic acid ($C_2H_4O_2$), Ethanol ($C_2H_5OH$), FB dye ($C_{20}H_{19}N_3.HCl$) were obtained from Loba Chemie (India). Fly ash (FA) was obtained from Rajpura Power Plant (India). Ultrafiltration equipment Milli-Q (Millipore), produced double-distilled water (D.I.).

### 2.2.2 Synthesis of $TiO_2$

$TiO_2$ was synthesized by the sol-gel method displayed in Scheme S1. Solution A was made by dissolving 10 mL of titanium butoxide in anhydrous ethanol. Under vigorous stirring (250 rpm), 10 mL of 3M acetic acid was added dropwise to the solution and agitated for another 15 minutes. At room temperature, 1.1 mL didecyl dimethyl ammonium chloride, 30 mL anhydrous ethanol, and 10 mL distilled water were combined for 15 min to get Solution B. Eventually, solution B was gradually added to solution A. The resulting mixture was then aggressively stirred with a magnetic stirrer at 600 rpm for 45 minutes. The liquid in the Erlenmeyer flask was then cooked for an additional 24 h at 70°C in the oven, producing a clear solution. The resulting $TiO_2$ sample underwent a de-ionized water rinse, was dried at 100°C for 12 hours, and then was subjected to a 3 h calcination process at 400°C [13]**.**

### 2.2.3 Synthesis of FA-$TiO_2$ (FT) Composites

FA-$TiO_2$ composites with different weight percentages of $TiO_2$ were prepared by the wet-impregnation method (shown in **Scheme 2.1**). 10g of fly ash was ultrasonically dispersed in a

beaker containing 100 ml of distilled water. Then a specified amount of $TiO_2$ (0.05g, 0.1g, 0.3g and 0.5 g) was introduced. The mixture was stirred at 600 rpm for 2h, followed by filtration and drying in an oven at 70°C for 24 h. The FA-$TiO_2$ composite catalyst containing 0.5wt%, 1wt%, 3wt% and 5wt% of $TiO_2$ are named as $FT_{0.5}$, $FT_1$, $FT_3$ and $FT_5$ respectively [27].

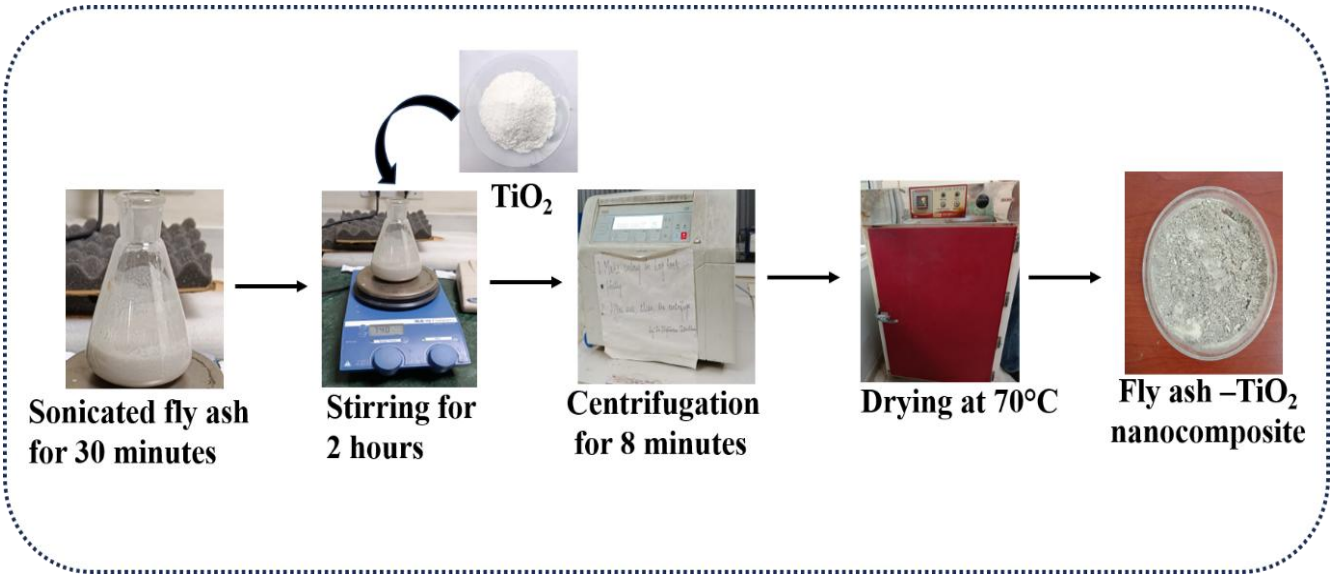


**Scheme 2.1** Schematic presentation of the synthesis of the fly ash-$TiO_2$ nanocomposites.

### 2.2.4 Catalyst Characterization

The X-ray diffraction patterns of the synthesized materials were obtained using an X-ray powder diffraction PAN Analytical-Xpert-PRO machine outfitted with a Cu-Kαradiation source (1.54), functioning at 45kV, with a diffraction angle (2θ) extending from 5°- 80° and a scan rate of 5°/min. Raman spectroscopic observations were conducted using a Labram HR, Horiba micro-Raman spectrometer with a 532nm laser excitation. Surface area and porosity were determined using the BET $N_2$ adsorption-desorption isotherm at 77.3 K using a surface analyzer, Quanta Chrome Nova-1000. Furthermore, the BJH method was used to investigate pore size distribution. Field Emission Scanning Electron Microscopy (JEOL JSM-7600F operating at 30kV) (FESEM) was used to describe the surface morphology of the catalyst. Elemental mapping and analysis were done using an energy-dispersive X-ray spectrometer (EDS). Utilizing a reference of $BaSO_4$, the optical properties were assessed using a diffuse reflectance spectrophotometer (DRS, Avantes). High-Resolution Mass Spectroscopy (Waters, QTOF mass spectrometer equipped with XEVO G2 XS UPLC combined with APCI and ESI ionization source with negative and positive mode scans at various intervals, retention duration of 10 min) was employed to identify degradation products, which provided insightful information about the photocatalytic degradation pathway.

### 2.2.5 The point of zero charge (PZC) of the composite

The point of zero charge is a significant physicochemical parameter since it shows the pH at which the adsorbent's surface will have zero net charge. The point charge of the $FT_5$ composite were computed using the solid addition technique using 0.002 M cetrimide ($C_{19}H_{42}Br_N$) and 0.1 M KCl solutions. In this approach, 25 mL of 0.002 M cetrimide and 25 mL of 0.1 M KCl solution were placed in test tubes, and the preliminary pH of the various solutions was roughly adjusted between 2 and 10 using 0.1 M NaOH and 0.1 M HCl solutions. Following that, 5 mg of $FT_5$ composite was added individually to each test tube, resulting in a suspension that was kept for 3 hours and allowed to equilibrate with constant shaking. After 3 hours, filter the solution and properly determine the ultimate pH.

### 2.2.6 Adsorption of FB dye

The adsorption behaviour of $TiO_2$, FA (Fly ash), and various FT composites (0.5wt%, 1wt%, 3 wt%, and 5wt% of $TiO_2$) was studied with a 10 ml pollutant solution. The effect of various parameters such as fuchsin dye concentration (5-30 mg/L), adsorbent amount (1-9 mg), and contact time (30-180) minutes was studied. In the dark, a magnetic stirrer was used to mix and agitate a series of test tubes containing 10 ml of pollutant solution at various concentrations and the required amount of adsorbent. After agitating each test tube for a specific period, it was removed, and 10 ml of its aqueous sample was taken and centrifuged to separate the adsorbent. A UV-visible spectrophotometer was utilized to determine the amount of adsorbate in the supernatant at its maximum absorbance ($\lambda_{max}$ = 546 nm for FB dye) using the standard calibration curves shown in **Fig. 2.1**. The adsorbent's adsorption efficiency (adsorbed mass per unit mass, mg/ g) was determined by using the formula:

$$\text{Adsorption capacity} = Q_e = (C_o - C_e) \times \frac{V}{W} \quad (1)$$

where $C_o$ denotes the initial concentration (mg/L) of fuchsin dye, $C_e$ denotes the FBs equilibrium concentration in the solution (mg/L), W denotes the amount of adsorbent (g), V denotes the volume of FB solution (L) and $Q_e$ is the adsorbent's efficiency (mg/g) at equilibrium [28] The following equation was used to estimate the percentage (R%) of FB absorbed into adsorbents.

$$\text{Percentage removal of FB dye} = R\% = \left( \frac{C_o - C_e}{C_o} \right) \times 100 \quad (2)$$

$C_0$ and $C_e$ are the initial and equilibrium concentrations of the fuchsin dye in the solution, and R% is the percentage of the fuchsin dye that has been removed [29].

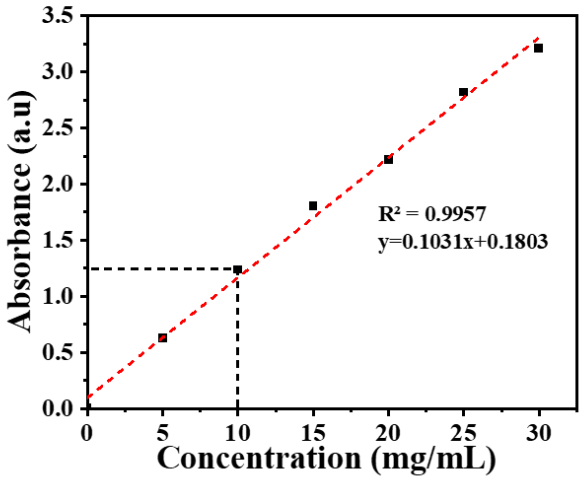


**Fig. 2.1** Calibration curve of FB pollutant at different concentrations

### 2.2.7 Photocatalytic degradation of FB dye

The photocatalytic activity of the synthesized materials $TiO_2$, FA and different $TiO_2$-FA nanocomposites, were evaluated by FB dye degradation. The photocatalytic reaction was carried out in separate test tubes at room temperature; 5 mg of each catalyst was dispersed in 10 mL of FB solution in a typical reaction. The test tubes containing various catalysts were then subjected to UV light (125 W Hg arc, 104 mW/cm$^2$). After 150 minutes, the samples were removed from each test tube and centrifuged at 9000 rpm for 7 min to remove any residual solid catalyst particles. The optical absorbance spectra of FB dye were analyzed using a UV-vis spectrophotometer at $\lambda_{max}$ of 546 nm. According to Beer-Lambert's law, the concentration is directly proportional to the absorbance, and the following formula was used to calculate the photodegradation efficiency:

$$\text{Rate of FB dye degradation (\%)} = \frac{A_o - A_t}{A_o} \times 100 = \frac{C_o - C_t}{C_o} \times 100 \quad (3)$$

where $A_o$, $C_o$ stands for the initial FB dye absorbance and concentration at time 0 and $A_t$, $C_t$ for the absorbance and concentration of FB dye at time t, respectively [30].

## 2.3 Results and discussion

### Catalyst Characterization

### 2.3.1 X-Ray Diffraction

The XRD spectra of $TiO_2$ are shown in **Fig. 2.2(a)**. Diffractograms of $TiO_2$ derived from Titanium-butoxide show anatase crystalline phase (seen 2θ at 25.3° (101), 37.9° (004), 48.3°

(200), 54.1° (105), 55.1° (211), 62.8° (204), 69.2° (116), 70.3° (220) and 75.4° (215). A reference to JCPDS Card no. 21-1272 confirms that anatase $TiO_2$ peaks are found in the spectrum [31]. The X-ray diffractogram of fly ash shows that the phase composition of fly ash has four essential crystalline components: quartz ($SiO_2$), mullite ($Al_6Si_2O_{13}$), magnetite ($Fe_3O_4$), and hematite ($Fe_2O_3$). The typical peaks in the XRD diffractogram at 16.45°, 25.98°, and 26.30° and 20.86°, 26.58°, and 36.55° show the mullite and quartz phases, respectively. There was a good match between the presence of these phases and their respective JCPDS cards: mullite (JCPDS card no.89-2644), quartz (JCPDS card no.89-1962), and hematite (JCPDS card no.33-664). The diffractogram shows a distinctive rise in intensity at angles ranging from 21 to 28° 2θ, as well as the comparatively low intensity of the quartz and mullite phase peaks showing microscopic particle size and a high activity index of FA [32].

The XRD spectra of $TiO_2$, FA and different (1wt%,3wt% and 5wt% $TiO_2$) FA- $TiO_2$ composites were investigated are shown in **Fig. 2.2(b)** Peaks observed at 2θ values of 16.45°, 25.98°, and 26.30° and at 20.86°, 26.58°, and 36.55° in the FA sample correspond to the presence of mullite and quartz phases, respectively. The characteristic peak at 2θ = 25.3° is attributed to pure $TiO_2$. All the FA diffraction peaks were retained in the FA–$TiO_2$ composites containing 0.5 wt%, 1 wt%, 3 wt%, and 5 wt% $TiO_2$. Additionally, a $TiO_2$-specific peak at 2θ = 25.3° becomes increasingly prominent with higher $TiO_2$ loadings, confirming the successful incorporation of $TiO_2$ onto the FA surface and the effective formation of the composite structure.

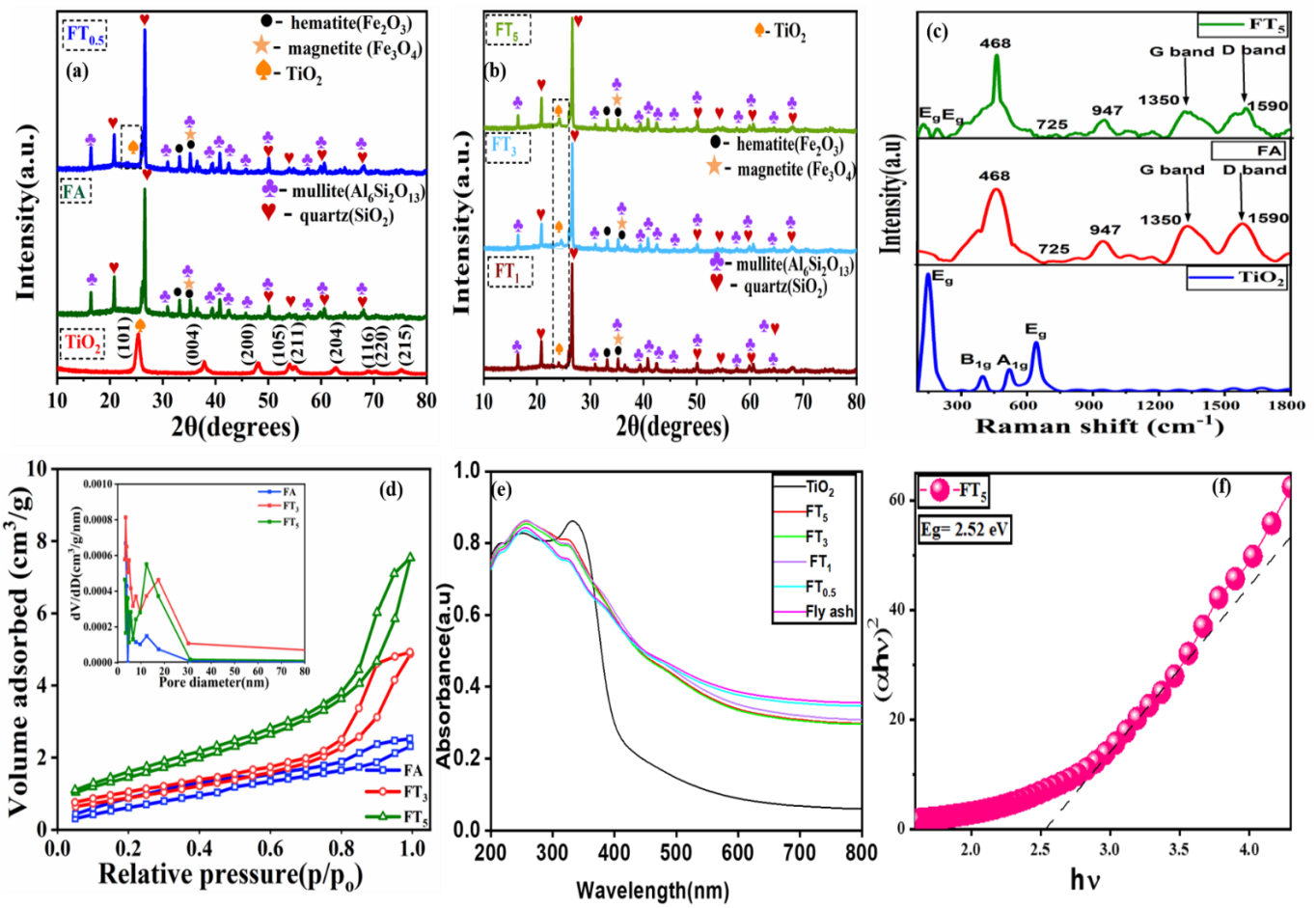


**Fig. 2.2** XRD patterns of (a) $TiO_2$, fly ash (FA), and 0.5wt% $TiO_2$ loaded FA composites ($FT_{0.5}$), (b) $FT_1$, $FT_3$, $FT_5$, (c) Raman spectra of $TiO_2$, fly ash (FA) and $FT_5$ composite, (d) $N_2$ adsorption-desorption isotherms, (inset) BJH plot distribution curves of FA, $FT_3$, and $FT_5$ nanocomposites,(e) Diffuse Reflectance Spectra of several composites and (f) Tauc Plot of $FT_5$ composite

### 2.3.2 Raman analysis

**Fig. 2.2(c)** shows the Raman spectra of FA, $TiO_2$ and $FT_5$ nanocomposite in the range of 200–1800 $cm^{-1}$. Raman spectroscopy was used to analyze structural defects and show the uneven structure of the products. Raman spectra of fly ash showed 2 sharp peaks. arises from disorder-induced vibrations and indicates defects or structural irregularities in the graphitic carbon present, and the G-band observed near 1590 $cm^{-1}$, attributed to the in-plane vibrational mode of $sp^2$-bonded carbon atoms and represents more ordered, graphite-like domains associated with symmetry and crystallinity. These peaks confirm the presence of carbonaceous species in fly ash and help assess the degree of structural order within the material. The prominent band of about 467 $cm^{-1}$ indicated the presence of quartz that corresponded to the symmetric Si-O

stretching mode of quartz. The peak at 725 $cm^{-1}$ displayed intra- and inter-tetrahedral deformation modes involving tetrahedral cation mobility in fly ash due to silica content. The presence of the mullite phase in fly ash has been shown by a conspicuous band around 960 $cm^{-1}$ [33]. Four distinct Raman active modes of anatase $TiO_2$ with symmetries $E_g$, $B_{1g}$, $A_{1g}$, and $E_g$ were detected at 144, 396, 519, and 638 $cm^{-1}$, respectively. Raman spectra demonstrated the development of the anatase phase of $TiO_2$ [34]. Raman spectra of $FT_5$ nanocomposite showed both $TiO_2$ and fly ash peaks; however, Raman modes of $TiO_2$ in $FT_5$ composite became reduced due to the low concentration of $TiO_2$ on the surface, due to more fly ash coverage.

### 2.3.3 BET analysis

The BET analysis in **Fig. 2.2 (d)** depicts the $N_2$ adsorption-desorption isotherms and the associated BJH pore-size distribution curves of fly ash, $FT_3$, and $FT_5$ nanocomposites. Following the IUPAC classification, nitrogen ($N_2$) adsorption-desorption isotherms of fly ash and composites showed a type-IV isotherm with significant H3 hysteresis loops, indicating multilayer adsorption on the mesoporous surface. The specific surface area, pore volume, and pore sizes of all the samples are reported in **Table 2.1**. The pore size of the samples is predominantly distributed within the 2–10 nm range, confirming their mesoporous characteristics. The analysis further reveals that the $TiO_2$–fly ash nanocomposites exhibit a substantially greater total pore volume and specific surface area in comparison to raw fly ash. The incorporation of $TiO_2$ introduces additional active energetic sites for pollutant adsorption and enhances pore accessibility, thereby facilitating faster diffusion of reactants and products. These features collectively contribute to the improved photocatalytic performance of the composite material activity [35].

**Table 2.1.** Pore volume, surface area and pore diameter of $TiO_2$, fly ash, $FT_3$ and $FT_5$ composites.

| Photocatalyst | BET surface area ($m^2/g$) | Pore volume ($cm^3/g$) | Pore diameter (nm) |
|---|---|---|---|
| **$TiO_2$** | 99.70 | 0.20 | 12.31 |
| **Fly ash** | 1.35 | 0.00 | 3.05 |
| **$FT_3$** | 3.27 | 0.01 | 3.41 |
| **$FT_5$** | 5.43 | 0.01 | 7.81 |

### 2.3.4 UV-vis diffuse reflectance spectroscopy

UV-vis diffuse reflectance spectra of $TiO_2$, fly ash, and FT composites (0.5wt%,1wt%,3wt%, and 5wt% $TiO_2$) are shown in **Fig. 2.2 (e).** The DRS spectra depict peaks with wavelength below 400 nm in the UV region exhibiting transition of electrons from the valence band of (2p) $O^{2-}$ orbital to (3d) $Ti^{3+}$ orbital to the conduction band. The fly ash-$TiO_2$ composite shows enhanced ultraviolet (UV) light absorption, resulting in a redshift to a longer wavelength. This shift may be attributed to the formation of Si-O-Ti bonds between the $TiO_2$ and fly ash surfaces. The bandgap of as-prepared composites was estimated using Tauc's equation. Tauc's expression is written as:

$$\alpha h\nu = A(h\nu - E_g)^n \tag{4}$$

Where α denotes the adsorption coefficient, hν indicates the photon's energy, A is a constant, and $E_g$ signifies the bandgap transition that occurs directly or indirectly (n=0.5 for a direct transition and 2 for an indirect transition). The bandgap values were estimated by projecting a straight line to the x-axis in the $(\alpha h\nu)^2$ graph vs. hν. The $E_g$ value formulated to be 2.52 eV for $FT_5$ composite is depicted in **Fig. 2.2(f),** whereas the $E_g$ value of 3.12 eV for $TiO_2$, 2.84 eV for fly ash, 2.83 eV, 2.79 eV, 2.55eV for $FT_{0.5}$, $FT_1$, $FT_3$, composites are shown in **Fig. 2.3 (a-e)**.

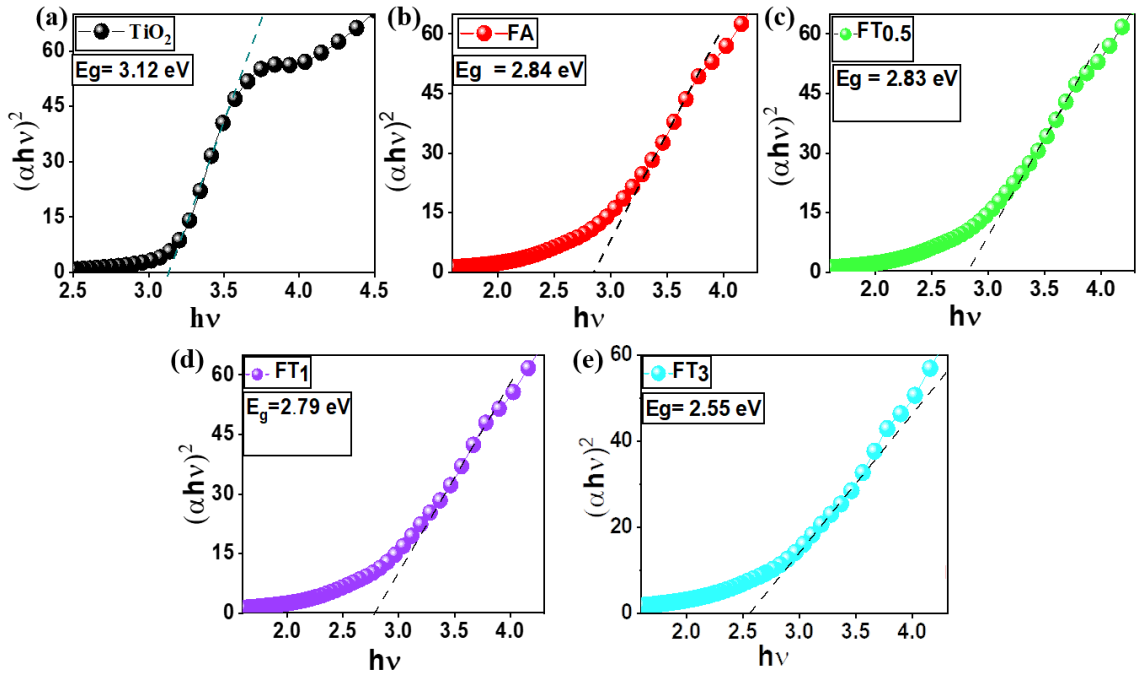


**Fig. 2.3 (a-e)** Tauc Plot of various photocatalysts.

### 2.3.5 Scanning Electron Microscopy

SEM analysis was performed to examine the morphology of the materials and their interactions within the composite samples. This provides insight into the structural characteristics of the FA-$TiO_2$ composites, particularly how varying $TiO_2$ loading influences the extent of $TiO_2$ coverage on the FA surface. The SEM images of $TiO_2$ shown in **Fig. 2.4(a)** reveal that the $TiO_2$ nanoparticles possess a predominantly spherical morphology. A noticeable degree of particle agglomeration is observed, indicating the tendency of $TiO_2$ nanoparticles to cluster together due to their high surface energy and nanoscale size. **Fig. 2.4 (b)** showed spherical-shaped FA particles with a smooth surface. SEM micrographs in **Fig. 2.4 (c-f)** show different FT composites with varying $TiO_2$ concentrations. In **Fig. 2.4 (c)** $FT_1$ nanocomposite shows FA particles covered partially by $TiO_2$ particles. **Fig. 2.4 (d)** presents an $FT_3$ nanocomposite in which $TiO_2$ concentration is higher, resulting in more $TiO_2$ coverage on the FA particles. **Fig. 2.4 (e, f)** presents the images of $FT_5$ nanocomposite, which reveal that the FA particles are even more extensively covered by $TiO_2$. [13].

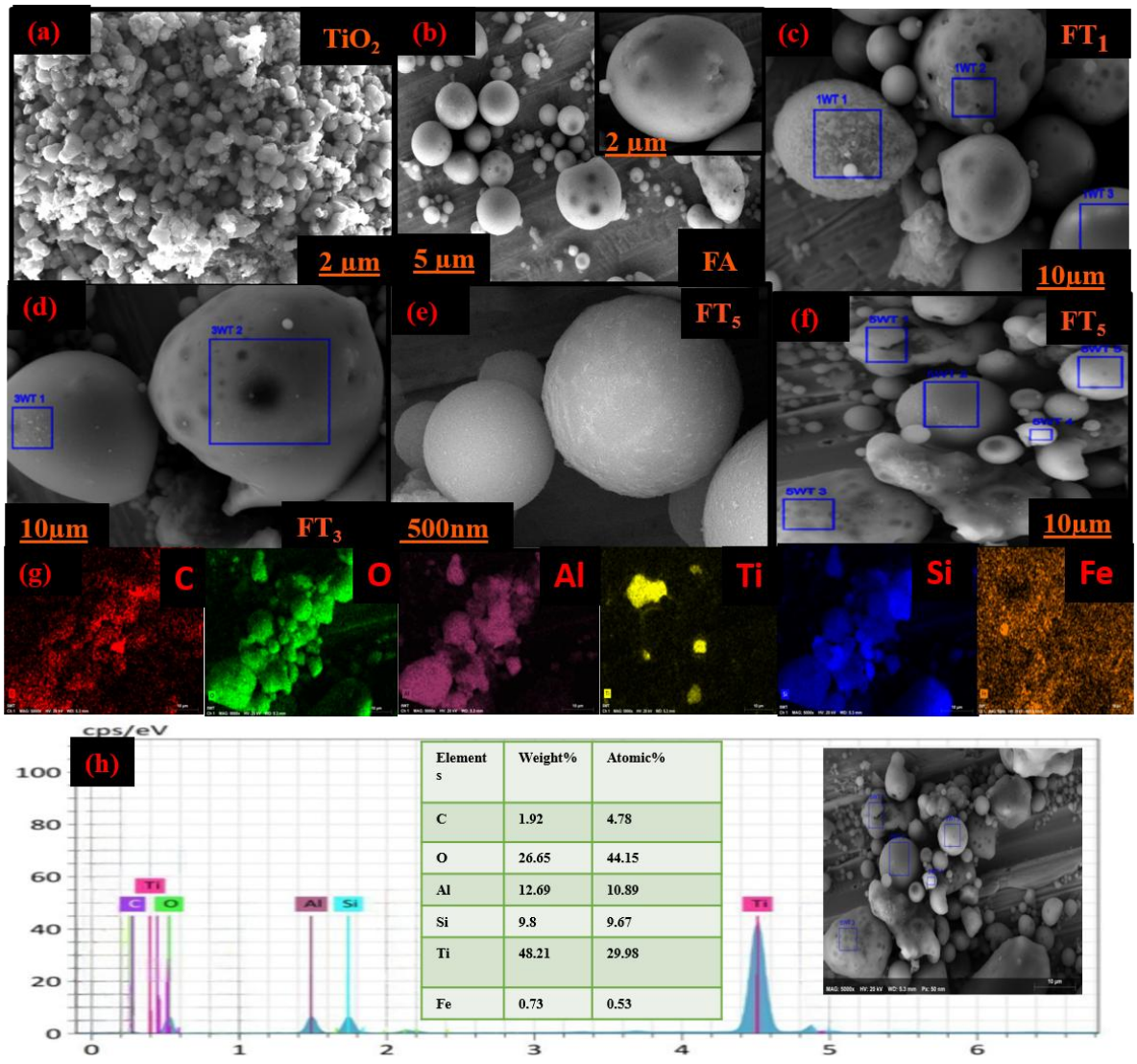


| Elements | Weight% | Atomic% |
|---|---|---|
| C | 1.92 | 4.78 |
| O | 26.65 | 44.15 |
| Al | 12.69 | 10.89 |
| Si | 9.8 | 9.67 |
| Ti | 48.21 | 29.98 |
| Fe | 0.73 | 0.53 |

**Fig. 2.4** FE-SEM images of (a) $TiO_2$, (b) FA, (c) $FT_1$, (d) $FT_3$, (e,f) $FT_5$ (g) Elemental mapping, (h) EDS spectra of $FT_5$.

### 2.3.6 EDS spectra

**Fig. 2.4 (g, h)** displays the elemental mapping and EDS spectra of the (5wt% $TiO_2$ in FA-$TiO_2$) $FT_5$ composite, which reflects the atomic and weight proportions of the elements. The elemental mapping verifies the existence of elements such as C, O, Al, Ti, Fe, and Si, shown in red, green, purple, yellow, orange, and blue, respectively. Similarly, their elemental composition is confirmed by EDS spectra. The weight distribution of elements is 4.78, 44.15, 10.89, 9.67, 29.98, and 0.53% for C, O, Al, Si, Ti, and Fe, respectively.

## 2.4 Adsorption studies

### 2.4.1 The effect of adsorbent dosage on the removal of FB dye

**Fig. 2.5(a**) demonstrates a notable improvement in FB dye removal efficiency with increasing catalyst (adsorbent) dosage from 2 mg to 5 mg. Specifically, the removal efficiency showed an increase from 39% to 57% for $TiO_2$, and from 49% to 59% for FA. For the composites $FT_{0.5}$, $FT_1$, $FT_3$, and $FT_5$, the removal efficiency enhanced from 52% to 65%, 60% to 66%, 63% to 70%, and 69% to 76%, respectively. This trend clearly indicates that higher catalyst loading provides more active surface sites for adsorption and photocatalytic interaction, resulting in greater dye removal performance**.** The removal effectiveness remained unchanged after increasing the dose from 5 mg to 7 mg. This observation suggests that the available active adsorption sites on the adsorbent surface become saturated beyond a dosage of 5 mg. Accordingly, 5 mg was identified as the optimal adsorbent mass for this system. At this dosage, the maximum adsorption capacity of the materials is reached, and further increases in adsorbent quantity do not result in higher dye removal efficiency. Determining the optimum adsorbent dosage is crucial in practical adsorption processes, as it ensures effective pollutant removal while maintaining cost efficiency. In this study, 5 mg of adsorbent was found to be optimal for achieving efficient FB dye removal.

### 2.4.2 The effect of adsorbate initial concentration on the removal of FB dye

The adsorptive performance of $TiO_2$, FA, and various FT nanocomposites was tested by modulating the FB dye concentration in the range of 5-30 mg/L, as shown in **Fig. 2.5 (b)**. With the increase in the initial dye concentration of fuchsin blue, the removal efficiency gradually increases up to the concentration of 10 ppm. This is because at low concentrations, more adsorption sites are available for the dye molecules, thereby increasing removal efficiency. The maximum removal efficiency (76%) was obtained at an initial concentration of 10 mg/L. As the concentration of the adsorbate increases, the removal efficiency decreases. The reduction in adsorption can be attributed to the progressive saturation of active sites as the initial concentration increases. As a result, the ideal concentration of FB adsorption was determined to be 10 ppm for further experiments.

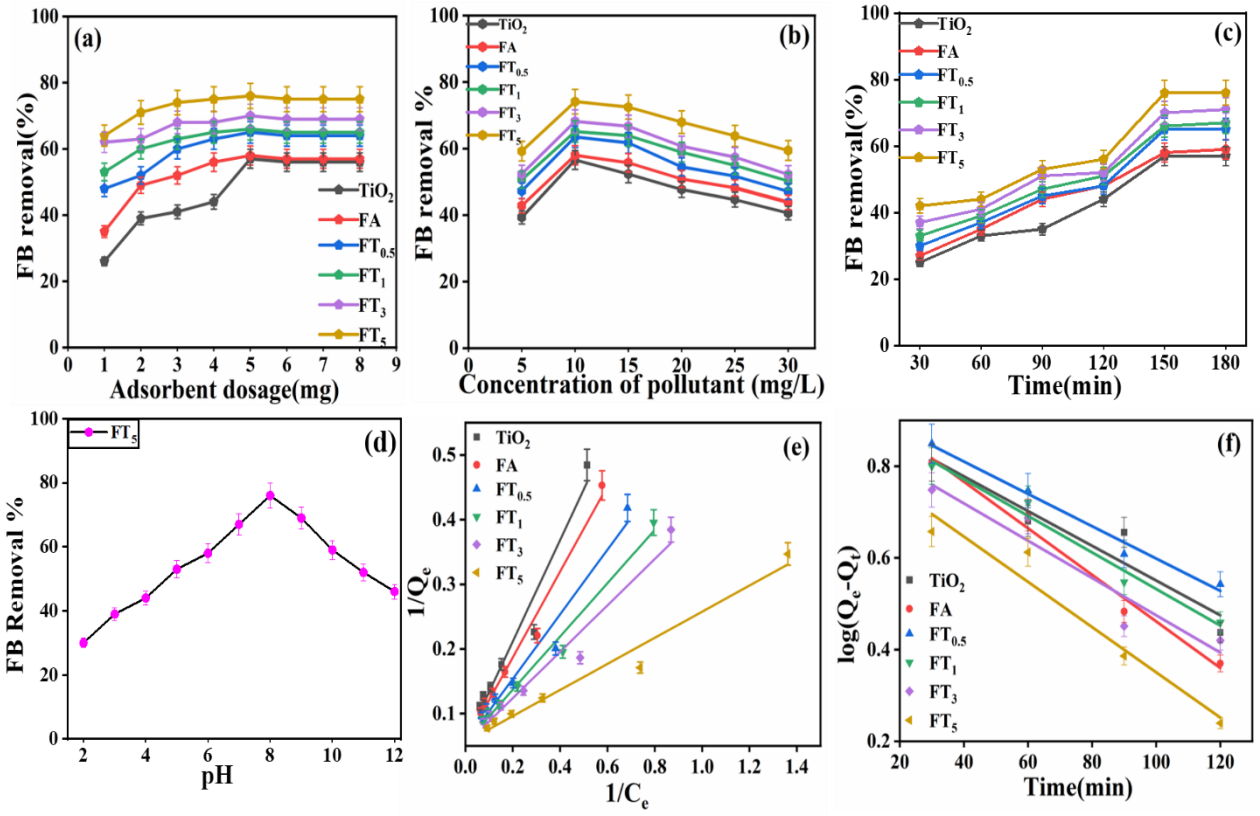


**Fig. 2.5** (a) The effect of adsorbent dose on FB removal, (0.005/L) (b) the effect of adsorbate concentration, (10mg/L) (c) the effect of contact time, (150min) (d) the effect of pH, (e) Langmuir isotherm (f) Pseudo-first-order kinetic model

### 2.4.3 The effect of contact time on the removal of FB dye

The duration of contact time between the adsorbate (fuchsin blue) and the adsorbents ($FT_5$) is a critical factor in the process of adsorption. Adsorption initially rises with an increase in contact time until equilibrium is reached. The initial concentration of the FB dye in the solution is 10 mg/L. The percentage removal of the dye increased as the contact time between the dye and the adsorbent increased. This means that longer contact times led to more efficient removal of the dye from the solution. The rate of adsorption slowed down as the contact time increased. This suggests that adsorption was more rapid in the early stages but gradually approached equilibrium. Equilibrium was reached after 150 minutes of contact. Between 150 minutes to 180 minutes, the removal efficiency of the dye by the various adsorbents ($TiO_2$, FA, and FT) remained constant due to the saturation of active sites with dye. Compared to FA, $TiO_2$, and other composites, the $FT_5$ was the best adsorbent, showing 76% fuchsin dye removal. However, all the adsorbents after 150 minutes showed in **Fig. 2.5 (c),** and further increase in contact time

did not improve adsorption behaviour.

### 2.4.4 The effect of pH on the removal of FB dye

Solution pH is a crucial parameter governing the overall adsorption process. pH refers to the concentration of the hydrogen ions in a solution. Additionally, it may increase surface charges, which may enhance the electrostatic contact between the surface of the adsorbent and the adsorbate. The adsorption of FB over the $FT_5$ composite was investigated in the range of pH 2-pH 10 for 150 min. **Fig. 2.5 (d)** illustrates that the removal efficiency of FB increases progressively as the value ranges from 2 to 10. The maximum removal percentage (76%) of FB by $FT_5$ was seen at pH 8. The results concluded that the remaining oxygen functional groups distributed on the surface of the composite transmit the negative charge, causing FB adsorption to be greatly reduced under alkaline circumstances. The adsorption happened because of electrostatic forces between the negatively-charged adsorbent and the positively-charged dye molecule due to the protonation of functional groups. At acidic conditions, the surface of the $FT_5$ composite gains a positive charge, resulting in a significant repellent force between the catalyst and dye molecules, leading to a significant reduction in the percentage eradication. Adsorption sites are deprotonated because of static attraction and H-bonding, leading to a significant loss of FB at alkaline pH. The point zero charge (pH $_{ZPC}$) of the $FT_5$ composite was determined to be 7.4, indicating that the adsorbent surface was negatively charged at pH > pH $_{ZPC}$ and became positively charged at pH < pH $_{ZPC,}$ which will assist in improved adsorptive removal. Considering the pH at which maximal dye removal efficiency was attained was larger than pH $_{ZPC}$, a significant electrostatic interaction between dye molecules and $FT_5$ Composite has occurred. Therefore, an alkaline environment with a pH of 8 is optimal for the adsorption of FB onto $FT_5$ [36].

### 2.4.5 Adsorption equilibrium studies

Adsorption isotherms investigate how pollutant molecules interact with the adsorbent surface at equilibrium. The isotherms of adsorption were studied by altering the initial concentration of FB (5-30 mg/L) at a fixed amount of adsorbent (5 mg). As described by the Langmuir isotherm model, adsorption occurs on a surface with uniformly energetic sites, resulting in monolayer adsorption of the adsorbate molecules onto the adsorbent. It is also acknowledged that adjacent molecules that are adsorbed do not interact with one another. The Langmuir adsorption isotherm is written as:

$$\frac{1}{Q_e} = \left( \frac{1}{K_L Q_{max}} \right) \times \frac{1}{C_e} + \frac{1}{Q_{max}} \quad (5)$$

where $C_e$ (mg/L) is the equilibrium adsorbate concentration, $Q_e$ (mg/g) is the equilibrium adsorption capacity of the adsorbent, Langmuir constant, $K_L$ (L/mg) represents the affinity of the adsorbate for the adsorbent, and $Q_{max}$ (mg/g) is the maximum adsorption capacity of the adsorbent before full monolayer formation [37]. The graph was drawn between $1/Q_e$ versus 1/Ce in **Fig. 2.5 (e),** and the intercept and slope were utilized to derive $K_L$ and $Q_{max}$ values. Using the dimensionless constant $R_L$, it is possible to identify the adsorption nature and examine whether the process is favourable or unfavourable.

$$R_L = \frac{1}{1 + K_L C_o} \quad (6)$$

where $K_L$ signifies the Langmuir constant, and $C_o$ is the highest concentration of a contaminant initially. The adsorption type is represented by the value of $R_L$. If $R_L = 1$ (linear), $R_L = 0$ (irreversible), or $R_L > 1$ (unfavourable), $0 < R_L < 1$ (favourable). The Freundlich isotherm assumes the surface of the adsorbent to be heterogeneous and that there are substantial interactions between adsorbate molecules. The adsorption takes place on the surface of the adsorbent by the development of multilayers of adsorbate molecules. The Freundlich isotherm's equation is shown as follows:

$$\log Q_e = \log K_F + \left( \frac{1}{n} \right) \log C_e \quad (7)$$

Adsorption favorability is described by the Freundlich constant, $K_F$, and the heterogeneity factor, 1/n, where $Q_e$ (mg/g) is the amount of contaminant adsorbed at equilibrium, and Ce (mg/L) is the concentration of contaminant in solution at equilibrium. The graph was plotted between log $Q_e$ versus log Ce. Values of n larger than unity suggest that the method is favourable [37]. The Freundlich and Langmuir models adequately predicted the experimental findings, as shown in **Table 2.2**. Compared to the Freundlich model, the Langmuir model appears to be a better fit for describing the adsorption behaviour of the pollutants on the mentioned adsorbents. The $K_L$ values reflect the adsorption equilibrium constants for each adsorbent. The $R_L$ values in the range of 0-1 indicate favourable adsorption, which supports the suitability of the Langmuir model for describing the adsorption process. Overall, for all the adsorbents, the correlation coefficient ($R^2$) values for the Langmuir model (0.9584–0.9830) were found to be closer to unity than those for the Freundlich model (0.9276–0.9562), indicating a better fit of the Langmuir isotherm. The Freundlich parameter "n >1" in **Table 2.2**. suggests that adsorption is non-linear and favours higher concentrations of the solute.

**Table 2.2. Adsorption isotherm parameters for removal of FB dye over $TiO_2$, FA, and FT composites.**

| | Langmuir model | | | | Freundlich model | | |
|---|---|---|---|---|---|---|---|
| **Adsorbent** | **$Q_{max}$ (mg/g)** | **$K_L$ (L/mg)** | **$R_L$** | **$R^2$** | **$K_F$ [mg/g.(L/mg)]$^{1/n}$** | **n** | **$R^2$** |
| **$TiO_2$** | 18.182 | 0.070 | 0.322 | 0.958 | 1.637 | 1.590 | 0.934 |
| **FA** | 18.382 | 0.081 | 0.289 | 0.981 | 1.813 | 1.576 | 0.956 |
| **$FT_{0.5}$** | 18.552 | 0.107 | 0.236 | 0.962 | 2.348 | 1.717 | 0.928 |
| **$FT_1$** | 18.382 | 0.132 | 0.207 | 0.983 | 2.619 | 1.716 | 0.947 |
| **$FT_3$** | 19.230 | 0.144 | 0.187 | 0.965 | 2.957 | 1.778 | 0.929 |
| **$FT_5$** | 20.325 | 0.235 | 0.124 | 0.971 | 4.126 | 1.956 | 0.935 |

### 2.4.6 Adsorption kinetics

To investigate the mechanism of the adsorption process of FB dye onto FA-$TiO_2$ composites, the experimental kinetic data were tested using the pseudo-first-order and pseudo-second-order kinetic models. The linearized form of Lagergren's pseudo-first-order rate equation can be expressed as follows [38].

$$\log\left(Q_e - Q_t\right) = \log Q_e - \frac{k_1}{2.303} t \tag{8}$$

where $Q_t$ and $Q_e$ denote adsorption rates (mg/g) at time t (min) and equilibrium, respectively, and $k_1$ is the first-order rate constant (min**). Fig. 2.5 (f)** shows the log ($Q_e$-$Q_t$) vs t plot for the FB linear regression equation for the pseudo-second-order model as follows:

$$\frac{t}{Q_t} = \frac{1}{k_2 Q_e^{\,2}} + \frac{t}{Q_e} \tag{9}$$

where $k_2$ represents the rate constant for the 2nd order and $Q_e$ and $Q_t$ denote amounts of pollutant adsorbed per gram of adsorbent (mg/g) at equilibrium and time t (min), respectively [39]. The 2nd-order kinetic model posits that the rate-limiting phase is chemisorption, which entails the exchange or movement of electrons among the adsorbent and adsorbate. The first- and second-order kinetics parameters were calculated using the slope and intercept shown in the graphs, as shown in **Table 2.3**. Compared to the second-order model, the first-order model was shown to have a rate constant which is simultaneously bigger and nearer to unity. It demonstrates that the adsorption of FB dye onto $TiO_2$, FA, and FA-$TiO_2$ composites is governed by first-order kinetics. The pseudo-first-order kinetic model explains adsorption

behavior based on the assumption that the rate of occupation of adsorption sites is proportional to the number of unoccupied sites. In Fig. 2.5(f), the plots of log(Qe − Qt) versus time show an approximately linear relationship for all samples, which confirms that the adsorption process follows pseudo-first-order kinetics. The straight-line nature of the curves in Fig. 2.5(f) indicates that adsorption is controlled mainly by physical adsorption interactions between FB dye molecules and the composite surface. The steeper slope observed for $FT_5$ suggests a higher adsorption rate constant and stronger adsorption efficiency compared to $TiO_2$ and fly ash alone. This demonstrates that adsorption is the dominant initial mechanism responsible for dye removal before photocatalytic degradation occurs.

**Table 2.3.** Kinetic model parameters for removal of FB dye over various photocatalysts

| | **Pseudo-first-order Model** | | | **Pseudo-second-order Model** | | |
|---|---|---|---|---|---|---|
| **Adsorbent** | **$Q_e$ (mg/g)** | **$k_1$ ($min^{-1}$)** | **$R^2$** | **$Q_e$ (mg/g)** | **$k_2$ (g/mg. min)** | **$R^2$** |
| **$TiO_2$** | 8.499 | 0.009 | 0.909 | 8.453 | 0.001 | 0.859 |
| **FA** | 11.402 | 0.012 | 0.984 | 16.638 | 0.001 | 0.962 |
| **$FT_{0.5}$** | 15.100 | 0.008 | 0.984 | 18.416 | 0.001 | 0.896 |
| **$FT_1$** | 18.407 | 0.009 | 0.977 | 18.348 | 0.001 | 0.913 |
| **$FT_3$** | 18.967 | 0.009 | 0.909 | 18.975 | 0.001 | 0.893 |
| **$FT_5$** | 22.698 | 0.011 | 0.948 | 20.040 | 0.008 | 0.884 |

### 2.5 Photocatalytic degradation of FB dye

Variations in the UV–visible absorption spectra of the FB dye solution treated with the $FT_5$ composite at different irradiation times are shown in **Fig. 2.6 (a, b).** The characteristic maximum absorption peak of FB occurs at 546 nm, and its intensity gradually decreases with increasing illumination, indicating progressive adsorption and photocatalytic degradation. Photocatalytic degradation using the $FT_5$ composite achieved an 88% reduction in dye concentration, whereas adsorption alone resulted in only 76% removal. This indicates that degradation is more effective than adsorption for the complete elimination of fuchsin dye. Additionally, experiments performed without a catalyst showed that only 14% of FB underwent photolysis after 180 minutes of UV irradiation, demonstrating the high stability of the dye in the absence of a photocatalyst.

**Table 2.4** Kinetic parameters of pseudo-first order model over various photocatalysts

| Pseudo-first-order Model | | |
|---|---|---|
| **Photocatalyst** | **$k_1$** | **$R^2$** |
| **$TiO_2$** | 0.0010 | 0.9907 |
| **FA** | 0.0005 | 0.9912 |
| **$FT_{0.5}$** | 0.0007 | 0.9948 |
| **$FT_1$** | 0.0007 | 0.9895 |
| **$FT_3$** | 0.0013 | 0.9833 |
| **$FT_5$** | 0.0016 | 0.9956 |

UV–visible absorption spectra of FB dye after photodegradation using bare and $TiO_2$-loaded FA nanocomposites under 180 minutes of UV irradiation are shown in **Fig. 2.6 (c).** The absorption intensity depends on the $TiO_2$ concentration in the composite. $TiO_2$ loading significantly enhanced the photoactivity of fly ash, with 5wt% $TiO_2$ showing the highest catalytic efficiency, beyond which additional loading did not yield further improvement. To determine the optimal $TiO_2$ loading on fly ash for effective FB degradation, the time-dependent photodegradation profiles **(Fig. 2.6(d))** and the corresponding kinetic plots **(Fig. 2.6(e))** were analyzed. The results demonstrate that the degradation kinetics conform to a pseudo-first-order model, in accordance with the given equation (10).

$$\ln (C_o / C_t) = kt \quad (10)$$

Where $C_0$ is the initial concentration of the FB dye in the solution at time 0, $C_t$ refers to the FB dye concentration at time t. k represents the rate constant ($min^{-1}$), and t indicates the reaction time [30]. In this highly dilute system, the absorbance intensity ratio $A_t$ at irradiation time $t$is proportional to the initial absorbance $A_0$ at $t = 0$, which can be ensured by adjusting the FB concentration ratio $C_0/C_t$. The pseudo-first-order rate constants and the corresponding squared linear correlation coefficients ($R^2$) for $TiO_2$, FA, $FT_{0.5}$, $FT_1$, $FT_3$, and $FT_5$ are summarized in **Table 2.4.** The histogram in **Fig. 2.6 (f)** compares the percentage removal of fuchsin blue dye by $TiO_2$, fly ash, and various FT composites during the dark adsorption and degradation process under UV light.

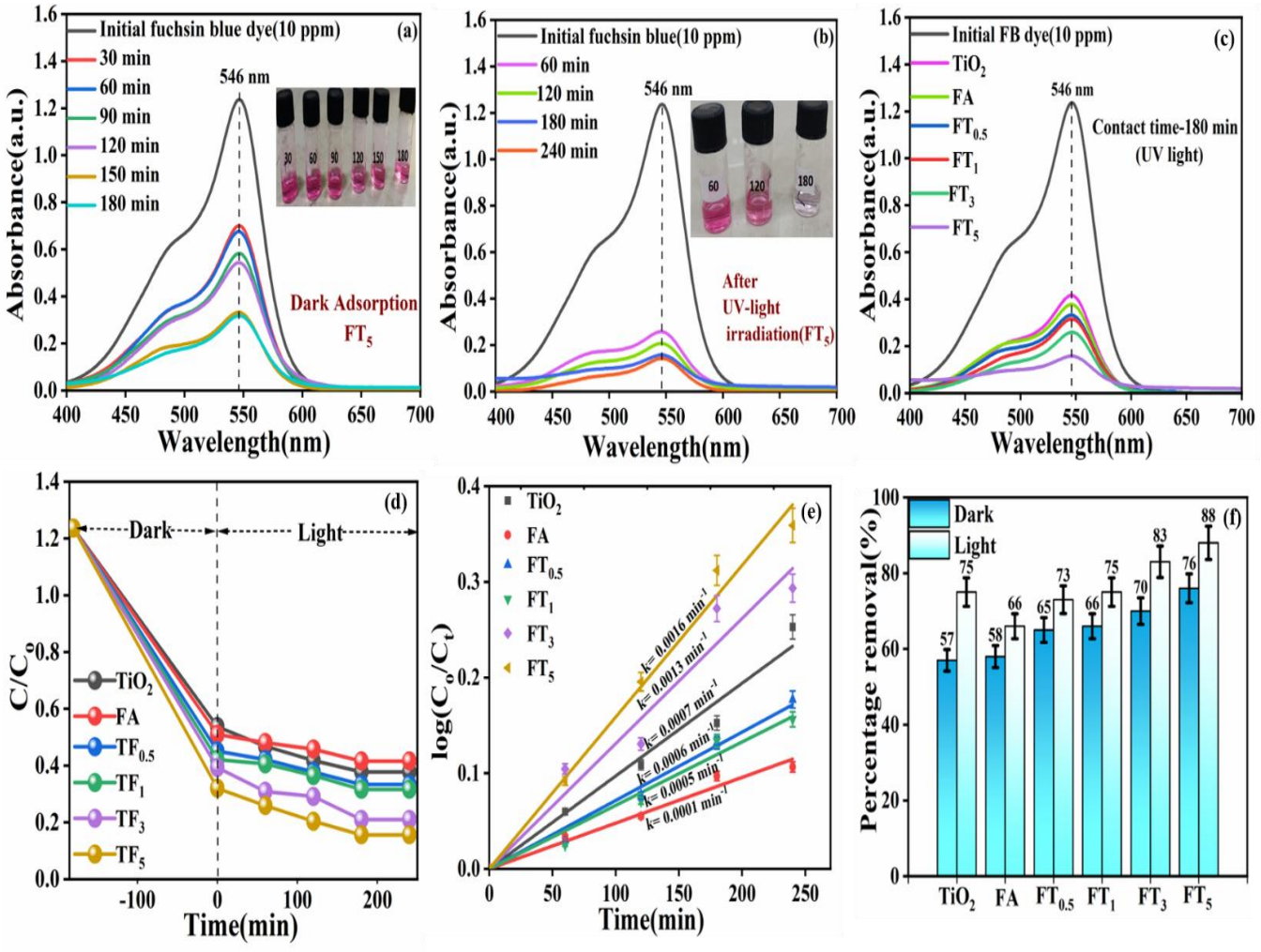


**Fig. 2.6** Changes in UV absorption spectra of fuchsin blue dye (a) dark adsorption (b) after photocatalytic degradation by 5wt% $TiO_2$-loaded FA nanocomposite under UV irradiation, and (c) after 180 minutes by different wt% $TiO_2$-loaded FA composites, (d) time course kinetic plots of fuchsin dye in dark and light, (e) Pseudo first-order model, (f) histogram representing comparison of percentage removal of fuchsin blue dye under dark and light irradiation

## 2.6 Degradation pathway analysis

HRMS analysis was done to analyze the mass(m) /charge(z) ratio and identify the molecular formula. The precise m/z measurement for the fuchsin ion 330 was 330.0928. The degradation pathways of basic fuchsin (also known as fuchsin) are described as shown in **Fig. 2.7 (a, b),** determined by mass spectrometry analysis, and two potential degradation pathways for this dye. These pathways represent how basic fuchsin molecules can degrade into various intermediates and eventually into simpler, inorganic compounds like water ($H_2O$) and carbon dioxide ($CO_2$)

under the influence of different reactions involving demethylation, hydroxylation, ring-opening reactions, and oxidation. Through pathway 1, Fuchsin (m/z = 365.91) undergoes demethylation to form Product B (m/z = 316.18). Product B undergoes another demethylation step to yield Product C (m/z = 302.17). Product C undergoes a ring-opening reaction with reactive oxygen species ($\bullet O_2^-$ and •OH) to generate Product D (m/z = 205.11). Product D is subsequently oxidized to form Product E, i.e., 3-Heptynoic acid (m/z = 126.07). Product E 3-Heptynoic acid m/z = 126.07) is finally mineralized to $H_2O$, $CO_2$, and some inorganic ions. In pathway 1, the other side of product C (m/z = 302.17) undergoes the ring-opening reaction, transforms into product H (m/z = 282.16), and finally transforms into $CO_2$ and $H_2O$.

Through pathway 2, Product A (m/z = 330.09), which is produced by the ionization of fuchsin, goes through hydroxylation, i.e., the addition of a hydroxyl group, to form Product F, i.e., carbinol of Pararosaniline (m/z = 347.21). Product F is oxidized to give Product G (m/z = 223.14). Product G is eventually mineralized to $H_2O$, $CO_2$, and certain inorganic ions [40].

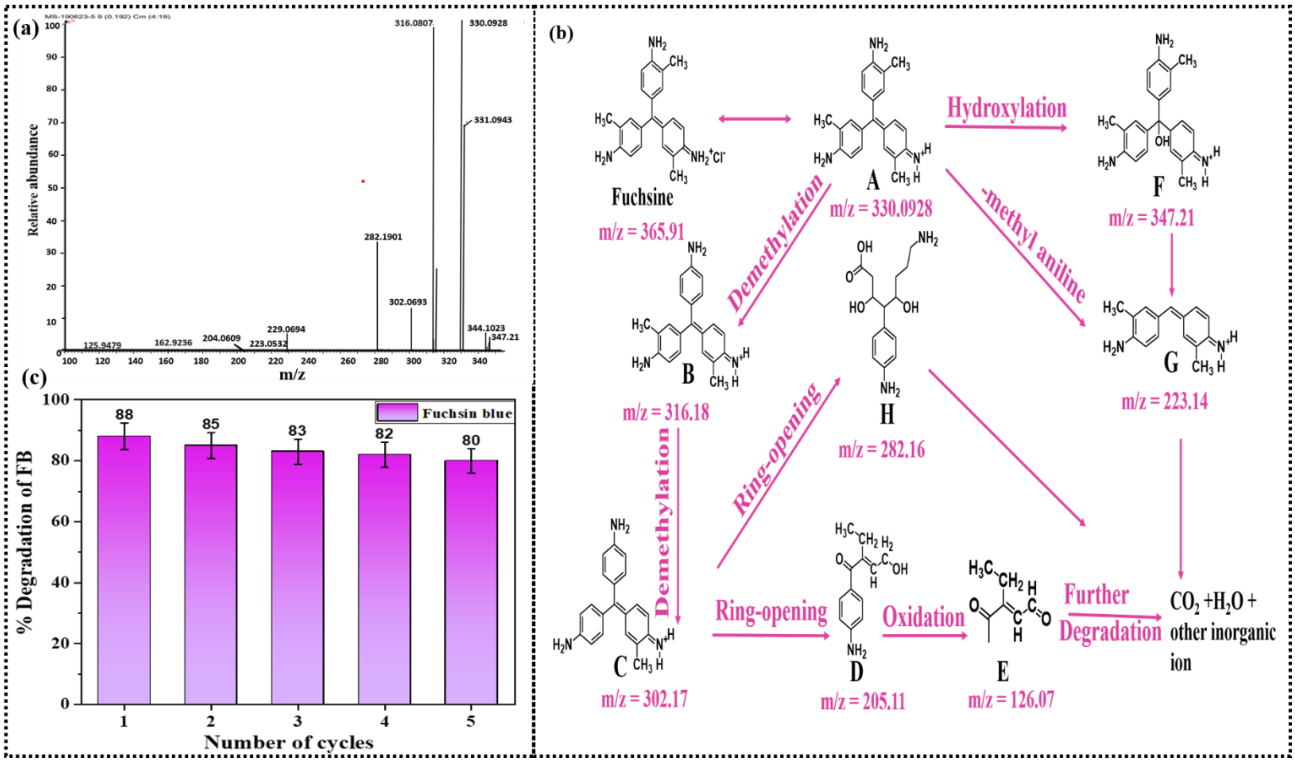


**Fig. 2.7** (a) High-Resolution Mass Spectroscopy, (b) degradation pathway of fuchsin blue dye after degradation by $FT_5$ nanocomposite, (c) Reusability studies of $FT_5$ nanocomposite.

### 2.7 Reusability studies

In the first UV irradiation cycle, the $FT_5$ composite (5wt% FA–$TiO_2$) achieved an 88% reduction in FB dye concentration over 180 minutes. This result highlights the excellent

photocatalytic performance of the material and its suitability for dye removal applications. Interestingly, the degradation efficiency remains close even after five successive cycles of UV irradiation displayed in **Fig. 2.7 (c).** This suggests that the photo-catalytic activity of the composites remains almost stable and does not significantly degrade over multiple uses. The stable degradation efficiency observed over multiple cycles indicates that the $FT_5$ composite has a high re-usability performance. It can be used repeatedly without a substantial drop in its catalytic activity. Furthermore, an ICP-OES analysis was done to estimate the amount of metal ions (Al and Fe) leached from the composite. After 5 cycles of photocatalytic degradation, the concentration of Fe was 1.40 ppm, instead of 1.69 ppm before degradation. Aluminium metal concentrations were 2.53ppm before the procedure and 2.08ppm after five degradation cycles. This minimal leaching is further confirmed by a lower drop in removal efficiency in the re-usability test. This shows that the composites are stable and reusable. The high re-usability of the composite is attributed to the formation of Si-O-Ti linkages between FA (presumably a silica-based material) and $TiO_2$. These linkages immobilize the $TiO_2$ component, preventing its loss during the photocatalytic reactions. This immobilization of $TiO_2$ helps maintain the composite's catalytic activity over successive cycles. The $FT_5$ composite appears to be an efficient and repeatedly reusable photocatalyst for the degradation of FB dye.

### 2.8 Plausible Mechanism

The photocatalytic degradation of FB dye (shown in **Scheme 2.2**) involves a combined adsorption–photocatalytic mechanism in which FA and $TiO_2$ work synergistically to enhance dye removal efficiency. Initially, FA adsorbs FB dye molecules from the aqueous solution onto its porous surface through electrostatic interactions, pore diffusion, hydrogen bonding. Due to its porous aluminosilicate structure, FA provides abundant active adsorption sites and concentrates the dye molecules near the catalyst surface. Simultaneously, the $TiO_2$ loaded onto the surface of FA is exposed to UV light, enhancing the movement of electrons from the valence band to the conduction band of $TiO_2$ [14]. This electron excitation is a crucial step in initiating the photocatalytic process. Positive holes form as electrons move from the VB to the CB. These positive holes are highly reactive species that can participate in oxidative reactions. The excited electrons in the CB of $TiO_2$ are trapped on the $TiO_2$ surface by oxygen molecules, leading to the formation of peroxide radicals ($O_2^-$). Simultaneously, the positive holes can oxidize water molecules adsorbed on the $TiO_2$ surface, generating hydroxyl radicals ($OH^{\cdot}$). These peroxide radicals and hydroxyl radicals are potent oxidative species. The peroxide radicals ($O_2^{\cdot -}$) and hydroxyl radicals ($OH^{\cdot}$) oxidize FB dye molecules in the solution. This

oxidation process facilitates the breakdown of FB into simpler, less harmful organic molecules. FA is crucial in retaining free radicals (such as $O_2^{\cdot-}$ and $OH^{\cdot}$) on its surface. This retention enhances the rate of FB breakdown on the $TiO_2$ surface because the free radicals continue to react with FB in proximity. Over time, peroxide and hydroxyl radicals' oxidative reactions may eventually oxidize Fuchsin dye into harmless inorganic molecules like $CO_2$ and $H_2O$. The improved photocatalytic degradation efficiency observed with FT nanocomposites is attributed to the synergistic impact of FA's adsorption efficiency and $TiO_2$'s photocatalytic activity. FA concentrates the pollutant molecules on its surface, making them more accessible to the $TiO_2$ photocatalyst, initiating the degradation process.

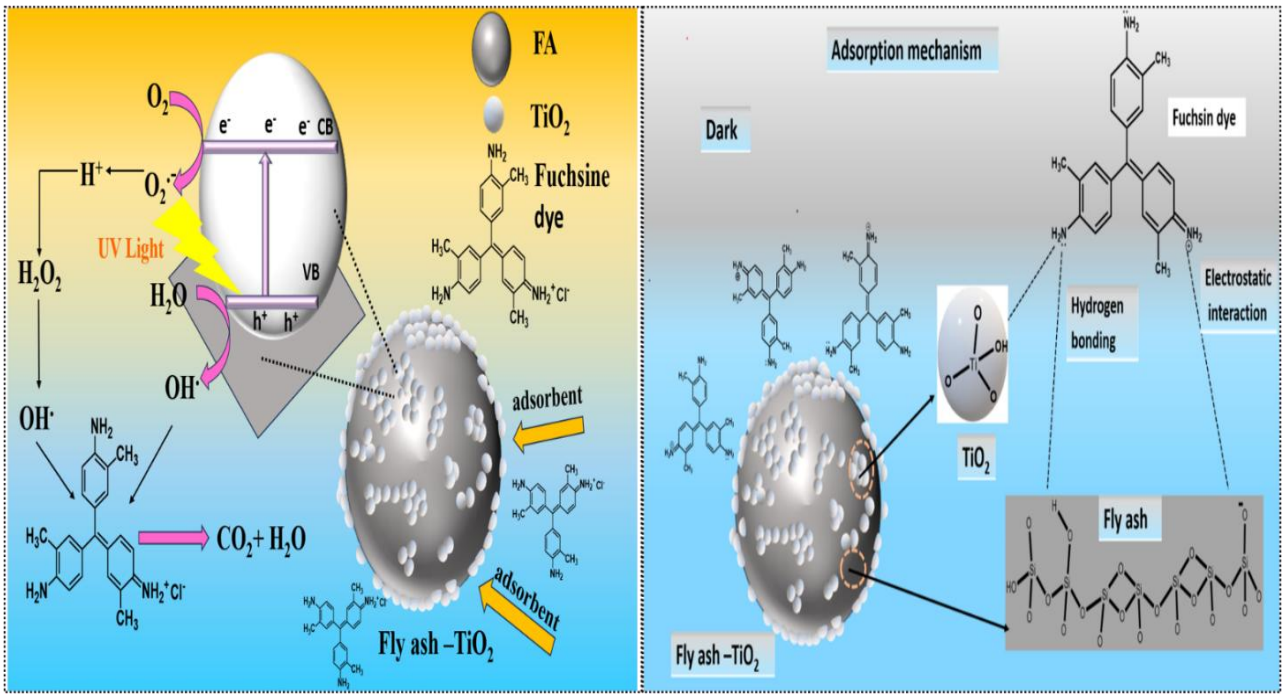


**Scheme 2.2.** The proposed adsorption and photocatalytic mechanisms of an FT nanocomposite under UV light irradiation.

### 2.9 Conclusion

Fly ash and $TiO_2$ (FT) composites were synthesized using a sol–gel method combined with wet impregnation. The maximum adsorptive removal of FB dye (76%) was achieved over $FT_5$ composite at an initial dye concentration of 10 mg/L within 150 minutes, as compared to $TiO_2$, which exhibited an adsorption efficiency of 57%. The adsorption data were found to fit the Langmuir isotherm more accurately than the Freundlich model, indicating that monolayer adsorption predominated and suggesting a specific and well-defined adsorption mechanism for

FB removal. Furthermore, the $FT_5$ composite exhibited the highest photocatalytic activity, achieving an 88% degradation of FB dye within 180 minutes of UV irradiation, in contrast to $TiO_2$, which showed 75% degradation. The photocatalytic degradation kinetics followed a pseudo-first-order model, which is typically employed to describe such processes and provides a quantitative measure of the degradation rate. The photocatalyst exhibited remarkable stability and maintained its performance across four consecutive cycles of degradation, which can be attributed to the formation of Si–O–Ti linkages between fly ash and $TiO_2$. These chemical bonds effectively immobilize $TiO_2$ on the fly ash surface, thereby minimizing catalyst leaching during operation.

## References


[1] Hussain Z, Lizhen G, Moeen M, Treatment of coal fly ash and environmentally friendly use with rubber in cable wires as insulation material, Sustainability. 12 (2020) 5218, https://doi.org/10.3390/su12125218.

[2] Yao ZT, Ji XS, Sarker PK, Tang JH, Ge LQ, Xia MS, et al., A comprehensive review on the applications of coal fly ash, Earth Sci Rev. 141 (2015) 105–121, https://doi.org/10.1016/j.earscirev.2014.11.016.

[3] Okte AN, Karamanis D, Tuncel D, Dual functionality of $TiO_2$–fly ash nanocomposites: Water vapor adsorption and photocatalysis, Catal Today. 230 (2014) 205–213, https://doi.org/10.1016/j.cattod.2014.01.031.

[4] Visa M, Andronic L, Duta A, Fly ash–$TiO_2$ nanocomposite material for multi-pollutants wastewater treatment, J Environ Manage. 150 (2015) 336–343, https://doi.org/10.1016/j.jenvman.2014.10.026.

[5] Bartoňová L, Unburned carbon from coal combustion ash: An overview, Fuel Process Technol. 134 (2015) 136–158, https://doi.org/10.1016/j.fuproc.2015.01.028.

[6] Ding MS, Han WZ, Li J, Ma E, Shan ZW, In situ study of the mechanical properties of airborne haze particles, Sci China Technol Sci. 58 (2015) 2046–2051, https://doi.org/10.1007/s11431-015-5935-8.

[7] Blissett RS, Rowson NA, A review of the multi-component utilisation of coal fly ash, Fuel. 97 (2012) 1–23, https://doi.org/10.1016/j.fuel.2012.03.024.

[8] Saud PS, Pant B, Park M, Chae SH, Park SJ, El-Newehy M, et al., Preparation and photocatalytic activity of fly ash incorporated $TiO_2$ nanofibers for effective removal of organic pollutants, Ceram Int. 41 (2015) 1771–1777, https://doi.org/10.1016/j.ceramint.2014.09.123.

[9] Ma M, Guo W, Yang Z, Huang S, Wang G, Preparation and photocatalytic activity of $TiO_2$/fine char for removal of rhodamine B, J Nanomater. (2015) 538275, https://doi.org/10.1155/2015/538275.

[10] Zhao ZH, Liu WH, Xue YQ, Yin S, Synthesis of $TiO_2$/fly ash cenospheres by sol–gel method and their photocatalytic activities under visible light, J Nanosci Nanotechnol. 18 (2018) 3306–3313, https://doi.org/10.1166/jnn.2018.14641.

[11] Yang H, Yang B, Chen W, Yang J, Preparation and photocatalytic activities of $TiO_2$- based composite catalysts, Catalysts. 12 (2022) 1263, https://doi.org/10.3390/catal12101263.

[12] Arsalan M, Rhithuparna D, Khan MA, Rahman WU, Alajmi MF, Hussain A, et al. Multifaceted CA@$TiO_2$ nanocomposite-based thin film composite membrane for advanced separation and environmental detoxification. Next Materials 8 (2025)100907, https://doi.org/10.1016/j.nxmate.2025.100907

[13] Gilja V, Katancic Z, Krehula LK, Mandic V, Hrnjak-Murgic Z, Efficiency of $TiO_2$ catalyst supported by modified waste fly ash during photodegradation of RR45 dye, Sci and Engin of Compo. Mater. 26 (2019) 292–300, https://doi.org/10.1515/secm-2019-0017.

[14] Tu Y, Zhong J, Ding H, Zhang H, Lv G, Zhang J, et al., Preparation of fly ash-supported nano-$TiO_2$ composite photocatalyst by a wet mechanical grinding method, Chem Phys Lett. 805 (2022) 139978, https://doi.org/10.1016/j.cplett.2022.139978.

[15] Jimenez-Relinque E, Lee SF, Plaza L, Castellote M, Synergetic adsorption–photocatalysis process for water treatment using $TiO_2$ supported on waste stainless steel slag, Environ Sci Pollut Res. 29 (2022) 39712–39722, https://doi.org/10.1007/s11356-022-18728-8.

[16] Mpelane A, Katwire DM, Mungondori HH, Nyamukamba P, Taziwa RT, Application of novel c-$TiO_2$–CFA/PAN photocatalytic membranes in the removal of textile dyes in wastewater, Catalysts. 10 (2020) 909, https://doi.org/10.3390/catal10080909.

[17] Duta A, Visa M, Simultaneous removal of two industrial dyes by adsorption and photocatalysis on a fly ash–$TiO_2$ composite, J Photochem Photobiol A Chem. 306 (2015) 21–30, https://doi.org/10.1016/j.jphotochem.2015.03.007.

[18] Kanakaraju D, Jasni MAA, Pace A, Ya MH, Enhanced dye-removal performance of Cu–$TiO_2$–fly ash composite under visible light irradiation, Environ Sci Pollut Res. 28 (2021) 68834–68845, https://doi.org/10.1007/s11356-021-15440-x.

[19] Ba Mohammed B, Hsini A, Abdellaoui Y, Abou Oualid H, Laabd M, El Ouardi M, et al., Fe-ZSM-5 zeolite for efficient removal of basic fuchsin dye, J Environ Chem Eng. 8 (2020) 104419, https://doi.org/10.1016/j.jece.2020.104419.

[20] Ben Aissa MA, Khezami L, Taha K, Elamin N, Mustafa B, Al-Ayed AS, et al., Yttrium oxide-doped ZnO for adsorption of basic fuchsin dye, Int J Environ Sci Technol. 19 (2022) 9901–9914, https://doi.org/10.1007/s13762-021-03816-y.

[21] El Haddad M, Removal of basic fuchsin dye using mussel shell biomass waste, J Taibah Univ Sci. 10 (2016) 664–674, https://doi.org/10.1016/j.jtusci.2015.08.007.

[22] Bessashia W, Berredjem Y, Hattab Z, Bououdina M, Removal of basic fuchsin from water using mussel eggshell membrane, Environ Res. 186 (2020) 109484,

https://doi.org/10.1016/j.envres.2020.109484.

[23] Khezami L, Bessadok A, Ben Aissa MA, Ahmed AH, Modwi A, Benhamadi N, et al., g-$C_3N_4$-modified ZnO nanocomposite for adsorption of basic fuchsin dye, Inorg Chem Commun. 164 (2024) 112413, https://doi.org/10.1016/j.inoche.2024.112413.

[24] El-Azazy M, El-Shafie AS, Ashraf A, Issa AA, Biosorptive removal of basic fuchsin using pistachio nutshells, Appl Sci. 9 (2019) 4855, https://doi.org/10.3390/app9224855.

[25] Varadharaj VP, Ramesh G, Kumar A, Jeyabalan J, Narayanasamy S, Oxidant-modified biochar for sequestration of basic fuchsin dye, Biomass Convers Biorefin. 13 (2023) 9525–9536, https://doi.org/10.1007/s13399-023-04210-z.

[26] Fernandes EP, Silva TS, Carvalho CM, Selvasembian R, Chaukura N, Oliveira LMTM, et al., Efficient adsorption of dyes by γ-alumina synthesized from aluminum wastes, J Environ Chem Eng. 9 (2021) 106198, https://doi.org/10.1016/j.jece.2021.106198.

[27] Kanakaraju D, Ravichandar S, Lim YC, Combined effects of adsorption and photocatalysis by $TiO_2$/ZnO–calcium alginate beads, J Environ Sci. 55 (2017) 214–223, https://doi.org/10.1016/j.jes.2016.05.043.

[28] Kaur H, Singh S, Pal B, Impact of g-$C_3N_4$ loading on NiCo LDH for adsorptive removal of organic pollutants, Korean J Chem Eng. 38 (2021) 1248–1259, https://doi.org/10.1007/s11814-021-0784-6.

[29] Singh K, Singh AK, Kumar A, Agarwal A, Fly ash and $TiO_2$-modified fly ash for Cd(II) and Pb(II) removal, J Hazard Mater Adv. 10 (2023) 100256, https://doi.org/10.1016/j.hazadv.2023.100256.

[30] Bansal M, Pal B, Starch-modified NiFe LDH composites for adsorption and photocatalysis, Environ Sci Pollut Res. 30 (2023) 73825–73848, https://doi.org/10.1007/s11356-023-27592-z.

[31] Chu L, Qin Z, Yang J, Li X, Anatase $TiO_2$ nanoparticles with exposed {001} facets, Sci Rep. 5 (2015) 12143, https://doi.org/10.1038/srep12143.

[32] Golewski GL, Fracture toughness of concrete containing fly ash, Coal Fly Ash Beneficiation (2018), https://doi.org/10.5772/intechopen.69405.

[33] Yin Y, Yin H, Wu Z, Qi C, Tian H, Zhang W, et al., Si content determination using combined second-derivative method, Crystals. 9 (2019) 1–12, https://doi.org/10.3390/cryst9100513

[34] Hashem AM, Ghany AEA, Indris S, Ehrenberg H, Mauger A, Julien CM, Anatase $TiO_2$ nanoparticles for lithium-ion batteries, Ionics. 24 (2018) 2925–2934, https://doi.org/10.1007/s11581-017-2425-y.

[35] Li G, Mang C, Xing L, Cao P, Cai Y, Luo J, et al., Mo-doped $TiO_2$/FAC for degradation of methylene blue, Colloids Surf A Physicochem Eng Asp. 651 (2022) 129669, https://doi.org/10.1016/j.colsurfa.2022.129669.

[36] Rajumon R, Anand JC, Ealias AM, Desai DS, George G, Saravanakumar MP, Adsorption of textile dyes using green reduced graphene oxide, J Environ Chem Eng. 7 (2019) 103479, https://doi.org/10.1016/j.jece.2019.103479.

[37] Shaheed MA, Hussein FH, Adsorption of reactive black 5 on $TiO_2$ nanoparticles, J Nanomater. (2014) 198561, https://doi.org/10.1155/2014/198561.

[38] Goyal N, Barman S, Bulasara VK, Adsorptive removal of biochanin A using zeolite NaA, Desalin Water Treat. 57 (2016) 20608–20618, https://doi.org/10.1080/19443994.2015.1108872.

[39] Rathi A, Basu S, Barman S, Adsorptive removal of fipronil using modified HZSM-5 zeolite, J Mol Liq. 283 (2019) 867–878, https://doi.org/10.1016/j.molliq.2019.02.140.

[40] Qin J, Sun H, Zhang S, Yi L, Ruan Y, Wang S, et al., Hydrodynamic cavitation degradation of basic fuchsin dye, Sep Purif. Technol. 287 (2022) 120501, https://doi.org/10.1016/j.seppur.2022.120501.

# Chapter-3

## Influence of copper deposition on fly ash–$TiO_2$ composites for combined adsorption and visible-solar photocatalytic degradation of fuchsin blue

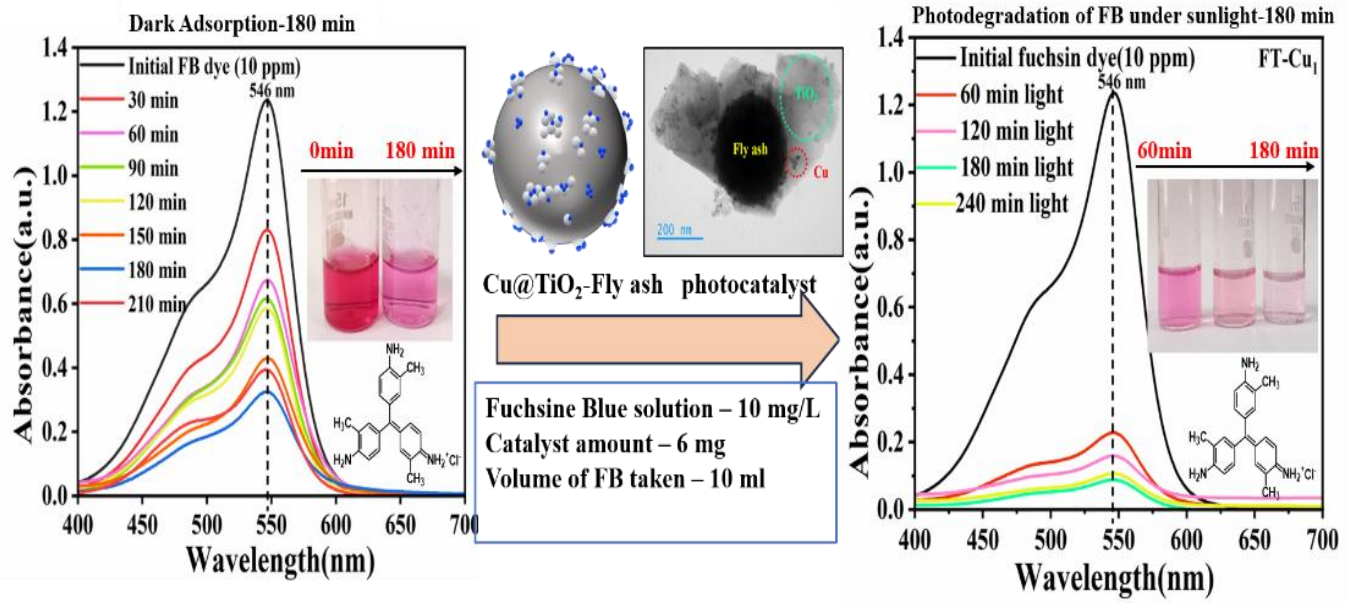


**Schematic summary**

### 3.1 Introduction

Environmental integrity and public health are significantly impacted by the harmful effects of industrial dye pollution in wastewater. These dyes, widely used in many industries, including leather and textiles, showed significant resistance to deterioration, extending their longevity in the environment [1]. Unregulated dye pollution harms the ecosystem over time, affecting the aesthetics of water bodies and endangering aquatic life [2]. A decrease in biodiversity may result from the toxic, mutagenic, or even carcinogenic effects of certain dyes, which put marine life in danger [3]. Therefore, employing an environmentally and economically sustainable technique is essential to remove all colour molecules from wastewater before it is released into the environment[4, 5]. Its high toxicity, carcinogenicity, and lack of biodegradability make it a hazardous contaminant [6]. Fuchsin blue dye contact may result in serious health complications such as headaches, skin and respiratory tract irritations, vertigo, and vomiting [7]. This dye has poor biodegradability and is toxic and carcinogenic; it must be eliminated from wastewater before discharge into the water effluents to reduce environmental contamination [8].

Several approaches have been developed for the extraction and elimination of contaminants from wastewater, including membrane separation, biological oxidation process, chemical precipitation, ion exchange, photocatalytic degradation, and adsorption[9, 10]. Nevertheless, these techniques have drawbacks such as high operating costs, energy consumption, poor selectivity, regeneration, and reusability problems [11]. The adsorption process is extensively employed in wastewater treatment because of its ease of operation, environmental friendliness, excellent efficacy, and minimal energy requirement [12, 13]. Photocatalysis is a promising and eco-friendly advanced oxidation approach for treating wastewater. Photocatalysis can degrade many contaminants, including substances resistant to conventional treatment methods, and convert them into non-toxic substances like water and carbon dioxide. This method can drastically save operating expenses because it uses relatively little energy, especially when sunlight is employed as the light source. Photocatalysis reduces the possibility of secondary contamination because it does not involve chemical additives and yields nontoxic byproducts [14]. Adsorption combined with photocatalysis is a novel way to combine the benefits of both technologies while minimizing the limitations of each one alone [15]. There are disadvantages to using adsorption and photocatalysis independently, including expensive adsorbent renewal as well as the potential risk of secondary pollution due to insufficient degradation of contaminants or exhausted adsorbents [16]. The combination of adsorbent and photocatalyst cuts the expense and frequency of adsorbent regeneration. Adsorbents can be regenerated in situ, increasing their lifespan and decreasing waste through the photocatalytic destruction of contaminants directly on their surface. Adsorbents and photocatalysts can work together to enhance photocatalytic activity. $TiO_2$ has emerged among the most researched photocatalysts due to its remarkable chemical stability, significant photosensitivity, and low toxicity [17]. $TiO_2$ is less efficient under normal sunlight because a limited part of the solar spectrum falls within the UV region. Wide band gap and exclusive sensitivity to UV light activation (e.g., $TiO_2$ anatase <390 nm with a band gap energy of 3.2 eV) make its practical implementation difficult, especially in solar-driven photocatalysis [18–20]. A bathochromic shift, which narrows the band gap, can be induced in the $TiO_2$ lattice by adding metal [21] (Fe, Cu, V, etc.) dopants. This modification causes $TiO_2$ to absorb visible light, enhancing its efficiency under solar radiation and boosting its photocatalytic activity beyond the UV spectrum. Among the various transition metal dopants, copper (Cu) has been extensively researched and is highly recommended for doping $TiO_2$ to achieve superior performance. Additionally, copper is relatively less toxic, an essential and abundant element [22], and is more cost-effective than other dopants such as silver [23]. Incorporating Cu into the $TiO_2$ lattice modifies the band gap

and inhibits the recombination of photo-induced electron-hole pairs, increasing catalytic activity [24].

To address the challenge of difficult recovery, $TiO_2$ can be loaded onto various carriers, including activated carbon fibers [25], silica [26], and fly ash [27]. Fly ash exhibits several benefits compared to other carriers: inexpensive, readily available, non-toxic, and resistant to high temperatures, exhibiting a substantial surface area, small particle size, and excellent dispersibility in solution. These properties facilitate simple recycling and the prevention of secondary pollution [28]. Additionally, fly ash embodies the principle of "using waste to treat waste," making it an ideal carrier for $TiO_2$ [29]. Fly ash-$TiO_2$ composites, due to the porous structure and high surface area of fly ash, exhibit excellent adsorption characteristics, which enhance their overall performance in pollutant removal. The ability to perform both adsorption and photocatalysis significantly broadens the usefulness in environmental remediation processes. The photocatalytic activity of Fly ash-$TiO_2$ composites for FB dye removal was 88% compared to the removal of 75% over bare $TiO_2$ as determined in the previous work, which is currently under review.

Studies have reported that over the past few decades, numerous studies utilising metal (Ag/Cu /Fe/Pt)-$TiO_2$, $TiO_2$-loaded fly ash and metal-loaded $TiO_2$-fly ash composites for the photodegradation of organic pollutants in the presence of UV light and visible light have been conducted in the past. Li et al. [30] utilized the sol-gel method to produce Mo-doped $TiO_2$ coated on fly ash cenospheres (CTAB-Mo-$TiO_2$/FAC), which demonstrated 99.75% elimination of methylene blue under visible light. Wang et al. [31] synthesised $Fe^{3+}$-doped $TiO_2$ on fly ash cenospheres (Fe–$TiO_2$/FAC) using the sol-gel method, demonstrating enhanced photocatalytic activity for methyl blue degradation under visible light, with optimal performance at 450°C and 0.01% Fe doping. Ag-doped $TiO_2$ supported on fly ash magnetic beads (Ag-$TiO_2$-FAMB) was synthesized by Li et al. [29] to enhance photocatalytic efficiency and recovery, achieving 98.5% xanthate degradation under visible light. Kanakaraju et al. [32] synthesized a Cu/$TiO_2$/FA composite using the wet impregnation method to achieve a 99% removal of methyl orange under visible light. However, reports of studies utilising Cu-deposited fly ash-$TiO_2$ composites for efficient removal of fuchsin blue under visible and solar light are less explored.

This study aims to develop and evaluate the adsorptive and photocatalytic performance of Cu-loaded fly ash-$TiO_2$ (FT-Cu) composites for the removal of FB dye from its aqueous medium under visible/solar light conditions. The objectives of the present work are to determine the role of Cu nanoparticles in enhancing the activity of adsorption and photocatalytic degradation of

FB dye. Also, to determine the photodecomposition pathway, and assess the photostability and recyclability of the composites.

The present investigation elucidates the synthesis of Cu-loaded Fly ash-$TiO_2$ (FT-Cu) composites with different percentages of copper (0.5,1, 2wt%) by sol-gel, wet impregnation method, and photo-deposition method. The comparative adsorption and photocatalytic degradation of FB dye were studied to evaluate the influence of Cu loading onto FT composite on its photocatalytic performance when exposed to visible light and sunlight. Moreover, the kinetic rate law and the photodegradation pathways of the fuchsin blue dye are also investigated by analysing various reactive oxygen species and identifying intermediate photoproducts using high-resolution mass spectral analysis. This research introduces a cost-effective, non-toxic, and solar light-driven highly efficient photocatalyst that can be recycled and reused, thereby addressing the complexities related to the wastewater treatment process and the recovery of photocatalysts, making it a more environmentally friendly approach.

## 3.2 Materials and methods

### 3.2.1 Materials and reagents

Titanium butoxide ($Ti(OC_4H_9)_4$, 97%) and Didecyl dimethyl ammonium chloride ($C_{22}H_{48}ClN$) were procured from Sigma-Aldrich, India. Acetic acid ($C_2H_4O_2$, 99.8%), Ethanol ($C_2H_5OH$, 99.9%), Cupric nitrate ($Cu(NO_3)_2 \cdot 3H_2O$, 99.5%), isopropyl alcohol ($C_3H_8O$, 99.5%) and FB dye ($C_{20}H_{19}N_3.HCl$) were sourced from Loba Chemie, India. Fly ash was sourced from the Rajpura Power Plant, India. These reagents were of analytical quality and thus used directly without further purification. Deionized water (DI) was produced using an ultra-filtration system (Milli-Q, Millipore) with a conductivity of 35 mhos $cm^{-1}$ at 25°C.

### 3.2.2 Characterization methods of prepared samples

The crystal structure diffraction data were recorded using a Smart Lab SE X-ray diffractometer equipped with Cu-Kα radiation (1.54 Å) and operated at an accelerating voltage of 45 kV. The measurements were conducted over a diffraction angle range of $5° \leq 2\theta \leq 80°$, with a slit width of 10 mm, a step scan size of 0.01, at a scanning speed of 5° per minute. FESEM (JEOL JSM-7600F, JAPAN, working at 30kV) was utilized to characterize the morphology of the surface and microstructures of the catalyst. The composition and distribution of elements were identified via energy dispersive spectroscopy (Bruker EDS). High-resolution TEM images

were taken by a High-Resolution Transmission Electron Microscope (HRTEM, JEOL JEM - 2100 model, JAPAN). The sample surface area and pore size profile were analyzed with the BET Autosorb iQ (Quantachrome Instruments, version 3.01, U.S.A.) The oxidation states of the elements in the composite were analyzed using X-ray Photoelectron Spectroscopy (XPS) with a Thermo Fisher Scientific NEXSA instrument, UK. Approximately 100–150 mg of the sample was degassed in the presence of helium gas at 200°C for 2 hours to remove moisture. Following degassing, liquid nitrogen was used for adsorption and desorption analysis. The optical properties were assessed using a Diffuse Reflectance Spectrophotometer (JASCO V-750, JAPAN) and $BaSO_4$ as a reference. High-resolution mass spectroscopy (Waters QTOF mass spectrometer equipped with XEVO G2 XS UPLC and coupled to APCI and ESI ionization sources,10 min retention time) was employed to detect degradation products, which offered important insights regarding the photocatalytic degradation pathway.

**Preparation of Cu deposited fly ash-$TiO_2$ particles**

### 3.2.3 Cu photo-deposited fly ash-$TiO_2$ (FT- Cu) composite

The synthesis procedures for $TiO_2$ and fly ash–$TiO_2$ (FT) composites have been described in detail in Chapter 2 (Sections 2.22 and 2.2.3). The deposition of Cu on the FT composite was carried out using the photo deposition method. A 100 mg sample of the prepared FT composite was dispersed in 10 mL of a 50% aqueous isopropyl alcohol solution in a test tube. Then, the required amount of 0.01 M copper nitrate solution (0.5–2 wt% Cu) was mixed with this FT dispersion and purged with Argon gas for 15 minutes to eliminate dissolved oxygen. The solution in the test tube was enclosed using rubber septa and exposed to a UV light source (125 W Hg arc, 10.4 mW/cm²) when subjected to constant magnetic agitation for 2 hours. After that, grey-coloured Cu-deposited FT composite (FT-Cu) was separated using centrifugation at 8000 rpm for 8 minutes, rinsed with distilled water and ethanol, and dried at room temperature. This approach was repeated to obtain an adequate quantity of FT-Cu composite for photocatalytic applications. The Cu-deposited FT composite catalyst containing 0.5wt%, 1wt% and 2wt% of Cu are named as FT-$Cu_{0.5}$, FT-$Cu_1$, and FT-$Cu_2$ respectively [32].

### 3.2.4 Measurement of the point of zero charge (pzc) of composite:

The zero-point charge is an important physicochemical parameter that indicates the pH at which the adsorbent surface has no net charge. This parameter was evaluated using the solid addition method with 0.002 M cetrimide ($C_{19}H_{42}BrN$) and 0.1 M KCl solutions. In this procedure, 25 mL of each solution was placed in separate test tubes, and the initial pH of these solutions was

adjusted to 2 to 10 using 0.1 M NaOH and 0.1 M HCl. Next, 6 mg of FT-$Cu_{0.5-2}$ composite was introduced into each test tube, which was kept for 3 hours with constant shaking to allow equilibration. The solution underwent filtration, and the final pH was recorded. The zero-point charge was ascertained by plotting the change in pH ($\Delta pH = pH_i - pH_f$) versus the initial pH and finding the intersection point on the graph.

### 3.2.5 Dark adsorption study of FB dye

The adsorption properties of FT and FT-$Cu_{0.5-2}$ composites were systematically evaluated using a 10 ml solution of the FB dye pollutant based on the influence of several critical parameters, e.g., the concentration (5 to 30 mg/L) of FB dye, the adsorbent dosage (1-10 mg) and the contact time (30 to 180 min). Under dark conditions, a magnetic stirrer was employed to uniformly mix and agitate multiple test tubes, each containing 10 mL of FB dye solution with varying concentrations and corresponding amounts of adsorbent. After the designated agitation period, the test tubes were withdrawn and subjected to centrifugation to ensure efficient separation of the FT/FT-Cu composite adsorbents from the liquid phase. The residual dye concentration in the supernatant was quantified using a UV–visible spectrophotometer at the characteristic maximum absorbance of FB dye ($\lambda\_max = 546$ nm), based on previously established calibration curves in accordance with Lambert–Beer's law. The adsorption performance of the adsorbents, expressed as the pollutant mass adsorbed per unit adsorbent mass (mg/g), was calculated using the following formula:

$$\text{Adsorption capacity} = Q_e = (C_o - C_e) \times \frac{V}{W} \quad (1)$$

In this equation, $C_o$ signifies the starting concentration of the FB dye (mg/L), whereas $C_e$ denotes the dye's equilibrium concentration in the solution (mg/L). W indicates the adsorbent mass (g), V is the volume of the FB dye solution (L), and $Q_e$ corresponds to the adsorption capacity of the adsorbent at equilibrium (mg/g) [33]. The percentage of dye absorbed by the adsorbents (R%) was evaluated using the subsequent equation.

$$\text{\% removal of FB dye} = R\% = \left( \frac{C_o - C_e}{C_o} \right) \times 100 \quad (2)$$

$C_0$ and $C_e$ represent the initial and equilibrium concentrations, while R% indicates the percentage of FB dye eliminated from the solution.

### 3.2.6 Photocatalytic degradation study

The photocatalytic degradation was conducted in a test tube containing 10 ml of FB dye (10 ppm) and different photocatalysts (6 mg) dispersion with continuous magnetic stirring and visible light (Wipro Garnet B22 50-Watt LED bulb (wavelength > 360 nm) irradiation for different times (60-240 min). Before exposure to light radiation sample was magnetically agitated for 180 minutes in the dark to ensure that the catalyst and FB dye molecules were in a state of adsorption-desorption equilibrium. After photo-irradiation at various time intervals, the test tube was extracted, and the mixture was subjected to centrifugation for 8 minutes at 8000 rpm. The clear supernatant FB dye solution was analyzed and quantified using a UV-visible spectrophotometer at the FB dye's $\lambda_{max}$ = 546 nm.The absorbance spectra of the FB dye were monitored to assess the degree of degradation, yielding valuable information regarding the efficacy of the photocatalytic process [34]. The photodegradation efficiency was derived using the following formula:

$$\text{Rate of FB degradation (\%)} = \frac{A_o - A_t}{A_o} \times 100 = \frac{C_o - C_t}{C_o} \times 100 \quad (3)$$

In this context, $A_0$ and $C_0$ represent the initial absorbance and initial FB dye concentration at time zero, while $A_t$ and $C_t$ pertain to the absorbance and the dye concentration at a specific time t, respectively [35, 36] .

## 3.3 Results and discussion

### 3.3.1 XRD analysis

The crystal planes and corresponding diffraction angles for the synthesized FT and FT-$Cu_1$ nanocomposites observed in the XRD spectra are presented in **Fig. 3.1.** The characteristic anatase crystalline phase of $TiO_2$ is evident from the diffraction peaks at 25.3° (101), 37.9° (004), 48.3° (200), 54.1° (105), 55.1° (211), 62.8° (204), 69.2° (116), 70.3° (220), and 75.4° (215), confirming the presence of anatase $TiO_2$ consistent with the JCPDS Card No. 21-1272 [37]. The X-ray diffractogram of fly ash reveals four primary crystalline phases: quartz ($SiO_2$), mullite ($Al_6Si_2O_{13}$), magnetite ($Fe_3O_4$), and hematite ($Fe_2O_3$). Characteristic peaks in the XRD profile at 16.45°, 25.98°, and 26.30° align with the mullite phase, while peaks at 20.86°, 26.58°, and 36.55° are attributed to the quartz phase. These phases effectively match with their respective JCPDS cards: mullite (JCPDS card no. 89-2644), quartz (JCPDS card no. 89-1962), and hematite (JCPDS card no. 33-664) [38]. Additionally, the diffractogram exhibits a notable increase in intensity within the 21 and 28° 2θ range, accompanied by relatively low-intensity

peaks of quartz and mullite, suggesting a fine particle size and high activity index of the fly ash. All the peaks identified in the fly ash were also found in the FT composite, with an additional peak at 2θ = 25.3° corresponding to $TiO_2$. This peak in the FT composite highlights the successful incorporation of $TiO_2$ onto the fly ash surface, demonstrating the effective formation of the composite. Conversely, in the FT-$Cu_1$ photocatalyst, no distinct peak for the Cu co-catalyst was detected following the deposition of Cu metal onto the FT composite. Previous research has established that metal nanoparticles with a low weight percentage (<5wt%) are usually not visible in XRD spectra.

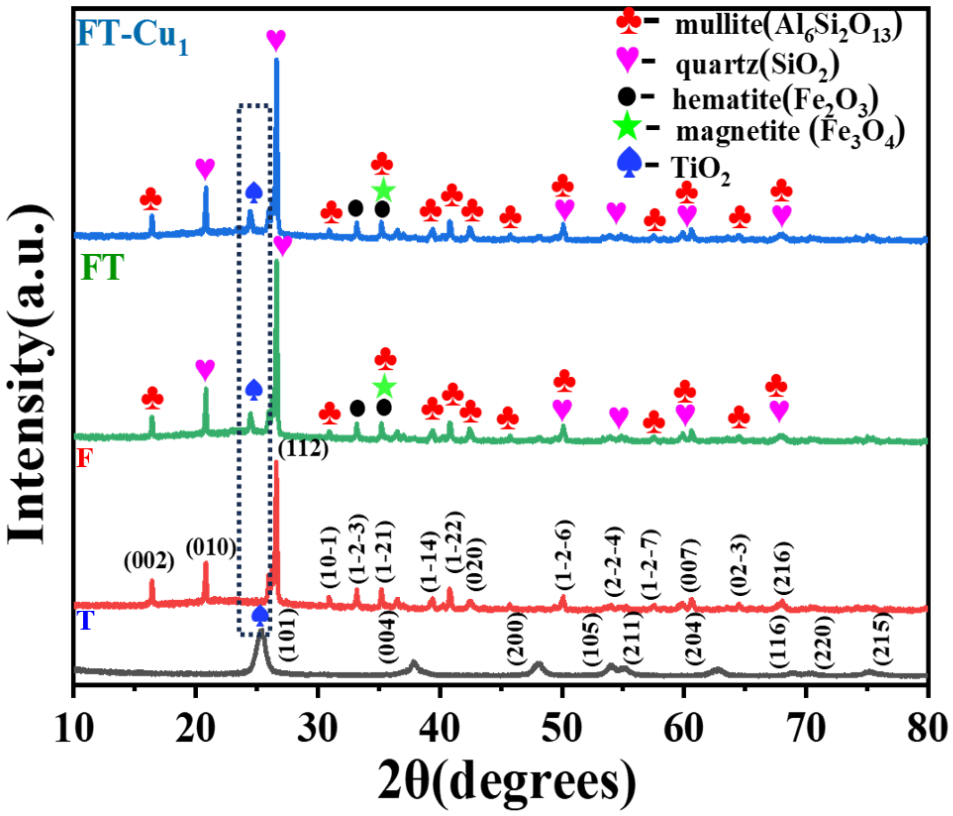


**Fig. 3.1** XRD patterns of $TiO_2$(T), Fly ash (F), FT and (FT-$Cu_1$).

### 3.3.2 FESEM, HRTEM and EDS analysis

The morphological and microstructural characteristics are illustrated in **Fig. 3.2(a)**; the SEM images of $TiO_2$ nanoparticles exhibit a spherical morphology. However, the $TiO_2$ particles tend to agglomerate and form clusters [39]. The Fly ash particles depicted in **Fig. 3.2(b)** demonstrated a spherical morphology and a uniformly smooth surface [40]. The FESEM

images of the FT and the FT-$Cu_1$ in composite **Fig. 3.2(c-f)** show that the spherical fly ash particles were more thoroughly coated with $TiO_2$. However, the Cu nanoparticles were not visible in the FESEM images due to their tiny size within the nm range. Nevertheless, the EDS spectra confirmed the presence of oxygen, aluminium, silicon, titanium, iron, and copper within the FT-$Cu_1$ composite.

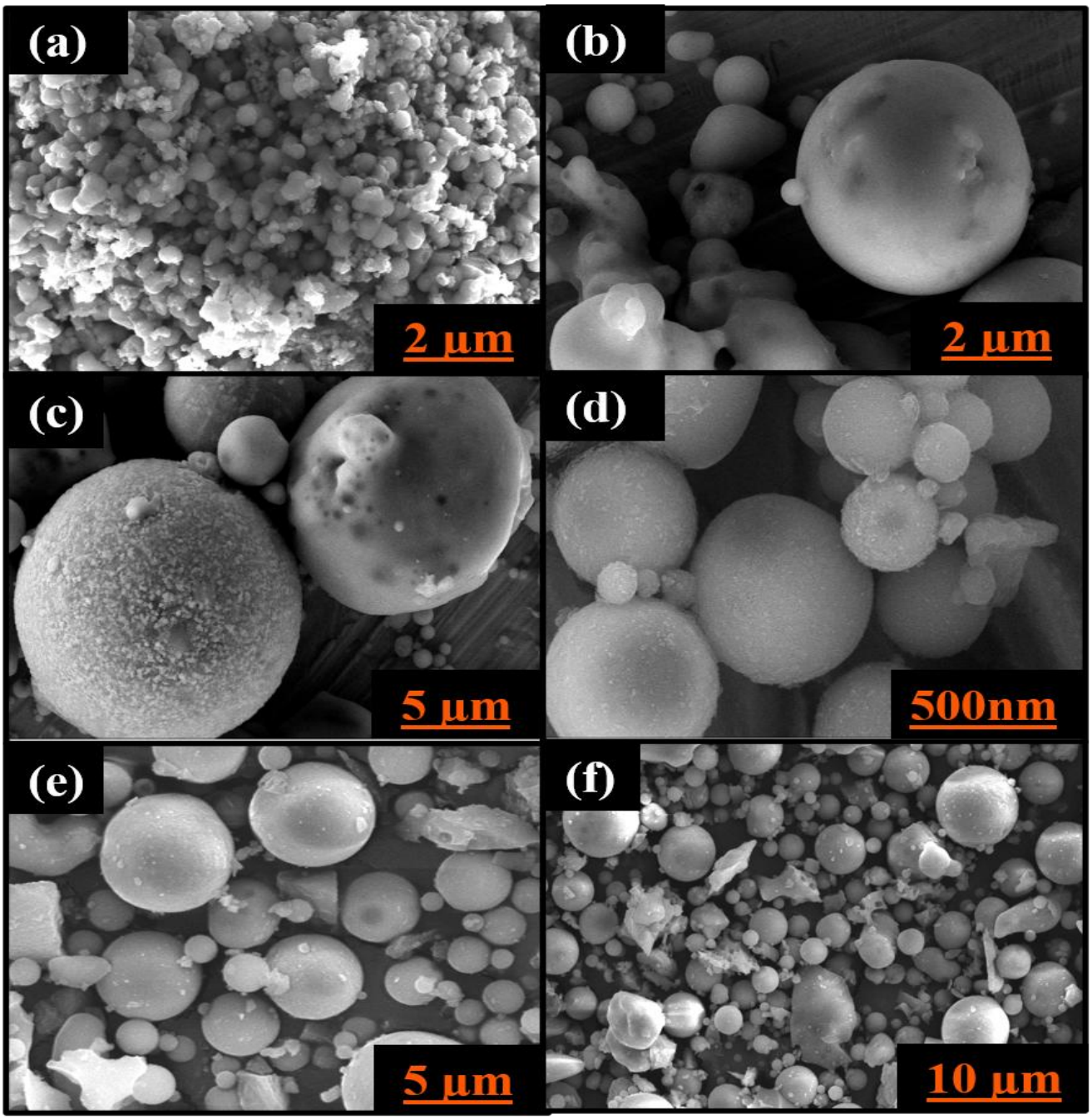


**Fig. 3.2** FE-SEM images of (a) $TiO_2$(b) FA, (c & d) FT, and (e & f) FT-$Cu_1$ composite

In **Fig. 3.3 (a–c),** the TEM micrographs of the FT-$Cu_1$ composite at multiple resolutions demonstrate a homogeneous distribution of Cu nanoparticles over the FT surface. The nanoparticles, identifiable as dark spherical domains, exhibit a largely spherical morphology, confirming uniform deposition throughout the composite. The particle size of deposited Cu was observed in the 7 to 17 nm range. Their compact size potentially provides increased active sites, thereby enhancing photocatalytic activity. Moreover, the HRTEM micrographs in **Fig. 3.3(d)** distinctly reveal two distinct sets of lattice fringes of $TiO_2$ and Cu. One set is attributed to metallic Cu's (111) diffraction plane, characterized by an interplanar spacing of 0.21 nm. In contrast, the other set exhibits a lattice fringe spacing of 0.35 nm, corresponding to the (101) crystal plane of $TiO_2$. The image shows the lattice fringes for $TiO_2$ and Cu [41].

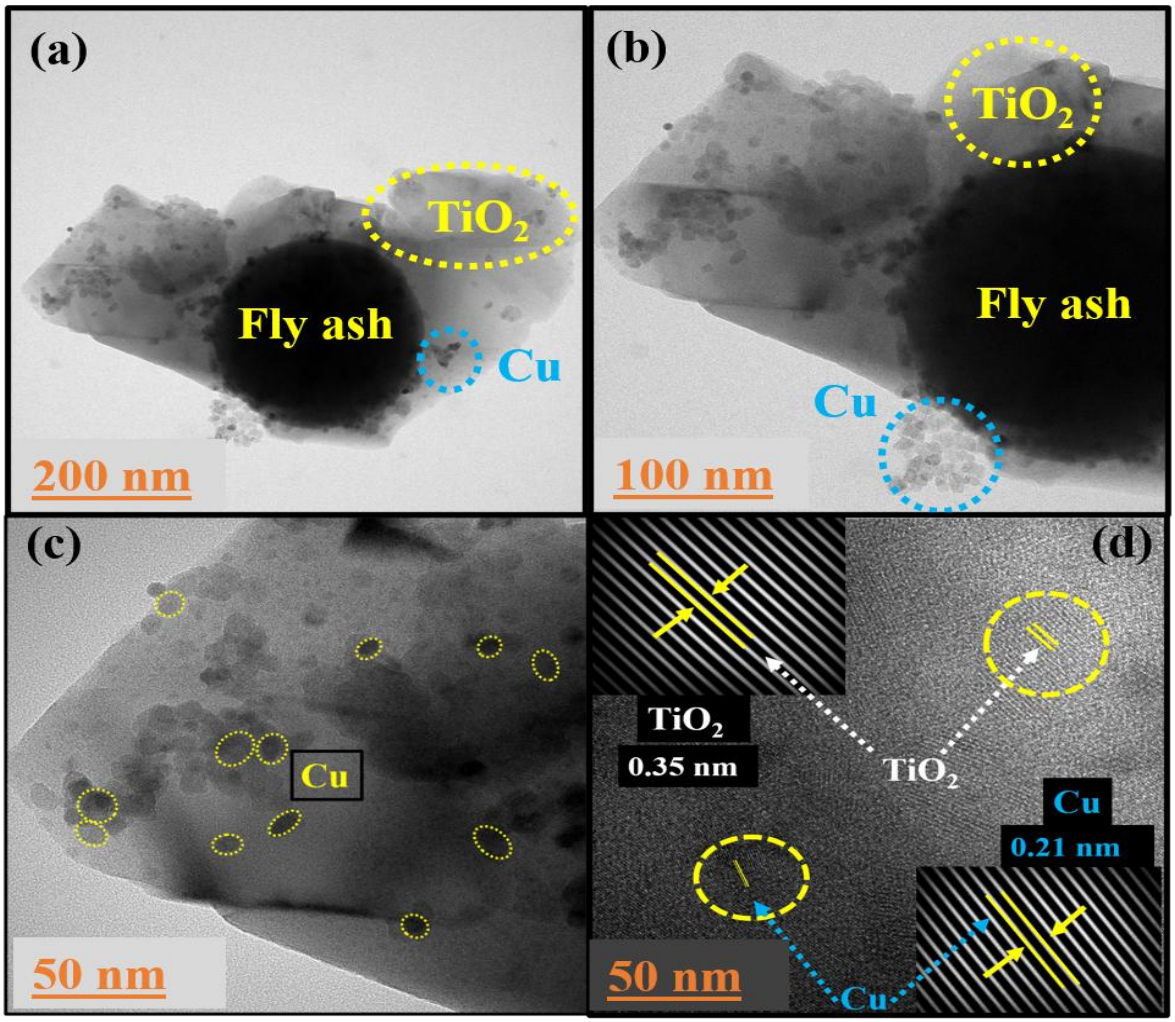


**Fig. 3.3** HRTEM images of (a-c) FT-$Cu_1$ composite and (d) corresponding Lattice fringes

As shown in **Fig. 3.4**, the EDS results provide a quantitative assessment of the elemental composition of the FT-$Cu_1$ composite. The composite predominantly contains oxygen (55.19%) and silicon (41.65%), consistent with the underlying fly ash–$TiO_2$ matrix. Minor proportions of aluminium (1.48%), titanium (0.15%), iron (0.17%), copper (1.05%), and magnesium (0.04%) are also detected, validating the elemental distribution within the material.

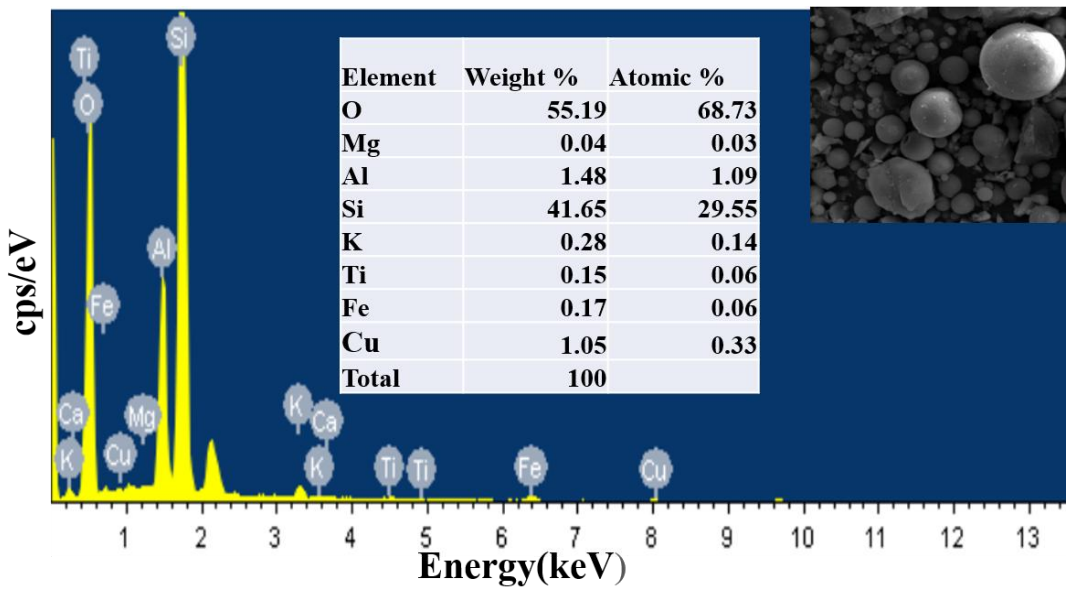


**Fig. 3.4** Elemental analysis (EDS) of FT-$Cu_1$ composite

### 3.3.3 Surface area and pore size analysis

The surface characteristics and pore size distributions of the synthesized materials were assessed by analysis of $N_2$ adsorption-desorption isotherms, and the associated BJH pore-size distribution graph of fly ash, FT and FT-$Cu_1$ composite are depicted in **Fig. 3.5 (a-b)**. The $N_2$ adsorption–desorption isotherms exhibit type-IV profiles with H3-type hysteresis loops, confirming the presence of mesoporous structures characteristic of multilayer adsorption [42]. The pore size distribution further validates mesoporosity, with pore diameters predominantly in the range of 2–10 nm. Incorporation of $TiO_2$ and copper significantly enhances the surface textural properties of the FT-$Cu_1$ composite, which displays a higher specific surface area and pore volume compared to the other samples. These improvements promote more efficient adsorption of FB dye and simultaneously enhance photocatalytic activity in both FT and FT-Cu systems by enabling better diffusion and interaction of reactant and product molecules. The observed enhancements can be attributed to the generation of additional active sites and

synergistic structural–functional effects. Detailed values of specific surface area, pore size, and pore volume for all samples are provided in **Table 3.1.**

**Table 3.1.** Pore volume, surface area and pore diameter of $TiO_2$, fly ash, $FT_3$ and $FT_5$ composites.

| Photocatalyst | BET surface area ($m^2/g$) | Pore volume ($cm^3/g$) | Pore diameter (nm) |
|---|---|---|---|
| **$TiO_2$** | 99.70 | 0.20 | 12.31 |
| **Fly ash** | 1.35 | 0.00 | 3.05 |
| **FT** | 3.27 | 0.01 | 3.41 |
| **FT-$Cu_1$** | 6.73 | 0.01 | 8.71 |

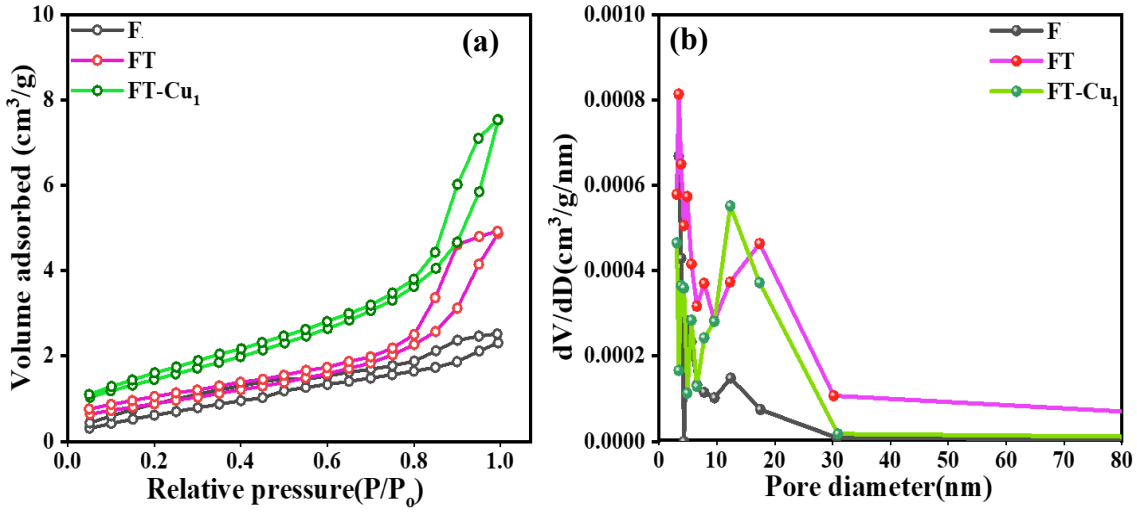


**Fig. 3.5** (a) $N_2$ adsorption-desorption isotherms and (b) BJH plot distribution curves of various (FA, FT, and FT-$Cu_1$) composites

### 3.3.4 Optical absorption and band gap analysis

The UV-vis diffuse reflectance spectra for FT and FT-$Cu_1$ composites with copper concentrations ranging from (0.5- 2wt%) are shown in **Fig. 3.6(a),** with the corresponding Tauc plots in **Fig. 3.6(b-d)**. The DRS spectra illustrate peaks at wavelengths under 400 nm in the ultraviolet region, denoting the electron transitions from the valence band, particularly the (2p) orbitals of $O^{2-}$ ions, to the conduction band, involving the (3d) orbitals of $Ti^{3+}$ ions. The FT composite demonstrates enhanced ultraviolet (UV) light absorption, which results in a shift to

longer wavelengths. This observed shift can be ascribed to the formation of Si-O-Ti bonds between $TiO_2$ and fly ash surfaces [43]. This absorption capability was further elevated with Cu loading on FT composites that reduces the bandgap, shifts the absorption edge to the visible light region by creating localized energy levels, forming strong heterojunctions, altering the electronic structure through doping, and synergistically interacting with the fly ash and enhances overall light absorption, thereby improving photocatalytic efficiency and resulting in a significant red shift in the absorption edge of the FT-Cu composite.

The bandgap of the as-prepared composites was determined using Tauc's equation, which is expressed as:

$$\alpha h\nu = A(h\nu - E_g)^n \quad (4)$$

α is defined as the absorption coefficient, hv refers to the photon energy, A is a proportionality constant, and $E_g$ signifies the bandgap, corresponding to either a direct or indirect transition (n=0.5 for a direct transition and n=2 for an indirect transition). The band gap values were determined by extrapolating a straight line to intersect the x-axis on the plot of $(\alpha h\nu)^2$ versus hv [44]. Based on the analysis, the $E_g$ values were found to be 2.27 eV for FT-$Cu_1$, followed by 3.12 eV for pure $TiO_2$, 2.84 eV for fly ash, 2.55 eV for the FT composite, and 2.35 eV for the FT-$Cu_2$ composite.

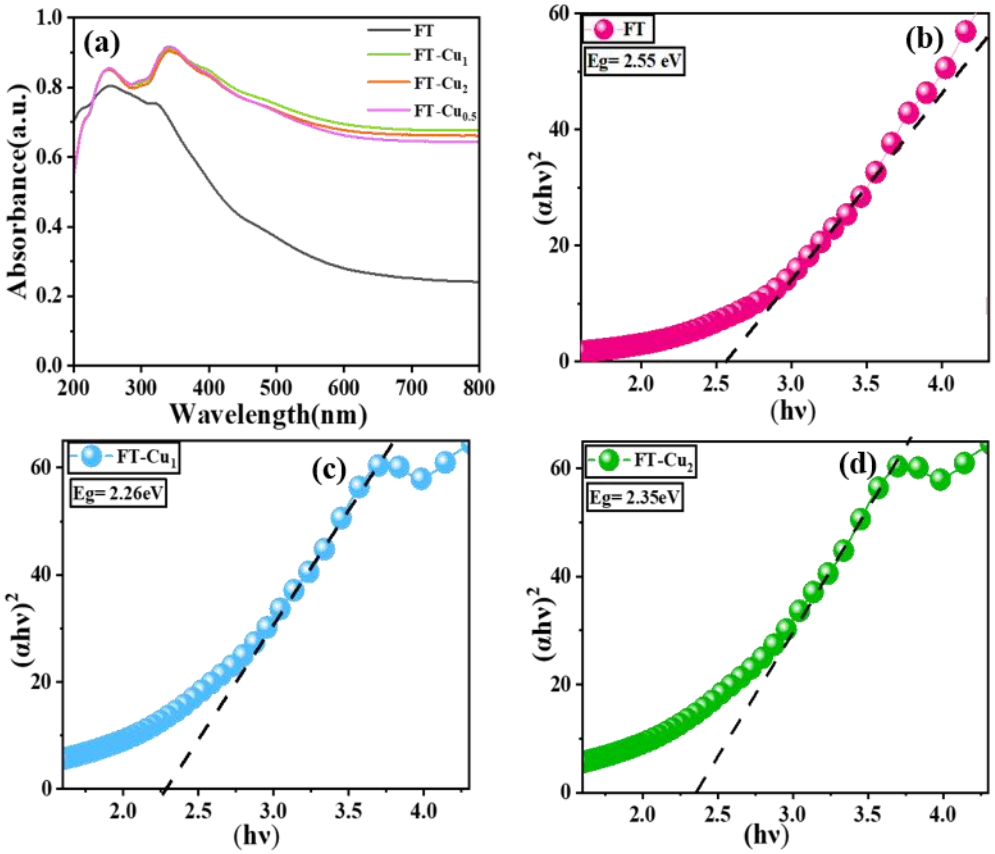


**Fig. 3.6** (a) Diffuse reflectance spectra of (b-d) Tauc Plot of FT, FT-$Cu_1$ and FT-$Cu_2$ composites.

### 3.3.5 XPS analysis

X-ray photoelectron spectroscopy (XPS) was conducted to determine the elemental composition and chemical states of the FT-Cu composite, as shown in **Fig. 3.7(a-f)**. The XPS analysis of $TiO_2$ revealed distinct peaks in the Ti 2p and O 1s regions, confirming the existence of titanium and oxygen species in the material. The Ti 2p spectra showed peaks at 458.6 eV ($2p_{3/2}$) and 464.3 eV ($2p_{1/2}$), indicating titanium in the +4 oxidation state, typical of $TiO_2$, with binding energies consistent with those found in pure $TiO_2$. The O 1s spectra revealed a dominant peak at 531.7 eV, which corresponds to surface hydroxyl groups or oxygen species associated with C–O bonds [45]. Peaks observed at 102.65 eV in the Si 2p spectra and 74.4 eV in the Al 2p spectra confirmed the presence of silicate species and $Al^{3+}$, respectively, derived from the fly ash [46, 47]. Furthermore, the Fe 2p spectra revealed peaks at 710.9 eV ($2p_{3/2}$) and 724.7 eV ($2p_{1/2}$), characteristic of $Fe^{3+}$ in iron oxides [48]. The Cu 2p spectra, as illustrated in **Fig. 3.7(e),** displayed binding energy peaks at 932.9 eV ($2p_{3/2}$) and 952.7 eV ($2p_{1/2}$), with a 6-eV energy separation, indicative of copper in the Cu (0) oxidation state. Moreover, the presence

of a satellite peak in the Cu 2p spectra suggests the coexistence of $Cu_2O$ and CuO, reflecting mixed oxidation states of copper within the composite. These findings demonstrate the effective incorporation of copper within the $TiO_2$ matrix while retaining essential fly ash components, including silicon, aluminium, and iron, which contribute to the composite's surface chemistry.

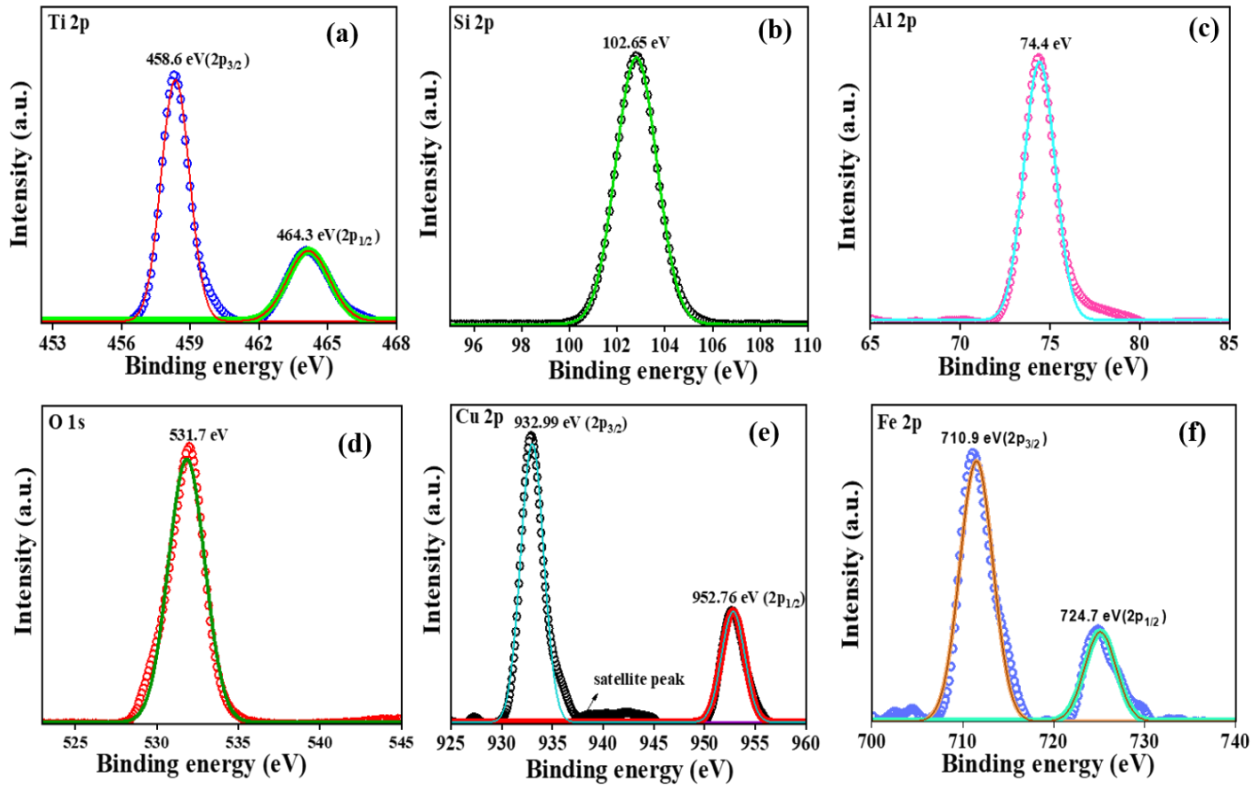


**Fig. 3.7.** XPS spectra of the synthesized FT-Cu composite: (a) Ti 2p, (b) Si 2p, (c) Al 2p, (d) O 1s, (e) Cu 2p, and (f) Fe 2p.

## 3.4 Adsorption study

### 3.4.1 Effect of adsorbent dosage on the removal of FB dye

The influence of the FT adsorbent and its composite on the removal efficiency of FB dye is depicted in **Fig. 3.8(a).** The data demonstrate that an increase in adsorbent dosage corresponds to an improvement in removal efficiency. This enhancement is likely attributable to the greater number of available adsorption sites and the increased adsorbent mass. Notably, FT-$Cu_1$ exhibited significantly higher adsorption efficiency compared to the unmodified FT material. By increasing the catalyst dose from 1 to 6 mg, the percentage removal of FB dye rises from

12 to 60% for FT, 21 to 66% for 0.5wt% FT-$Cu_{0.5}$, 34 to 73% for 2wt% FT-$Cu_2$ and 44 to 77% for FT-$Cu_1$ composite. Increasing the adsorbent dose from 5 to 7 mg produces no significant increase in removal efficiency. However, raising the dose over 7 mg reduces efficacy, most likely owing to particle aggregation obstructing the active sites. Thus, the optimal dosage for this experiment was ascertained to be 6 mg of adsorbent.

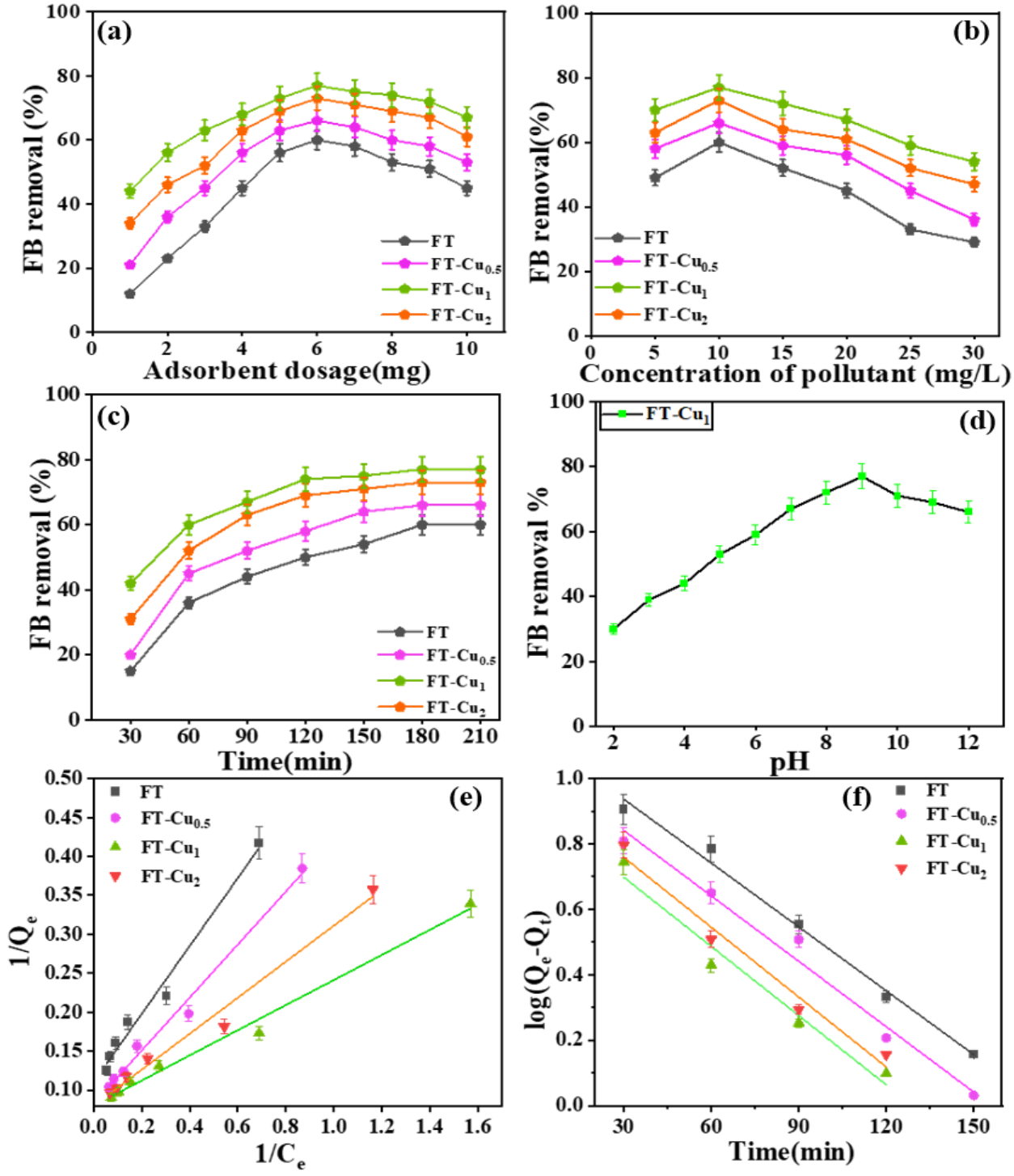

**Fig. 3.8** (a) Effect of adsorbent dose on FB removal, (0.006 g/L) (b) Effect of adsorbate concentration, (10mg/L) (c) the effect of contact time, (180 min) (d) effect of pH, (e) Langmuir isotherm adsorption isotherm (f) Pseudo-first-order kinetic model.

### 3.4.2 Impact of initial dye concentration on FB dye removal

In the batch adsorption experiments, the initial FB dye concentration was varied from 5 to 30 mg/L, as shown in **Fig. 3.8(b).** The removal efficiency of the adsorbent decreased with increasing initial dye concentration. At lower dye concentrations, the number of available adsorption sites exceeds the number of dye molecules, resulting in higher removal efficiency. However, beyond a certain concentration threshold, dye molecules outnumber the available adsorption sites, leading to reduced adsorption efficiency. With an increase in FB dye concentration from 5 to 30 mg/L, the percentage removal of dye decreased from 60 to 29% for FT, 66% to 36% for FT-$Cu_{0.5}$, 73% to 47% FT-$Cu_2$ and 77% to 54%. (FT-$Cu_1$) composites. This decline in adsorption occurs due to the saturation of active sites with the rise in the FB dye's initial concentration. Therefore, a 10 (ppm) initial concentration of FB dye was taken as an optimum value for further study.

### 3.4.3 The effect of contact times on the removal of FB dye

As shown in **Fig. 3.8(c),** the adsorption of FB dye onto FT and FT-$Cu_{0.5–2}$ gradually improves with increasing contact time at a dye concentration of 10 mg/L. The extended contact period allows more dye molecules to interact with the available adsorption sites, thereby enhancing overall removal efficiency. The adsorption rate decreases when the quantity is raised further until equilibrium is attained after 180 minutes. After 180 minutes, the maximum removal percentage (66, 77, and 73%) was achieved with no further rise in efficiency observed. The dye removal efficacy of the different adsorbents, FT and various FT-$Cu_{0.5\text{-}2,}$ remained consistent between 180 and 210 minutes due to dye saturation of active sites. Compared to FT and other FT-Cu composites, FT-$Cu_1$ was the most effective adsorbent that notably removed 77% of FB dye.

### 3.4.4 The pH effect on FB dye removal

The solution pH plays a crucial role in determining the surface charge of the adsorbent and the ionization state of the dye, both of which significantly impact adsorption efficiency. In this study, adsorption experiments were conducted with an adsorbent dosage of 6 mg at room

temperature, using a fixed adsorbate concentration of 10 ppm and a contact time of 180 minutes. The pH was adjusted using either 0.1M HCl or 0.1M NaOH, and the variation in dye adsorption was analyzed across a pH range of 2 to 12. As shown in **Fig. 3.8(d),** the removal efficiency of FB dye increased gradually with rising pH from 2 to 12. The adsorption behaviour of FB dye onto the FT-$Cu_1$ composite was investigated over this pH range for a duration of 180 minutes. The maximum dye removal efficiency, 77%, was observed at pH 9.

The $pH_{pzc}$ of FT-$Cu_1$ is 7.4. At lower pH values (acidic conditions), the surface of the FT-$Cu_1$ composite becomes protonated, acquiring a net positive charge. Simultaneously, the functional groups of the FB dye molecules undergo protonation, leading to a positively charged state for the dye. This results in strong electrostatic repulsion between the positively charged adsorbent surface and the protonated dye molecules.

At higher (alkaline) pH values, the FB dye molecules become either neutral or partially negatively charged due to deprotonation. The FT-$Cu_1$ composite, possessing a negative surface charge at pH values above its point of zero charge (pHpzc), now engages in electrostatic attraction with the dye molecules, facilitating enhanced adsorption onto the composite surface. The optimal dye removal at pH 9 is due to the enhanced electrostatic interactions between the negatively charged FT-$Cu_1$ composite (above its pHpzc of 7.4) and the positively charged or partially protonated FB dye molecules. This pH also facilitates secondary interactions, such as hydrogen bonding, between the deprotonated sites on the FT-$Cu_1$ surface and the dye's functional groups. However, at pH values greater than 9, the dye molecules undergo further deprotonation, becoming neutral or negatively charged, which reduces electrostatic attraction with the negatively charged adsorbent.

### 3.4.5 Adsorption isotherm studies

Adsorption isotherms are necessary to ascertain the equilibrium interactions between adsorbates and adsorbents. They represent a relationship between the adsorbate concentration in the liquid phase and the amount adsorbed onto the adsorbent surface at a specific temperature. According to the Langmuir isotherm model, the substance forms a monolayer on the surface when each molecule binds to its specific site. The model also states that there are no interactions between the molecules of the adsorbate, indicating that the adsorption of one molecule does not affect the adsorption of any other molecules. The following equation (5) mathematically expresses the Langmuir isotherm:

$$\frac{1}{Q_e} = \left( \frac{1}{K_L Q_{max}} \right) \times \frac{1}{C_e} + \frac{1}{Q_{max}} \tag{5}$$

$$R_L = \frac{1}{1+K_L C_o} \quad (6)$$

Where $C_e$ (mg/L) is the concentration of adsorbate at equilibrium, $Q_e$ (mg/g) is the equilibrium adsorption capacity of the adsorbent, $K_L$ (L/mg) is the Langmuir constant related to the affinity of binding sites, and $Q_{max}$ (mg/g) is the maximum adsorption capacity (mg/g) representing a complete monolayer on the adsorbent surface. $C_0$ is the initial concentration of the contaminant. [49]. The dimensionless separation factor $R_L$ describes the Langmuir isotherm and demonstrates the favourability of the adsorption process. Adsorption is favourable when the value is 0 to 1 and unfavourable when the value exceeds 1. A value of 1 indicates reversible adsorption, while 0 signifies irreversible adsorption. The graph plotted $1/Q_e$ against $1/C_e$ in **Fig. 3.8(e)** with the intercept and slope used to determine the $K_L$ and $Q_{max}$ values. [50, 51]. An empirical model known as the Freundlich isotherm describes heterogeneous surfaces where the heat of adsorption is not distributed uniformly over the surface. The Freundlich isotherm defines the formation of several layers (multilayer adsorption) on a surface, which involves some interaction between the adsorbed molecules. It assumes that the adsorbent surface is assumed to be heterogeneous, indicating significant interactions between the molecules of the adsorbate. The equation represents Freundlich's isotherm:

$$\log Q_e = \log K_F + \left(\frac{1}{n}\right) \log C_e \quad (7)$$

where $K_F$ is the Freundlich constant, which corresponds to adsorption capacity; 1/n is the heterogeneity factor, which is related to adsorption intensity; $Q_e$ (mg/g) is the adsorption capacity at the equilibrium time, and $C_e$ (mg/L) represents the concentration of pollutant in solution at equilibrium [49] where n>1 indicates a favourable adsorption procedure. The parameters for both models are shown in **Table 3.2**. Langmuir isotherm $R^2$ values are greater and closer to unity (0.9839-0.99) than the Freundlich isotherm $R^2$ values (0.9405-0.9549), suggesting that the Langmuir model better explains FB dye adsorption. The Freundlich parameter "n>1" in **Table 3.2** indicates that adsorption is non-linear and prefers larger solute concentrations.

**Table 3.2.** Langmuir and the Freundlich adsorption isotherm parameter for FB dye over FT, and various FT-$Cu_{0.5–2}$ composites.

| Langmuir model | | | | | Freundlich model | | |
|---|---|---|---|---|---|---|---|
| **Adsorbent** | **$Q_{max}$ (mg/g)** | **$K_L$ (L/mg)** | **$R_L$** | **$R^2$** | **$K_F$ [mg/g.(L/mg)]$^{1/n}$** | **n** | **$R^2$** |
| **FT** | 9.041 | 0.253 | 0.116 | 0.984 | 2.263 | 2.289 | 0.953 |
| **FT-$Cu_{0.5}$** | 12.077 | 0.243 | 0.120 | 0.990 | 2.766 | 2.083 | 0.955 |
| **FT-$Cu_1$** | 25.009 | 0.495 | 0.063 | 0.990 | 4.164 | 2.063 | 0.942 |
| **FT-$Cu_2$** | 20.000 | 0.345 | 0.088 | 0.984 | 3.509 | 2.283 | 0.941 |

**Table 3.3.** Kinetic model parameters of adsorption of FB dye over FT-$Cu_{0.5–2}$ composite

| (a) Pseudo-first-order Model | | | | Pseudo-second-order Model | | |
|---|---|---|---|---|---|---|
| **Adsorbent** | **$Q_e$ (mg/g)** | **$k_1$ ($min^{-1}$)** | **$R^2$** | **$Q_e$ (mg/g)** | **$k_2$ (g/mg. min)** | **$R^2$** |
| **FT** | 13.548 | 0.015 | 0.992 | 9.813 | 0.001 | 0.981 |
| **FT-$Cu_{0.2}$** | 17.619 | 0.015 | 0.983 | 8.613 | 0.002 | 0.978 |
| **FT-$Cu_1$** | 25.003 | 0.016 | 0.969 | 10.384 | 0.001 | 0.939 |
| **FT-$Cu_2$** | 19.678 | 0.016 | 0.976 | 10.351 | 0.001 | 0.956 |

### 3.4.6 Adsorption kinetics

The adsorption kinetics of FB dye on FT-Cu have been evaluated using a pseudo-first-order, pseudo-second-order kinetic model by the following equations (8) and (9).

$$\log(Q_e - Q_t) = \log Q_e - \frac{k_1}{2.303} t \quad (8)$$

$$\frac{t}{Q_t} = \frac{1}{k_2 Q_e^2} + \frac{t}{Q_e} \quad (9)$$

$Q_t$ and $Q_e$, in mg/g, respectively, indicate the adsorption rates at equilibrium and time t, respectively, whereas $k_1$ is the first-order rate constant. The second-order rate constant is denoted by $k_2$. The chemisorption process, in which electrons are transferred from the adsorbent to the adsorbate, is determined to be the rate-limiting phase according to the second-order kinetic model [52, 53]. As indicated in **Table 3.3**, the slopes and intercepts of the graphs were used to calculate the parameters for first- and second-order kinetics. The first-order model was

closer to unity and had a more significant rate constant value than the second-order model in **Fig. 3.8(f).** This suggests that first-order kinetics govern the adsorption of FB dye onto FT and other FT-Cu composites.

## 3.5 Photocatalytic studies

### 3.5.1 Photocatalytic degradation under visible light

**Fig. 3.9(a, b)** illustrates variations in the absorption spectra due to the FB dye degradation by FT-$Cu_1$ composite at varying irradiation times under visible light. During adsorption and photocatalytic degradation, the typical maximum absorption peak of FB dye is found at 546 nm, and its absorption intensity steadily decreases with increasing illumination time. In the visible light photodegradation of FB dye resulted in 94% removal by the FT-$Cu_1$ catalyst, which is significantly higher than the removal rate achieved via adsorption only. After 180 minutes of degradation under visible light, the dye solution shifted from dark pink to colourless, further confirming the significant removal of dye by photocatalytic degradation **(Fig. 3.9).** This suggests that for complete removal of dye, photocatalytic degradation plays a significant role than adsorption whereas, in the absence of a photocatalyst, only 14% removal of FB dye was achieved within 180 minutes under visible light. In **Fig. 3.9(a),** the dark adsorption of fuchsin blue dye in the FT-$Cu_{0.5–2}$ composite is driven by the porous nature of fly ash, which offers a high surface area for adsorption through electrostatic and van der waals forces. Copper enhances this by forming coordination bonds and modifying the surface charge of $TiO_2$, making the composite more attractive to fuchsin dye molecules. Together, these interactions allow for effective dye binding, which results in effective removal of dye under dark conditions.

The absorption spectra of FB dye after photodegradation by bare FT and FT-Cu exposed to 180 minutes of visible light are shown in **Fig. 3.9(c)**. The photoactivity of the FT composite was significantly increased after 1wt% Cu photo-deposition over fly ash-$TiO_2$ composite, displaying the highest photocatalytic activity. The time course duration plot **Fig. 3.9(d)** and kinetic graphs **Fig. 3.9(e)** were analyzed to validate the optimal amount of Cu deposition on FT for FB dye degradation under visible light. The photodegradation followed a pseudo-first-order kinetic model, as the reaction rate is only influenced by the concentration of the FB dye without any change in the concentration of water and oxygen. Additionally, with light intensity kept constant and the amount of FT-Cu composites fixed (6 mg) and thus negligible in rate variation, as shown in equation (10):

$$\ln (C_o / C_t) = kt \qquad (10)$$

**Table 3.4.** (a) Kinetic parameter of pseudo first order model of various photocatalysts under visible light (b) Kinetic parameter of pseudo first order model of various photocatalysts under sunlight.

| **(a)** | **Pseudo-first-order Model (visible light)** | |
|---|---|---|
| **Photocatalyst** | **$k_1$** | **$R^2$** |
| **FT** | 0.0008 | 0.9922 |
| **FT-$Cu_{0.2}$** | 0.0015 | 0.9903 |
| **FT-$Cu_1$** | 0.0031 | 0.9921 |
| **FT-$Cu_2$** | 0.0020 | 0.9915 |

| **(b)** | **Pseudo-first-order Model (sunlight)** | |
|---|---|---|
| **Photocatalyst** | **$k_1$** | **$R^2$** |
| **FT** | 0.0009 | 0.9944 |
| **FT-$Cu_{0.2}$** | 0.0023 | 0.9906 |
| **FT-$Cu_1$** | 0.0016 | 0.9900 |
| **FT-$Cu_2$** | 0.0021 | 0.9970 |

Where $C_0$ is the initial concentration of the FB dye at time zero, min and $C_t$ at reaction time t, and k is the rate constant ($min^{-1}$) [54, 55]. The pseudo-first-order rate constant and the square of the linear correlation coefficient ($R^2$) of FT and various FT-Cu composites under visible light and sunlight are shown in **Table 3.4 (a, b).** The rate constant for FT-$Cu_1$ composites (0.0031 $min^{-1}$) is higher than that for FT composites (0.0008 $min^{-1}$), indicating that the presence of copper enhances the photocatalytic activity of $TiO_2$, potentially due to improved charge separation and increased light absorption. The histogram in **Fig. 3.9 (f)** compares the percentage removal of FB dye by FT and FT-Cu during dark adsorption and degradation under visible light.

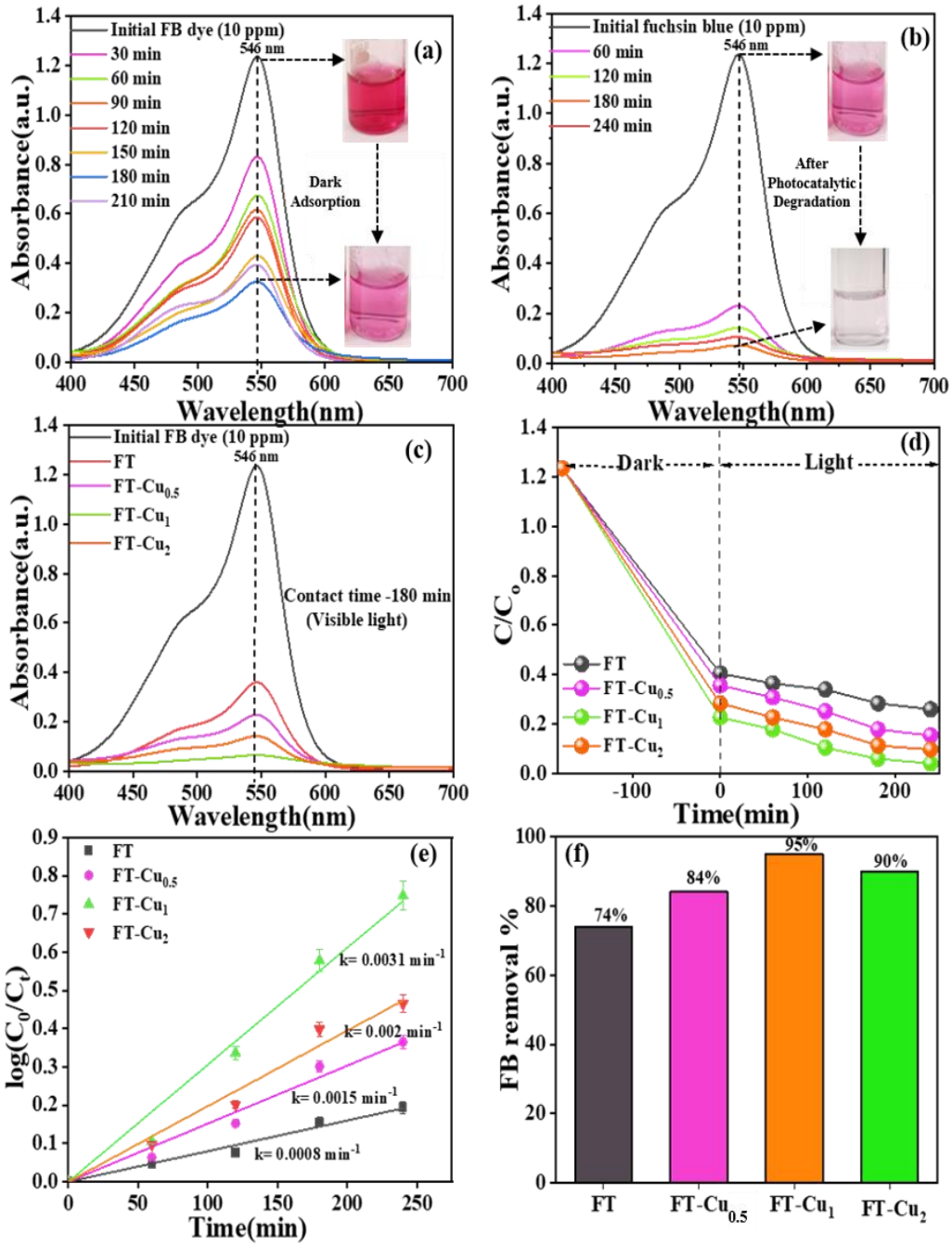


**Fig. 3.9.** Changes in the colour and absorption spectra of fuchsin blue dye: (a) dark adsorption, (b) photocatalytic degradation by the FT-$Cu_1$ composite at various time intervals, (c) degradation performance of different wt% FT-Cu composites after 180 min, (d) time-dependent kinetic plots, (e) pseudo–first-order kinetic fitting, and (f) FB degradation efficiency of various composites under visible-light irradiation.

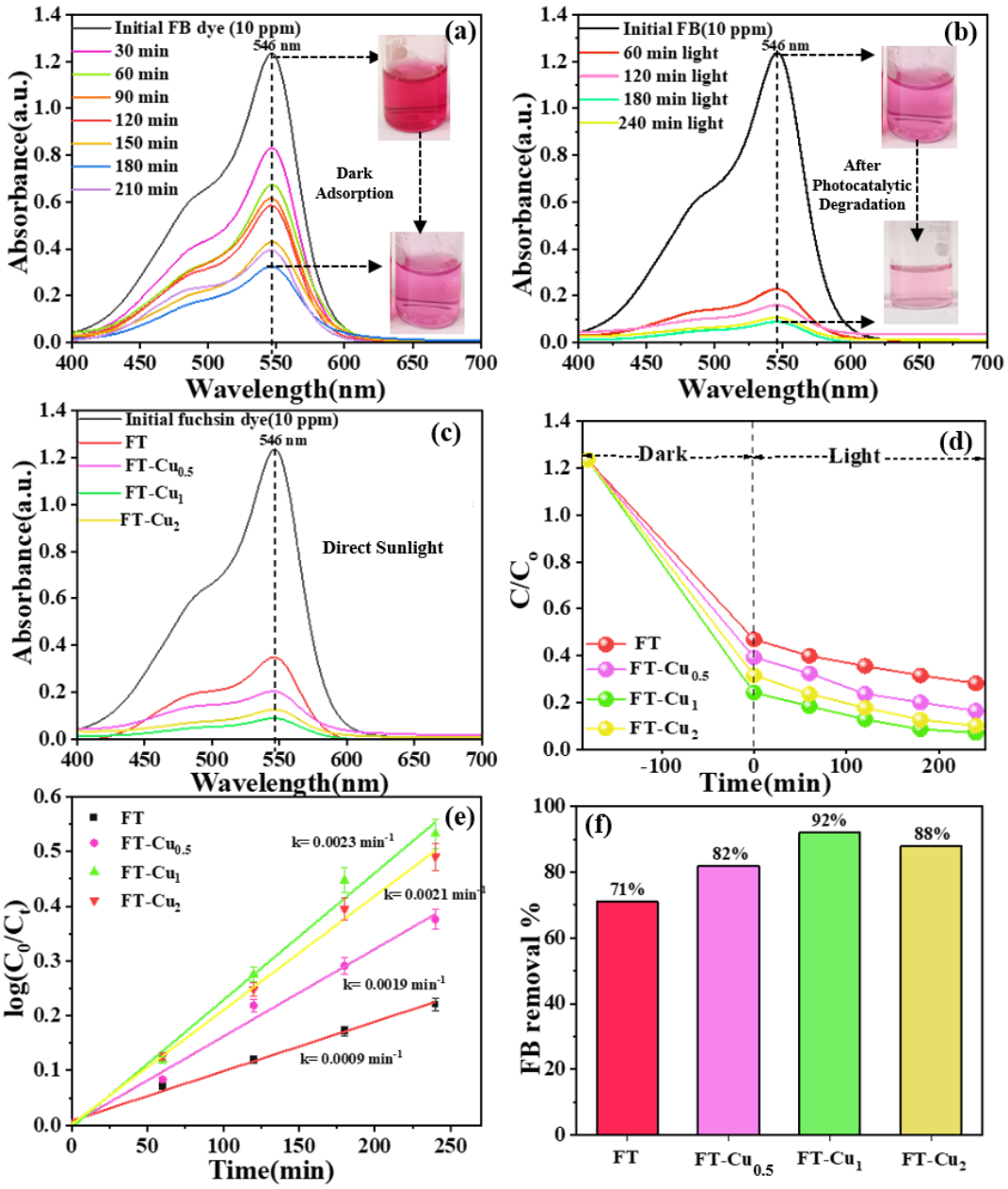


**Fig. 3.10** Changes in the colour and absorption spectra of FB dye (a) dark adsorption, (b) after photocatalytic degradation by FT-$Cu_1$ composite under different periods and (c) different wt% Cu-FT composites after 180 min (d) time course kinetic plots (e) Pseudo first-order model and (f) FB degradation efficiency by various composites under direct sunlight irradiation.

### 3.5.2 Photocatalytic degradation of FB under direct sunlight

To increase the usefulness and applicability of Earth's most abundant energy source, photocatalytic degradation of FB dye was conducted under direct sunshine. Different test tubes

containing 6 mg of catalysts (FT/FT-Cu) and 10 ml FB dye (10 ppm) are kept under sunlight on 21-05-24 for different periods (180 min) with constant magnetic stirring. The ambient temperature fluctuated between 35°C and 40°C. and solar intensity of 670 $Wm^{-2}$, June, 2024. In **Fig. 3.10(a),** the FB dye absorption spectra change from dark pink to light pink, indicating 77% removal, while **Fig. 3.10(b)** shows 92% removal, and the colour changes from light pink to colourless under sunlight. The UV-visible absorption spectra shown in **Fig. 3.10(c)** illustrate the relative variations in the absorbance of FB dye after it is photodegraded by bare FT and different FT-Cu nanocomposites exposed to sunlight for 180 minutes. The photoactivity of the FT composite was significantly increased by Cu loading. The change in colour of FB dye showed that photocatalytic activity increased after 1 wt% Cu deposition over FT catalysts and declined after that. The time course plot **Fig. 3.10(d)** and kinetic graphs **Fig. 3.10(e)** were shown to further confirm the optimal amount of Cu loading on FT composite for FB degradation. According to the findings, the photodegradation process follows a pseudo-first-order rate law, and similarly, FT-$Cu_1$ composites have a higher rate constant value (0.0023 $min^{-1}$) as compared to the FT composite (0.0009 $min^{-1}$). A histogram in **Fig. 3.10(f)** shows the comparative percentage removal of FB dye by FT and different FT-Cu composites. The 1wt% Cu-loaded FT composite exhibited the highest percentage removal of 92% relative to other Cu-loaded FT catalysts under identical experimental conditions.

### 3.5.3 Active species detection

In the scavenging experiments, different scavengers were used to investigate the roles of active species in the photocatalytic degradation of FB dye. Argon gas purging was employed to remove dissolved oxygen from the reaction mixture, thereby suppressing the formation of superoxide anion radicals ($O_2{\cdot}^-$), which led to a significant decrease in degradation efficiency to 18%. Ethanol and isopropanol (IPA) were used as hydroxyl radical (·OH) scavengers, reducing the dye degradation efficiency to 17% and 20%, respectively, by neutralizing the reactive species. Furthermore, $NH_4SCN$ acted as a hole ($h^+$) scavenger, preventing the oxidation of water molecules and reducing the degradation efficiency to 11%. These findings highlight the crucial involvement of superoxide anion radicals, hydroxyl radicals, and holes in the photocatalytic degradation process [56]. The percentage degradation of FB dye by FT-$Cu_1$ with and without the addition of different scavengers is shown in **Fig. 3.11(a).** EDTA, IPA, and $NH_4SCN$ reduced FB dye degradation from 94% to 17%, 20%, and 11%, respectively.

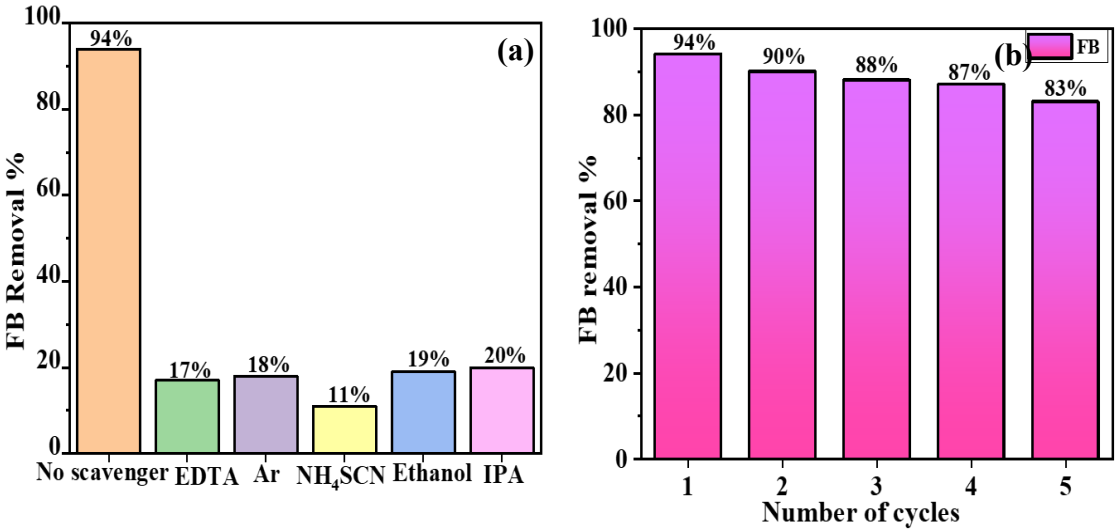


**Fig. 3.11** (a) Study the effect of different hole scavenger additions on the FB photocatalytic degradation efficiency and (b) reusability test by FT-$Cu_1$ under visible light irradiation.

### 3.6 Proposed photocatalytic degradation mechanism

The photocatalytic process over FT-$Cu_1$ has several important stages that improve composite performance and stability. Cu-photo-deposited $TiO_2$ nanoparticles are uniformly spread across the fly ash surface, stabilizing the catalyst and increasing catalytic reaction surface area. Copper plays an important role in enhancing the photocatalytic performance of fly ash–$TiO_2$ composites. The incorporation of Cu improves visible light absorption and acts as an electron trapping center, which suppresses the recombination of photogenerated electron–hole pairs. In addition, Cu modification broadens the photoresponse of $TiO_2$ from the UV region toward visible light, thereby improving photocatalytic efficiency under solar and visible light irradiation. Visible light generates electron-hole pairs in $TiO_2$ in the composite. Holes stay in the valence band while photoexcited electrons enter the conduction band. Cu nanoparticles on $TiO_2$ capture photoexcited electrons, minimizing electron-hole pair recombination. Charge separation is essential to produce reactive oxygen species (ROS), such as superoxide radicals ($\bullet O_2^-$) and hydroxyl radicals (•OH), through interactions with oxygen and water. Copper doping lowers the bandgap of $TiO_2$, allowing it to absorb visible light and create electron-hole pairs. FB dye molecules on FT/FT-$Cu_1$ catalysts can be degraded by extremely reactive ROS. This breakdown breaks the dye into smaller, less toxic molecules and can lead to complete mineralization into $CO_2$, $NO_3^-$, and $H_2O$. The porous structure and large surface area of fly ash increase the adsorption of dye, improving process efficiency [48, 49]. As demonstrated in **Scheme 3.1**, this synergistic interaction creates a more efficient and sustainable photocatalytic system for the breakdown of FB dye.

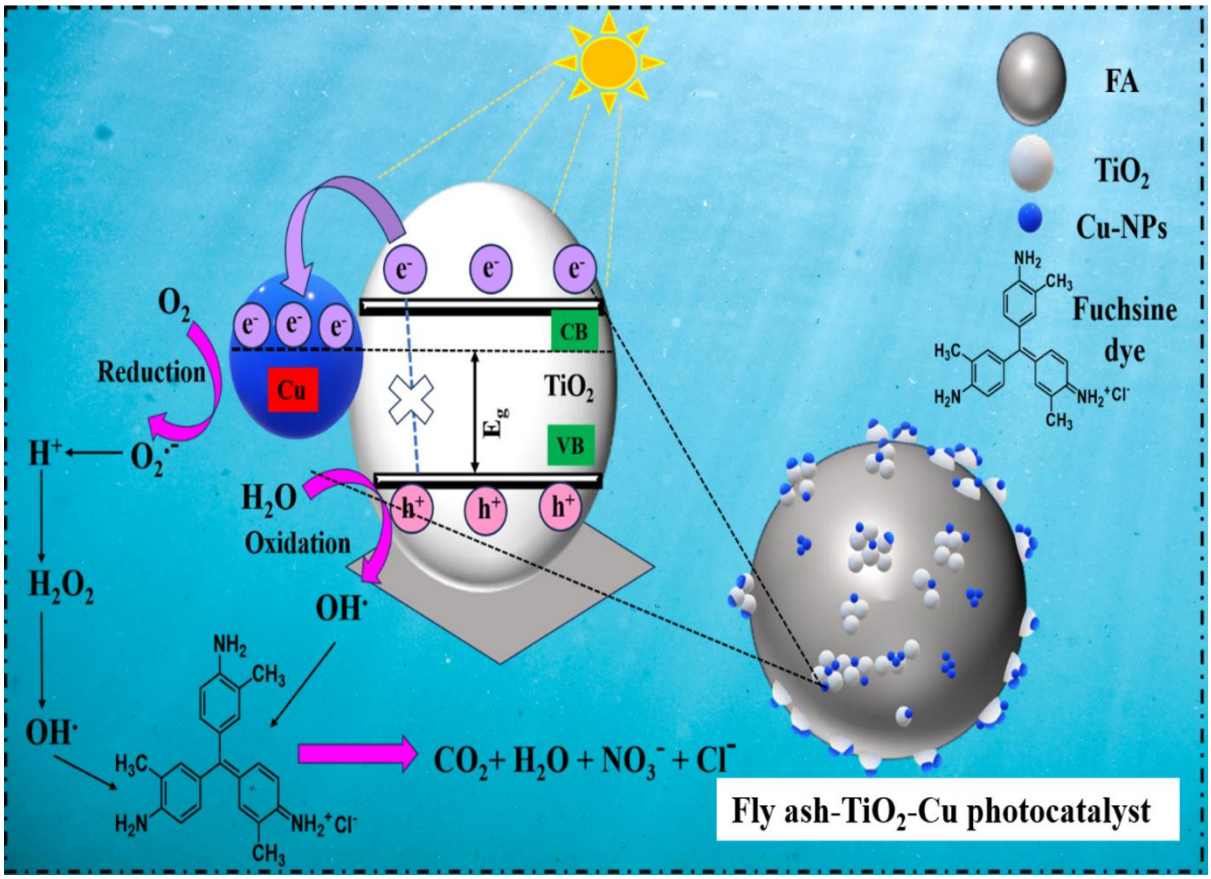


**Scheme 3.1.** The proposed photodegradation mechanism of FB dye by FT-Cu composite under solar/visible light irradiation.

### 3.7 Identification of intermediate photoproducts during the FB dye degradation pathway

After photocatalytic degradation of FB dye by FT-$Cu_1$ catalysts under 180 min visible light irradiation, the reaction mixture is subjected to centrifuging and filtered to separate the catalyst powders. The clear supernatant solution is used for HRMS analysis to investigate the various intermediate photoproducts formed after FB dye degradation. The separation of the mass(m)/charge(z) ratio was studied using the HRMS technique to determine the molecular formula. For the FB ion 330, the exact m/z measurement was 330.0928. Mass spectrometry analysis for basic FB dye determined two possible degradation pathways, as shown in **Fig. 3.12(a, b)**. These pathways show how different reactions involving ring-opening reactions, oxidation, demethylation, and hydroxylation can cause basic FB dye molecules to break down into various intermediates and decompose to $NO_3^-$, $CO_2$ and $H_2O$, etc.

First, FB (m/z = 365.91) dye is demethylated to produce Product B (m/z = 316.18) through

pathway 1. After further demethylation, Product B yields Product C (m/z = 302.17). Product C uses a ring-opening process with reactive oxygen species (•$O_2$- and •OH) to produce Product D (m/z = 205.11). Product D is then oxidized to produce 3-Heptynoic acid (m/z = 126.07), which is Product E. Ultimately, Product E 3-Heptynoic acid (m/z = 126.07) mineralizes to form $H_2O$, $CO_2$, and a few inorganic ions. In pathway one, the other side of product C (m/z = 302.17) experiences the ring-opening reaction, changes into product H (m/z = 282.16), and then changes again into $NO_3$, $CO_2$ and $H_2O$. Product F forms via Pathway 2, i.e., carbinol of pararosaniline (m/z = 347.21), from Product A (m/z = 330.09), which is the result of ionizing FB dye, through hydroxylation. Product F undergoes oxidation to yield Product G (m/z = 223.14) and finally Product G mineralizes to form $H_2O$, $CO_2$, and specific inorganic ions [57].

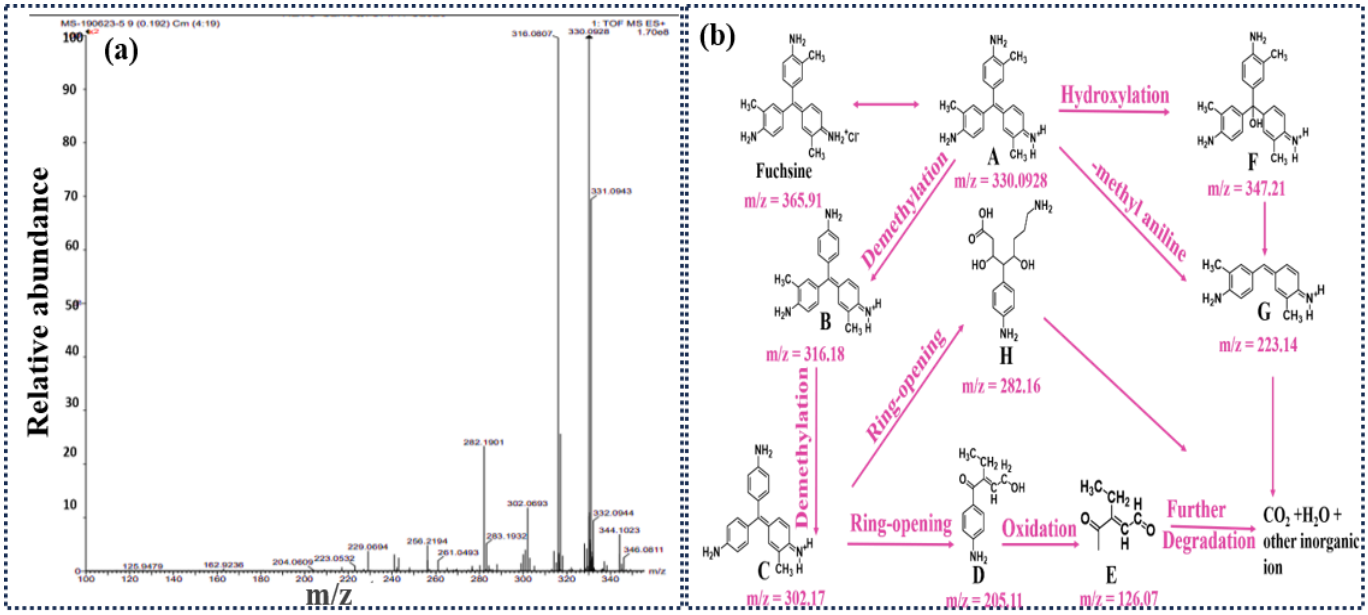


**Fig. 3.12** (a) High-Resolution Mass Spectra (HRMS) and (b) identification/degradation pathways of different intermediate photoproducts formed during photocatalytic degradation of FB dye by FT-$Cu_1$ nanocomposite under 180 min visible light irradiation.

### 3.8 Photostability and reusability of the prepared photocatalyst

For real-world applications, photocatalyst durability must be assessed along with catalytic performance. The reproducibility and photostability of the synthesized FT-$Cu_1$ catalyst were tested through consecutive recycling experiments for the photodegradation of FB dye under identical experimental conditions. The catalyst underwent multiple photochemical reactions, and after each cycle, it was centrifuged, washed, and dried before being reused in the next cycle. This process is illustrated in **Fig. 3.11(b),** where the FT-$Cu_1$ catalyst showed excellent

effectiveness when subjected to visible light irradiation in the 1st cycle, degrading the FB dye 94% after 180 minutes. Despite undergoing five continuous cycles of visible irradiation, the degradation efficiency stays relatively close to 83%, and its catalytic performance remains largely unaffected by repeated use, suggesting that the composite degrades the dye effectively, and FT-$Cu_1$ is a reusable catalyst. The decrease in removal efficiency from 94% to 83% can be ascribed to the unavoidable loss of catalyst during the recovery process. Additionally, over the recycling cycles, some unreacted intermediates may have adhered to the catalyst's surface, blocking certain active sites and pores and contributing to the decline in its performance. The 1wt% Cu deposited on fly ash-$TiO_2$ composite has a strong reusability performance, as evidenced by the consistent degrading efficiency over several cycles. Comparison of percentage removal of Fuchsin blue dye by various composites and Cu- loaded $TiO_2$-fly ash composites is shown in **Table 3.5.**

To confirm the adsorption and photodegradation of FB on the FT-Cu surface, XPS survey spectra were recorded following the adsorption and degradation processes **(Fig. 3.13).** The analysis revealed notable changes in the FT-Cu composite. After adsorption, the appearance of an N 1s peak at 399 eV confirmed the incorporation of nitrogen from the dye, while an increase in the C 1s peak at 284.6 eV indicated the adsorption of organic dye molecules. Following photodegradation, the disappearance of the N 1s peak signified the breakdown of the nitrogen-containing group [58] and the reduction in C 1s peaks, particularly those associated with aromatic structures, confirmed the degradation of the dye into smaller fragments or mineralized products. These results highlight the dual functionality of the FT-Cu composite in effectively adsorbing and degrading fuchsine dye.

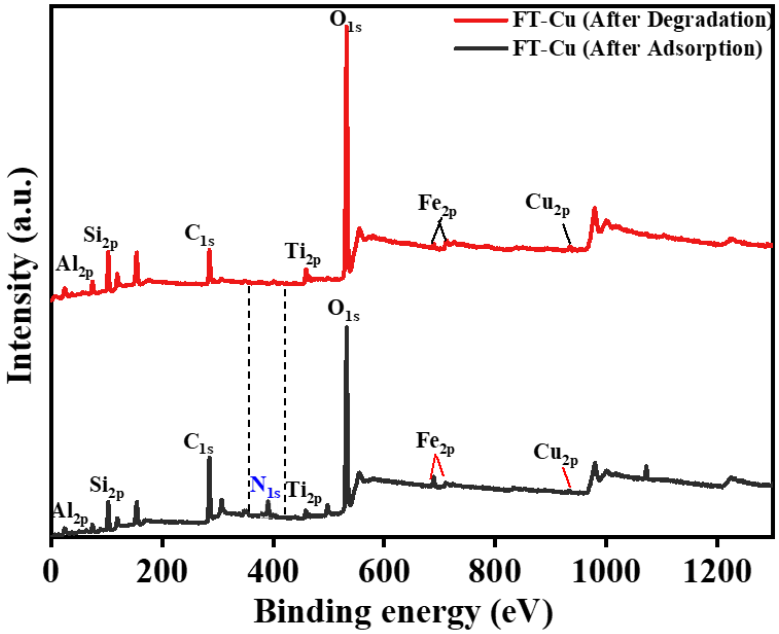


**Fig. 3.13.** XPS survey spectra of the FT-Cu composite after the adsorption and degradation of fuchsin dye.

**Table 3.5.** Comparison of percentage removal of fuchsin blue dye by various composites and fly ash-$TiO_2$-Cu composites.

| **Adsorbent/Catalyst** | **% Removal of FB dye** | **References** |
|---|---|---|
| **Fe-ZSM-5 zeolite** | 99.6% | [59] |
| **Sugarcane bagasse** | 97% | [60] |
| **Mg- Fe $TiO_2$ nanocomposites** | 95% | [61] |
| **g-$C_3N_4$-modified ZnO nanocomposite** | 70% | [62] |
| **FT-$Cu_1$ nanocomposite** | 95% | Present work |

### 3.9 Conclusion

Cu-deposited fly ash-$TiO_2$ (FT-Cu) composite was synthesized successfully and assessed by different characterization techniques. The FT-Cu composite exhibited superior adsorption due to the presence of fly ash containing other metal oxides and photo-catalytic activity due to the presence of $TiO_2$ and copper. Among the prepared composites, the maximum adsorptive removal (77%) of FB dye was achieved by FT-$Cu_1$ composites, which followed the Langmuir isotherm, confirming monolayer adsorption. 1wt% Cu-deposited fly ash-$TiO_2$ (FT-$Cu_1$) attained the maximum removal of 92% of FB dye under solar light and 94% under visible light in less than 180 minutes, whereas the (fly ash–$TiO_2$) FT composite without Cu showed only 71% removal under sunlight and 74% under visible light. It revealed that Cu deposition not only improved the photocatalytic activity of fly ash-$TiO_2$ catalysts, but it also sensitized the absorption of visible/solar light. The XPS results of the FT-Cu composite, including the analysis before and after illumination, provided valuable insights into the interactions between the catalyst and the dye, reinforcing the role of surface chemistry in the photocatalytic process. Furthermore, HRMS results revealed that the composites decomposed the FB dye into smaller molecules. Based on the identification of various degraded photoproducts, band energy analysis, and hole scavenger experiments, a feasible photocatalytic mechanism was proposed where the different reactive oxygen species, OH radical and superoxide anions made a vital contribution to the FB dye degradation process. The resulting Cu-loaded fly ash-$TiO_2$ composite demonstrated high durability and photostability throughout consecutive degradation cycles. Thus, the synergistic effects of fly ash incorporation and Cu modification within the fly ash–$TiO_2$ heterostructure highlight its potential as an efficient photocatalyst for complete mineralization of hazardous pollutants in industrial wastewater under natural sunlight, supporting a more environmentally sustainable remediation strategy.

## REFERENCES

[1] Ismail M, Jobara A, Bekouche H, Abd Allateef M, Ben Aissa MA, Modwi A, Impact of Cu ions removal onto MgO nanostructures: adsorption capacity and mechanism, J. Mater. Sci.Mater. Electron. 33 (2022) 12500–12512, https://doi.org/10.1007/s10854-022-08207-8

[2] Eltabey RM, Abdelwahed FT, Eldefrawy MM, Elnagar MM, Fabrication of poly(maleic acid)- grafted cross-linked chitosan/montmorillonite nanospheres for ultra-high adsorption of anionic acid yellow-17 and cationic brilliant green dyes in single and binary systems, J.

Hazard. Mater. 439 (2022) 129589, https://doi.org/10.1016/j.jhazmat.2022.129589.

[3] Duarte EDV, Brião GV, Ribeiro NFP, da Silva MGC, Vieira MGA, de Carvalho SML, Ternary adsorption of Auramine-O, Rhodamine 6G, and Brilliant Green onto Arapaima gigas scales hydroxyapatite: adsorption mechanism investigation using CCD and DFT studies, Sustain. Mater. Technol. 31 (2022) e00391, https://doi.org/10.1016/j.susmat.2022.e00391.

[4] Binaeian E, Babaee Zadvarzi S, Yuan D, Anionic dye uptake via composite using chitosan–polyacrylamide hydrogel as a matrix containing $TiO_2$ nanoparticles: comprehensive adsorption studies, Int. J. Biol. Macromol. 162 (2020) 150–162, https://doi.org/10.1016/j.ijbiomac.2020.06.158.

[5] Khan SB, Khan MSJ, Kamal T, Asiri AM, Bakhsh EM, Polymer-supported metallic nanoparticles as a solid catalyst for the removal of organic pollutants, Cellulose 27 (2020) 5907–5921, https://doi.org/10.1007/s10570-020-03193-8.

[6]Mahmoud ME, Nabil GM, Elsayed SM, Rashad AR, Synthesis of innovative and sustainable gelatin@graphene oxide-crosslinked-zirconium silicate@gelatin nano-biosorbent for effective biosorption of basic fuchsin dye, Sci. Rep. 13 (2023) 31584, https://doi.org/10.1038/s41598-023-31584-x.

[7] Radha FHS, Shwan DMS, Kaufhold S, Adsorption study and removal of basic fuchsin dye from medical laboratory wastewater using local natural clay, Adsorpt. Sci. Technol. 2023 (2023) 9398167, https://doi.org/10.1155/2023/9398167.

[8] Huerta-Ángeles G, et al., Sustainable aerogels based on biobased poly(itaconic acid) for adsorption of cationic dyes, Int. J. Biol. Macromol. 259 (2024) 129727, https://doi.org/10.1016/j.ijbiomac.2024.129727.

[9] Atlas H, et al., Sustainable biosorption of methylthioninium chloride in wastewaters using new Cystoseira barbata seaweed: equilibrium isotherm, kinetic modelling, and mechanism analysis, Arab. J. Chem. 17 (2024) 105532, https://doi.org/10.1016/j.arabjc.2023.105532.

[10] Amar A, et al., Unveiling the potency of silica–alumina-rich clay in phenol remediation and its repurposing prospects, Inorg. Chem. Commun. 154 (2023) 110983, https://doi.org/10.1016/j.inoche.2023.110983.

[11] Razzak SA, et al., A comprehensive review on conventional and biological-driven heavy metals removal from industrial wastewater, Environ. Adv. 7 (2022) 100168, https://doi.org/10.1016/j.envadv.2022.100168.

[12] Kim S, et al., Review of adsorption–membrane hybrid systems for water and wastewater treatment, Chemosphere 286 (2022) 131916, https://doi.org/10.1016/j.chemosphere.2021.131916.

[13] Luo Z, et al., Novel insights into the adsorption of organic contaminants by biochar: a review, Chemosphere 287 (2021) 132113, https://doi.org/10.1016/j.chemosphere.2021.132113.

[14] Al-Nuaim MA, Alwasiti AA, Shnain ZY, The photocatalytic process in the treatment of polluted water, Chem. Pap. 77 (2023) 677–701, https://doi.org/10.1007/s11696-022-02468-7.

[15] Raval NP, Shah PU, Shah NK, Adsorptive amputation of hazardous azo dye Congo red from wastewater: a critical review, Environ. Sci. Pollut. Res. 23 (2016) 14810–14853, https://doi.org/10.1007/s11356-016-6970-0.

[16] Yue Y, et al., Synergistic adsorption and photocatalysis study of $TiO_2$ and activated carbon composite, Heliyon 10 (2024) e30817, https://doi.org/10.1016/j.heliyon.2024.e30817.

[17] Chiappara C, Arrabito G, Ferrara V, Scopelliti M, Sancataldo G, Vetri V, et al. Improved Photocatalytic Activity of Polysiloxane $TiO_2$ Composites by Thermally Induced Nanoparticle Bulk Clustering and Dye Adsorption. Langmuir 37(2021) 10354–65, https://doi.org/10.1021/acs.langmuir.1c01475 .

[18] Ruan X, Li S, Huang C, Zheng W, Cui X, Ravi SK, Catalyzing artificial photosynthesis with $TiO_2$ heterostructures and hybrids, Adv. Mater. 36 (2024) 2305285, https://doi.org/10.1002/adma.202305285.

[19] Kaur D, Singh K, Reynolds WT, Pal B, Graphene oxide-coated Ag–$TiO_2$ hybrid nanocomposites for superior photocatalytic activity, Environ. Sci. Pollut. Res. 30 (2023) 97660–97672, https://doi.org/10.1007/s11356-023-29301-2.

[20] Rani S, Singh S, Pal B, Core–shell structure of reduced graphene oxide@Ag–$TiO_2$ for photocatalytic $H_2O$ splitting and $CH_3OH$ dehydrogenation under UV light irradiation, Int. J. Hydrogen Energy 49 (2024) 910–924, https://doi.org/10.1016/j.ijhydene.2023.09.214.

[21] Rehan M, Elhaddad E, An efficient multifunctional ternary reusable nanocomposite based on chitosan@$TiO_2$@Ag NP immobilized on cellulosic fiber for wastewater treatment, Environ. Pollut. 340 (2024) 122850, https://doi.org/10.1016/j.envpol.2023.122850.

[22] Prajapati AK, Mondal MK, Comprehensive kinetic and mass transfer modeling for methylene blue dye adsorption onto CuO nanoparticles loaded on nanoporous activated carbon prepared from waste coconut shell, J Mol Liq. 307(2020)112949, https://doi.org/10.1016/j.molliq.2020.112949 .

[23] Azam A, Iqbal T, Efficient fabrication of Cu-doped $TiO_2$ nanoparticles for enhanced visible-light photocatalysis and antimicrobial efficacy, J. Inorg. Organomet. Polym. Mater. 34 (2024) 1–24, https://doi.org/10.1007/s10904-024-03232-y.

[24] Li J, Zheng J, Liu X, Huang Z, Rules for selecting metal additives based on electron structure and HCHO oxidation efficiency between modified-$TiO_2$(B) photocatalyst and metal cocatalyst Pd/Cu/Na, Mol. Catal. 544 (2023) 113176, https://doi.org/10.1016/j.mcat.2023.113176.

[25] Yue T, et al., Enhancement of biohydrogen production by photo-fermentation of corn stover via visible-light-catalyzed $TiO_2$/activated carbon fiber, Bioresour. Technol. 399 (2024) 130459, https://doi.org/10.1016/j.biortech.2024.130459.

[26] Li R, Wu Z, Yang Y, Sun S, Tu Y, Ding H, Photocatalytic persulfate activation by highly dispersed nano-$TiO_2$ supported by silica for efficient carbamazepine degradation, Chem. Phys. Lett. 840 (2024) 141157, https://doi.org/10.1016/j.cplett.2024.141157.

[27] Aljabbari R, Alomayri T, AL-Maqate FG, AlSuwat A, The effect of $TiO_2$ nanoparticle doping on the structural and optical properties of coal fly ash thin films, J. Electron. Mater. 53 (2024) 4812–4828, https://doi.org/10.1007/s11664-024-11205-7.

[28] Gupta P, Nagpal G, Gupta N, Fly ash-based geopolymers: an emerging sustainable solution for heavy metal remediation from aqueous media, Beni-Suef Univ. J. Basic Appl. Sci. 10 (2021) 89, https://doi.org/10.1186/s43088-021-00179-8.

[29] Li G, Teng Q, Sun B, Yang Z, Liu S, Zhu X, Synthesis of scaly Ag–$TiO_2$-loaded fly ash magnetic bead particles for xanthate wastewater treatment, Colloids Surf. A 624 (2021) 126795, https://doi.org/10.1016/j.colsurfa.2021.126795.

[30] Li G, et al., Surfactant-assisted synthesis of Mo-doped $TiO_2$/fly ash cenospheres for visible-light degradation of methylene blue, Colloids Surf. A 651 (2022) 129669, https://doi.org/10.1016/j.colsurfa.2022.129669.

[31] Wang B, Li Q, Wang W, Li Y, Zhai J, Preparation and characterization of $Fe^{3+}$-doped $TiO_2$ on fly ash cenospheres for photocatalytic application, Appl. Surf. Sci. 257 (2011) 3473–3479, https://doi.org/10.1016/j.apsusc.2010.11.050.

[32] Kanakaraju D, Jasni MAAA, Pace A, Ya MH, Enhanced dye-removal performance of Cu–$TiO_2$–fly ash composite via optimized adsorption and photocatalysis under visible light, Environ. Sci. Pollut. Res. 28 (2021) 68834–68845, https://doi.org/10.1007/s11356-021-15440-x.

[33] Singh K, Singh AK, Kumar A, Agarwal A, Fly ash and $TiO_2$-modified fly ash as adsorbents for Cd(II) and Pb(II) removal, J. Hazard. Mater. Adv. 10 (2023) 100256, https://doi.org/10.1016/j.hazadv.2023.100256.

[34] Nien YH, Lai MM, Lin YL, Liu MS, Preparation of Cu/$TiO_2$/rice husk ash nanofibers and their visible-light degradation of methylene blue, J. Polym. Res. 31 (2024) 185, https://doi.org/10.1007/s10965-024-04044-x.

[35] Jemini, Singh S, Pal B, $Ag_2$@$WO_3$/MgAl layered double hydroxide with superior adsorption and visible-light photocatalytic activity, Appl. Clay Sci. 250 (2024) 107281, https://doi.org/10.1016/j.clay.2024.107281.

[36] Rohilla P, Pal B, Das RK, Bi-doped g-$C_3N_4$/$Bi_2WO_6$ ternary composites for enhanced visible-light photocatalytic degradation of reactive orange 16, J. Ind. Eng. Chem. (2024) Article in press, https://doi.org/10.1016/j.jiec.2024.07.007.

[37] Oleiwi HF, Rahma AJ, Salih SI, Beddai AA, Comparative study of sol–gel and green synthesis of $TiO_2$ nanoparticles using orange peel extract, Baghdad Sci. J. 21 (2024) 1702–1711, https://doi.org/10.21123/bsj.2023.8089.

[38] Mahima Kumar M, et al., Characterization of fly ash by ED-XRF and INAA for synthesis

of low-silica zeolites, J. Radioanal. Nucl. Chem. 325 (2020) 941–947, https://doi.org/10.1007/s10967-020-07243-0.

[39] Gilja V, Katancic Z, Krehula LK, Mandic V, Hrnjak-Murgic Z, Efficiency of $TiO_2$ supported on modified waste fly ash in photodegradation of RR45 dye, Sci. Eng. Compos. Mater. 26 (2019) 292–300, https://doi.org/10.1515/secm-2019-0017.

[40] Chen Y, Zhao Y, Wang Y, Fly ash-based zeolite–PEG composite electrode for high-performance diabetes determination, Int. J. Nanomed. 15 (2020) 6619–6629, https://doi.org/10.2147/IJN.S264645.

[41] Jiang J, Ding Y, Hydrogenation of C=N bonds on $TiO_2$: effect of $Cu_2O/TiO_2$ p–n heterojunction photocatalyst, Surf. Interfaces 37 (2023) 102625, https://doi.org/10.1016/j.surfin.2022.102625.

[42] Fan H, et al., Mesoporous $TiO_2$-coated $ZnFe_2O_4$ nanocomposite loaded on activated fly ash cenospheres for visible-light photocatalysis, RSC Adv. 8 (2018) 1398–1406, https://doi.org/10.1039/c7ra11055c.

[43] Tu Y, et al., Preparation of fly ash-supported nano-$TiO_2$ composite photocatalyst by wet mechanical grinding, Chem. Phys. Lett. 805 (2022) 139978, https://doi.org/10.1016/j.cplett.2022.139978.

[44] Naveenkumar R, Karthikeyan B, Senthilvelan S, Facile green synthesis of activated biocarbon–cobalt-doped $TiO_2$ nanocomposite for antibacterial activity and dye degradation, Braz. J. Phys. 54 (2024) 170, https://doi.org/10.1007/s13538-024-01543-6.

[45] Zhao W, Liu C, Mesoporous Cu–$Cu_2O$@$TiO_2$ heterojunction photocatalysts derived from metal–organic frameworks, RSC Adv. 10 (2020) 14550–14555, https://doi.org/10.1039/d0ra01327g.

[46] Liang Y, et al., Acid-etched coal fly ash/$TiO_2$ nanocomposites with high photocatalytic degradation efficiency: a high value-added application of coal fly ash, J. Sol-Gel Sci. Technol. 103 (2022) 185–194, https://doi.org/10.1007/s10971-022-05822-z.

[47] Zhang Z, et al., Reaction behavior and influencing mechanisms of different fly ashes on NO removal using ultraviolet-irradiating chlorite method, ACS Omega 7 (2022) 8739–8752, https://doi.org/10.1021/acsomega.1c06930.

[48] Fu B, Hower JC, Dai S, Mardon SM, Liu G, Determination of chemical speciation of arsenic and selenium in high-As coal combustion ash by XPS, ACS Omega 3 (2018) 17637–17645, https://doi.org/10.1021/acsomega.8b02929.

[49] Jia J, et al., β-Cyclodextrin-based adsorbents integrated with N-doped $TiO_2$ photocatalysts for enhanced dye elimination from industrial wastewater, Surf. Interfaces 45 (2024) 103901, https://doi.org/10.1016/j.surfin.2024.103901.

[50] Bansal M, Pal B, Starch-modified NiFe layered double hydroxide composites for adsorption and photocatalytic removal of reactive dye and piroxicam-20, Environ. Sci. Pollut. Res. 30 (2023) 73825–73844, https://doi.org/10.1007/s11356-023-27592-z.

[51] Bansal M, Pal B, Enhanced elimination of nitrate and nitrite ions using chitosan sphere-modified Mg–Al layered double hydroxide composite, J. Ind. Eng. Chem. (2024) 1–16, https://doi.org/10.1016/j.jiec.2024.08.007.

[52] Goswami L, Kushwaha A, Kafle SR, Kim BS, Surface modification of biochar for dye removal from wastewater, Catalysts 12 (2022) 817, https://doi.org/10.3390/catal12080817.

[53] Sudan S, Kaushal J, Khajuria A, Efficient adsorption of Congo red using copper–carbon dots-doped magnetic biochar: kinetic, isothermal, and regeneration studies, Clean Technol. Environ. Policy 26 (2024) 481–497, https://doi.org/10.1007/s10098-023-02621-0.

[54] Baha AA, et al., Synergistic photocatalysis of bayerite/zeolite-loaded $TiO_2$ nanocomposites for degradation of organic pollutants, Silicon 16 (2024) 4843–4856, https://doi.org/10.1007/s12633-024-03056-y.

[55] Passi M, Pal B, Ternary Fe(III)–$SrTiO_3$–GO nanocomposite for LED-light-driven photocatalytic degradation of norfloxacin antibiotic, Chem. Eng. J. 479 (2024) 147685, https://doi.org/10.1016/j.cej.2023.147685.

[56] Garg S, Kataria J, Sharma S, Choudhary MK, Kinetic investigation of enhanced photocatalytic performance of phytogenically synthesized Ag@$TiO_2$ composites, Mater. Chem. Phys. 294 (2023) 127005, https://doi.org/10.1016/j.matchemphys.2022.127005.

[57] Qin J, et al., Hydrodynamic cavitation-assisted degradation of basic fuchsin in wastewater using by-pass line orifice plate, Sep. Purif. Technol. 287 (2022) 120501, https://doi.org/10.1016/j.seppur.2022.120501.

[58] Rieß J, et al., XPS studies on dispersed and immobilized carbon nitrides for dye degradation, Photochem. Photobiol. Sci. 18 (2019) 1833–1839, https://doi.org/10.1039/c9pp00144a.

[59] Ba Mohammed B, et al., Fe-ZSM-5 zeolite for efficient removal of basic fuchsin dye: synthesis, characterization and adsorption optimization, J. Environ. Chem. Eng. 8 (2020) 104419, https://doi.org/10.1016/j.jece.2020.104419.

[60] Elamin MR, Elamin NY, Taha KK, Modwi A, Fabrication of ternary $Co_3O_4$@β-$Bi_2O_3$@g-$C_3N_4$ nanosorbent for basic fuchsin dye decontamination, Inorg. Chem. Commun. 159 (2024) 111840, https://doi.org/10.1016/j.inoche.2023.111840.

[61] Latif S, Abdulaziz F, Al-Ahmed A, Efficient removal of carcinogenic rosaniline hydrochloride dye using Mg-doped FeTiO nanocomposites, J. Saudi Chem. Soc. 28 (2024) 101778, https://doi.org/10.1016/j.jscs.2023.101778.

[62] Khezami L, et al., g-$C_3N_4$-modified ZnO nanocomposite for exceptional adsorption of basic fuchsin dye, Inorg. Chem. Commun. 164 (2024) 112413, https://doi.org/10.1016/j.inoche.2024.112413.

# Chapter-4

## Fabrication and evaluation of ZSM-5-fly ash–$TiO_2$–Cu hybrid catalysts for efficient photocatalytic and adsorptive removal of crystal violet dye

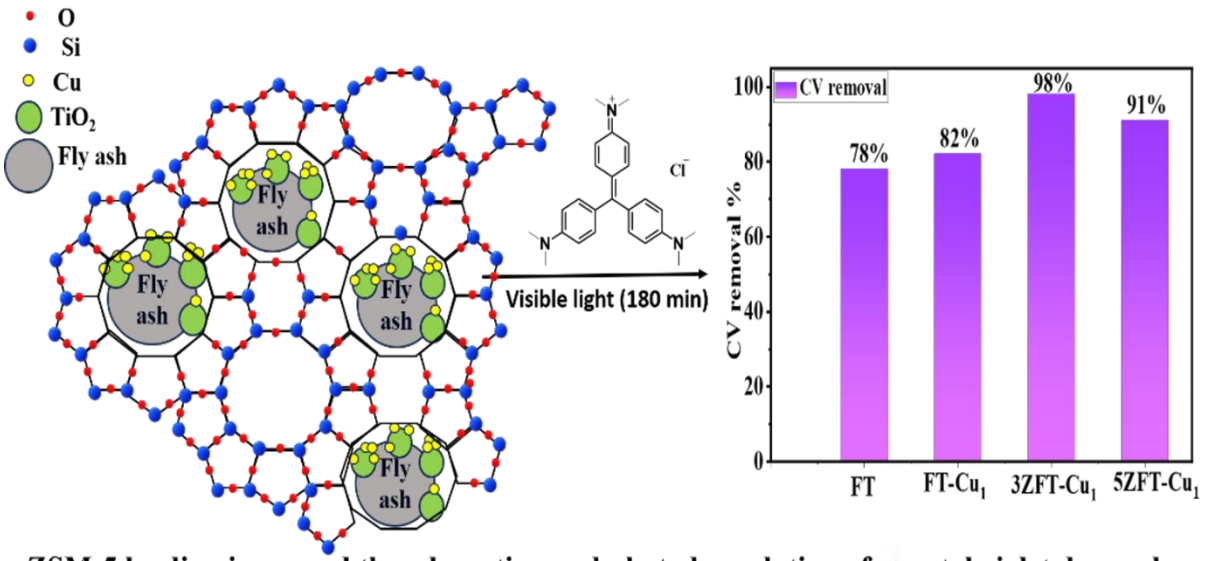


**ZSM-5 loading improved the adsorption and photodegradation of crystal violet dye under visible light**

**Schematic summary**

### 4.1 Introduction

Water contamination from organic dyes is a serious issue that endangers the ecosystem. Industries including paper, plastics, leather, textiles, and pharmaceuticals discharge large volumes of wastewater tainted with dyes into natural water pools. [1, 2] The toxic organic dyes often disrupt the ecosystems by lowering the oxygen levels and killing the aquatic life [3, 4]. Human exposure to polluted water can cause a range of health problems. Certain dyes are carcinogenic, mutagenic, and teratogenic, posing long-term risks such as cancer and genetic mutations. Drinking contaminated water can cause gastrointestinal disorders, damage to the kidneys, and the liver. [5–7].

Crystal violet (CV) is a dye derived from aniline that has been widely utilized as a disinfectant, a staining agent in biomedical applications, a pH indicator, and a colouring agent in the textile industry [8]. It is a potent mutagen and has been classified as a potential carcinogen. Excessive exposure to CV dye can cause cancer, organ damage, and reproductive disorders over time.

Direct skin contact might irritate the skin with respiratory difficulties [9]. Thus, developing efficient, cost-effective, and ecologically sustainable techniques for extracting crystal violet from wastewater is critically important.

Numerous approaches, such as adsorption, electrochemical processes, photocatalytic degradation, and biological methods, have been established to remove organic dyes from wastewater. Adsorption is the most beneficial of these techniques because of its low cost, ease of setup, user-friendliness, low production of harmful byproducts, wide availability of adsorbent materials, and ease of recovery [10]. However, a key challenge in this process is the saturation of the adsorbent, which must then be either regenerated or replaced. In contrast, photocatalysis can decompose particles that are challenging to remove from treated water through conventional methods completely. The photocatalysis process breaks down various contaminants into harmless compounds like carbon dioxide and water [11]. This technique could remarkably decrease the operation cost due to low energy consumption. Combining photocatalytic decomposition with adsorption would be a practical approach to enhance the degradation of dyes.

Titanium dioxide ($TiO_2$) is the best-known and widely studied photocatalyst for the degradation of various toxic organic pollutants, particularly due to its high oxidative power upon illumination. It is a non-toxic, chemically inert, low-cost, and biocompatible material with interesting physical, optical, and electrical properties. UV radiation activates $TiO_2$ and causes ROS, such as superoxide ions and hydroxyl radicals, potent oxidizers that may quickly break down a range of organic contaminants into nontoxic inorganic compounds like $CO_2$ and $H_2O$ [12]. Despite its potential, the practical use of $TiO_2$ is hindered by its wide band gap of about 3.2 eV, which confines its photoactivation primarily to the ultraviolet region of the spectrum, which constitutes only about 5% of sunlight. Additionally, the fast recombination of photo-induced electron–hole pairs significantly diminishes its overall photocatalytic efficiency [13].

The best way to get around these restrictions is by metal doping. A practical method for enhancing $TiO_2$ involves doping with transition metals such as nickel (Ni), copper (Cu), and silver (Ag), which induces a substantial modification of its optical absorption characteristics. These metal dopants significantly reduce the band gap of $TiO_2$, allowing photoexcitation in visible light (red shift) while also preventing the recombination of photogenerated electron-hole pairs [14, 15]. It is not easy to produce stable, reasonably priced doped nanomaterials with distinct properties that can efficiently absorb visible light. Among the various transition metals, copper (Cu) is a particularly strong dopant due to its special characteristics and capacity to promote charge separation and transfer. Doping of copper ($Cu^{2+}$) produces additional energy

levels in the $TiO_2$ band gap, thereby increasing visible light absorption and photocatalytic activity. Moreover, $Cu^{2+}$ ions favour photogenerated electron-hole separation and reduce charge carrier recombination by functioning as electron traps [16, 17]. Recent research have emphasized the impact of multi-metal doping and surface modification in increasing photocatalytic stability. Sun et al. [18] developed Cu–Mn catalysts for carbon monoxide (CO) removal using a co-precipitation approach and comprehensively examined the influence of additional metal dopants (Fe, Ce, and Sn), precipitation temperature, and hydrophobic modification with polyvinyl alcohol (PVA) and polyvinylpyrrolidone (PVP). The catalyst containing Ce prepared at 70 °C showed roughly 50 % greater CO removal efficiency than the other samples and, after PVA/PVP treatment, retained about 85 % removal efficiency under 90 % relative humidity, indicating excellent water resistance.

One technique is to anchor $TiO_2$ particles onto high-surface-area supports, such as ZSM-5 zeolite, a synthetic aluminosilicate with a well-ordered microporous framework, excellent thermal and chemical stability, and the ability to modify its hydrophilic or hydrophobic characteristics [19]. ZSM-5 not only enhances adsorption by trapping organic pollutants near the photocatalytic surface but also aids in better dispersion of $TiO_2$ nanoparticles, preventing aggregation and promoting efficient charge transfer. Its shape-selective pore structure and strong adsorption affinity make ZSM-5 particularly effective in capturing dye molecules, such as crystal dyes, before their degradation [20].

Fly ash, a solid byproduct of burning coal in thermal power plants, is frequently employed as a support material in photocatalytic applications because of its abundance, affordability, and favourable chemical compatibility with metal oxides. Silica, alumina, and other inorganic oxides comprise most of its composition. It forms a structurally rigid and chemically stable matrix that permits the uniform dispersion of photocatalytic particles such as $TiO_2$. This homogeneous distribution not only prevents nanoparticle aggregation, but it also enhances the composite's surface area and structural robustness, resulting in increased photocatalytic activity [21]. The integration of fly ash with ZSM-5 and Cu-doped $TiO_2$ results in a multifunctional composite material that offers improved surface area, enhanced pollutant adsorption, enhanced photocatalytic performance when exposed to visible light, and cost-effectiveness.

Over the last few years, several research studies have investigated photo-catalytic degradation of organic pollutants under UV and visible light using ZSM-5/$TiO_2$, $TiO_2$-supported fly ash, and metal-modified fly ash- $TiO_2$ composites. Mergenbayeva et al. [22] developed $TiO_2$ /zeolite composites, $TiO_2$ /Z-45 (TZ) and $TiO_2$ /ZSM-5 (TZSM), by mechanical mixing and liquid impregnation processes. These composites were used in the photocatalytic breakdown

of sulfamethoxazole (SMX) in water using UV light. Photocatalytic testing revealed that TZSM2600 and TZSM1450 produced 65% and 67% mineralisation of SMX, respectively, after 120 minutes. Al-Wasidi et al. [23] synthesized ZSM-5/$TiO_2$/Ni photocatalyst to degrade methylene blue dye under ultraviolet light. The ZSM-5/$TiO_2$/Ni nanocomposite had a maximum degradation efficiency of 99.17% for 50 mL of 15 mg/L methylene blue dye under 140 minutes. Zhu et al. [24] developed a copper (II)-modified ZSM-5/$TiO_2$ composite using a sol–gel technique combined with an impregnation method. This composite was applied for the photocatalytic degradation of ammonia gas under visible light conditions. The catalyst containing 0.5wt% Cu exhibited the highest efficiency, removing nearly 94.2% of ammonia within 60 minutes of exposure to visible light. Stojanović et al. [25] synthesized $TiO_2$/zeolite composites via a solid-state dispersion technique, incorporating synthetic and natural zeolites with P25 $TiO_2$ and $TiO_2$ nanocrystals derived from nanotubes. Among the tested materials, the $TiO_2$ /ZSM-5 (P25) composite demonstrated the most effective photocatalytic performance under simulated solar light, achieving nearly 94% removal of atenolol within 70 minutes.

In the previous work, Cu photo-deposited fly ash-$TiO_2$ composite was synthesized, and its performance was evaluated for removing fuchsin blue dye [26]. In the present work, the influence of ZSM-5 zeolite loading on Cu photo-deposited fly ash-$TiO_2$ composite for the degradation of crystal violet dye under visible and solar light is investigated. However, the novelty of the present work lies in the design and application of ZSM-5–loaded fly ash–$TiO_2$–Cu (ZFT-Cu) hybrid composites, which, to the best of our knowledge, have not been reported earlier. The composite was prepared using the wet impregnation process. A synergistic effect is produced when visible-light-active flyash-$TiO_2$-Cu and high-surface-area, highly porous ZSM-5 are combined. The novel composite catalyst is used to destroy the CV dye molecules once they have been adsorbed onto the surface of the ZSM-5. Additionally, the photocatalytic degradation of crystal violet under sunlight was investigated to evaluate the impact of ZSM-5 incorporation onto copper photo-deposited $TiO_2$/fly ash composite. The degradation of crystal violet using ZFT-Cu composites has not been reported elsewhere, thereby establishing the novelty and significance of this research. This study contributes to developing efficient, environmentally friendly, and cost-effective composites for the removal of dye-contaminated wastewater.

## 4.2 Materials and methods

### 4.2.1 Materials and reagents

All chemicals were of analytical grade and used as received, without further purification. ZSM-5 was procured from Thermo Fisher Scientific India Pvt. Ltd. Fly ash was collected from the Rajpura Power Plant in India. Deionised water, with a conductivity of 35 μS $cm^1$ at 25 °C, was produced using a Milli-Q ultrafiltration system (Millipore). Titanium butoxide ($Ti(OC_4H_9)_4$, 97%) and didecyl dimethyl ammonium chloride ($C_{22}H_{48}ClN$) were obtained from Sigma-Aldrich, India. Loba Chemie, India, supplied acetic acid ($C_2H_4O_2$, 99.8%), ethanol ($C_2H_5OH$, 99.9%), cupric nitrate trihydrate ($Cu(NO_3)_2 \cdot 3H_2O$, 99.5%), isopropyl alcohol ($C_3H_8O$, 99.5%), and crystal violet dye ($C_{25}H_{30}ClN_3$).

### 4.2.2 Techniques Used for Characterizing the Synthesized Samples

Diffraction images were recorded using an X-ray diffractometer (Smart Lab SE) equipped with Cu-Kα radiation (λ = 1.54 Å) and operated at 45 kV to analyze the crystalline structure. Scans were performed across a 2θ range of 5° to 80°, using a 10 mm slit, at a resolution of 0.01° per scan and a scan speed of 5 ° $min^{-1}$. Field emission scanning electron microscopy (FESEM, JEOL JSM-7600F, JAPAN, operated at 30 kV) was used to examine the surface morphology and microstructure of the catalyst. Elemental composition and spatial distribution were analysed using energy dispersive spectroscopy (Bruker EDS). FTIR spectra of the synthesized samples were obtained using an Agilent FTIR spectrophotometer. The BET Autosorb iQ (Quanta chrome Instruments, version 3.01, USA) was employed to assess the surface area and pore size distribution of the samples. A JASCO V-750 diffuse reflectance spectrophotometer (Japan) was used to determine the optical properties, employing $BaSO_4$ as the standard reference material.

### 4.2.3 Synthesis of ZSM-5 loaded fly ash-$TiO_2$-Cu ($ZFT\text{-}Cu_1$) composite

A wet impregnation method was used to produce the ZSM-5 modified fly ash-$TiO_2$-Cu ($ZFT\text{-}Cu_1$) composites. 500 mg of the Cu-deposited fly ash–$TiO_2$ ($FT\text{–}Cu_1$) composite, prepared as described in chapter 3 (section 3.2.3), was used for the experiment. On the $FT\text{–}Cu_1$ composite, ZSM-5 was added in varying weight percentages (1wt%, 3wt%, and 5wt%). After a thorough stirring for 2 hours followed by centrifugation, the components were frequently washed with ethanol and deionized water multiple times to remove any last traces of impurities. After

washing, ZSM-5 modified composites were calcined at 400°C to strengthen their structure after being dried for 24 h at 70°C. The substance was ground into a fine powder using a mortar and pestle. 1ZFT-$Cu_1$, 3ZFT-$Cu_1$, and 5ZFT-$Cu_1$ were the end products having loaded with 1wt%, 3wt%, and 5wt% ZSM-5 zeolite onto the fly ash-$TiO_2$-Cu (ZFT-$Cu_1$) composite respectively.

### 4.2.4 Adsorption in Dark and Photocatalytic Studies

Batch adsorption studies were carried out to evaluate the adsorption performance of FT-$Cu_1$ and (3–5wt%) ZFT-$Cu_1$ composites toward crystal violet (CV) dye. A 10 mL CV solution with initial concentrations of 3–15 mg/L was contacted with adsorbent dosages of 1–10 mg for contact times ranging from 0 to 240 min. The effect of solution pH (2–12) was also examined. All experiments were conducted at room temperature (25 ± 2 °C) under dark conditions with continuous stirring. After adsorption, the suspensions were centrifuged, and the residual CV concentration was measured using a UV–visible spectrophotometer at $\lambda_{max}$ = 598 nm, as determined from the calibration curve. The adsorption capacity and removal efficiency were calculated using equations 1 and 2 as described in Chapter 3 (Section 3.2.5).

Under visible light, photocatalytic degradation experiments were carried out to evaluate the degradation of crystal violet (CV) dye using FT-$Cu_1$ and (3–5wt%) ZFT-$Cu_1$ composites. The reaction mixtures were irradiated using a Wipro Garnet B22 50-W LED bulb ($\lambda > 360$ nm) under continuous magnetic stirring for predetermined time intervals. Before light irradiation, the suspensions were stirred in the dark for 180 min to establish adsorption–desorption equilibrium between the catalyst and CV dye molecules. At specified irradiation times, the samples were withdrawn and centrifuged at 8000 rpm for 8 min to separate the photocatalyst. The residual CV dye concentration in the clear supernatant was quantified using a UV–visible spectrophotometer. The photodegradation efficiency was calculated using equations 3 and 4 as described in Chapter 3 (Section 3.2.6).

### 4.2.5 Adsorption Isotherm Models

To determine the effectiveness of the adsorption process, the data were fitted to various isotherm models, including Langmuir, Freundlich, Temkin, and Dubinin-Radushkevich (D–R) isotherms. The corresponding models are expressed as:

Langmuir isotherm model: $$\frac{1}{Q_e} = \left(\frac{1}{K_L Q_{max}}\right) \times \frac{1}{C_e} + \frac{1}{Q_{max}} \quad (1)$$

Freundlich's isotherm model: $$\log Q_e = \log K_F + \left(\frac{1}{n}\right) \log C_e \quad (2)$$

Temkin isotherm model: $Q_e = B_T \ln A + B_T \ln C_e$ (3)

Dubinin-Radushkevich (D-R) isotherm model: $\ln Q_e = \ln Q_m - \beta\varepsilon^2$ (4)

Here, $Q_e$ (mg/g) is the quantity of pollutant adsorbed at equilibrium, and $C_e$ (mg/L) denotes the pollutant concentration at equilibrium. $Q_{max}$ (mg/g) is the maximum adsorption capacity. The Langmuir constant, $K_L$ (L/mg), signifies the affinity between the substance that adsorbs and the adsorbate that occurs at the active binding sites. To what extent the adsorption process is favoured is determined by the Langmuir isotherm, which is in turn described by the dimensionless separation factor ($R_L$) [27]. The model constants, $K_L$ and $K_F$, are obtained by fitting the experimental data to the linear forms of the isotherms [28]. The quantities A (L/g) and B represent the Temkin isotherm constant and the adsorption heat, respectively. In this context, β is the Dubinin-Radushkevich isotherm constant (mol²/kJ²), and ε is the Polanyi potential.

### 4.2.6 Adsorption Kinetic Models

The adsorption kinetics were analyzed using pseudo-first-order, pseudo-second-order, intraparticle diffusion, and Elovich models:

Pseudo-first order kinetic model: $\log(Q_e - Q_t) = \log Q_e - \frac{k_1}{2.303} t$ (5)

Pseudo-second order kinetic model: $\frac{t}{Q_t} = \frac{1}{k_2 Q_e^2} + \frac{t}{Q_e}$ (6)

Intra-particle diffusion kinetic model: $Q_t = K_{dif} \sqrt{t} + C_i$ (7)

Elovich kinetic model: $Q_t = \frac{1}{\beta} \ln(\alpha\beta) + \frac{1}{\beta} t$ (8)

$Q_t$ and $Q_e$ denote the adsorption capacity at time t and equilibrium, respectively. $C_t$ and $C_o$ denote the pollutant concentrations at time t (min) and at the initial time, respectively. The rate constant for the pseudo-first-order model is $k_1$ ($min^{-1}$), and for the pseudo-second-order model is $k_2$ (g $mg^{-1}$ $min^{-1}$). In this model, $K_{dif}$ (mg $g^{-1}min^{-0.5}$) represents the intra-particle diffusion rate constant, whereas $C_i$ (mg $g^{-1}$) measures diffusion resistance. In the Elovich model, α (mg $g^{-1}$ $min^{-1}$) represents the initial adsorption rate, while β (g $mg^{-1}$) is the desorption constant [29].

## 4.3 Results and discussion

### 4.3.1 XRD analysis

The XRD image of the synthesised FT, FT-$Cu_1$, and ZFT-$Cu_1$ nanocomposites, along with their crystal planes and associated diffraction angles, is shown in **Fig. 4.1**. The FT sample has a diffraction peak at 25.3° of 2θ, which corresponds to the anatase (101) phase. $TiO_2$ verifies the presence of the anatase phase besides the crystalline phases that are frequently found in fly ash, such as hematite ($Fe_2O_3$), magnetite ($Fe_3O_4$), mullite ($Al_6Si_2O_{13}$), and quartz ($SiO_2$) [30].
The appearance of this peak confirms the successful integration of $TiO_2$ [31] onto the fly ash surface, signifying effective composite formation. There are no noticeable diffraction peaks in the FT-$Cu_1$ photocatalysts' XRD patterns that correspond to the Cu co-catalyst. This finding is in agreement with other studies that found that metal nanoparticles at low concentrations (often less than 5wt%) are often undetected when analysed by XRD [26]. The ZFT-$Cu_1$ composite similarly lacks distinct peaks associated with ZSM-5, likely attributable to the low loading level of ZSM-5 and the overlap of peaks with the predominant crystalline phases of quartz and mullite in fly ash [32] . The lack of ZSM-5 diffraction peaks in the XRD indicates that the particles are either extensively dispersed within the support matrix or present in a partially amorphous state, notably reducing the diffraction intensity.

### 4.3.2 FESEM analysis

A uniform dispersion of $TiO_2$ nanoparticles across the surface of the spherical fly ash particles is revealed by the FE-SEM images of the synthesized composites, which are displayed in **Fig. 4.2 (a, b).** The FT composite predominantly consists of spherical particles characterized by smooth surfaces, affirming successful surface modification. At lower magnification, the boundaries may appear indistinct; however, $TiO_2$ nanoparticles are likely dispersed across the fly ash particles. The irregular surface roughness indicates a heterogeneous composition of the fly ash [26,33].
The FT-$Cu_1$ composite shown in **Fig. 4.2 (c, d)** exhibits enhanced surface uniformity in $TiO_2$-coated fly ash. Cu doping reduces agglomeration, potentially due to enhanced dispersion or interaction with $TiO_2$ particles, but it is not shown on the surface in FESEM images, due to a smaller nanometer size. This modification may enhance electron mobility or reduce the recombination rate in photocatalytic systems [26]. The FESEM structure of 3ZFT-$Cu_1$ and 5ZFT-$Cu_1$ composites is shown in **Fig. 4.3 (a, b)** and **Fig. 4.3 (c, d),** respectively. Both composites' coarse and porous surfaces make them suitable for adsorption and photocatalytic

degradation [34]. The presence of cluster particles in the 3ZFT-$Cu_1$ composites' coarse structure suggests that the zeolite, fly ash, and $TiO_2$ were well incorporated. Furthermore, the marked circles in Fig. 4.3 confirm the presence of ZSM-5 zeolite particles distributed over the composite surface, enhance surface area and adsorption efficiency.

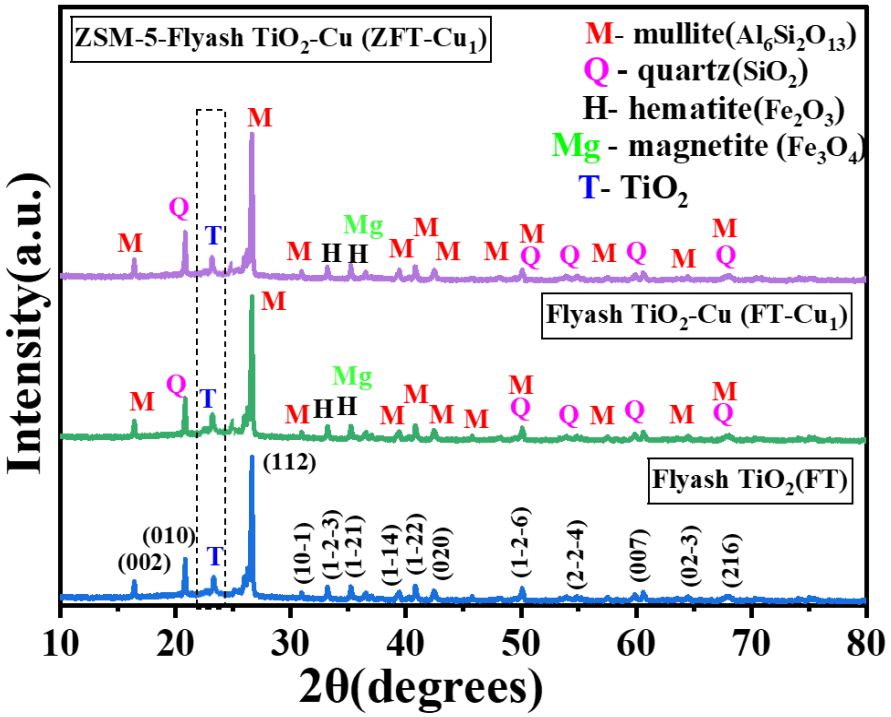


**Fig. 4.1** XRD profiles of Fly ash-$TiO_2$ (FT), Copper loaded fly ash-$TiO_2$ composite (FT-$Cu_1$) and ZSM-5 loaded Fly ash- $TiO_2$- copper composite (ZFT-$Cu_1$)

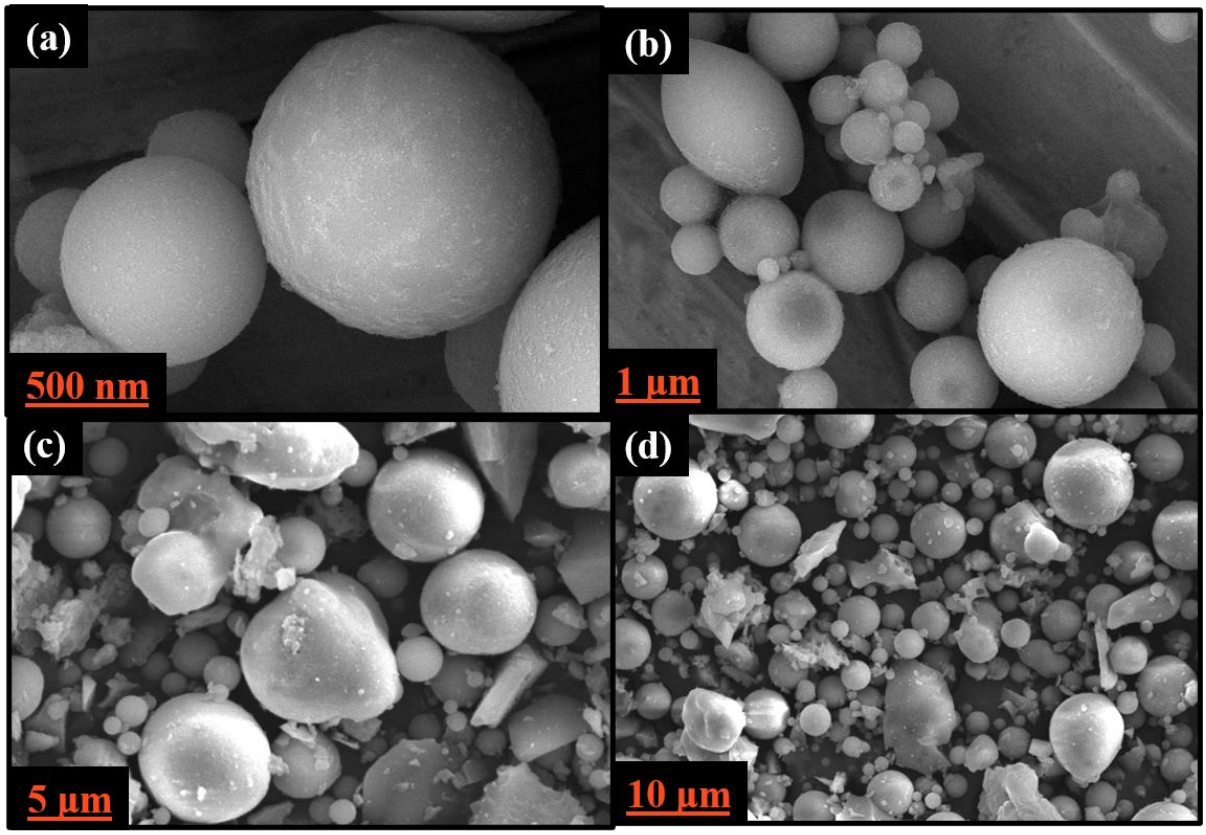


**Fig. 4.2** FE-SEM micrographs of (a, b) FT, and (c, d) FT-$Cu_1$ composite

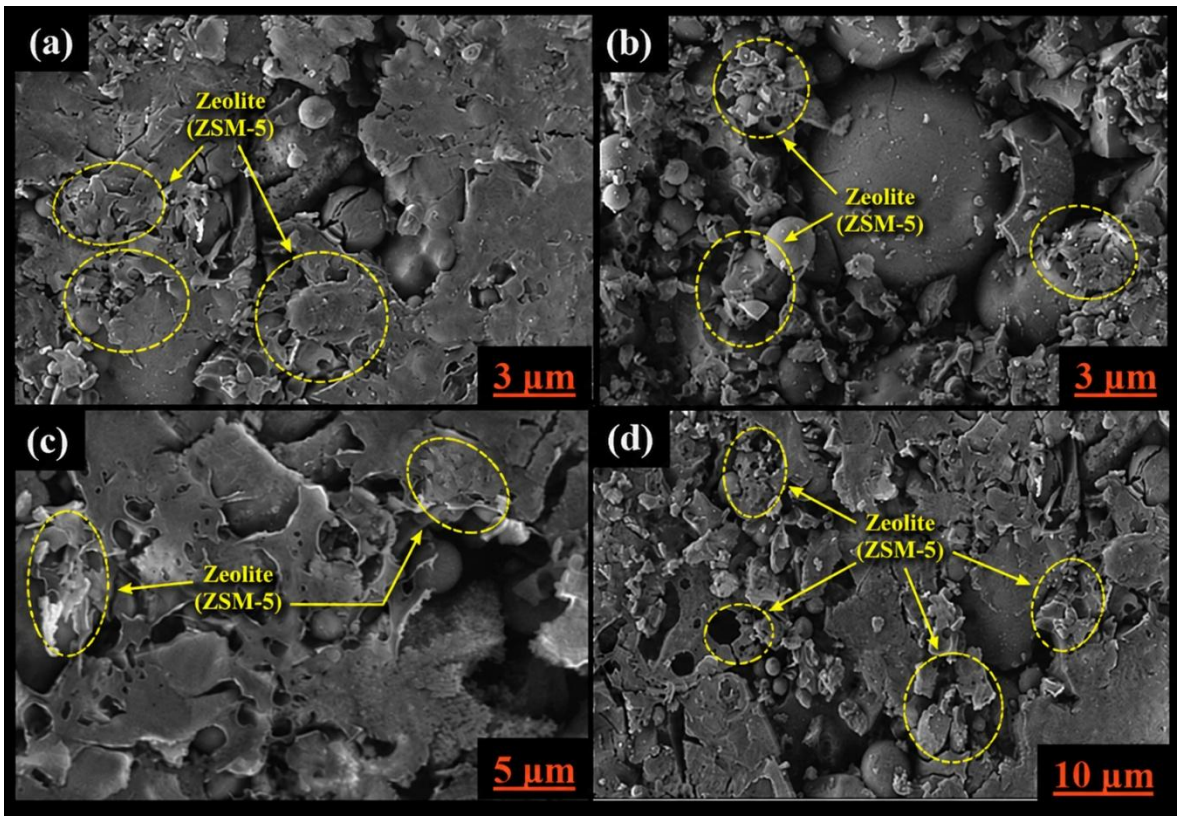

**Fig. 4.3** FE-SEM micrographs of (a, b) 3ZFT-$Cu_1$ and (c, d) 5ZFT-$Cu_1$ composite.

### 4.3.3 EDS analysis

Energy dispersive spectroscopy (EDS) was used to analyze the elemental composition of 3ZFT-$Cu_1$ composite, which showed the distribution of the elemental composition, as well as their atomic and weight percentages. **Fig. 4.4** shows the elemental composition of the composite as confirmed by the EDS spectra, which show the presence of oxygen (O), silicon (34.07%), aluminium (12.88%), copper (1.05%), iron (1.1%), titanium (4.32%), and sodium (0.82%) in the composite.

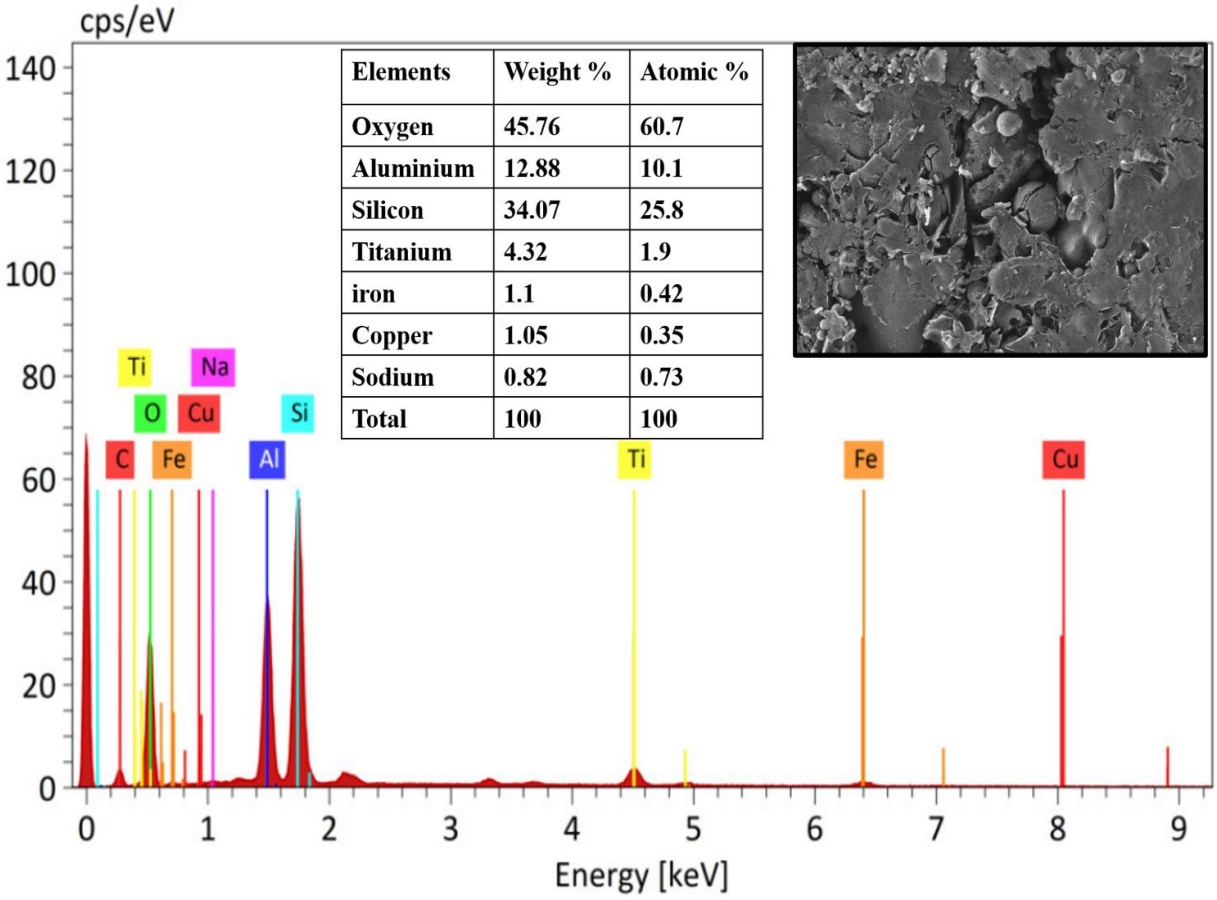


| Elements | Weight % | Atomic % |
|---|---|---|
| Oxygen | 45.76 | 60.7 |
| Aluminium | 12.88 | 10.1 |
| Silicon | 34.07 | 25.8 |
| Titanium | 4.32 | 1.9 |
| iron | 1.1 | 0.42 |
| Copper | 1.05 | 0.35 |
| Sodium | 0.82 | 0.73 |
| Total | 100 | 100 |

**Fig. 4.4** EDS analysis of 3ZFT-$Cu_1$ composite confirming the presence of constituent elements.

### 4.3.4 FT-IR analysis

The FTIR spectra of ZSM-5, $TiO_2$, fly ash, and the Cu-modified composites (1ZFT-$Cu_1$, 3ZFT-$Cu_1$, and 5ZFT-$Cu_1$) are presented in **Fig. 4.5**. For ZSM-5, the typical framework vibrations are evident, with strong bands at 1080–1100 $cm^{-1}$ corresponding to asymmetric T–O–T stretching

(T = Si or Al), at 790–800 $cm^{-1}$ for symmetric Si–O–Si stretching, and at 450–500 $cm^{-1}$ attributed to Si–O–Si/Al–O–Si bending [35]. These characteristic peaks persist in the ZFT-Cu composites, confirming that the zeolite lattice remains intact after compositing and Cu incorporation. $TiO_2$ displays a broad band below 800 $cm^{-1}$ assigned to Ti–O–Ti vibrations, which is also distinguishable in the composites, signifying the presence of $TiO_2$ within the hybrid framework [36]. The FTIR profile of fly ash reveals broad Si–O–Si stretching absorptions between 1000–1080 $cm^{-1}$ and a band near 1630–1640 $cm^{-1}$ linked to bending of adsorbed water molecules [37]; both signals are retained in the ZFT-Cu materials. Incorporation of Cu into the composites leads to subtle shifts and variations in the intensities of the ZSM-5 framework peaks, suggesting interaction among ZSM-5, $TiO_2$, and fly ash components while preserving the fundamental crystalline structure. In addition, all spectra show a broad band around 3400–3450 $cm^{-1}$, assigned to O–H stretching of surface hydroxyl groups and physisorbed water, which appears more intense in the composites, indicating an increased number of active surface sites. Overall, the FTIR results demonstrate that ZSM-5, $TiO_2$, and fly ash were successfully integrated with Cu, maintaining the structural integrity of the zeolite and producing composites with potential for enhanced adsorption and photocatalytic performance.

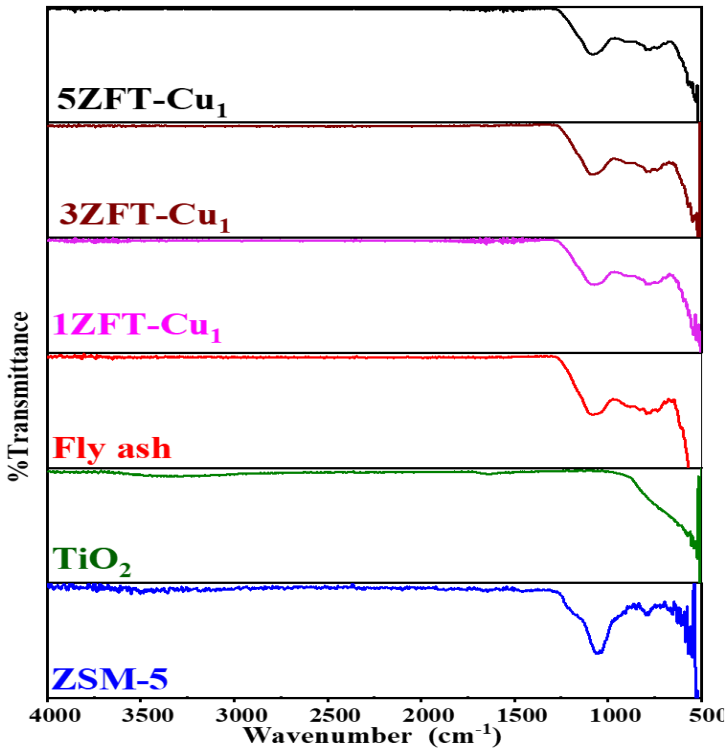


**Fig. 4.5** FTIR spectra of $TiO_2$, fly ash, ZSM-5, and ZSM-5-loaded Fly ash-$TiO_2$-Cu composites

(1ZFT-$Cu_1$, 3ZFT-$Cu_1$, 5ZFT-$Cu_1$)

### 4.3.5 BET Surface Area and Pore Size Distribution

**Fig. 4.6 (a, b)** displays the results of the $N_2$ adsorption-desorption experiments conducted on FT, FT-$Cu_1$, and 3ZFT-$Cu_1$ composites using BJH plots for the purpose of evaluating the surface area and pore distribution. Type IV isotherms confirm the existence of mesopores with multilayer adsorption and $H_3$ hysteresis loops, which are seen in all composites. As compared to FT and FT-$Cu_1$, 3ZFT-$Cu_1$ achieves the highest nitrogen adsorption quantity. After ZSM-5 modification, FT-$Cu_1$ exhibits a greater surface area. The study of the BJH pore distribution, derived from the desorption branch of the nitrogen adsorption–desorption isotherms, indicated a more homogeneous mesoporous structure, with a sharp and narrow peak between 4 and 6 nm and a total pore diameter range of 2 to 10 nm. The enhanced adsorption of dye molecules and the greater mass movement during photocatalytic degradation are two potential advantages of the larger pores and more surface features. Our results show that adding ZSM-5 to FT-$Cu_1$ composites improves their photocatalytic effectiveness when exposed to visible and solar light [38] **Table 4.1** shows the specific surface area, pore diameter, and pore volume data for each sample.

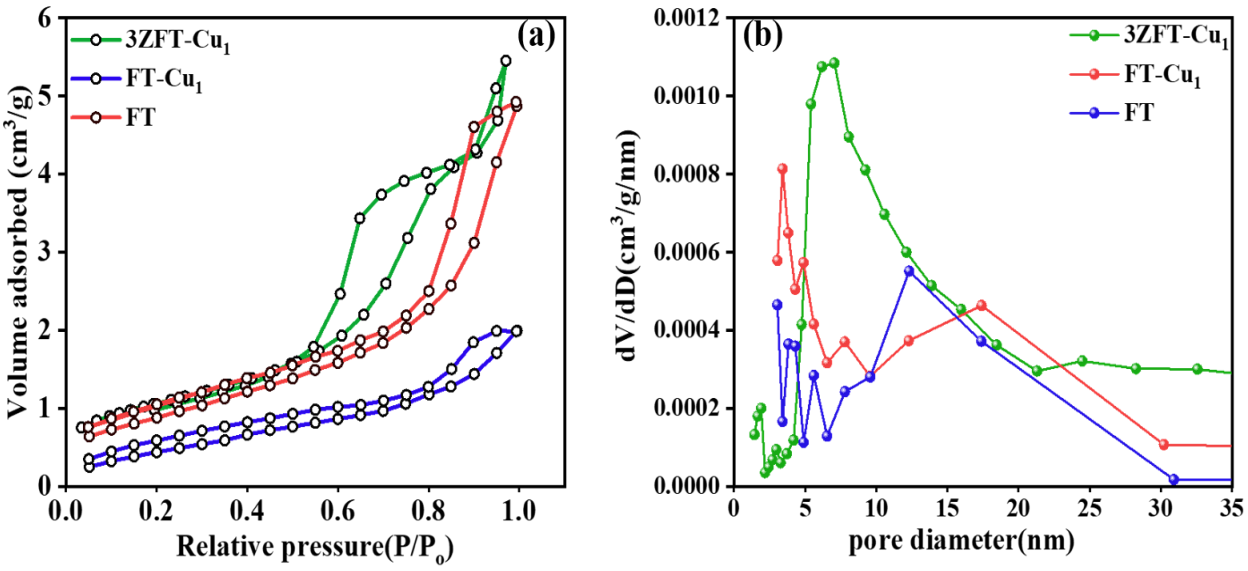


**Fig. 4.6**. (a) Nitrogen sorption isotherms and (b) Barrett–Joyner–Halenda (BJH) plot of various (FT, FT-$Cu_1$ and 3ZFT-$Cu_1$) composites.

**Table 4.1.** Pore volume, surface area and pore diameter of $TiO_2$, fly ash, FT, and FT-$Cu_1$, 3ZFT-$Cu_1$ and ZSM-5 composites.

| Photocatalyst | BET surface area ($m^2/g$) | Pore volume ($cm^3/g$) | Pore diameter (nm) |
|---|---|---|---|
| $TiO_2$ | 99.703 | 0.195 | 12.309 |
| Fly ash | 1.347 | 0.003 | 3.054 |
| FT | 3.268 | 0.007 | 3.411 |
| FT-$Cu_1$ | 6.725 | 0.010 | 8.712 |
| 3ZFT-$Cu_1$ | 10.562 | 0.012 | 11.552 |
| ZSM-5 | 24.600 | 0.169 | 23.740 |

### 4.3.6 DRS analysis

Diffuse reflectance spectra (DRS) obtained via UV-vis spectroscopy of $TiO_2$, FT, FT-$Cu_1$, and 3ZFT-$Cu_1$ composites are presented in **Fig. 4.7**. The corresponding Tauc plots of $TiO_2$, FT, and FT-$Cu_1$ are shown in **Fig. 4.8(a).** At the same time, **Fig. 4.8(b)** illustrates the Tauc plots of composites containing different ZSM-5 loadings (1–5wt%). Unique absorption peaks can be observed below 400 nm in the DRS spectra. The observed peaks signify the transitions of electrons from $O^{2-}$ (2p) orbitals in the valence band to $Ti^{3+}$(3d) orbitals in the conduction band. Enhanced UV absorption and a red shift in the FT composite are likely due to the formation of Si–O–Ti bonds between $TiO_2$ and the fly ash surface [39]. The photocatalytic effectiveness of the Cu-loaded $TiO_2$-fly ash composite is enhanced because the addition of Cu induces localized energy levels and heterojunctions, which in turn decrease the bandgap and move the absorption edge to the visible area [26]. The 3ZFT-$Cu_1$ composite, although showing improved light absorption compared to the bare FT composite, exhibits a relatively smaller red shift than the Cu-loaded FT composites as determined from the Tauc plot analysis. The data suggest that although the integration of ZSM-5 improves light absorption and promotes charge separation due to its elevated porosity and surface acidity, its effect on bandgap reduction is rather minimal. Thus, the modulation of the bandgap is mostly dictated by copper modification, whereas ZSM-5 has little effect on the electronic transition characteristics [40]. The bandgap energies of the synthesized composites were evaluated using Tauc's method, defined by the following equation (4):

$$\alpha h\nu = A(h\nu - E_g)^n \quad (12)$$

In the Tauc equation, α signifies the optical absorption coefficient, hν refers to the photon energy, A is a proportionality constant, and Eg signifies the optical bandgap energy. The exponent n characterizes the electronic transition, where n = 0.5 corresponds to a direct allowed transition and n = 2 to an indirect allowed transition. Eg values were estimated by projecting the linear section of the $(\alpha h\nu)^2$ versus hν curve onto the photon energy axis, with the intercept on the x-axis indicating the bandgap. The estimated bandgap ($E_g$) values were estimated to be 2.3 eV for 3ZFT-$Cu_1$, 2.2 eV for FT-$Cu_1$, 3.12 eV for pristine $TiO_2$, 2.55 eV for the FT composite, 2.36 eV for 5ZFT-$Cu_1$, and 2.48 eV for 1ZFT-$Cu_1$, as shown in **Fig. 4.8 (a, b)**

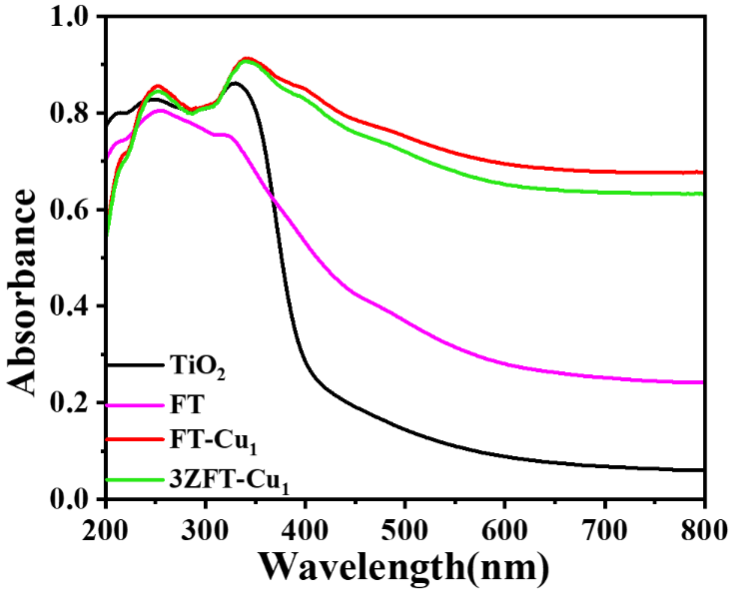


**Fig. 4.7** UV-Vis diffuse reflectance spectra of $TiO_2$, FT, FT-$Cu_1$ and 3ZFT-$Cu_1$ samples

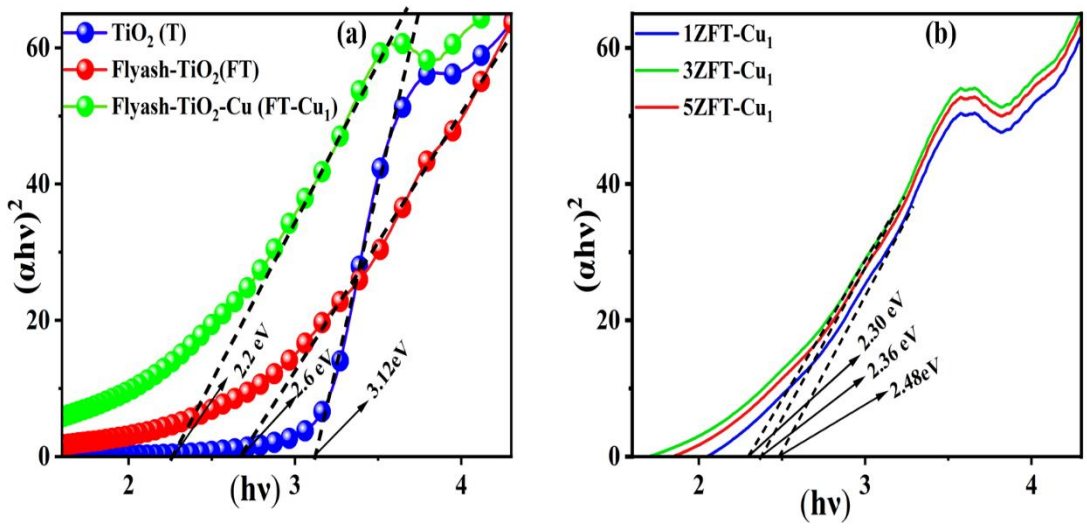


**Fig. 4.8** (a) Optical bandgap estimation using Tauc plots for $TiO_2$, FT and FT-$Cu_1$ (b) for 1ZFT-$Cu_1$, 3ZFT-$Cu_1$ and 5ZFT-$Cu_1$ composites.

## 4.4 Adsorption study

### 4.4.1 Influence of adsorbent dosage on CV dye removal

**Fig. 4.9(a)** demonstrates the impact of adsorbent dosage on the removal of CV dyes. It is seen that the % removal of CV dye increases with the increase of adsorbent dose of all the composites, including FT, FT-$Cu_1$, and ZSM-5 integrated composites (1ZFT-$Cu_1$, 3ZFT-$Cu_1$, and 5ZFT-$Cu_1$). This is due to the increased availability of surface-active sites, allowing the dye molecules to interact more efficiently with the adsorbent surface. Among the composites, the 3ZFT-$Cu_1$ composite exhibited the highest removal efficiency of 71% followed by 5ZFT-$Cu_1$ (66%), 1ZFT-$Cu_1$ (61%), FT-$Cu_1$ (55%), and FT (49%) at a 5 mg dose. Composites loaded with ZSM-5 have superior performance compared to those without because of the synergistic interaction between copper and zeolite, which enables efficient dye absorption through the mesoporous nature of zeolite and its enhanced surface area. However, the % removal of CV for all samples decreased when the dose was increased from 5 mg to 10 mg. This is likely because of agglomeration at higher dosages and potential interaction among active sites. The results indicate that 5 mg is the optimal dose for removing CV dye.

### 4.4.2 Role of initial dye concentration on the removal of CV dye

The impact of initial pollutant concentration on crystal violet dye removal was investigated

using several modified composites, including FT, FT-$Cu_1$, 1ZFT-$Cu_1$, 3ZFT-$Cu_1$, and 5ZFT-$Cu_1$. **Fig. 4.9(b)** shows that with the increase in dye concentration from 3mg/L to 15 mg/L, a gradual decline in % removal of CV dye was observed. 3ZFT-$Cu_1$ exhibited the highest removal of 71% CV dye at 5mg/L concentration, indicating enhanced active sites availability and synergistic effects due to optimal ZSM-5 loading. In contrast, the FT composite demonstrated the lowest removal efficiency of 49%, highlighting the role of surface modification in improving adsorption performance. As dye concentration rises, the reduction in efficiency may result from the saturation of active adsorption sites, leading to insufficient surface area to accommodate the additional dye molecules.

### 4.4.3 Impact of contact duration on the removal of CV dye

The effect of contact duration on the removal of CV dye over all the composites is shown in **Fig. 4.9(c).** Initially, the CV removal efficiency increased with increasing contact time due to the availability of a large number of vacant active sites on the adsorbent surface, which promoted rapid adsorption of dye molecules. The maximum removal was achieved at 180 min, indicating optimum interaction between the dye molecules and the active sites of the composites. Beyond this contact duration, the removal efficiency slightly decreased, which may be due to the saturation of active sites and the establishment of adsorption–desorption equilibrium. At prolonged contact time, some weakly adsorbed CV molecules may desorb back into the solution, leading to a slight reduction in overall removal efficiency. The combined benefits of porous ZSM-5 and copper-mediated composite (3ZFT-$Cu_1$) enabled the most effective and quick dye adsorption at 180 minutes, removing 71% of the CV dye. Beyond 180 minutes, the removal efficiency plateaued or slightly declined, indicating that equilibrium had been attained and active sites were saturated.

### 4.4.4 The effect of solution pH on CV dye removal

The overall adsorption efficiency is affected by solution pH, which is a major factor determining the adsorbent surface charge and ionization behavior of the dye. The adsorption occurred at ambient temperature using 5 mg of the 3ZFT-$Cu_1$ composite, with a dye concentration of 5 ppm and a contact time of 180 minutes. The pH of the solution was altered from 2 to 12 using 0.1 M HCl and 0.1 M NaOH. **Fig. 4.9(d)** illustrates the influence of pH on the elimination of crystal violet (CV) dye throughout a pH range from 2 to 12. The result shows that with a rise in solution pH, CV removal increases up to pH 9, followed by a decline at higher

pH levels. Among all the composites, 3ZFT-$Cu_1$ showed the highest removal efficiency, reaching over 70% at pH 9, indicating a synergistic effect of ZSM-5 and copper incorporation. The removal order at the optimum pH was 3ZFT-$Cu_1$ > 5ZFT-$Cu_1$ > 1ZFT-$Cu_1$ > FT-$Cu_1$ > FT. The superior performance of ZFT-$Cu_1$ composites is ascribed to the increased surface area, active sites, and charge interactions with dye molecules. The point of zero charge ($pH_{pzc}$) of the 3ZFT-$Cu_1$ composite was quantified to be around 7.4. When exposed to acidic circumstances (pH < 7.4), the surface of the composite undergoes protonation, becoming positively charged. The positive charge of the cationic CV dye molecules induces electrostatic repulsion with the adsorbent surface, hence reducing the quantity of dye that may be adsorbed. Conversely, at alkaline pH values (pH > 7.4), the surface of the 3ZFT-$Cu_1$ composite acquires a negative charge as a result of deprotonation. Although CV dye remains cationic across a broad pH range, the electrostatic attraction between the negatively charged adsorbent and the positively charged dye molecules becomes more favourable, enhancing adsorption.

The enhanced electrostatic interaction between the negatively charged 3ZFT-$Cu_1$ surface and the cationic CV dye accounts for the optimal dye removal at pH 9. Additionally, hydrogen bonding and π–π interactions between CV aromatic rings and the adsorbent surface might boost adsorption effectiveness at this pH level. Adsorption of CV dye decreases at pH levels over 9, probably due to greater competition with $OH^-$ ions and partial neutralization of dye molecules, lowering electrostatic attraction.

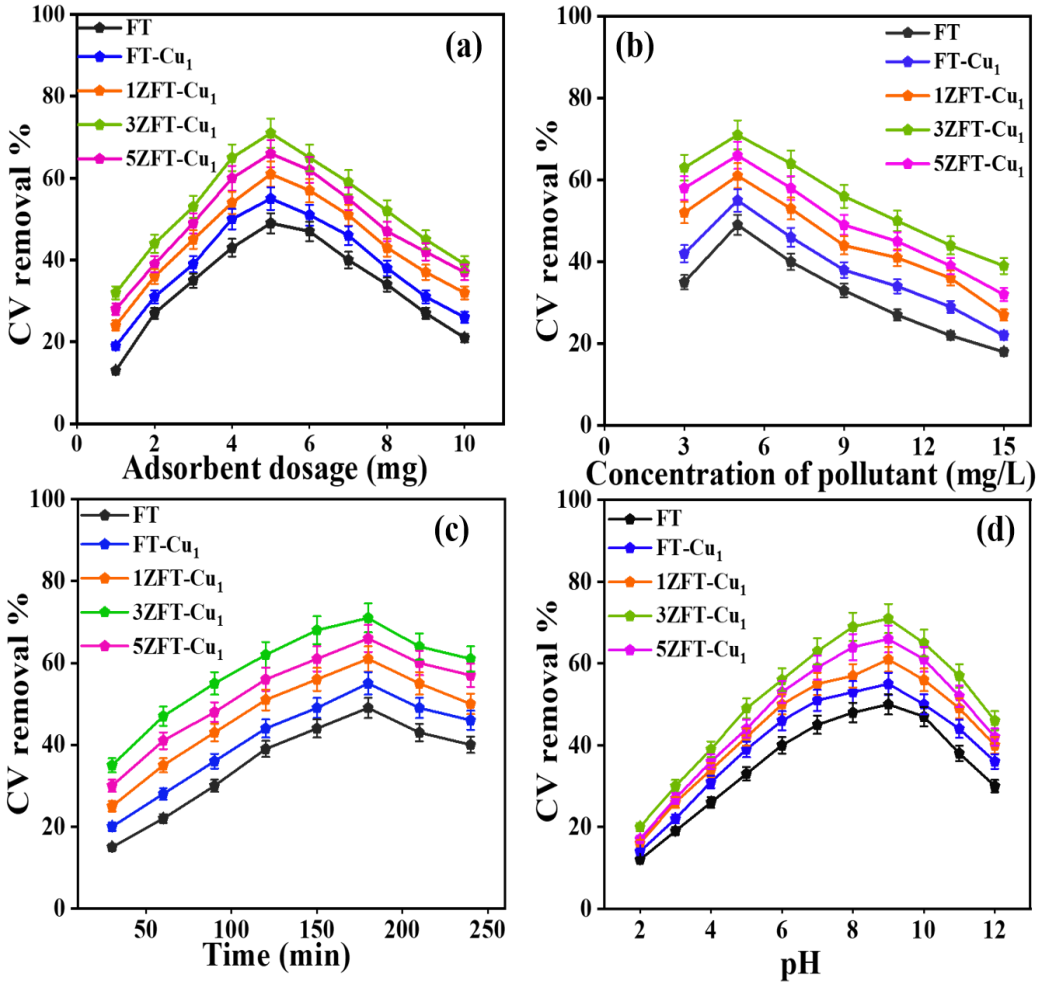


**Fig. 4.9** Plots illustrating the impact of (a) adsorbent dose, (0.005 g/L), (b) adsorbate concentration, (5mg/L), (c) the contact time, (time 180 min) and (d) Effect of solution pH on removal of CV dye by FT, FT-$Cu_1$, 1ZFT-$Cu_1$, 3ZFT-$Cu_1$ and 5ZFT-$Cu_1$composites.

### 4.4.5 Adsorption isotherm studies

The adsorption of crystal violet (CV) onto FT-$Cu_1$ and ZFT-$Cu_1$ composites was analyzed using Langmuir, Freundlich, Temkin, and Dubinin–Radushkevich (D–R) isotherms. The initial fitting of the data was conducted utilizing the Langmuir isotherm model, as outlined in equation (4). This model suggests that adsorption takes place via the establishment of a monolayer over ZSM-Cu-flysh-$TiO_2$ composite, wherein each molecule occupies a unique adsorption site on the surface. The graph of $1/Q_e$ vs. $1/C_e$ is shown in **Fig. 4.10(a)**. The intercept and slope of this curve determine $K_L$ and $Q_{max}$.

Adsorption on heterogeneous surfaces is described by the Freundlich isotherm shown in

equation (5), where the adsorption energy varies across locations. It takes surface heterogeneity into account, which in turn considers multilayer adsorption and interactions between adsorbed molecules. Here, 1/n is the heterogeneity factor, which is related to adsorption intensity, and $K_F$ is the Freundlich constant, which stands for adsorption capacity [41]. The plot of log $Q_e$ vs log $C_e$ may be seen in **Fig. 4.10(b).** The results indicate that for the 3ZFT-$Cu_1$ composite, the Freundlich isotherm best described the adsorption process, with a correlation coefficient $R^2$= 0.997, compared to $R^2$ = 0.982 for the Langmuir model. This suggests that the adsorption occurs predominantly on heterogeneous surfaces rather than through ideal monolayer formation.

According to the Temkin isotherm presented in equation (6), it is suggested that the heat of adsorption diminishes as the number of interactions between the adsorbate and adsorbent increases **(Fig. 4.10(c)).** The heat of adsorption, represented by BT, is calculated using the equation BT = RT / β, where β signifies the maximum binding energy. The value of β was found to be 8.55 kJ/mol, suggesting a physisorption process [42].

The Dubinin–Radushkevich (D–R) isotherm model in equation (7), illustrated in **Fig. 4.10(d),** serves as a prevalent tool for differentiating between the mechanisms of physical and chemical adsorption. The adsorption of crystal violet onto ZFT-$Cu_1$ composites yielded low values for the constant β ($mol^{-2}$ $kJ^2$), resulting in mean free energy values ranging from 0.705 to 1.120 kJ $mol^{-1}$ [43]. The evidence indicates that the adsorption process is primarily governed by physisorption. The specifications for the models, as mentioned above, are presented in **Table 4.2**. Although nonlinear fitting is generally recommended for adsorption and kinetic modelling, linear models were employed in this study for consistency and comparability with previous literature. Overall, the analysis demonstrates that ZSM-5 loading improves adsorption efficiency by offering more active sites and promoting interactions between the dye molecules and the composite surface.

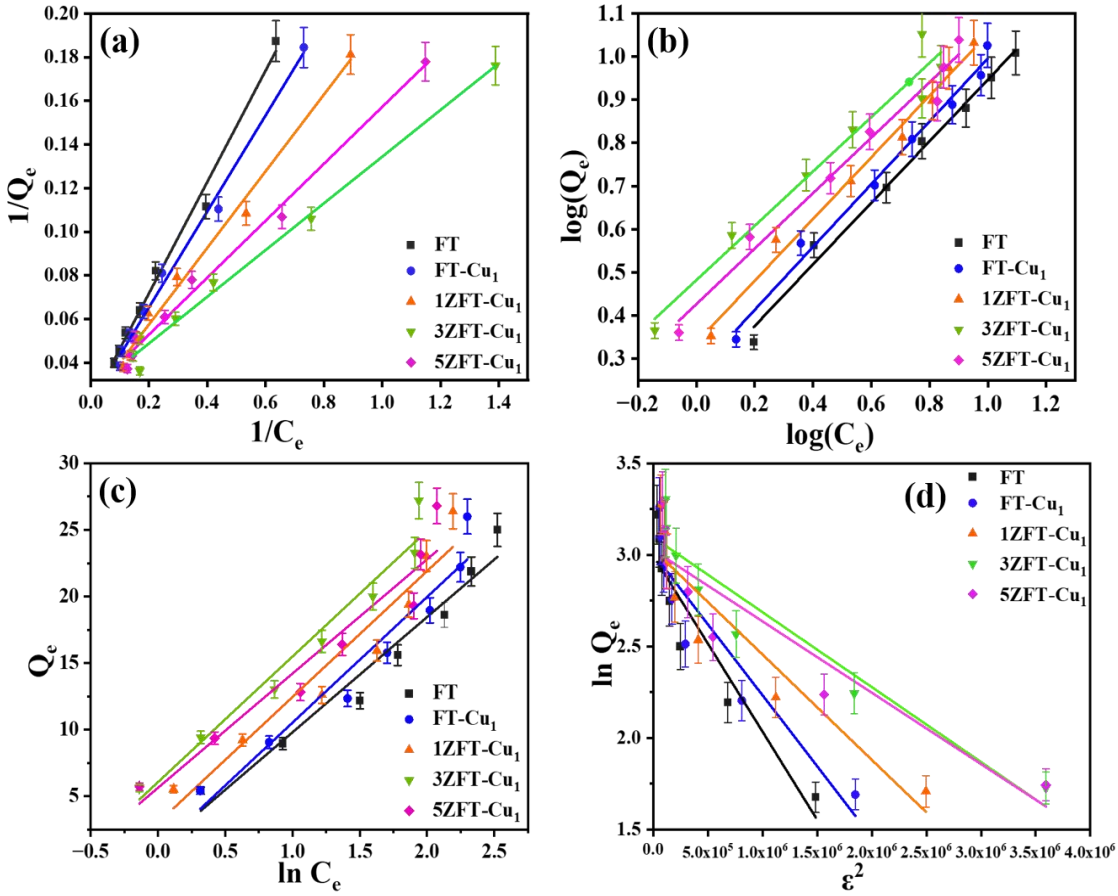


**Fig. 4.10** Linear fitting of adsorption isotherm plots for CV dye adsorption over FT, FT-$Cu_1$, 1ZFT-$Cu_1$, 3ZFT-$Cu_1$, and 5ZFT-$Cu_1$ composites using (a) Langmuir adsorption isotherm, (b) Freundlich adsorption isotherm, (c) Temkin adsorption isotherm, and (d) Dubinin-Radushkevich adsorption isotherm model.

**Table 4.2.** Isotherm parameter of Langmuir, Freundlich, Temkin and D-R models for adsorption of crystal violet dye by FT and different wt.% ZFT-$Cu_1$ composites.

| | **Langmuir isotherm** | | | **Freundlich isotherm** | | |
|---|---|---|---|---|---|---|
| **Adsorbent** | **$Q_{max}$(mg/g)** | **$K_L$** | **$R^2$** | **$K_F$** | **1/n** | **$R^2$** |
| FT | 34.480 | 0.003 | 0.995 | 1.774 | 1.436 | 0.993 |
| 1ZFT-$Cu_1$ | 42.190 | 0.006 | 0.990 | 2.329 | 1.478 | 0.992 |
| 3ZFT-$Cu_1$ | 50.000 | 0.020 | 0.983 | 3.064 | 1.587 | 0.997 |
| 5ZFT-$Cu_1$ | 43.290 | 0.005 | 0.988 | 2.802 | 1.628 | 0.983 |

| | Temkin isotherm | | | D-R isotherm | | |
|---|---|---|---|---|---|---|
| **Adsorbent** | **B (KJ mol$^{-1}$)** | **A (Lmg$^{-1}$)** | **$R^2$** | **β× $10^{-8}$ (mol$^{-2}$ kJ$^2$)** | **E** | **$R^2$** |
| FT | 0.011 | 0.714 | 0.958 | 0.010 | 0.705 | 0.889 |
| FT-$Cu_1$ | 0.009 | 1.159 | 0.934 | 0.008 | 0.791 | 0.870 |
| 1ZFT-$Cu_1$ | 0.009 | 1.561 | 0.922 | 0.006 | 0.913 | 0.871 |
| 3ZFT-$Cu_1$ | 0.009 | 2.362 | 0.944 | 0.004 | 1.120 | 0.915 |
| 5ZFT-$Cu_1$ | 0.008 | 2.138 | 0.917 | 0.004 | 1.120 | 0.865 |

### 4.4.6 Adsorption Kinetics study

The experimental kinetic data **(Fig. 4.11)** were analysed using several models, including pseudo-first-order, pseudo-second-order, Elovich and intraparticle diffusion. As shown in **Fig. 4.11(a)**, the pseudo-first-order model (Eq. 9; log (Qe–Qt) vs. t) gave an excellent fit for the adsorption of CV dye on 3ZFT-$Cu_1$, with an $R^2$ value of 0.9945 and a rate constant of 0.0225 $min^{-1}$. In comparison, the pseudo-second-order model (Eq. 10; **Fig. 4.11(b)**) yielded an $R^2$ of 0.9725 and a rate constant of 0.0004 $min^{-1}$. These results indicate that the adsorption of CV dye onto FT-$Cu_1$ and ZFT-$Cu_1$ composites follows predominantly pseudo-first-order kinetics, suggesting that physisorption is the main adsorption mechanism under the studied conditions. The calculated equilibrium capacities ($Q_e$), rate constants ($k_1$ and $k_2$) and $R^2$ values for all samples are already summarized in Table 2, which clearly shows the superiority of the pseudo-first-order model over the pseudo-second-order model for these systems.

As shown in **Fig. 4.11(c)** of the Elovich model in equation (11), the adsorbate appears to be removed from solution using chemisorption onto a surface that contains energetically different active sites [44]. The β values ranged from 0.217 to 0.240 g $mg^{-1}$, which are relatively low and suggest that the adsorption mechanism is primarily controlled by physisorption rather than chemisorption. Furthermore, although the Elovich model provided a reasonably good fit ($R^2$ = 0.8868–0.9844), the pseudo-first-order model exhibited higher correlation coefficients ($R^2$ = 0.8968-0.9962), indicating it more accurately described the adsorption kinetics and thus followed the physisorption process.

**Fig. 4.11(d)** displays the intra-particle diffusion model equation (12) plots for all the composites, including FT, FT-$Cu_1$, and ZFT-$Cu_1$ (1ZFT, 3ZFT, and 5ZFT). The fact that $Q_t$ and $t_{1/2}$ are linear in all samples suggests that intraparticle diffusion plays a substantial role in adsorption [44]. Intraparticle diffusion is not the only step that determines the rate because the

plots do not go through the origin. The 3ZFT-$Cu_1$ composite showed the steepest slope and highest intercepts in the figure, meaning that the surface improvements allowed for an increase in intraparticle diffusion capacity; **Table 4.3** shows the values correlating to the various kinetic models. In this study, linear models were used to maintain consistency with prior literature, despite the general recommendation of nonlinear fitting for adsorption and kinetic modelling. These results collectively highlight that the synergistic incorporation of ZSM-5 and copper enhances both adsorption capacity and adsorption kinetics of the fly ash–$TiO_2$ composites.

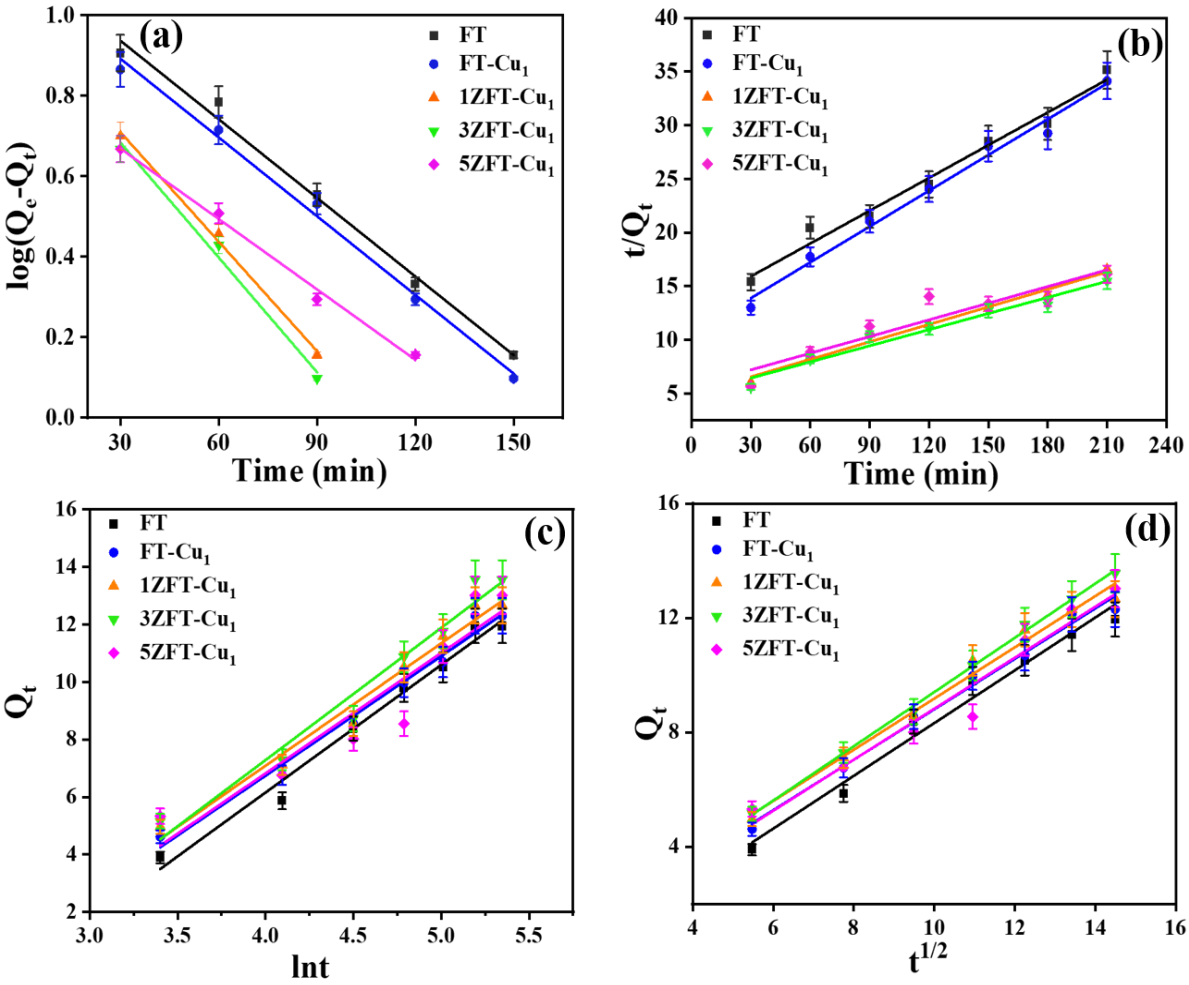


**Fig. 4.11** Linear fitted plots of kinetic models for CV dye adsorption over FT, FT-$Cu_1$, 1ZFT-$Cu_1$, 3ZFT-$Cu_1$, and 5ZFT-$Cu_1$ composites using (a) Pseudo-first-order kinetic model, (b) Pseudo-second-order kinetic model, (c) Elovich kinetic model and (d) Intra-particle diffusion kinetic model.

**Table 4.3** Kinetic parameter of Pseudo-first-order, Pseudo-second-order, Elovich and Intra-particle models for adsorption of crystal violet dye by FT and different wt.% ZFT-$Cu_1$ composites.

| | **Pseudo-first-order** | | | **Pseudo-second-order** | | |
|---|---|---|---|---|---|---|
| **Adsorbent** | **$Q_e$ (mg/g)** | **$k_1$ ($min^{-1}$)** | **$R^2$** | **$Q_e$ (mg/g)** | **$k_2$ ($min^{-1}$)** | **$R^2$** |
| FT-$Cu_1$ | 17.621 | 0.015 | 0.994 | 8.993 | 0.002 | 0.988 |
| 1ZFT-$Cu_1$ | 19.567 | 0.021 | 0.996 | 18.420 | 0.001 | 0.985 |
| 3ZFT-$Cu_1$ | 27.003 | 0.023 | 0.995 | 20.240 | 0.000 | 0.973 |
| 5ZFT-$Cu_1$ | 20.678 | 0.021 | 0.897 | 19.300 | 0.000 | 0.876 |

| | **Elovich model** | | | **Intra-particle diffusion model** | | |
|---|---|---|---|---|---|---|
| **Adsorbent** | **α (mg $g^{-1}$ $min^{-1}$)** | **β (g $mg^{-1}$)** | **$R^2$** | **$K_{ip}$** | **C (mg $g^{-1}$)** | **$R^2$** |
| FT | 0.325 | 0.225 | 0.983 | 0.923 | -0.902 | 0.979 |
| FT-$Cu_1$ | 0.385 | 0.240 | 0.984 | 0.882 | -0.017 | 0.990 |
| 1ZFT-$Cu_1$ | 0.412 | 0.235 | 0.979 | 0.896 | 0.220 | 0.985 |
| 3ZFT-$Cu_1$ | 0.313 | 0.235 | 0.968 | 0.948 | 0.071 | 0.998 |
| 5ZFT-$Cu_1$ | 0.391 | 0.239 | 0.887 | 0.892 | 0.096 | 0.959 |

## 4.5 Photocatalytic studies

### 4.5.1 Photocatalytic efficacy under visible light irradiation

Photocatalytic degradation of crystal violet (CV) dye under visible light using a Wipro Garnet B22 50-Watt LED bulb equipped with a cut-off filter (wavelength > 360 nm) by ZFT-$Cu_1$ composites containing ZSM at various weight percentages (1, 3, and 5wt%) is illustrated in **Fig. 4.12. Fig. 4.12(a)** displays the UV-vis absorption spectra of CV dye (5 ppm) with the 3ZFT-$Cu_1$ composite at different irradiation periods (60-240 minutes), showing a maximum absorption peak at 589 nm. The visual evidence shows that 98% of the CV dye has been removed, and the decomposition of the dye has been noticeable, with a noticeable shift from a violet to a colourless dye solution, and a significant decrease in the distinctive absorption peak at 589 nm. In **Fig. 4.12(b)**, after being exposed for 180 minutes under visible light. ZSM-5-fly ash-$TiO_2$-Cu composites (1ZFT-$Cu_1$, 3ZFT-$Cu_1$, and 5ZFT-$Cu_1$) are compared to FT and FT-$Cu_1$ in terms of their photocatalytic activity. The 3ZFT-$Cu_1$ composite has the best degradation

efficiency, with the largest drop in absorbance, compared to the other materials.

**Fig. 4.12(c)** displays concentration profiles ($C/C_0$) that change over time; this data sheds information on the degradation kinetics in both dark and visible light. Under illumination, the 3ZFT-$Cu_1$ catalyst demonstrates a steep drop in CV concentration. **Fig. 4.12(d)** shows the results of the kinetic analysis, which provide a pseudo-first-order model in equation (13) for the degradation process. This model is mainly controlled by the concentration of CV dye and is defined by the following equation:

$$\ln (C_o/C_t) = kt. \quad (13)$$

$C_0$ is the CV dye concentration at 0 minutes, $C_t$ is the concentration at time t, and k is the rate constant. This indicates the breakdown rate remains unchanged regardless of variations in the content of water or oxygen [45]. When the light intensity and amount of photocatalyst are held constant, the rate changes are considered insignificant. According to the rate constant obtained from the linear plots, 3ZFT-$Cu_1$ has the highest rate constant ($k = 0.0054\ min^{-1}$), which is greater than the FT composite ($k = 0.0013\ min^{-1}$) shown in **Table 4.4.** suggesting that the combination of Cu doping, ZSM-5, and fly ash has a synergistic effect that improves charge separation and light absorption.

**Table 4.4.** Kinetic parameter of pseudo pseudo-first-order model of different wt.% ZFT-$Cu_1$ composites under visible and under sunlight.

| | **Pseudo-first-order (visible light)** | | **Pseudo-first-order(sunlight)** | |
|---|---|---|---|---|
| **Photocatalyst** | **$k_1$** | **$R^2$** | **$k_1$** | **$R^2$** |
| FT | 0.0013 | 0.9927 | 0.0012 | 0.9943 |
| FT-$Cu_1$ | 0.0015 | 0.9948 | 0.0014 | 0.9915 |
| 1ZFT-$Cu_1$ | 0.0019 | 0.9907 | 0.0019 | 0.9926 |
| 3ZFT-$Cu_1$ | 0.0054 | 0.9950 | 0.0044 | 0.9980 |
| 5ZFT-$Cu_1$ | 0.0024 | 0.9938 | 0.0023 | 0.9952 |

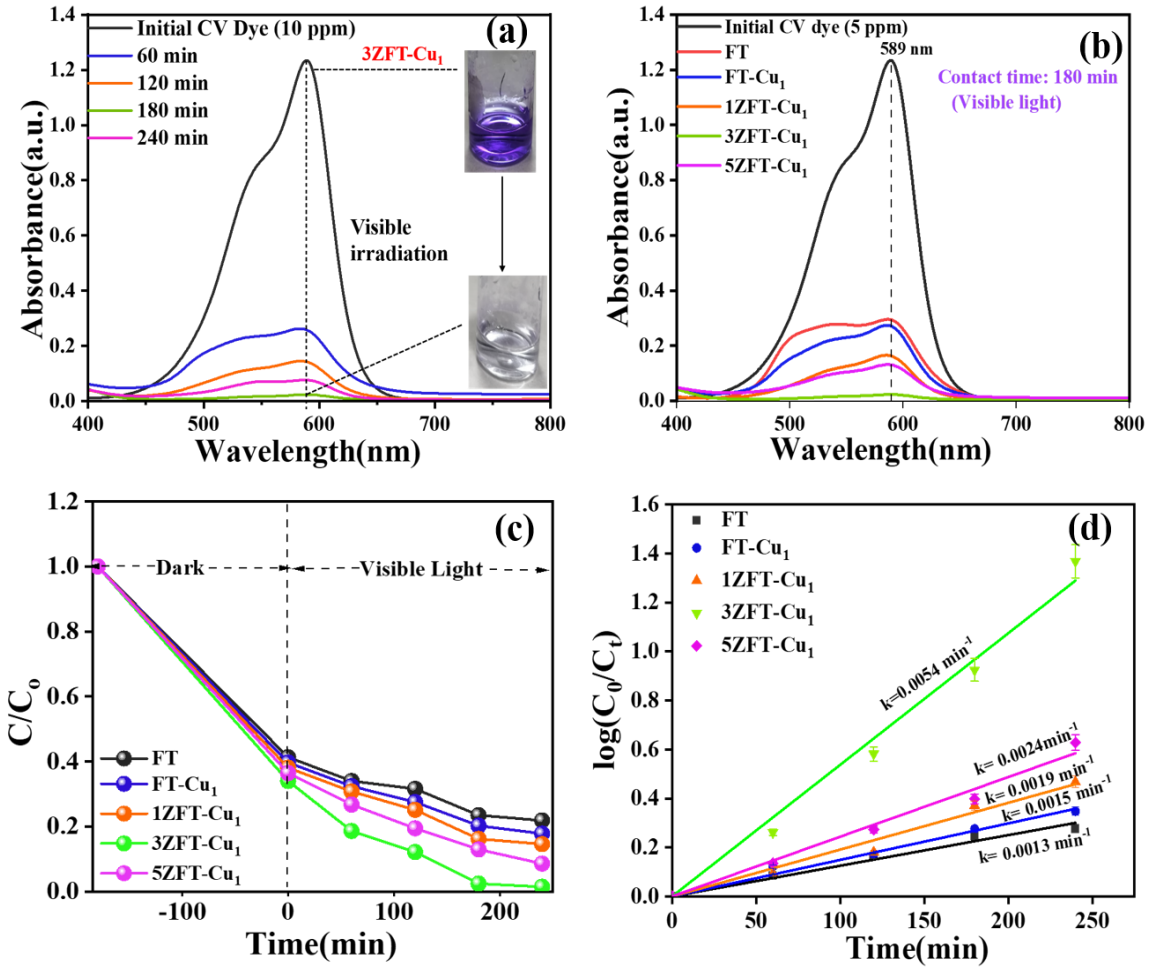


**Fig. 4.12** (a) Absorption spectra and visual colour changes of CV dye during photocatalytic degradation under visible light by 3ZFT-$Cu_1$ composite over different time periods (b) Absorption spectra of CV dye after 180 min of visible light by different wt% ZFT-$Cu_1$ composites, (c) time dependent kinetic plots (d) Pseudo first-order kinetic fitting illustrating the degradation efficiency by various composites under visible light irradiation.

### 4.5.2 Photocatalytic degradation under direct sunlight

The photocatalytic performance of ZFT-$Cu_1$ composites was thoroughly investigated under natural sunlight for the degradation of crystal violet (CV) dye. The experiments were conducted on 20 May 2025 in Patiala, Punjab, wherein 5 mg of each composite was dispersed in 10 mL of 5 ppm CV dye solution and exposed to sunlight for 180 minutes under constant magnetic stirring. The solar light intensity during the process averaged 620 W/m², and the ambient temperature remained between 34 and 38°C.

As depicted in **Fig. 4.13(a),** the time-dependent absorption spectra and corresponding visual

colour changes of the dye solution indicate the gradual photodegradation of CV dye by the 3ZFT-$Cu_1$ composite. The intense violet colour of the dye faded significantly with increasing irradiation time, eventually turning nearly colourless after 180 minutes, suggesting substantial breakdown of the dye molecules. **Fig. 4.13(b)** compares the photocatalytic performance of ZFT-$Cu_1$ composites with different ZSM-5 loadings. The composite with 3wt% ZSM-5 loading (3ZFT-$Cu_1$) demonstrated the highest photocatalytic efficiency, achieving around 95% degradation of CV dye when subjected to solar irradiation. The improvement is due to the combined effects of Cu doping and ZSM-5 incorporation, which enhance surface area, dye adsorption, and charge carrier mobility.

The degradation kinetics are further elaborated in **Fig. 4.13(c),** which shows the time course plots of dye concentration over 180 minutes. The 3ZFT-$Cu_1$ composite demonstrated the steepest decline, indicating the most rapid degradation rate among all tested samples. The kinetic behaviour of the composites follows a pseudo-first-order model, as shown in **Fig. 4.13(d)**. The calculated rate constant for 3ZFT-$Cu_1$ was found to be 0.0044 $min^{-1}$, notably higher than other composites, underscoring its excellent photocatalytic performance under solar light. The pseudo-first-order kinetic constants, along with the corresponding $R^2$ values for FT and ZFT-$Cu_1$ composites under visible and solar light irradiation, are presented in Table 3. These findings support that the 3ZFT-$Cu_1$ composite is a highly efficient photocatalyst for the solar-assisted degradation of crystal violet dye and holds strong potential for application in sustainable wastewater treatment technologies**.**

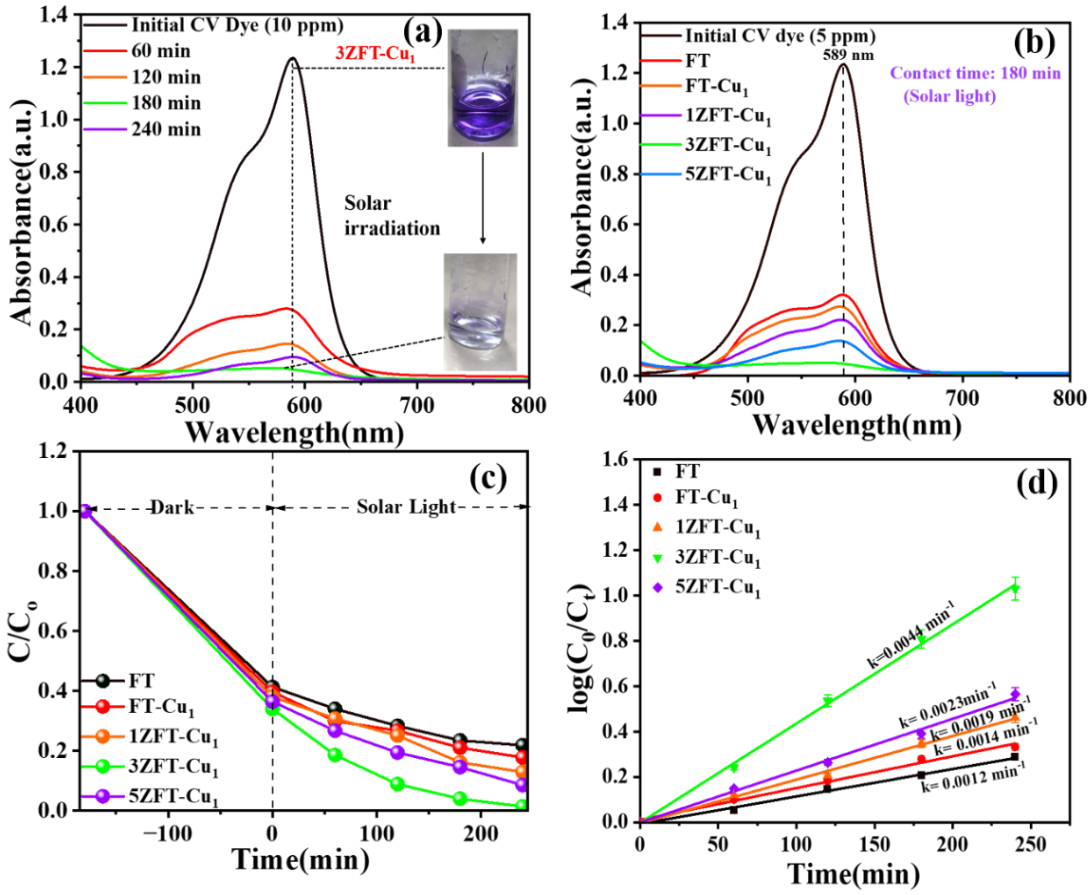


**Fig. 4.13** (a) Absorption spectra and visual colour changes of CV dye during photocatalytic degradation under solar light by 3ZFT-$Cu_1$ composite over different time periods and (b) Absorption spectra of CV dye after 180 min of solar light by different wt% ZFT-$Cu_1$ composites, (c) time dependent kinetic plots (d) Pseudo first-order kinetic fitting illustrating the degradation efficiency by various composites under solar light irradiation.

## 4.6 Detection of active species

The experiment aimed to determine the main reactive species involved in the degradation process. **Fig. 4.14(a)** shows the function of different scavengers in the photocatalytic degradation of crystal violet (CV) dye using the 3ZFT-$Cu_1$ composite. The degradation efficiency reached a peak of 98% without any scavenger, demonstrating the exceptional photocatalytic activity of the composites used. The introduction of EDTA, recognized as a hole ($h^+$) scavenger, reduced degradation efficiency to 19%, indicating that photogenerated holes

are vital to the degradation mechanism. Similarly, the introduction of argon (Ar), which removes dissolved oxygen and consequently suppresses the formation of superoxide radicals ($O_2$-) [46], resulted in a 20% degradation rate, indicating the involvement of superoxide radicals.

The presence of ammonium thiocyanate ($NH_4SCN$), an electron scavenger, resulted in a degradation efficiency of 15%, underscoring the role of electrons in the redox reactions. Adding ethanol and isopropanol, functioning as hydroxyl radical (.OH) scavengers, resulted in 22% and 21% degradation efficiencies, respectively. This signifies that hydroxyl radicals significantly contribute to the breakdown process. The significant decrease in photocatalytic performance with the introduction of each scavenger indicates that various reactive species, such as holes, electrons, superoxide radicals, and hydroxyl radicals, play a role in the degradation mechanism of CV dye removal by the 3ZFT-$Cu_1$ composites under visible light.

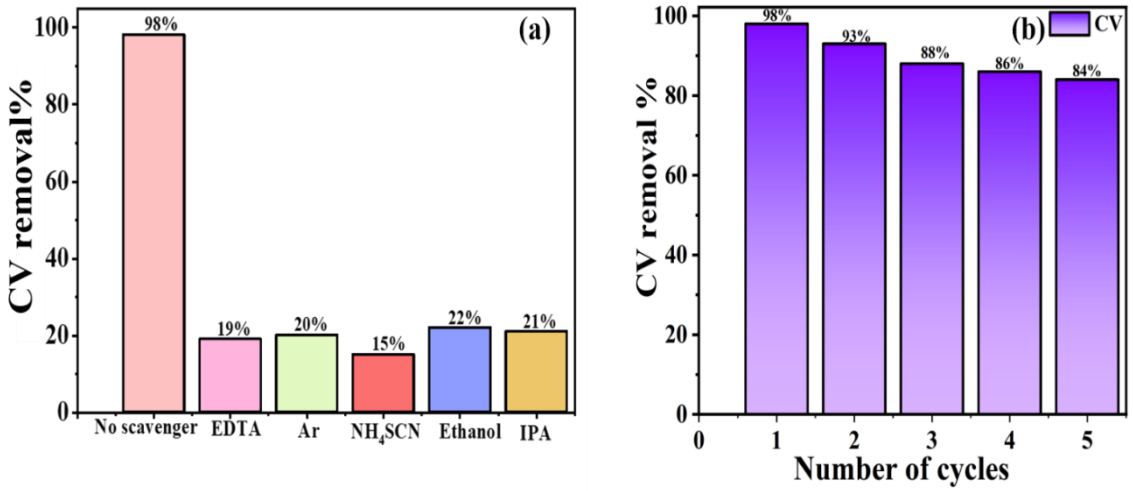


**Fig. 4.14.** (a) Effect of different hole scavengers on the photocatalytic degradation efficiency of FB dye using the 3ZFT-$Cu_1$ composite, (b) Reusability performance of the 3ZFT-$Cu_1$ composite over multiple photocatalytic cycles under visible light irradiation.

### 4.7 Proposed photocatalytic degradation mechanism

As shown in **Scheme 4.1**, the photocatalytic degradation of crystal violet (CV) dye using a ZSM-5-loaded-flyash-$TiO_2$-Cu (ZFT-$Cu_1$) composite occurs through a combined process of adsorption, charge separation, and reactive species production when exposed to visible or solar light. The extensive surface area and porous structure of ZSM-5 facilitate the adsorption of CV molecules onto the catalytic surface, increasing the dye concentration at the active sites. In

addition, the interconnected micropores of ZSM-5 also provide pathways for charge migration, enhancing charge separation efficiency. Exposure to visible light induces Cu doping, hence decreasing the band gap of $TiO_2$ and enhancing its photon absorption within the visible spectrum. Photoexcitation causes the formation of electron-hole pairs ($e^-/h^+$). Electrons are transported from the conduction band of $TiO_2$ to $Cu^{2+}$, which is then reduced to $Cu^+$, suppressing charge recombination and promoting interfacial charge separation. In this context, the Cu sites act as effective electron traps that further suppress electron–hole recombination, thereby prolonging the lifetime of photogenerated charge carriers and facilitating subsequent redox reactions. Electrons reduce dissolved oxygen ($O_2$) to form superoxide radicals ($O^{2-}$), whereas photogenerated holes in the valence band react with surface-bound water or hydroxyl ions to produce hydroxyl radicals ($\cdot OH$) [47]. Both radicals exhibit high reactivity and facilitate the progressive oxidative degradation of the CV dye into simpler intermediates, which ultimately decompose into $CO_2$, $H_2O$, and inorganic ions. Furthermore, the fly ash matrix adds stability and offers additional adsorption sites. This cooperative behaviour of ZSM-5, Cu, and $TiO_2$ is consistent with recent studies on the optimization of Cu-doped photocatalysts by surface modification [18] and with catalytic shunt mechanisms proposed for multi-component catalysts [48], which together support the enhanced charge separation and reactive species formation observed in this work. So, improved CV dye degradation efficiency under visible light irradiation is guaranteed by the combined impacts of ZSM-5 textural features, Cu electron trapping function, and $TiO_2$ photocatalytic activity.

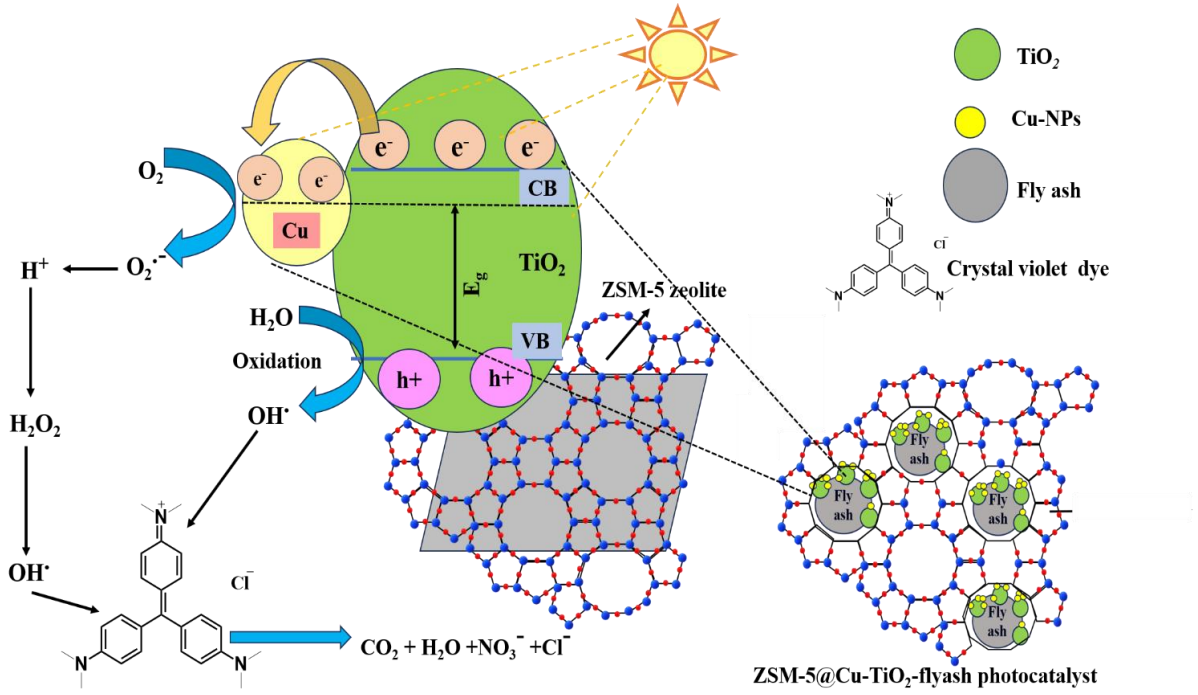


**Scheme 4.1.** The proposed photodegradation mechanism of CV dye by ZFT-Cu composite

under solar/visible light irradiation.

To better understand the contribution of Cu and ZSM-5, the photocatalytic behavior of the developed composites was evaluated in comparison with previously reported fly ash–$TiO_2$ and fly ash–$TiO_2$–Cu systems. In the fly ash–$TiO_2$ composite, $TiO_2$ serves as the main photocatalytic active component by producing electron–hole pairs under light exposure, whereas fly ash primarily functions as a supporting matrix with additional adsorption capability. Upon Cu incorporation, the fly ash–$TiO_2$–Cu composite exhibited improved charge separation because Cu species acted as electron acceptors, thereby reducing electron–hole recombination and promoting the formation of reactive oxygen species involved in dye degradation. In the present study, the addition of ZSM-5 further enhanced the surface area, pore structure, and adsorption properties of the composite, facilitating higher adsorption of dye molecules around the active photocatalytic sites. Consequently, the combined influence of fly ash, $TiO_2$, Cu, and ZSM-5 resulted in superior adsorption and photocatalytic degradation performance relative to the earlier catalyst systems.

### 4.8 Reusability and photostability of the prepared photocatalyst

The 3ZFT-$Cu_1$ composite was tested for its photostability and reusability by exposing it to visible light for five cycles of crystal violet (CV) dye photocatalytic degradation. For each reusability test, 5 mg of the composite was dispersed in 10 mL of 5 ppm CV dye solution and irradiated with a visible light source (300 W Xe lamp, $\lambda > 420$ nm) for 180 minutes under constant magnetic stirring to maintain uniform suspension and efficient photon–catalyst interaction. After every cycle, the used catalyst was obtained by centrifugation, regenerated using water and ethanol as desorbing agents to remove the adsorbed dye molecules, and dried at 80 °C for 6 h before reuse. The catalyst weight was measured after each run and showed only negligible loss (<3%) across the five cycles, confirming good structural stability.

As shown in **Fig. 4.14(b),** after reaching 95% in the first cycle, the CV removal effectiveness dropped to 84% in the fifth cycle. The 3ZFT-$Cu_1$ composite has remarkable photocatalytic stability and structural longevity, as seen by this little performance drop. The slight decrease is because the catalyst is lost somewhat during the washing and recovery processes between cycles, with minor surface fouling and possible blockage of active sites also contributing. But this didn't diminish the remarkable degrading efficiency of the composite, which bodes well for its future reusability in real-world wastewater treatment applications. These results validate that the catalyst maintains its structural integrity and functionality even after several reuses,

demonstrating excellent stability, recyclability, and sustained photocatalytic activity under repeated operating conditions.

### 4.9 Comparative discussion with reported photocatalysts

The ZSM-5/Fly ash-$TiO_2$/Cu composite exhibits comparable or superior photocatalytic performance toward organic pollutants compared to the catalysts reported in **Table 4.5** [22, 49–54], owing to the synergistic effect of Cu, porous ZSM-5, and fly ash support, which enhances adsorption and light absorption.

In addition to its superior activity toward dye degradation, the ZSM-5/Fly ash–$TiO_2$/Cu composite also shows strong potential for scale-up and broader environmental application. Its preparation by wet impregnation and calcination, combined with the use of low-cost fly ash as a support, makes the material cost-effective and compatible with large-scale or pilot-scale implementation. Moreover, the composite's high surface area, porous structure and visible-light activity indicate that it can be extended beyond dyes to the removal of other classes of organic pollutants such as antibiotics [55], phenolic compounds [56] and pesticides [57]. These attributes highlight its promise as a sustainable and economically viable photocatalyst for diverse wastewater treatment scenarios.

The use of fly ash-composite photocatalysts provides major environmental advantages by converting plentiful industrial waste into a valuable resource for pollution removal. However, integrating metals into the composite could potentially cause leaching. ICP–OES analysis showed minimal release of Fe and Al after five photocatalytic cycles, with Fe decreasing from 1.20 ppm to 0.45 ppm and Al from 1.56 ppm to 0.65 ppm, indicating the material's stability. The catalyst not only removes pollutants but also degrades them, reducing the overall toxicity of the treated water. The low metal leaching is supported by the minor decline in removal efficiency during reusability tests, indicating that the composites remain stable and can be reused effectively.

**Table 4.5** Comparative photocatalytic performance of different reported catalysts for the degradation of various pollutants.

| Photocatalyst | Pollutant | Light Source | Key Features / Improvements | Removal Efficiency | Reference |
|---|---|---|---|---|---|
| **$TiO_2$/Analcime zeolite** | Methyl Orange | UV | High surface area, larger pore volume, uniform $TiO_2$ dispersion, | ≈94.7 % removal of MO in 60 min | [50] |

| Photocatalyst | Pollutant | Light Source | Key Features / Improvements | Removal Efficiency | Reference |
|---|---|---|---|---|---|
| | | | more active sites | | |
| **CuO/$TiO_2$/ZSM-5** | Methyl Orange | UV/Visible | Defective ZSM-5: active sites & adsorption; CuO: electron trapping; extended visible-light absorption | ≈99 % removal of MO in 60 min | [51] |
| **$Fe_3O_4$@$TiO_2$@zeolite** | Levofloxacin | Dark (adsorption) | Magnetic separation, high surface area, $TiO_2$ adsorption | ≈96.5 % adsorption of levofloxacin | [52] |
| **$TiO_2$/ZSM-5 (TZSM)** | Sulfamethoxazole (SMX) | UV | Mechanical mixing, impregnation, and improved mineralization | ≈67 % SMX degradation within 120 min | [53] |
| **$Ag_2O$@Y Zeolite** | Ranitidine | Sunlight | Calcination, simultaneous adsorption & photocatalysis | $Ag_2O$–zeolite systems achieve ~97.51 | [54] |
| **$TiO_2$/$Fe_2O_3$/Zeolite** | Cyanide | UV | Impregnation enhanced structural stability | ≈89 % cyanide removal within 90 min | [55] |
| **CuO/Ag-Zeolite** | Methylene Blue | Dark (adsorption + antibacterial) | CuO/Ag modification, antibacterial | ≈99 % MB adsorption in 30–60 min (dark) | [56] |
| **ZSM-5/Flyash/$TiO_2$-Cu (This work)** | Crystal violet | Visible/Solar light | Synergistic effect of Cu, porous ZSM-5, fly ash support, enhanced adsorption & light absorption | 98% degradation under visible light | This work |

## 5.0 Conclusion

In the present study, ZSM-5-loaded fly ash-$TiO_2$-Cu (ZFT-$Cu_1$) composites were successfully synthesized using the wet impregnation method for the abatement of crystal violet dye and examined using XRD, FESEM, FTIR, UV-Vis DRS and BET analysis. The crystal violet (CV)

dye was degraded by this catalyst under visible and solar light irradiation. The modified composite catalyst (3ZFT-$Cu_1$) containing 3wt% ZSM-5 zeolite showed the best photocatalytic activity among all prepared catalysts, with a maximum dye removal efficiency of 98% under visible light and 95% under solar light, whereas the FT-Cu catalyst showed only 80% and 76% removal under visible and solar light, respectively. The integrated effects of Cu doping, the large surface area, porosity of fly ash, the higher crystallinity and light absorption caused by ZSM-5 inclusion are responsible for this increased efficiency. The catalyst loss was the major reason for the slight decrease, yet even after five cycles, the composites maintained 84% removal efficiency. The experimental results were more accurately described by the Freundlich isotherm than the Langmuir isotherm, indicating that multilayer adsorption is taking place. whereas the kinetic investigations demonstrated pseudo-first-order behaviour. Free radical production dominated the degradation route, as shown by scavenger experiments. The findings indicate that 3ZFT-$Cu_1$ composites serve as recyclable, stable, and effective photocatalysts under visible and solar light, presenting an environmentally sustainable solution for treating wastewater contaminated with dyes.

## References


[1] Badawi AK, Abd Elkodous M, Ali GAM, Recent advances in dye and metal ion removal using efficient adsorbents and novel nano-based materials: An overview, RSC Adv. 11(2021) 36528–53,https://doi.org/10.1039/D1RA06892J.

[2] Bouzid T, Grich A, Naboulsi A, Regti A, Tahiri AA, El Himri M, El Haddad M**,** Adsorption of Methyl Red on porous activated carbon from agriculture waste: Characterization and response surface methodology optimization, Inorg Chem Commun. 158 (2023)111544, https://doi.org/10.1016/j.inoche.2023.111544.

[3] Zhao X, Liu S, Tang Z, Niu H, Cai Y, Meng W, Wu F, Giesy JP, Synthesis of magnetic metal-organic framework (MOF) for efficient removal of organic dyes from water, Sci Rep. 5(2015)1–10, https://doi.org/10.1038/srep11849.

[4] Jiao T, Liu Y, Wu Y, Zhang Q, Yan X, Gao F, Bauer AJP, Liu J, Zeng T, Li B, Facile and Scalable Preparation of Graphene Oxide-Based Magnetic Hybrids for Fast and Highly Efficient Removal of Organic Dyes, Sci Rep. 5(2015) 1–10, https://doi.org/10.1038/srep12451.

[5] Kamaraj M, Suresh Babu P, Shyamalagowri S, Pavithra MKS, Aravind J, Kim W, Govarthanan M, β-cyclodextrin polymer composites for the removal of pharmaceutical substances, endocrine disruptor chemicals, and dyes from aqueous solution- A review of recent trends, J Environ. Manage. 351 (2024)119830, https://doi.org/10.1016/j.jenvman.2023.119830.

[6] Aouaini F, Dhaouadi F, Georgin J, Stracke Pfingsten Franco D, Alyousef H, Bonilla-Petriciolet A, Ben Lamine A, Statistical physics analysis of the adsorption of reactive red 141 dye on residual avocado peel (Persea americana) chemically modified with $H_2SO_4$ and $HNO_3$, Inorg Chem. Commun,165(2024) 1-10, https://doi.org/10.1016/j.inoche.2024.112547.

[7] Elzahar MMH, Bassyouni M, Removal of direct dyes from wastewater using chitosan and polyacrylamide blends. Sci Rep. 13(2023)1–16, https://doi.org/10.1038/s41598-023-42960-y.

[8] Christopher JJ, Srinivasan R, Lydia S, Merlin JP, Investigation of $Fe_2(MoO_4)_3$@Ppy Composite for Effective Photocatalytic Degradation of Crystal Violet Under Visible Light, J Inorg. Organomet. Polym. Mater. (2025)1-19, https://doi.org/10.1007/s10904-025-03745-0.

[9] Mulla B, Ioannou K, Kotanidis G, Ioannidis I, Constantinides G, Baker M, Hinder S, Mitterer C, Pashalidis I, Kostoglou N, Rebholz C, Removal of Crystal Violet Dye from Aqueous Solutions through Adsorption onto Activated Carbon Fabrics, C-Journal of Carbon Research.10(2024) 19, https://doi.org/10.3390/c10010019.

[10] Oladoye PO, Kadhom M, Khan I, Hama Aziz KH, Alli YA, Advancements in adsorption and photodegradation technologies for Rhodamine B dye wastewater treatment: fundamentals, applications, and future directions, Green Chemical Engineering. 5(2024) 440–60, https://doi.org/10.1016/j.gce.2023.12.004.

[11] Rahman M, Shaheen S, Ahmad T, Photocatalytic transformation of organic pollutants and remediation strategies of carbon emissions and nitrogen fixation in inland water, Materials Today Catalysis. 9(2025) , https://doi.org/10.1016/j.mtcata.2025.100103.

[12] Ramesh N, Lai CW, Johan MR Bin, Mousavi SM, Badruddin IA, Kumar A, Sharma G, Gapsari F, Progress in photocatalytic degradation of industrial organic dye by utilising the silver-doped titanium dioxide nanocomposite, Heliyon. 10(2024)1-21, https://doi.org/10.1016/j.heliyon.2024.e40998.

[13] Anucha CB, Altin I, Bacaksiz E, Stathopoulos VN, Titanium dioxide ($TiO_2$)-based photocatalyst materials activity enhancement for contaminants of emerging concern (CECs) degradation: In the light of modification strategies, Chemical Engineering Journal Advanc.10(2022)1-16, https://doi.org/10.1016/j.ceja.2022.100262.

[14] Sultana M, Mondal A, Islam S, Khatun MA, Rahaman MH, Chakraborty AK, Rahman MS, Rahman MM, Nur ASM, Strategic development of metal-doped $TiO_2$ photocatalysts for enhanced dye degradation activity under UV–Vis irradiation: A review, Current Research in Green and Sustainable Chemistry.7(2023)1-15, https://doi.org/10.1016/j.crgsc.2023.100383.

[15] Harris J, Silk R, Smith M, Dong Y, Chen WT, Waterhouse GIN. Hierarchical $TiO_2$ Nanoflower Photocatalysts with Remarkable Activity for Aqueous Methylene Blue Photo-Oxidation. ACS Omega 5 (2020)18919–34, https://doi.org/10.1021/acsomega.0c02142.

[16] Yuan Z, Zhu X, Gao X, An C, Wang Z, Zuo C, Dionysiou DD, He H, Jiang Z, Enhancing photocatalytic $CO_2$ reduction with $TiO_2$-based materials: Strategies, mechanisms, challenges, and perspectives, Environmental Science and Ecotechnology. 20(2024)1-16, https://doi.org/10.1016/j.ese.2023.100368.

[17] Mathew S, Ganguly P, Rhatigan S, Kumaravel V, Byrne C, Hinder SJ, Bartlett J, Nolan M, Pillai SC, Cu-Doped $TiO_2$: Visible light-assisted photocatalytic antimicrobial activity. Applied Sciences. 8(2018)1-20, https://doi.org/10.3390/app8112067.

[18] Sun Y, Zhu Y, Xin T, Li X, Zhou X, Bai G, et al, Preparation, modification and water resistance optimization of Cu–Mn CO catalyst, Appl. Surf. Sci. 708 (2025) 163768, https://doi.org/10.1016/j.apsusc.2025.163768.

[19] Aghajari N, Ghasemi Z, Younesi H, Bahramifar N, Synthesis, characterization and photocatalytic application of Ag-doped Fe-ZSM-5@$TiO_2$ nanocomposite for degradation of reactive red 195 (RR 195) in aqueous environment under sunlight irradiation, J. Environ. Health Sci. Eng. 17(2019)219–32, https://doi.org/10.1007/s40201-019-00342-5.

[20] Mahadwad OK, Parikh PA, Jasra R V, Patil C, Photocatalytic degradation of reactive black-5 dye using $TiO_2$ impregnated ZSM-5, Bull. Mater. Sci. 34 (2011)551-556, https://doi.org/10.1007/s12034-011-0124-2.

[21] Singh K, Singh AK, Kumar A, Agarwal A, Fly ash and $TiO_2$ modified fly ash as adsorbing materials for removal of Cd(II) and Pb(II) from aqueous solutions, J. of Hazardous Materials Advances.10(2023)1-18, https://doi.org/10.1016/j.hazadv.2023.100256.

[22] Mergenbayeva S, Abitayev Z, Batyrbayeva M, Vakros J, Mantzavinos D, Atabaev TS, Poulopoulos SG, $TiO_2$/Zeolite Composites for SMX Degradation under UV Irradiation. Catalysts. 14(2024)1-16, https://doi.org/10.3390/catal14020147.

[23] Al-Wasidi AS, Saad FA, AlReshaidan S, Naglah AM, Facile Synthesis of ZSM-5/$TiO_2$/Ni Novel Nanocomposite for the Efficient Photocatalytic Degradation of Methylene Blue Dye, J Inorg. Organomet. Polym. Mater. 32(2022)3040–52, https://doi.org/10.1007/s10904-022-

02336-7.

[24] Zhu J, Qi R, Tian K, Lu S, Pu S, Jian Y, Copper(II) ion-modified ZSM-5/$TiO_2$ composite material for photocatalytic degradation of ammonia gas, J. Photochem. Photobiol. A Chem.3(2025) 116472, https://doi.org/10.1016/j.jphotochem.2025.116472.

[25] Stojanović S, Vranješ M, Šaponjić Z, Rac V, Rakić V, Ignjatović Lj, Damjanović-Vasilić Lj, Photocatalytic performance of $TiO_2$/zeolites under simulated solar light for removal of atenolol from aqueous solution, Int J Environ Sci Technol. 5(2023) 1–16, https://doi.org/10.1007/s13762-022-04305-6.

[26] Sharma R, Pal B, Barman S, Synergistic effect of adsorption and photocatalytic activity of Cu deposited fly ash-$TiO_2$ composites for fuchsin blue removal under visible-solar light, Solar Energy. 287(2025) 113198, https://doi.org/10.1016/j.solener.2024.113198.

[27] Sulaiman NS, Amini MHM, Danish M, Sulaiman O, Hashim R, Kinetics, thermodynamics, and isotherms of methylene blue adsorption study onto cassava stem activated carbon, Water 13(2021)1-16, https://doi.org/10.3390/w13202936.

[28] Moustafa MT, Preparation and characterization of low-cost adsorbents for the efficient removal of malachite green using response surface modelling and reusability studies. Sci Rep. 13(2023)1-33, https://doi.org/10.1038/s41598-023-31391-4.

[29] Sumanjit, Rani S, Mahajan RK, Equilibrium, kinetics and thermodynamic parameters for adsorptive removal of dye Basic Blue 9 by ground nut shells and Eichhornia, Arabian Journal of Chemistry. 9(2016) S1464–77, https://doi.org/10.1016/j.arabjc.2012.03.013.

[30] Wijesekara DA, Sargent P, Hughes DJ, Ennis CJ, Sintered Bottom and Vitrified Silica Ashes Derived from Incinerated Municipal Solid Waste as Circular Economy-Friendly Partial Replacements for Cement in Mortars, Waste Biomass Valorization. 15(2024) 2735–56, https://doi.org/10.1007/s12649-023-02347-6.

[31] Oleiwi HF, Rahma AJ, Salih SI, Beddai AA, Comparative Study of Sol-Gel and Green Synthesis Technique Using Orange Peel Extract to Prepare $TiO_2$ Nanoparticles, Baghdad Science Journal. 21(2024) 1702–1711, https://doi.org/10.21123/bsj.2023.8089.

[32] Suguna A, Sridevi C, Parthibavarman M, Manikandababu CS, Ramachandran K, BoopathiRaja R, Design and fabrication of Zeolite Socony Mobil-5 incorporated ZnO composite for enhanced visible light photocatalytic performance, Chemical Physics Impact. 8(2024)1-11, https://doi.org/10.1016/j.chphi.2024.100621.

[33] Bahadur NM, Chowdhury F, Obaidullah M, Hossain MS, Rashid R, Akter Y, Furusawa T, Sato M, Suzuki N, Ultrasonic-Assisted Synthesis, Characterization, and Photocatalytic Application of $SiO_2$@$TiO_2$ Core-Shell Nanocomposite Particles. J Nanomater.

2019(2019)1-11, https://doi.org/10.1155/2019/6368789.

[34] Zhao Z, Wang N, Zhang H, Shang R, Xing J, Zhang D, Li J, Fabrication of ZSM-5 zeolite supported $TiO_2$-NiO heterojunction photocatalyst and research on its photocatalytic performance, J Solid State Chem. 309(2022)122895, https://doi.org/10.1016/j.jssc.2022.122895.

[35] Liu Y, Lu H, Synthesis of ZSM-5 zeolite from fly ash and its adsorption of phenol, quinoline and indole in aqueous solution, Mater. Res. Express 7 (2020) 055506, https://doi.org/10.1088/2053-1591/ab8fec.

[36] Armaković SJ, Armaković S, Zeolite-supported $TiO_2$ for enhanced photocatalytic performance in environmental applications: A review, Catalysts 15 (2025) 1–28, https://doi.org/10.3390/catal15020174.

[37] Vavouraki A, Bartzas G, Komnitsas K, Synthesis of zeolites from Greek fly ash and assessment of their copper removal capacity, Minerals 10 (2020) 1–18, https://doi.org/10.3390/min10100844.

[38] Manyepedza T, Gaolefufa E V., Beas IN, Maubane-Nkadimeng M, Kabomo MT, ZSM-5 Zeolite Synthesis from Coal Fly Ash Synthesised Silica: Sole Silica & Alumina Source. ChemistryOpen. 14(2025)1-8, https://doi.org/10.1002/open.202400314.

[39] Tu Y, Zhong J, Ding H, Zhang H, Lv G, Zhang J, et al, Preparation of fly ash supporting nano-$TiO_2$ composite photocatalyst by a wet mechanical grinding method, Chem. Phys. Lett. 805 (2022) 139978, https://doi.org/10.1016/j.cplett.2022.139978.

[40] Azam A, Iqbal T, Efficient fabrication of Cu-doped $TiO_2$ nanoparticles for enhanced visible-light photocatalysis and antimicrobial efficacy, J. Inorg. Organomet. Polym. Mater. 34 (2024) 5596–619, https://doi.org/10.1007/s10904-024-03232-y.

[41] Shikuku VO, Mishra T, Adsorption isotherm modelling for methylene blue removal onto magnetic kaolinite clay: A comparison of two-parameter isotherms, Appl. Water Sci. 11 (2021), https://doi.org/10.1007/s13201-021-01440-2.

[42] Edet UA, Ifelebuegu AO, Kinetics, isotherms, and thermodynamic modelling of the adsorption of phosphates from model wastewater using recycled brick waste, Processes 8 (2020), https://doi.org/10.3390/pr8060665.

[43] Bansal M, Pal B, Kumar Das R, Improved adsorption of Fuschin Blue with $Sn^{2+}$ impregnated Zn–Bi mixed metal hydroxide, Next Sustainability 4 (2024) 100060, https://doi.org/10.1016/j.nxsust.2024.100060.

[44] Abdoul HJ, Yi M, Prieto M, Yue H, Ellis GJ, Clark JH, et al, Efficient adsorption of

bulky reactive dyes from water using sustainably derived mesoporous carbons, Environ. Res. 221 (2023), https://doi.org/10.1016/j.envres.2023.115254.

[45] Abdu M, Tibebu S, Babaee S, Worku A, Msagati TAM, Nure JF, Optimization of photocatalytic degradation of Eriochrome Black T from aqueous solution using $TiO_2$-biochar composite, Results Eng. 25 (2025) 104036, https://doi.org/10.1016/j.rineng.2025.104036.

[46] Menon K, Lopis AD, Choudhari KS, Kulkarni B, Maradur S, Kulkarni SD, Scavenger-free solar photocatalytic degradation of textile dyes and antibiotics using magnetically separable bi-junctional photocatalyst, Mater. Res. Bull. 181 (2025) 113074, https://doi.org/10.1016/j.materresbull.2024.113074.

[47] Kanakaraju D, Jasni MAA, Pace A, Ya MH, Enhanced dye-removal performance of Cu-$TiO_2$-fly ash composite by optimized adsorption and photocatalytic activity under visible light irradiation, Environmental Science and Pollution Research. 48(2021) 68834–45, https://doi.org/10.1007/s11356-021-15440-x.

[48] Tian G, Li Z, Liao D, Zhang C, Peng HJ, Liu X, et al, Efficient syngas conversion via catalytic shunt, Nat. Sustain. 8 (2025) 508–19, https://doi.org/10.1038/s41893-025-01551-7.

[49] Huayna G, Laura A, Churata R, Lazo L, Guzmán R, Ramos PG, et al, Synthesis and characterization of a photocatalytic material from $TiO_2$ nanoparticles supported on zeolite obtained from ignimbrite residue used in decolorization of methyl orange, Appl. Sci. 14 (2024), https://doi.org/10.3390/app14083146.

[50] Wang C, Liang X, Wang L, Yu Q, Du F, Liu S, et al, Multicomponent modification of nano-$TiO_2$ with defective ZSM-5, CuO and Ag for enhanced photocatalytic and antibacterial performance, J. Photochem. Photobiol. A Chem. 472 (2026) 116787, https://doi.org/10.1016/j.jphotochem.2025.116787.

[51] Ramutshatsha-Makhwedzha D, Mavhungu ML, Baloyi J, Mbaya R, Synthesis and characterization of $Fe_3O_4$@$TiO_2$@zeolite nanocomposite adsorbent for the removal of levofloxacin antibiotic from environmental water matrices, J. Iranian Chem. Soc. 22 (2025) 113–28, https://doi.org/10.1007/s13738-024-03135-2.

[52] Al-Jubouri SM, Sabbar HA, Khudhair EM, Ammar SH, Al Batty S, Yas Khudhair S, et al, Silver oxide–zeolite for removal of an emerging contaminant by simultaneous adsorption–photocatalytic degradation under simulated sunlight irradiation, J. Photochem. Photobiol. A Chem. 442 (2023) 114763, https://doi.org/10.1016/j.jphotochem.2023.114763.

[53] Eskandari P, Farhadian M, Solaimany Nazar AR, Jeon BH, Adsorption and photodegradation efficiency of $TiO_2$/$Fe_2O_3$/PAC and $TiO_2$/$Fe_2O_3$/zeolite nanophotocatalysts

for the removal of cyanide, Ind. Eng. Chem. Res. 58 (2019) 2099–112, https://doi.org/10.1021/acs.iecr.8b05073.

[54] Yahya NAA, Samir OM, Al-Ariki S, Ahmed AAM, Swillam MA, Synthesis of novel antibacterial nanocomposite CuO/Ag-modified zeolite for removal of MB dye, Sci. Rep. 13 (2023) 1–16, https://doi.org/10.1038/s41598-023-40790-6.

[55] Hu XY, Zhou K, Chen BY, Chang CT, Graphene/$TiO_2$/ZSM-5 composites synthesized by mixture design for photocatalytic degradation of oxytetracycline under visible light: Mechanism and biotoxicity, Appl. Surf. Sci. 362 (2016) 329–34, https://doi.org/10.1016/j.apsusc.2015.10.192.

[56] Abdul Razzaq GH, Saeed LI, Humadi JI, An eco-friendly approach towards fast phenolic removal from refinery wastewater by ZSM-5 zeolite–CuO catalysts, Int. J. Environ. Sci. Technol. 22 (2025) 9113–28, https://doi.org/10.1007/s13762-024-06211-5.

[57] Stojanović S, Rac V, Mojsilović K, Vasilić R, Marković S, Damjanović-Vasilić L, Photocatalytic degradation of bisphenol A in aqueous solution using $TiO_2$/clinoptilolite hybrid photocatalyst, Environ. Sci. Pollut. Res. 30 (2023) 84046–60, https://doi.org/10.1007/s11356-023-28397-w.

# Conclusion and Future Prospects

The utilization of semiconductor-based photocatalysts for environmental remediation has gained considerable attention, and the present thesis focuses on advancing this concept through the development of sustainable, waste-derived materials. Fly ash–$TiO_2$ composites were first fabricated to exploit the synergistic benefits of a low-cost industrial by-product with a proven photocatalyst. The incorporation of fly ash enhanced the surface area, adsorption capacity, and dispersion of $TiO_2$, thereby improving pollutant–catalyst interaction and overall photocatalytic performance. To further extend the light absorption capability and suppress electron–hole recombination, copper was introduced into the $TiO_2$–fly ash framework. The Cu-modified composites exhibited significantly improved photocatalytic efficiency under visible and solar irradiation, confirming the role of metal loading in facilitating charge separation and broadening the photo-response region. Building upon this, ZSM-5 was incorporated into the Cu/$TiO_2$–fly ash system to create a multifunctional composite with superior porosity, enhanced adsorption–photocatalysis coupling, and better structural stability. The resulting ZSM-5–Cu/$TiO_2$–fly ash material demonstrated excellent dye removal efficiency, recyclability, and robustness, highlighting its strong potential as a cost-effective photocatalyst for wastewater treatment. Overall, this work establishes that the strategic integration of fly ash, metal modification, and porous supports such as ZSM-5 can significantly enhance photocatalytic activity, providing an environmentally friendly pathway for harnessing solar energy to degrade organic pollutants.

Future studies should focus on optimizing ZSM-5 and metal content to maximize adsorption–photocatalysis synergy, conducting long-term stability and regeneration tests, and performing pilot-scale experiments with real wastewater. In addition, advanced analytical techniques such as gas chromatography–mass spectrometry (GC–MS) should be employed to track degradation pathways and accurately identify intermediate species, providing deeper mechanistic insight. Further development of ternary or quaternary nanohybrids, along with their integration into continuous-flow or immobilized reactor systems, could translate these materials into robust, scalable technologies for environmental remediation.

# List of publications

1. **Sharma, R.,** Pal, B., & Barman, S. (2024). Application of fly ash-$TiO_2$ composites for enhanced adsorption and photocatalytic degradation of fuchsin dye**.** ***Environmental Science and Pollution Research*****,** 31( December 2024), 66248–66261**.** **https://doi.org/10.1007/s11356-024-35673-w. (I.F. 5.8).**

2. **Sharma, R.,** Pal, B., & Barman, S. (2025). Synergistic effect of adsorption and photocatalytic activity of Cu deposited fly ash-$TiO_2$ composites for fuchsin blue removal under visible-solar light. ***Solar Energy*****,** 287(December 2024), 113198. **https://doi.org/10.1016/j.solener.2024.113198**. **(I.F. 6.0).**

3. **Sharma, R.,** Pal, B., & Barman, S. (2026). Improved adsorption and photocatalytic activity of ZSM-5-loaded fly Ash-$TiO_2$-Cu hybrid composites for crystal violet removal under visible-solar-light irradiation. **Microporous and Mesoporous Materials,** 400 **(**15 January 2026), 113892. **https://doi.org 10.1016/j.micromeso.2025.113892(. (I. F= 4.7)**

# List of conferences and workshops

1. **Attended** "International conference on emerging trends in science and technology" organized by the Department of Applied Sciences, Punjab Engineering College, Chandigarh, from 10-11 June 2022.
2. **Volunteered** in "International conference on Sustainable Development in Chemical and Environmental Engineering" organised by the Department of Chemical Engineering, Thapar Institute of Technology, Patiala, India, 22-24 Feb 2024.
3. **Participated** in **a** 2-day Workshop on Advanced Instrumentation Techniques in Chemical Analysis held at Thapar Institute of Engineering and Technology, Patiala, Punjab, on 4-5$^{th}$ October, 2023.
4. **Volunteered and presented a poster** in DST-PURSE SUPPORTED 24$^{th}$ National Symposium on Catalysis (CATSYMP-24) "Catalysis for Sustainable Chemicals, Materials & Energy" **(CSCME-2025)** on 24-26 February 2025 Golden Jubilee celebrations of the Catalysis Society of India (CSI).
5. **Oral Presentation** in 3$^{rd}$ International Conference on Energy, Functional Materials/ Molecules and Nanotechnology (ICEFN & NWSWM) 2025 on 19-22 March 2025.

Environmental Science and Pollution Research
https://doi.org/10.1007/s11356-024-35673-w

RESEARCH ARTICLE

# Application of fly ash-$TiO_2$ composites for enhanced adsorption and photocatalytic degradation of fuchsin dye

**Ridhima Sharma[1] · Bonamali Pal[1] · Sanghamitra Barman[2]**

Received: 10 February 2024 / Accepted: 25 November 2024


**Abstract**
It is important to accomplish both photocatalytic efficiency and adsorption capacity in the catalyst to produce a highly effective photocatalyst for complete dye removal from wastewater. In the current investigation, $TiO_2$ and fly ash-$TiO_2$ composites (0.5–5 wt%) were fabricated by sol–gel and wet-impregnation process, and their catalytic performance was evaluated for the effective adsorption and photocatalytic degradation of fuchsin blue dye. The catalysts were characterized by XRD, UV-DRS, SEM, EDS, RAMAN spectroscopy, and $N_2$ adsorption analysis Adsorption and degradation studies were conducted to investigate factors such as pH (2 – 10), adsorbent dose (1–9 mg), contact time (30–180 min), and initial adsorbate concentration (5–30 mg/L) to eradicate fuchsin dye from water. The 5 wt% fly ash-$TiO_2$ catalyst showed a maximum capacity for adsorption of 20.32 mg/g and 76% removal of fuchsin dye. The Langmuir isotherm model fitted well to the experimental data, whereas the adsorption process obeyed pseudo-first-order kinetics. When exposed to UV light, a 5 wt% fly ash-$TiO_2$ composite demonstrated maximum photocatalytic degradation of 88% after 180 min, followed by a pseudo-first-order kinetic model. The catalyst was easily reusable for five cycles without losing dye removal effectiveness.

**Keywords** Fly ash · Fly ash-$TiO_2$ composites · Fuchsin blue · Adsorption · Photocatalytic degradation

**Abbreviations**

| | |
|---|---|
| FA | Fly ash |
| XRD | X-ray diffraction |
| FESEM | Field emission scanning electron microscopy |
| EDS | Energy dispersive spectroscopy |
| DRS | Diffuse reflectance spectrophotometer |
| HRMS | High-resolution mass spectroscopy |
| BET | Brunner–Emmet–Teller |
| BJH | Barrett–Joyner–Halend |
| FB | Fuchsin blue |
| VB | Valence band |
| CB | Conduction band |

Responsible Editor: Sami Rtimi

✉ Sanghamitra Barman
sbarman@thapar.edu

[1] Department of Chemistry and Biochemistry, Thapar Institute of Engineering and Technology, Patiala 147004, Punjab, India

[2] Department of Chemical Engineering, Thapar Institute of Engineering and Technology, Patiala 147004, Punjab, India

## Introduction

Coal power stations significantly meet the world's energy needs (Hussain et al. 2020). Fly ash is a solid waste produced in huge from the combustion of raw coal in power plants (Yao et al. 2015). The amount of coal fly ash produced annually is expected to be 750 million tonnes and is only used in some industries to the extent of 25% (Hussain et al. 2020). Coal fly ash is one of many industrial solid wastes (by-products) that are an attractive and low-cost adsorbent with good specific surface area, porosity, and particle size due to its ability to adsorb a variety of hazardous and non-biodegradable dyes from coloured effluents (Okte et al. 2014; Visa et al. 2015). Fly ash is improperly handled, stored, and disposed which causes significant contamination to the earth, air, water, and even living creatures. The environment is contaminated, and human health is at risk when untreated fly ash from power plant chimneys is released into the atmosphere (Bartoňová 2015; Ding et al. 2015). As a result, recycling fly ash has sparked a lot of interest in research scientists to find sustainable and environmentally friendly ways to deal with this waste product (Blissett & Rowson 2012). The composite material made up of fly ash and $TiO_2$ is reported to show improved photocatalytic properties (Ma et al. 2015;

Published online: 02 December 2024

Solar Energy 287 (2025) 113198

Contents lists available at ScienceDirect

Solar Energy

journal homepage: www.elsevier.com/locate/solener

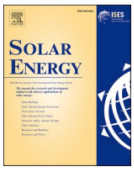

# Synergistic effect of adsorption and photocatalytic activity of Cu deposited fly ash-$TiO_2$ composites for fuchsin blue removal under visible-solar light

Ridhima Sharma [a], Bonamali Pal [a], Sanghamitra Barman [b,*]

[a] Department of Chemistry and Biochemistry, Thapar Institute of Engineering and Technology, Patiala 147004, Punjab, India
[b] Department of Chemical Engineering, Thapar Institute of Engineering and Technology, Patiala 147004, Punjab, India

ARTICLE INFO

*Keywords:*
Fly ash-$TiO_2$ composite
Cu loaded Fly ash-$TiO_2$
Adsorption
Photocatalytic degradation
Visible/solar light

ABSTRACT

In present investigation, $TiO_2$, fly ash (F)-$TiO_2$ (T), and Cu (0.5–2 wt%) photo-deposited fly ash-$TiO_2$ (FT-$Cu_{0.5\text{-}2}$) composites are fabricated to investigate their adsorption and photocatalytic degradation efficiency of (Fuchsin blue) FB dye under visible light and direct sunlight. Surface analysis was conducted using X-ray diffraction(XRD), Diffuse Reflectance Spectroscopy(DRS) while morphological analysis was performed using, High Resolution Transmission Electron Microscopy(HR-TEM), X-ray Photoelectron Spectroscopy(XPS) and $N_2$-adsorption Brunauer-Emmett-Teller (BET) confirming formation of Fly ash-$TiO_2$ (FT) and (FT-$Cu_{0.5\text{-}2}$) composites. Cu nanoparticles, ranging from 7-17 nm, were uniformly deposited upon FT composite surface. Various adsorption parameters, including adsorbent dosage, pH, contact duration and FB dye concentration, were studied. After 180 min of dark adsorption, 1 wt% Cu-loaded FT composite (FT-$Cu_1$) exhibited highest FB dye removal (77 %), following Langmuir adsorption isotherm. Photocatalytic degradation of FB dye by FT-$Cu_1$ was 92 % under direct sunlight and 94 % under visible light, which is significantly higher than bare FT catalyst (68 % under direct sunlight) and (71 % under visible light) achieved due to combined effect of Cu, fly ash, and $TiO_2$ particles. Cu loading improves charge ($e^-$-$h^+$) separation efficiency of photoexcited fly ash-$TiO_2$ and enhances visible light absorption by introducing intermediate energy levels in $TiO_2$ bandgap. Photodecomposition pathway of FB dye was identified through free radical trapping with hole scavengers and identification of intermediate photo-products using High-Resolution Mass Spectrometry (HRMS) analysis. FT-Cu composite demonstrated excellent photostability and recyclability, for degradation of organic pollutants. Degradation efficiency remained around 83 % even after five cycles confirming its durability for repeated use.

## 1. Introduction

Environmental integrity and public health are significantly impacted by the harmful effects of industrial dye pollution in wastewater. These dyes, widely used in many industries, including leather and textiles, showed significant resistance to deterioration, extending their longevity in the environment [1]. Unregulated dye pollution harms the ecosystem over time, affecting the aesthetics of water bodies and endangering aquatic life [2]. A decrease in biodiversity may result from the toxic, mutagenic, or even carcinogenic effects of certain dyes, which put marine life in danger [3]. Therefore, employing an environmentally and economically sustainable technique is essential to remove all colour molecules from wastewater before it is released into the environment [4,5]. Its high toxicity, carcinogenicity, and lack of biodegradability make it a hazardous contaminant [6]. Fuchsin blue dye contact may result in serious health complications such as headaches, skin and respiratory tract irritations, vertigo, and vomiting [7]. This dye has poor biodegradability and is toxic and carcinogenic; it must be eliminated from wastewater before discharge into the water effluents to reduce environmental contamination [8].

Several approaches have been developed for the extraction and elimination of contaminants from wastewater, including membrane separation, biological oxidation process, chemical precipitation, ion exchange, photocatalytic degradation, and adsorption[9,10]. Nevertheless, these techniques have drawbacks such as high operating costs, energy consumption, poor selectivity, regeneration, and reusability problems [11]. The adsorption process is extensively employed in wastewater treatment because of its ease of operation, environmental friendliness, excellent efficacy, and minimal energy requirement [12,13]. Photocatalysis is a promising and eco-friendly advanced

* Corresponding author.
*E-mail addresses:* bpal@thapar.edu (B. Pal), sbarman@thapar.edu (S. Barman).

https://doi.org/10.1016/j.solener.2024.113198
Received 27 September 2024; Received in revised form 27 November 2024; Accepted 12 December 2024

Microporous and Mesoporous Materials 400 (2026) 113892

Contents lists available at ScienceDirect

Microporous and Mesoporous Materials

journal homepage: www.elsevier.com/locate/micromeso

# Improved adsorption and photocatalytic activity of ZSM-5-loaded fly ash–$TiO_2$–Cu hybrid composites for crystal violet removal under visible-solar light irradiation

Ridhima Sharma [a], Sanghamitra Barman [b,*], Bonamali Pal [a,**]

[a] Department of Chemistry and Biochemistry, Patiala, 147004, Punjab, India
[b] Department of Chemical Engineering, Thapar Institute of Engineering and Technology, Patiala, 147004, Punjab, India

ARTICLE INFO

*Keywords:*
ZSM-5 loaded fly ash-$TiO_2$-Cu composite
Crystal violet degradation
Visible-light photocatalysis
Synergistic effect
Dye adsorption
Solar irradiation

ABSTRACT

In the present investigation, Cu photo-deposited fly ash–$TiO_2$ (FT-$Cu_1$) composites were synthesized. The prepared composite was modified with 1 wt%, 3 wt%, and 5 wt% of ZSM-5 zeolite and named as 1ZFT-$Cu_1$, 3ZFT-$Cu_1$, and 5ZFT-$Cu_1$, respectively, for the removal of crystal violet dye. Experiments were conducted to evaluate the performance of the ZFT-$Cu_1$ composites (1, 3, and 5 wt% ZSM-5 loadings) for the adsorption and photocatalytic degradation of crystal violet under visible and solar light. Structural and optical characterizations were performed using UV–VIS DRS, FE-SEM, XRD, FTIR, and BET surface area analysis. The results demonstrated enhanced crystallinity, decreased agglomeration, and improved visible-light absorption due to incorporation of ZSM-5 zeolite into the FT-$Cu_1$ composite. Among the modified composites, the 3ZFT-$Cu_1$ composite (3 wt% ZSM-5 loading) showed the highest photocatalytic activity, achieving 98 % removal of CV dye ($Q_e$ = 27 mg/g) under visible light and 95 % removal ($Q_e$ = 20.24 mg/g) under solar light at catalyst dose of 5 mg, dye concentration of 5 mg/L, contact time of 180 min, and pH 9. The adsorption data were well-fitted to Freundlich isotherms confirming multilayer coverage, and the kinetics adhered to a pseudo-first-order model. The enhanced efficiency is attributed to the synergistic effects of Cu doping, porous ZSM-5, and fly ash support, which improved light absorption and dye adsorption. Furthermore, 3ZFT-$Cu_1$ retained 84 % degradation efficiency after five cycles, confirming good stability and reusability. The photodecomposition pathway of CV dye was identified through free radical trapping using hole scavengers, confirming its visible-light-active potential for dye-based wastewater treatment.

## 1. Introduction

Water contamination from organic dyes is a serious issue that endangers the ecosystem. Industries including paper, plastics, leather, textiles, and pharmaceuticals discharge large volumes of wastewater tainted with dyes into natural water pools [1,2]. The toxic organic dyes often disrupt the ecosystems by lowering the oxygen levels and killing the aquatic life. [3,4]. Human exposure to polluted water can cause a range of health problems. Certain dyes are carcinogenic, mutagenic, and teratogenic, posing long-term risks such as cancer and genetic mutations. Drinking contaminated water can cause gastrointestinal disorders, damage to the kidneys, and liver [5–7].

Crystal violet (CV) is a dye derived from aniline that has been widely utilized as a disinfectant, a staining agent in biomedical applications, a pH indicator, and a colouring agent in the textile industry [8]. It is a potent mutagen and has been classified as a potential carcinogen. Excessive exposure to CV dye can cause cancer, organ damage, and reproductive disorders over time. Direct skin contact might irritate the skin with respiratory difficulties [9]. Thus, developing efficient, cost-effective, and ecologically sustainable techniques for extracting crystal violet from wastewater is critically important.

Numerous approaches, such as adsorption, electrochemical

*Abbreviations:* FT, Fly ash- $TiO_2$; FT-Cu, Flyash-$TiO_2$-Copper; XRD, X-ray diffraction; FESEM, Field emission scanning electron microscopy; EDS, Energy dispersive spectroscopy; DRS, Diffuse reflectance spectroscopy; FTIR, Fourier Transform Infrared Spectroscopy; BET, Brunner- Emmet and Teller; BJH, Barrett –Joyner –Halend; CV, Crystal Violet; VB, Valence Band; CB, Conduction Band; ZFT-Cu, ZSM-5-loaded- fly ash-$TiO_2$-Copper.

* Corresponding author.
** Corresponding author.
*E-mail addresses:* sbarman@thapar.edu (S. Barman), bpal@thapar.edu (B. Pal).

https://doi.org/10.1016/j.micromeso.2025.113892
Received 11 August 2025; Received in revised form 22 September 2025; Accepted 7 October 2025
Available online 8 October 2025

Ridhima
12/1/2026

12/01/26

12/1/2026

miss

ORIGINALITY REPORT

| 15% | % | 15% | % |
|---|---|---|---|
| SIMILARITY INDEX | INTERNET SOURCES | PUBLICATIONS | STUDENT PAPERS |

PRIMARY SOURCES

| | | |
|---|---|---|
| 1 | Mohd. Shkir, Atif M. Ali. "Novel 2D/3D BiOBr/TiO2 S-scheme heterostructures photocatalyst fabrication for remarkable ciprofloxacin degradation under solar light", FlatChem, 2025<br>Publication | <1% |
| 2 | Guanghui Li, Changye Mang, Lang Xing, Pengxu Cao, Yongfeng Cai, Jun Luo, Hao Jiang. "Surfactant-assisted synthesis of Mo-doped TiO2/FAC (fly ash cenosphere) for degradation of methylene blue dye under visible light irradiation", Colloids and Surfaces A: Physicochemical and Engineering Aspects, 2022<br>Publication | <1% |
| 3 | Rezika Bakri, Hakima Bozetine, Sabrina Aziri, Yacina Djebra, Nabila Berkane, Dyhia Aberkane, Toufik Hadjersi, Abdeltif Amrane. " Microwave synthesis of green /carbon nanocomposite with enhanced photocatalytic activity under and solar light ", Journal of the Chinese Chemical Society, 2025<br>Publication | <1% |
| 4 | G. León, F. García, B. Miguel, J. Bayo. "Equilibrium, kinetic and thermodynamic studies of methyl orange removal by adsorption onto granular activated carbon", Desalination and Water Treatment, 2015<br>Publication | <1% |